Dynamic wetting/dewetting processes in complex liquid-solid systems

by

James Edward Sprittles

A thesis submitted to
The University of Birmingham
for the degree of
Doctor of Philosophy

School of Mathematics
The University of Birmingham

Abstract

In this thesis, the phenomenon of a microdrop impacting onto and spreading over surfaces of constant and variable wettability is investigated. The study is motivated by wide-ranging industrial applications of ink-jet printing technologies, in particular used by our industrial sponsor Kodak Ltd. Mathematical models for dynamic wetting phenomena are incorporated into a specially developed finite element based numerical platform. By examining different models, it was found for the first time that the interface formation model is capable of describing the experimentally observed non-uniqueness of the relationship between the contact-line speed and the dynamic contact angle. It is shown that, the interface formation model naturally captures the effect which variations in the wettability of the solid surface have on an adjacent flow, so that the model can be used, without any ad-hoc alterations, to consider the spreading of microdrops on such solids. An investigation of the effect that variation of the model's parameters has on the characteristics of the impact and spreading of microdrops has been carried out.

Acknowledgements

My time as a PhD student has provided me with some of the most enjoyable years of my life. This is mainly due to the people I have been surrounded by: some are mentioned and many are not. Above all, it is thanks to my supervisor Professor Yulii Shikhmurzaev and my partner Dr Sarah Astill that these years will be remembered so fondly.

I have been very fortunate to have had Yulii as a supervisor and I will be forever indebted to him for the time which he has spent educating me. My industrial supervisor, Dr Andrew Clarke, has also been exceptionally supportive throughout the project.

I have been lucky enough to share my PhD years with Sarah and without her these years could not have been so special. The support of Sarah, my Parents and my Gran has enabled me to fulfil my ambitions and for this I am truly grateful.

I have harassed Dr Alex Lukyanov, Dr Paul Suckling and Dr Mark Wilson for help with the development of my code and I thank each of them for kindly sharing their knowledge without ever complaining. I also acknowledge Margrit Klitz with whom I have had many useful discussions throughout my PhD studies. I thank members of the department for making the last few years so much fun. In particular, Professor Chris Parker, who has been an inspiration, and the force that is Postgrad Mathletic.

Finally, I gratefully acknowledge the financial support of the EPSRC and Kodak Ltd.

Contents

Chapter 1

Introduction

The impact and spreading of liquid drops on solid substrates is the key element of a range of industrial processes. Examples include spray cooling of surfaces, crop spraying, spray coating, solder jetting and DNA synthesis (Grissom & Wierum, 1981; Bergeron & Quéré, 2001; Yarin, 2006; Attinger *et al.*, 2000; Maier *et al.*, 2000). Increasingly, there is an interest in the dynamics of small drops, on the scale of micrometres and hence called microdrops, whose behaviour is critical to the functioning of a number of microfluidic devices (Squires & Quake, 2005). The ink-jet printer is one such device which, as well as traditional image printing, has recently been used as a dispenser of molten metal to build up electronic circuits, in a more cost effective manner than traditional fabrication methods (Gao & Sonin, 1994; Hong & Wagner, 1999; Calvert, 2001; Burns *et al.*, 2003). The large surface-volume ratio of microdrops means that the properties of the solid surface can significantly influence the drop's dynamics and, consequently, much current research has focused on how chemically heterogeneous solid surfaces can be designed in order to control the spreading of liquid drops upon them (Renardy *et al.*, 2003; Mock *et al.*, 2005).

To make unambiguous experimental observations of the dynamics of millimetre-sized drops which impact and spread on solid surfaces is complicated due to the small spatial and temporal scales of interest. However, as one can see from recent images obtained

from drop impact and spreading experiments on microdrops and millimetre-sized drops in Figure 1.1, for microdrops the situation is considerably worse. In the microdrop experiment one can, at best, measure the distance which the drop has spread and its height. More complex measurements such as the flow field inside the drop; or the position of the drop's apex, which is often not the highest point of the drop; or the angle between the free-surface and the solid, that is the 'dynamic contact angle'; appear impossible. Consequently, the development of a mathematical model which can make accurate quantitative predictions of drop impact and spreading phenomena is highly sought after: specifically, Kodak Ltd have sponsored this research into the impact and spreading of microdrops on solid surfaces as part of their ongoing long-term programme of research and development of multipurpose ink-jet printing technologies. A theoretical model has the advantages over direct experimental techniques that (*i*) spatial and temporal resolution are greatly increased and (*ii*) one can map the flow regimes of the entire parameter space of interest with an ease and cost-effectiveness that cannot be matched by using experimental techniques.

1.1 Dynamic wetting: failure of the classical fluid mechanical approach

The spreading of liquid drops over solid surfaces is an example of a 'dynamic wetting' flow, i.e. one in which a liquid moving over a solid substrate displaces a second fluid. It is well known that classical fluid mechanics is unable to describe this class of flows in which a 'contact line', formed by the liquid-fluid interface joining the solid, moves along the solid substrate (Shikhmurzaev, 2007). Specifically, it was initially shown that if the liquid-fluid interface is assumed to be planar near the contact line, then there is a non-integrable tangential stress at the contact line (Huh & Scriven, 1971). This means that no finite force would be able immerse a solid body in a liquid! It was later shown, in Shikhmurzaev

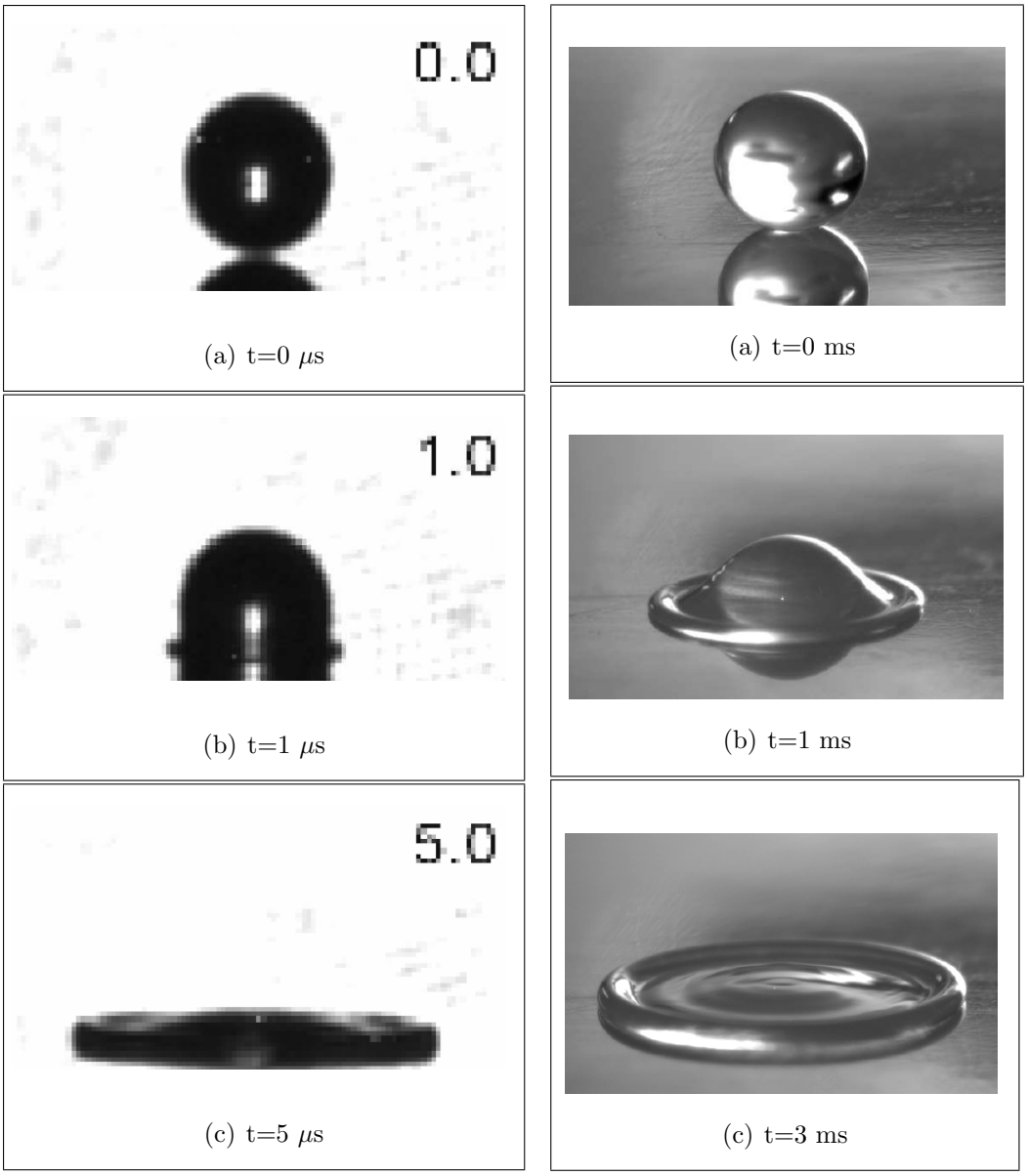

(a) t=0 μs (a) t=0 ms

(b) t=1 μs (b) t=1 ms

(c) t=5 μs (c) t=3 ms

Figure 1.1: Microdrop (left) versus millimetre-sized drop (right): a 25 μm radius drop of water impacting and spreading on a substrate (left) from Dong (2006) compared to a 1.3 mm drop of water impacting and spreading on a wax substrate (right) from Rioboo *et al.* (2002).

(2006), that in the general case, with the liquid-fluid interface free, no solution exists at all. The free surface is bent so strongly near the contact line, that it fails to meet the solid surface. The failure of the classical formulation to describe dynamic wetting flows became known as the 'moving contact-line problem'.

Before considering the theoretical approaches that have been proposed in the literature to overcome the moving contact-line problem, first, in the next section, we shall describe some observations from drop impact and spreading experiments. Particular attention is given to the behaviour of the dynamic contact angle, which must be specified in a model as it is a boundary condition for the equations which determine the free-surface's shape, and the flow field in the vicinity of the moving contact line. After, we consider if theoretical approaches are able to account for the experimental findings.

Numerous experimental and theoretical papers have been published on a wide variety of aspects of drop impact and spreading phenomena; here, we shall outline only a selected few of these and note that reviews of the subject can be found in Lesser & Field (1983), Rein (1993) and Yarin (2006).

1.2 Experimental observations

Images from drop impact and spreading experiments are usually taken using either high speed photography or a flash technique in which snapshots are taken at different instances of a repeated experiment. Popular measures of the drop's evolution are the position of the contact line (or, when non-dimensionalized with respect to the initial drop radius, the so-called spread factor), the apex height of the drop, the highest point of the drop and the dynamic contact angle, all as a function of time. Experimental investigations can be broadly split into those on microdrops, of which there have been very few, and those on millimetre-sized drops on which there is a comprehensive body of literature.

1.2.1 Microdrop impact and spreading

The droplets produced by ink-jet printers have a radius of $5 - 50$ μm and impact a solid at a speed in the range $1 - 30$ m s^{-1}. At these scales, experimental imaging becomes very challenging and, to date, only a few investigations, which are discussed below, have studied this parameter regime.

In Van Dam & Le Clerc (2004), the impact of $18-42$ μm radius droplets at speeds from $0.74 - 13.8$ m s^{-1} are studied on three different substrates. It is observed that the drops remain axisymmetric throughout spreading, which, we shall see, significantly simplifies the modelling of these flows. It is found that air bubbles may become entrapped near the centre of the drop, in a similar fashion to those observed in millimetre-sized drops (Chandra & Avedisian, 1991; Mehdi-Nejad *et al.*, 2003), and it is suggested that the mechanism for their formation could be air entrapment during impact.

In Dong *et al.* (2007), a similar parameter regime is investigated along with a comparison between microdrop and millimetre-sized drop experiments. The liquid used had density ρ, viscosity μ and a surface tension σ with air. Then, for a drop of radius a, the liquid and the impact speed U_0 were varied so that the same Weber($=\rho U_0^2 a/\sigma$) and Reynolds($=\rho U_0 a/\mu$) numbers were obtained for both the millimetre and micron sized drop impact experiments. The evolution of each drop was different. Therefore, one must conclude that there are missing similarity parameters and it seems most likely these are associated with the interfacial physics.

More complex situations, such as the impact and spreading of polymer microdrops (Perelaer *et al.*, 2009); the spreading of liquid microdrops on, and imbibition into, porous media (Clarke *et al.*, 2002; Holman *et al.*, 2002); the evaporation of microdrops (Lim *et al.*, 2009); and the freezing of spreading microdrops (Attinger *et al.*, 2000), have been considered experimentally, but fall outside the scope of this thesis.

The overwhelming majority of experimental studies have concentrated on the impact

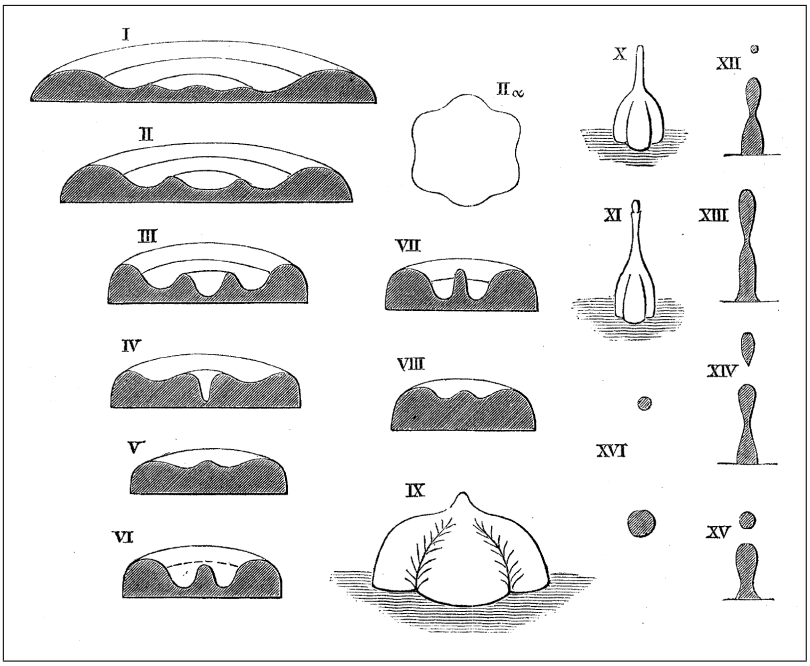

Figure 1.2: Sketches of a millimetre-sized drop of milk impacting, spreading and then rebounding off a smoked glass (hydrophobic) substrate. Features such as capillary waves and pinch-off of droplets on rebound can clearly be observed. From Worthington (1876-1877).

and spreading of millimetre-sized drops which impact at a speed of the order of metres per second.

1.2.2 Millimetre-sized drop impact and spreading

Worthington (1876-1877) was the first to uncover the variety of shapes that a drop, which has impacted a solid surface, forms while spreading. Using an experimental setup conceptually similar to those used today, he illuminated the drop with a spark at a given instance and sketched its form. The drawings, shown in Figure 1.2, exhibit diverse and remarkable features such as the formation of capillary waves and the partial rebound of the drop.

Despite huge improvements in experimental techniques, measuring a millimetre-sized drop's properties, such as its dynamic contact angle, still remains very challenging immediately after impact due to the extremely short time scales. Determining the initial time

at which impact occurs is a major source of error: for example, it is stated in Rioboo *et al.* (2002) that in the early stages of wetting there is an uncertainty in the time from impact of up to 25%.

Rioboo *et al.* (2002) conduct a thorough parameter investigation into the dynamics of millimetre-sized drops impacting a solid at a few metres per second. It is found that a drop's evolution can roughly be split into different stages. The first stage is the kinematic phase in which the contact-line radius, r_c, approximately follows the power-law $r_c \sim t^{0.5}$. This is followed by a spreading phase in which the other parameters (such as the wettability of the surface, viscosity and surface tension) begin to have an influence on the dynamics. After this period, there is a relaxation phase where the drop's dynamics depend heavily on the wettability of the substrate before finally, in the equilibrium phase, the drop reaches a constant diameter or, on a highly wettable surface, continues to spread at $r_c \sim t^{1/10}$, in agreement with the results of Tanner (1979).

Experimentalists have studied a range of events such as, for example, the position of maximum spread of a droplet and the time at which this occurs (e.g. Attané *et al.*, 2007), the possible rebound of the drop back off the solid (e.g. Mao *et al.*, 1997), the evolution of the drop into a toroidal shape (e.g. Renardy *et al.*, 2003) or the drop creating a splash after impact (e.g. Xu *et al.*, 2005). The role of a myriad of physical effects on the drop's dynamics have been thoroughly investigated; for example, to name just a few, surfactants on the free surface (e.g. Pasandideh-Fard *et al.*, 1996), the solidification of drops (e.g. Schiaffino & Sonin, 1997), the use of a non-Newtonian liquid (e.g. Bergeron *et al.*, 2000), compressibility of the liquid (Lesser & Field, 1983) and gradients in temperature through a drop (e.g. Chandra & Avedisian, 1991). Results in Xu *et al.* (2005) are particularly interesting: it is shown that by reducing the air pressure, one can inhibit the splash which an impacting drop creates at room pressure. It is apparent that there are a plethora of physical effects which have a significant influence on the dynamics of a drop. However, we shall now see that, when these additional effects are stripped away, experimental

investigations have shown that the model which underpins all of the previous theoretical works, fails to account for experimental results. These results concern the dynamics of the contact angle during spreading.

It has been observed experimentally in drop impact and spreading experiments (Bayer & Megaridis, 2006), as well as in other dynamic wetting flows (e.g. Hoffman, 1975), that the dynamic contact angle θ_d increases from its equilibrium value θ_e as the contact-line speed U_c increases. Often, in theoretical models for dynamic wetting, it is further assumed that the dynamic contact angle is a function of the contact-line speed and material parameters, which we henceforth refer to as a speed-angle relationship. For example, in the Hoffman-Voinov-Tanner law $\theta_d \propto U_c^{1/3}$ (Kistler, 1993; Eggers, 2004). Then, different impact speeds or drop sizes will not alter the speed-angle relationship. Such formulae form part of what we shall refer to as a 'conventional model'.

In Šikalo *et al.* (2005) and Bayer & Megaridis (2006) experiments were specifically designed to test the qualitative predictions of a speed-angle relationship. In these experimental setups, it is stated that the contact angle of a millimetre-sized drop impacting a substrate at a few metres per second can be measured with a maximum error of $\sim 5^\circ$. A simple experiment is designed to determine if, for a given liquid-solid combination, there is a unique relationship between the contact-line speed and dynamic contact angle. The authors considered different impact speeds and plotted the subsequent speed-angle relationship during spreading; these are shown in Figure 1.3. It is clear that there is no unique curve of best-fit which goes through all the data points and that even in a single drop impact and spreading experiment the relationship is multivalued[1]: this is in conflict with the idea of proposing *any* speed-angle relationship.

The conclusion of Šikalo *et al.* (2005, p. 11) is:

> "The apparent dynamic contact angle is not only a function of the contact-line speed but also a function of the flow field in the vicinity of the moving contact

[1]For example, look at the We=0.3 experiment in the top graph of Figure 1.3 near $U_c = 0.1$.

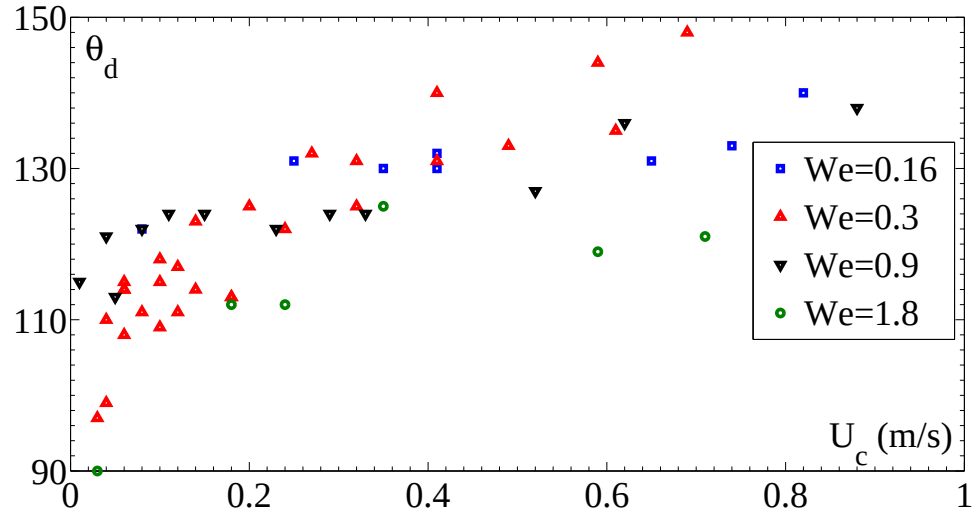

(a)

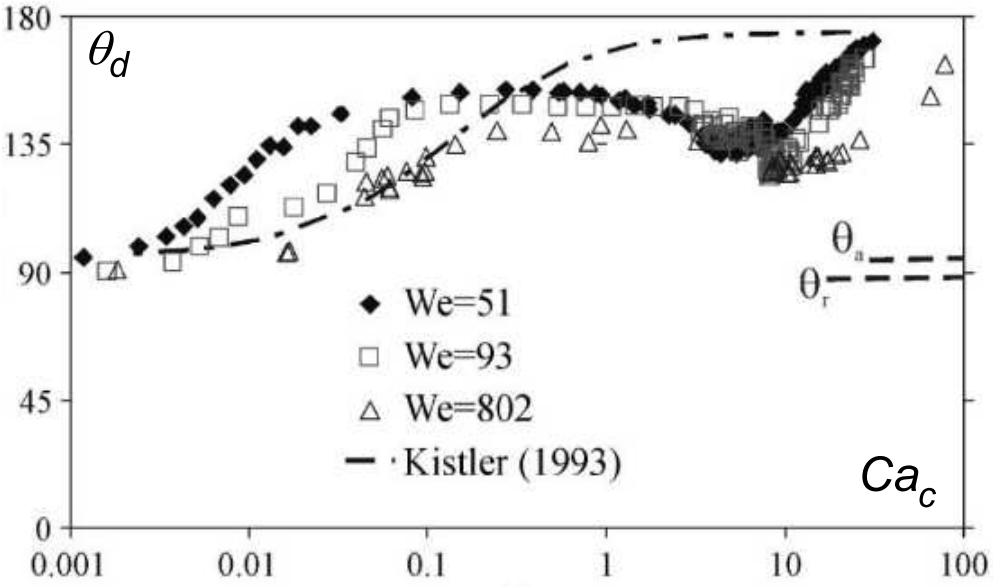

(b)

Figure 1.3: Relationship between the dynamic contact angle θ_d, and the contact-line speed U_c (or the Capillary number based upon it $Ca_c = \mu U_c/\sigma$) for different Weber numbers based on the impact speed, $We = \rho U_0^2 a/\sigma$, of a millimetre-sized drop of water on a partially wettable substrate. Published in (a) Bayer & Megaridis (2006) and (b) Šikalo *et al.* (2005).

line."

Bayer & Megaridis (2006, p. 415) similarly conclude that:

> "There is no universal expression to relate contact angle with contact-line speed."

Thus, experiments show that the dynamic contact angle is a functional of the flow field, as opposed to just a function of the contact-line speed and material parameters.

The effect of the flow field on the contact angle was first demonstrated experimentally in the curtain coating process (Blake *et al.*, 1994). In this experiment, a liquid curtain falls on a moving substrate and coats it with a thin film; industrially, amongst other things, this is used to create photographic films. In this process, one can manipulate the flow field whilst maintaining the same contact-line speed. The contact angle was observed to be dependent on the flow rate of the liquid and the height from which the curtain falls (Blake *et al.*, 1999; Clarke & Stattersfield, 2006), an effect which was termed the "hydrodynamic assist of dynamic wetting" (Blake *et al.*, 1994). Consequently, it became clear how the curtain coating process could be optimized to allow a solid to be coated as fast as possible without air entrainment into the liquid, which destroys a film's quality.

In curtain coating experiments, it has been observed that fluid particles initially on the free surface are advected through the contact line and onto the solid surface (Clarke, 1995), i.e. the motion of the fluid in the vicinity of the contact line is of a rolling nature. The contact line region is associated with a more intensive flow than that observed further away from the contact line. The same conclusion has been obtained from experiments on drops sliding down inclined planes (Dussan V & Davis, 1974) and for cylinders plunging into liquid baths (Chen *et al.*, 1997).

In summary, experiments have shown that in dynamic wetting flows, for the same liquid-solid-gas system, the speed-angle relationship can be manipulated by altering the

flow field. The flow field itself has a rolling motion in the vicinity of the contact line. We now consider if the models proposed in the literature for drop impact and spreading phenomena are able to account for these two experimental observations.

1.3 Theoretical approaches

The spreading of liquid drops has been considered in a number of different theoretical frameworks (Bonn *et al.*, 2009), encompassing a range of length scales of interest; from the microscopic, using Molecular Dynamics simulations (e.g. Gentner *et al.*, 2004), to mesoscopic approaches such as the Lattice Boltzmann method (e.g. Dupuis & Yeomans, 2004) or Diffuse Interface method (e.g. Khatavkar *et al.*, 2007) up to the Continuum Mechanics approach (e.g. Fukai *et al.*, 1993). The chosen framework depends on the level of description required. For example, if the drop size is comparable with the length of the mean free path in a liquid, then the Molecular Dynamics approach becomes attractive; however, if the drop size is relatively large, in reality anything above a few tens of nanometres, then in this method the problem becomes computationally untractable. Similar conclusions can be drawn for the mesoscopic approaches where, even to model drops on the micron scale, artificially large interfaces have to be used to provide a computationally viable formulation. It is noted in Summers *et al.* (2005) that, in the context of the Lattice Boltzmann method but equally applicable to the Diffuse Interface method, with only four or five nodes used to capture the interfacial dynamics, estimating the interface to have a thickness of 10^{-8} m, the dynamics of a 1 mm drop will require more than 20 billion nodes. Continuum theory gives a conceptual framework from which to investigate drop impact and spreading phenomena and is applicable to the overwhelming majority of problems of interest. In general, the solution to a drop impact and spreading problem formulated using this framework will require one to solve a set of analytically untractable partial differential equations (PDEs) subject to appropriate boundary conditions.

Rather than considering the full fluid mechanical problem, a number of authors have used arguments based on energy conservation to predict the maximum spread of a droplet (e.g. Park *et al.*, 2003; Attané *et al.*, 2007) and to determine if it will rebound or not (Mao *et al.*, 1997; Kim & Chun, 2001). This is achieved by balancing the kinetic, surface and potential energy prior to impact and at a chosen later stage. The major assumptions which these models make, and their main source of error, is (*i*) that the free surface of a droplet at maximum spread can be approximated by a simple shape, such as a spherical cap or pancake shape, and (*ii*) that it is possible to estimate the viscous dissipation between stages. Although these models can provide a reasonable rule-of-thumb, they are often only accurate in a small region of parameter space. In particular, most were designed for the impact and spreading of millimetre-sized drops and do not perform well for microdrop impact and spreading (Dong *et al.*, 2007).

We now consider previous attempts to solve the full fluid mechanical problem to a required degree of accuracy using computational techniques. In particular, we are interested in how the classical equations are modified to allow for a solution to be found, and how the dynamic contact angle is modelled.

1.3.1 Modelling and computation of drop impact and spreading

The majority of computational codes designed for drop impact and spreading phenomena use 'numerical slip' to overcome the moving contact line problem (e.g. Fukai *et al.*, 1995; Pasandideh-Fard *et al.*, 1996; Bussmann *et al.*, 2000; Yokoi *et al.*, 2009). That is, no-slip is applied all the way along the liquid-solid surface apart from at the contact line where, to stop it being pinned, this line is allowed to slip freely past the solid. From a mathematical viewpoint this approach is unacceptable because as the distance between nodes in the computational mesh tends to zero, in which the solution to the original PDE problem should be recovered, one has the moving contact line problem, i.e. no solution. Also, recent works on dynamic wetting have shown that using such schemes can also have

an undesirable effect on the dynamic contact angle (Schönfeld & Hardt, 2009; Afkhami *et al.*, 2009; Weinstein & Pismen, 2008).

A more satisfactory approach would be to resolve the moving contact line problem *before* discretization. It has been shown that by relaxing the no-slip condition on the solid surface, one can indeed obtain a solution to a moving contact line problem (Dussan V, 1976; Shikhmurzaev, 2007). A common approach in the dynamic wetting literature has been to use the Navier-slip condition (Navier, 1823) which states that slip, that is a difference between the tangential velocity of the solid and that of the liquid-facing side of the liquid-solid interface, is proportional to the tangential stress acting on it. Although using this condition allows for a solution to the initial PDE problem, the resulting solution predicts that (*i*) in contrast to experimental observations, fluid particles on the free surface will never reach the contact line and (*ii*) that the pressure is singular at the contact line (Shikhmurzaev, 2006). The reason that the Navier condition has rarely been used in the drop impact and spreading community is that to resolve the length scale on which the velocity deviates from no-slip, the so-called 'slip length', requires more spatial resolution near the contact line than previous codes have been designed to provide.

In a number of works on dynamic wetting, the actual contact angle[2] is set equal to its equilibrium value (e.g. Zhou & Sheng, 1990) and distinguished from the 'apparent' contact angle, that is the angle measured a finite distance from the contact line which, due to the finite spatial resolution of experimental results, is the experimentally observed angle. It is then claimed that the deviation between the actual (equilibrium) contact angle and the apparent one, caused by the curvature of the free surface near the contact line (Cox, 1986), accounts for experimental observations (e.g. Ding & Spelt, 2007). In other words, any experimentally observed dynamics of the contact angle is accounted for by the curvature of the free surface on a length scale below that of the experimental measurement, whilst the actual contact angle constantly remains at its equilibrium value.

[2]This is sometimes called the "microscopic contact angle", but still refers to an angle measured within the framework of continuum mechanics.

Pasandideh-Fard *et al.* (1996) considered whether the approach of setting the actual contact angle equal to its equilibrium value was sufficient to accurately describe experiments on the impact and spreading of millimetre-sized drops. They showed that using this assumption in their numerical simulations resulted in the maximum spread of the drop being over-predicted by more than 50%, see Figure 1.4. Pasandideh-Fard *et al.* (1996) then showed that prescribing the actual dynamic contact angle as a function of the contact line speed, using experimentally determined values, significantly improved their correlation with experiment, see Figure 1.4. This is an important result which demonstrates that to accurately describe millimetre-sized drop impact and spreading experiments one must correctly predict the dynamic contact angle behaviour. A similar result has recently been published in Yokoi *et al.* (2009). The aforementioned investigations conclude that the actual (microscopic) contact angle must deviate from its equilibrium value; this is in agreement with the results of Zhou & Sheng (1990), who considered the propagation of a meniscus through a capillary tube and showed that to fit theoretical curves to experimental data one has to assume that the actual contact angle is dynamic. The outstanding question is how the angle should be determined theoretically in order to provide a truly predictive model.

Šikalo *et al.* (2005) proposed removing the entire region of slip from the computational domain in an attempt to circumvent the problem of a numerical scheme not having enough resolution to capture the dynamics of the 'inner' region. Instead, an additional force is applied to the contact line which balances the capillarity and viscous forces in the inner region and which is dependent on the dynamic contact angle. By allowing the actual contact angle to vary with contact-line speed, it is shown that their simulations give better agreement with experiments on millimetre-sized drops than if the actual contact angle is fixed at a static value.

The group of Fukai have published a number of computational papers on drop impact and spreading phenomena (Fukai *et al.*, 1993, 1995, 1998) using a finite element based

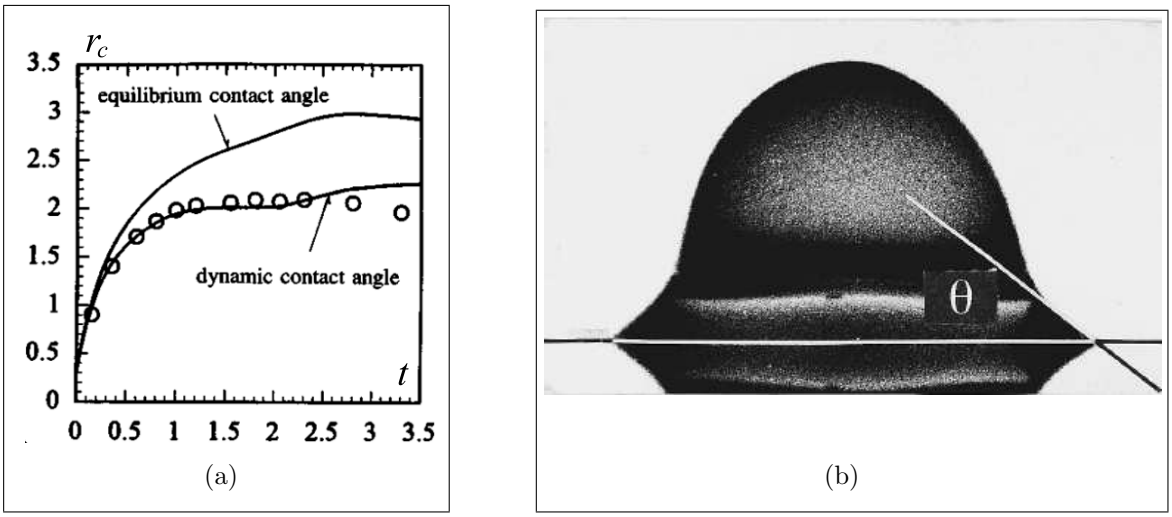

(a) (b)

Figure 1.4: (a) Plot of the non-dimensional contact line position r_c against time t comparing two simulations, one with a fixed dynamic contact angle and one with a varying one, against experimental result (circles). (b) Snapshot from an experiment used to determine the dynamic contact angle at a given instance. From Pasandideh-Fard *et al.* (1996).

numerical code. In Fukai *et al.* (1995) a fixed dynamic contact angle is used, determined from experiments on drops sliding down an inclined plate, which differs depending on whether the contact line is advancing or receding. This allows one to include the effects of the hysteresis of the dynamic contact angle in the simplest possible way: the mechanism which causes this phenomenon is not considered. Semi-empirical approaches such as this may be useful for the description of experiments in a small region of parameter space, but are not designed to provide predictive power when, for example, applied to a different regime such as microdrop spreading.

Below, we summarize the previous continuum approaches used to simulate drop impact and spreading.

1. In the most common case, the slip is prescribed in such a way that numerical results are mesh-dependent. If the Navier-slip boundary condition is used and the slip length correctly resolved, then results will become mesh-independent but predict a singular pressure and incorrect flow field.

2. The dynamic contact angle is usually specified as a function of the contact-line speed,

and is independent of the slip. Thus far, all attempts to model the contact angle fail to account for the experimentally observed non-uniqueness of the speed-angle relationship.

These conclusions have been obtained by comparing the theoretical and experimental results on the millimetre scale; the same verdict could have been reached by considering other dynamic wetting flows (e.g. Zhou & Sheng, 1990). When one attempts to simulate microdrops, where, due to the increasing surface-volume ratio, surface effects will become more important, the gap between conventional theory and experiment is likely to become more pronounced.

Allowing for slip near the contact line and using a speed-angle formula forms what we shall refer to as a *conventional model*[3]. An alternative approach to the modelling of dynamic wetting flows, initially proposed in Shikhmurzaev (1993), has already been shown to describe experimental data from free surface flows over a wide range of parameter values (Blake & Shikhmurzaev, 2002; Shikhmurzaev, 2007). The model, for the physics incorporated into the boundary conditions for the bulk equations of fluid mechanics, is known as the interface formation model and, so far, is the only continuum model to resolve all of the aforementioned inadequacies of classical and conventional modelling.

1.3.2 The interface formation model

Despite widespread interest in comparing the interface formation model's predictions with drop impact and spreading experiments (Šikalo *et al.*, 2002; Bayer & Megaridis, 2006; Attané *et al.*, 2007), the mathematical intricacy of the model has so far proved to be a barrier. The difficulty of comparing this model with experiments is a fundamental one: it is relatively simple to test a speed-angle formula from a conventional model, but, in the interface formation model, as in experiments, the contact angle is determined by

[3]These are sometimes referred to as *slip models*, e.g. in Wilson *et al.* (2006).

the flow field, i.e. it is obtained as part of the solution to a global problem which, in general, is analytically untractable. Although formulae for the dynamic contact angle as a function of the contact-line speed and material parameters exist in certain asymptotic limits (Shikhmurzaev, 1997*b*), these are of no use in the parameter range we shall consider.

The interface formation model also has the advantage of being able to simulate a number of other capillary phenomena, observed during drop impact and spreading, that cannot be handled by classical fluid mechanics (Shikhmurzaev, 2007). For example, the situation in which droplets pinch-off from the bulk of the drop or where the free surface ruptures and joins the solid surface to create a dry patch of solid, requires ad-hoc alterations to the classical formulation, see for example Ashgriz & Mashayek (1995) or Ruckenstein & Jain (1974), respectively. Additionally, if extra physical effects, such as the creation of microscopic residual films, which are known to affect the dynamic contact angle as the contact line recedes (Templeton & Rushing, 1956), need to be incorporated into the model, this can be achieved within a framework, as opposed to making an ad-hoc alteration to a conventional model which has been specifically designed for a different situation. Similarly, if the solid surface has been chemically altered, then its affect on an adjacent flow will manifest itself through the boundary conditions on the liquid-solid interface. The modelling of flow over these surfaces is an area of intensive research and, as we shall see, the interface formation model offers an attractive framework from which to consider such flows.

1.4 Impact and spreading on custom-made surfaces

So far we have considered dynamic wetting of solid substrates that are smooth chemically homogeneous. Recently, due to advances in soft matter physics, it has become possible to design surfaces with specific wetting properties which can be used to manipulate the flow of liquids over them.

1.4.1 Surfaces of variable wettability

The flow of liquids over surfaces of variable wettability is an exciting and new area of fluid mechanics with applications in many emerging technologies (Xia *et al.*, 2001). Such flows are of particular interest in microfluidics, where an increasing surface to volume ratio of liquids means that surface effects become of greater significance (Darhuber & Troian, 2005). The correct description of the physics at liquid-solid interfaces then becomes imperative to the success of any attempt to model this class of flows (Squires & Quake, 2005). It has been shown that, by patterning a substrate with hydrophillic and hydrophobic regions, it is possible to confine a liquid to a microchannel (Zhao *et al.*, 2001; Gau *et al.*, 1999; Mock *et al.*, 2005), to create a structured film (Braun & Meyer, 1999) or, alternatively, when a wettability gradient is present, unbalanced surface tension forces can lead to the movement of liquid drops (Chaudhury & Whitesides, 1992; Daniel *et al.*, 2001).

Experiments have shown that, by patterning a solid substrate with a varying wettability, it is possible to control the position at which a liquid drop, which impacts on such a substrate, is brought to rest (Dupuis & Yeomans, 2004; Dupuis *et al.*, 2005; Michel *et al.*, 2005; Mock *et al.*, 2005). In Figure 1.5, we see experimental photos from Mock *et al.* (2005), in which a substrate has been patterned with spots of higher wettability. Drops of liquid impacting off-centre of these spots are observed to spread so that they become completely contained within the spots. Thus, one can deposit a drop on a solid surface and be guaranteed that, providing the impact position is close enough to the target area, it will end up in the predefined position despite inaccuracies in the initial deposition. This technique of patterning the surface may be used in conjunction with an ink-jet printer for the printing of, for example, electronic circuits (Hong & Wagner, 1999; Gao & Sonin, 1994) and DNA gene chips (Calvert, 2001) which require a high degree of accuracy to avoid droplet coalescence on the solid substrate which can render a system useless. For example, when printing transistors, if two molten drops accidentally coalesce, then the

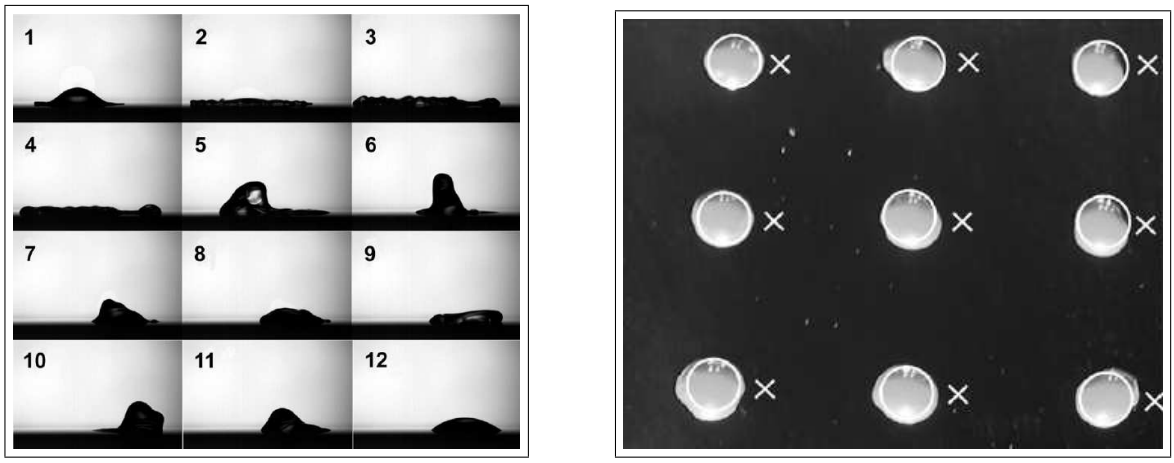

Figure 1.5: Left: the spreading of a 2.5 mm water drop which has impacted on a PFA coated substrate. A 6 mm diameter hydrophilic spot has a centre located 5 mm away from the impact centre. The drop is observed to run into this spot. Right: photograph of nine droplets which impacted near nine hydrophilic spots (white rings) that have a diameter of 3 mm. The impact centre (white crosses) had an x-offset of 2 mm. All drops are observed to spread into their intended positions. In Mock *et al.* (2005).

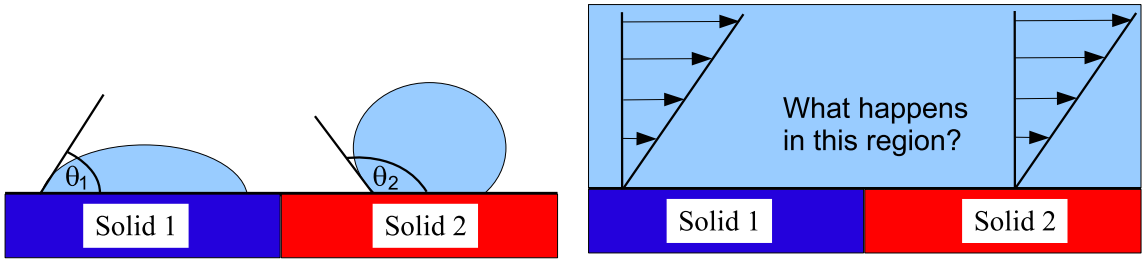

Figure 1.6: Left: wettability is defined in terms of the equilibrium contact angle θ_i which a liquid-gas free surface forms with a solid. Here Solid 1 is more wettable than Solid 2 as it has a lower equilibrium contact angle and consequently the drop wets more of the solid. Right: how will the change in wettability of the substrate affect the shear flow?

transistor could short-circuit.

Modelling flow over a surface of variable wettability

Wettability of a solid is defined by the equilibrium contact angle which is formed by a liquid-gas free surface in contact with it (see Figure 1.6). The question previously addressed by molecular dynamics simulations (Priezjev *et al.*, 2005; Qian *et al.*, 2005) is how a shear flow is affected by a change in the wettability of an adjacent solid surface (see Figure 1.6).

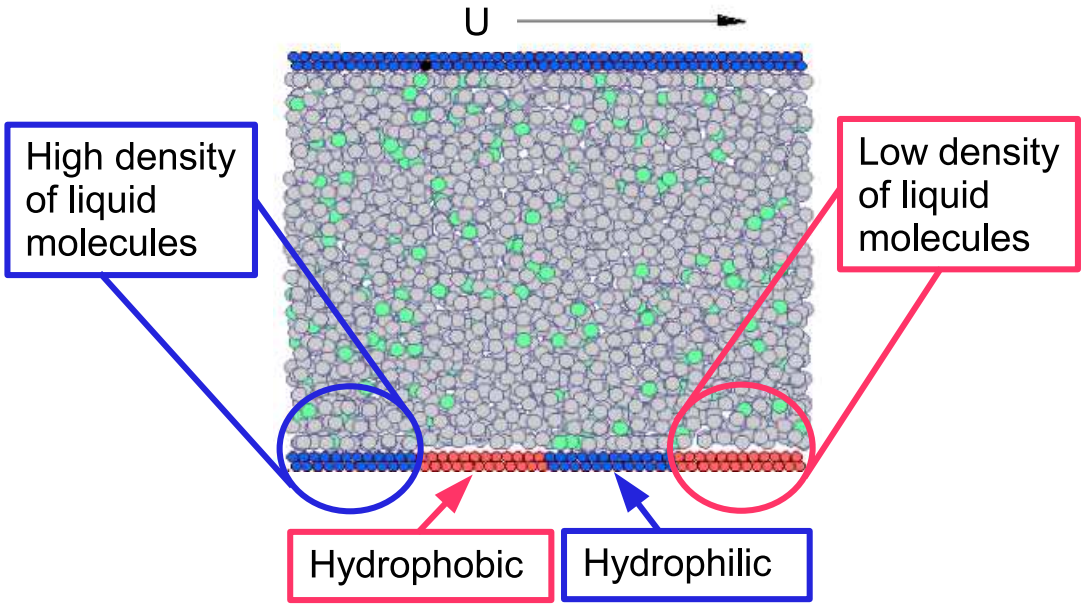

Figure 1.7: Molecular dynamics simulation of flow driven by the upper solid which has speed U over a solid with regions of high wettability (blue) and low wettability (red). Variations in density near the solid show that a normal component to the flow must exist. The green liquid molecules are for visualization purposes only. Courtesy of Professor N. Priezjev.

In molecular dynamics simulations, variations in wettability are modelled by varying an interaction potential between molecules of the solid and the fluid. The results show that a change in wettability does affect the flow. This can be seen in the snapshot of a molecular dynamics simulation of shear flow over a surface of variable wettability shown in Figure 1.7. Here, the red molecules form the hydrophobic substrate whilst the blue molecules form the hydrophilic one. It can be clearly seen that the density of the liquid molecules near the hydrophobic section of the substrate is less than near the hydrophilic one. Consequently, there must be fluxes of liquid normal to the solid which disturb the shear flow.

Given that "wettability" can be introduced as a macroscopic characteristic of a liquid-solid system, one should be able to model the effects discovered by molecular dynamics macroscopically using an appropriate formulation in the framework of continuum mechanics. The classical no-slip boundary condition leaves no room for incorporating the effects of variable wettability and, as previously mentioned, is inadequate for dealing with

processes of dynamic wetting where wettability of the solid plays a key role.

The Navier slip condition provides no conceptual relationship between slip and wettability. Alternatively, linking the slip coefficient (or any other slip condition) to wettability via molecular dynamics simulations negates the advantages of the self-contained and experimentally verifiable continuum modelling. Therefore, applying the no-slip or constant slip coefficient Navier boundary condition at a solid surface implies that the flow of a liquid will not be affected by variations in the wettability of an adjacent solid. This is in direct conflict with the conclusions of molecular dynamics simulations (Priezjev *et al.*, 2005; Qian *et al.*, 2005) that were specifically tailored to investigate this problem.

In this thesis, we shall establish that the interface formation model contains parameters which are related to the wettability of a surface and hence we are able to predict that surfaces of variable wettability will indeed affect an adjacent flow. This will allow us to consider the dynamic wetting of such substrates without any ad-hoc alterations to our model.

1.4.2 Super-hydrophobic surfaces

Recent experiments in Renardy *et al.* (2003) have shown the unexpected influence which a super-hydrophobic substrate can have on an impacting liquid drop. Such solids are created by texturing hydrophobic surfaces with microstructures. A liquid drop contacting such a substrate will sit on a patchwork of solid and air, and consequently exhibit equilibrium contact angles as high as 170°. In Figure 1.8 one can see that when a non-spherical millimetre-size drop impacts on such a substrate, the free surface forms pyramidal shapes, with a decreasing number of steps as the drop spreads. Eventually, the apex of the drop is thrown downwards with such ferocity that the drop takes a toroidal shape with a small dry region formed in the centre of the drop.

Currently, there is no established model for the dynamic wetting of a super-hydrophobic

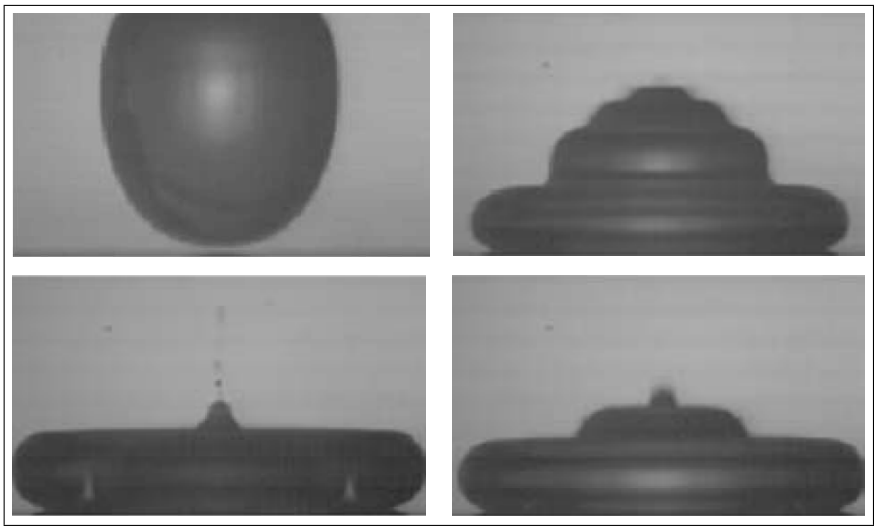

Figure 1.8: Sequence of experimental photos, going clockwise from the top left, showing the impact of a non-spherical millimetre-size drop on a super-hydrophobic substrate. In the second and third images the pyramidal shapes are seen and in the fourth image the drop is almost toroidal - one can just see the edge of the free surface which has disappeared below the main body by looking through the drop. From Renardy *et al.* (2003).

surface. Theoretically, one must determine the boundary conditions at the liquid-solid/gas interface and, as usual, a method for predicting the dynamic contact angle. Given the disparity between the length scale of the bulk flow in these experiments (millimetres) compared to the scale of the rough microstructure (microns) it seems possible to average over the microstructure to provide some effective boundary conditions for the liquid-solid/air interface. It has previously been shown that, using classical fluid mechanics, for a zero tangential-stress surface which contains random defects, such as those introduced by the tops of solid posts, that the resultant effective boundary condition will be the Navier-slip condition (Jansons, 1987). Ideally one would use a model that has satisfactorily described dynamic wetting on smooth surfaces of constant wettability, i.e. the interface formation model; however, this is beyond the scope of this thesis and, later in the thesis, as an initial step, we shall consider flow over a super-hydrophobic surface using our standard models.

1.5 Overview of the thesis

The scientific goal of this research is to develop a model which accurately describes drop impact and spreading phenomena. This model will allow us to determine the effect individual parameters have on the drop's dynamics and predict critical values for which certain physical effects will occur. By using the unsteady interface formation model, which has been fully incorporated into a numerical code for the first time, we have a framework into which we can include additional affects, such as variable wettability or residual film formation, in a logical manner.

First, in Chapter §2, the models which are used and referred to throughout this thesis are outlined. After this, in §3, the full formulation of a problem of an axi-symmetric drop impact and spreading on a solid surface of constant wettability is presented. The resulting set of equations are analytically untractable and so, in §4, we develop a finite element based approach that is capable of simulating drop impact and spreading phenomena. Having developed our own numerical platform, which is specifically designed to capture the small-scale dynamics near the contact line, in §5 we show, as a test of its reliability and accuracy, that it is able to reproduce published computational results for the oscillation of liquid drops and accurately approximates asymptotic results obtained using the interface formation model. The numerical platform is then used to simulate microdrop impact and spreading on solids of constant wettability in §6 where, notably, the non-uniqueness of the speed-angle relationship is theoretically predicted for the first time. We then show in §7 that the interface formation model is able to capture the affect which variations in the wettability of a solid have on an adjacent flow. We do so by solving a simplified problem, in which no free surfaces are present, of shear flow over such a surface and show favourable agreement with the results of molecular dynamics. Finally, we present results from the impact and spreading of microdrops on custom-made surfaces, such as those with a variable wettability in §8. In §9 we outline possible future directions of research before summarizing the results of this thesis in §10.

Chapter 2

Modelling dynamic wetting phenomena

In this chapter, we consider the continuum models which are used to describe dynamic wetting flows. The bulk equations remain the same for all the problems we consider: it is the boundary conditions to these equations that will differ. First, we present the 'classical' fluid mechanical boundary conditions. Then, by altering the classical boundary conditions in order to overcome the moving contact-line problem, we arrive at the boundary conditions of the 'conventional' model. Finally, the boundary conditions produced by the interface formation model are presented.

2.1 Bulk equations

We consider a Newtonian liquid, whose motion is fully described by the incompressible Navier-Stokes equations:

$$\nabla \cdot \mathbf{u} = 0, \qquad \rho \left[\frac{\partial \mathbf{u}}{\partial t} + \mathbf{u} \cdot \nabla \mathbf{u} \right] = \nabla \cdot \mathbf{P} + \mathbf{F}, \tag{2.1}$$

where $\mathbf{u}$, ρ and p are the fluid's velocity, density and pressure; $\mathbf{F}$ is the external force density and t is time. The stress tensor $\mathbf{P}$ is given by

$$\mathbf{P} = -p\mathbf{I} + 2\mu\mathbf{E}, \qquad \mathbf{E} = \frac{1}{2}\left(\nabla\mathbf{u} + [\nabla\mathbf{u}]^T\right), \tag{2.2}$$

where $\mathbf{I}$ is the metric tensor, μ is the fluid's viscosity and $\mathbf{E}$ is the rate of strain tensor.

2.2 Boundary conditions

In this section, the boundary conditions which are used for the incompressible Navier-Stokes equations are presented. First let us outline some notation.

Surface variables of a liquid-solid interface, liquid-gas interface and an axis of symmetry are denoted with a subscript S, G and A, respectively. We attach a superscript 's' to surface variables whilst a subscript 'e' denotes an equilibrium value. The unit normal vector $\mathbf{n}$ of a surface is defined to point in to the bulk of the liquid. The tangential components of a vector are denoted with a subscript '||' and may be extracted using the tensor $(\mathbf{I} - \mathbf{nn})$, i.e. $\mathbf{u}_{||} = \mathbf{u} \cdot (\mathbf{I} - \mathbf{nn})$.

The solid surface will be regarded as stationary. The gas is always considered inviscid with a constant atmospheric pressure p_G which is absorbed into the pressure, $p - p_G \to p$; i.e. it is p_G that sets the pressure level in the liquid. The liquid-gas interface is free, i.e. a-priori unknown, and its position is defined by the equation $f(\mathbf{x}_G, t) = 0$, where $\mathbf{x}_G$ is the position vector and f is to be found. The free surface has curvature κ_G given by

$$\kappa_G = \nabla \cdot \mathbf{n}_G. \tag{2.3}$$

Additionally, we shall use that

$$\nabla \cdot (\mathbf{I} - \mathbf{n_G n_G}) = -\mathbf{n}_G \nabla \cdot \mathbf{n}_G = -\mathbf{n}_G \kappa_G. \tag{2.4}$$

2.2.1 The classical model

The 'classical' boundary conditions that are used for the Navier-Stokes equations, which are derived in, for example, Davis (2000) and Shikhmurzaev (2007) are as follows.

On liquid-solid interfaces we have no-slip and impermeability:

$$\mathbf{u} = \mathbf{0}. \tag{2.5}$$

On free liquid-gas interfaces, we have the balance of bulk stress with capillary stress, caused by the presence of a (constant) surface tension σ^s_{Ge}, and the kinematic condition:

$$\mathbf{n}_G \cdot \mathbf{P} = -\nabla \cdot (\sigma^s_{Ge}(\mathbf{I} - \mathbf{n}_G\mathbf{n}_G)) = \sigma^s_{Ge}\kappa\mathbf{n}_G, \qquad \frac{\partial f}{\partial t} + \mathbf{u} \cdot \nabla f = 0. \tag{2.6}$$

2.2.2 A conventional model for moving contact line phenomena

The classical model of fluid mechanics is known to be inadequate for the description of dynamic wetting phenomena. Here we describe the standard way of altering the boundary conditions of the classical model to produce a conventional model.

In order to obtain a solution to a dynamic wetting problem, one must:

(i) remedy the non-existence of a solution in the classical formulation and

(ii) describe the dynamic contact angle, which is required as a boundary condition for the equations which determine the free surface shape (2.6).

As reviewed in §9 of Shikhmurzaev (1997a), in the conventional approach the two problems are treated separately by:

(i) relaxing the no-slip condition to allow a certain degree of slip along all, or some, of the liquid-solid interface and

(*ii*) prescribing the dynamic contact angle as a function of the contact-line speed and other material parameters.

A representative example, and the model we use in this thesis, is for (*i*) to apply the Navier slip condition (Navier, 1823) at the liquid-solid interface, which supposes that slip on the liquid-facing side of the interface is proportional to the tangential stress acting on the interface from the fluid, so that the new liquid-solid boundary conditions become

$$\mu \mathbf{n}_S \cdot \mathbf{P} \cdot (\mathbf{I} - \mathbf{n}_S \mathbf{n}_S) = \beta \mathbf{u} \cdot (\mathbf{I} - \mathbf{n}_S \mathbf{n}_S), \qquad \mathbf{u} \cdot \mathbf{n}_S = 0, \tag{2.7}$$

where β is the 'coefficient of sliding friction' and μ/β is often referred to as the 'slip length'. The Navier condition has been a popular choice for the modelling of moving contact line problems (Dussan V, 1976; Hocking & Rivers, 1982; Cox, 1986; Zhou & Sheng, 1990) and, also, is often proposed as an 'effective' boundary condition to account for the influence of imperfections in the solid surface on an adjacent flow. One such example, which we shall return to later in this thesis, is in the flow over a surface of variable wettability (Qian *et al.*, 2005; Priezjev *et al.*, 2005). The main problem with such an approach is that there is no defined link between the coefficient of slip β and the wettability of a substrate which is defined in terms of the equilibrium contact angle θ_e that a free surface forms with a solid.

For (*ii*) we use a formula suggested in Jiang *et al.* (1979) which, using experimental data from Hoffman (1975), is a least-square-error fit to the dynamic contact angle as a function of contact-line speed and has the advantage of not containing any parameters which require estimation. It is

$$\frac{\cos\theta_e - \cos\theta_d}{\cos\theta_e + 1} = \tanh\left[4.96(Ca_c)^{0.702}\right], \tag{2.8}$$

where $Ca_c = (\mu U_c)/\sigma^s_{Ge}$ is the capillary number based on the contact-line speed.

Having overcome the moving contact line problem by modifying the boundary conditions on the liquid-solid interface, one keeps the other classical boundary conditions (2.6) intact.

The unsurprisingly excellent agreement of the empirical formula (2.8) with a range of experimental data is shown in Kistler (1993). However, it should be noted that there is, in principle, no way in which *any* contact angle formula can describe experimentally observed phenomena, such as the hydrodynamic assist of dynamic wetting, which show that for the same contact-line speed, the flow field that affects the dynamic contact angle.

Notably, in the conventional approach, the surface tension on an interface is not included into consideration and hence assumed to be constant, right up to the contact line. This means that a force balance applied at the contact line, known as the Young equation (Young, 1805), $\sigma^s_{Se} = -\sigma^s_{Ge}\cos\theta_d$, for zero surface tension of the solid-gas interface, does not hold unless $\theta_d = \theta_e$. Therefore, in most conventional models, in which the dynamic contact angle deviates from its equilibrium value, this force balance is not satisfied. Some authors have considered the case in which the dynamic contact angle is always equal to its equilibrium one (Dussan V, 1976; Hocking, 1977); however, as shown by Pasandideh-Fard *et al.* (1996), see Figure 1.4, such a model is inadequate for drop impact and spreading problems and therefore is not considered here. In the interface formation model, to be described below, the surface tensions are allowed to deviate from their equilibrium values and the dynamic contact angle satisfies the Young equation. The angle is found as part of the solution, as opposed to being prescribed as a function of the contact-line speed.

2.2.3 The interface formation model

In the problems we shall encounter in this thesis, the interface formation process is most active near contact lines formed by the joining of surfaces of differing equilibrium properties. In the case of a spreading drop, this occurs at a liquid-solid-gas contact line. The

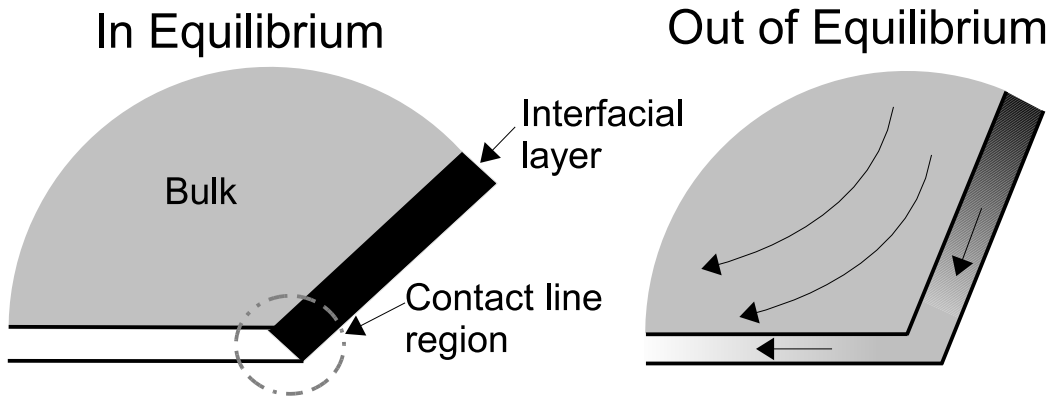

Figure 2.1: Illustration of the interface formation process using an interfacial layer of finite width for representation purposes only: in the continuum limit this layer becomes a mathematical surface of zero thickness. Left: two interfacial layers with different surface properties in equilibrium meet at a contact line. Right: an outer flow disturbs the balance and creates gradients in surface variables which, if at least one interface is free, alters the angle between the interfaces.

interface formation equations will determine the relaxation dynamics of fluid particles which are swept from one interface, through the contact line and onto the second interface, see Figure 2.1, a process which involves an exchange of mass, momentum and energy between the bulk and boundary. As a result, the dynamic contact angle, which is determined by the values of the surface variables at the contact line, becomes inextricably linked to the whole flow field, as is seen experimentally.

For a detailed exposition of the interface formation model, the reader is referred to the monograph Shikhmurzaev (2007) where, using principles of irreversible thermodynamics, the model, initially presented in Shikhmurzaev (1993), is derived and the assumptions which lead to the simplest irreducible set of equations are discussed. Here, we present the equations and will then briefly describe their meaning.

On liquid-gas interfaces we have

$$\frac{\partial f}{\partial t} + \mathbf{v}_G^s \cdot \nabla f = 0, \tag{2.9}$$

$$\mathbf{n}_G \cdot \mathbf{P} = -\nabla \cdot (\sigma_G^s (\mathbf{I} - \mathbf{n}_G \mathbf{n}_G)) \,, \tag{2.10}$$

$$\rho(\mathbf{u}-\mathbf{v}_G^s)\cdot\mathbf{n}_G=\frac{\rho_G^s-\rho_{Ge}^s}{\tau}, \tag{2.11}$$

$$\frac{\partial\rho_G^s}{\partial t}+\nabla\cdot(\rho_G^s\mathbf{v}_G^s)=-\frac{\rho_G^s-\rho_{Ge}^s}{\tau}, \tag{2.12}$$

$$(\mathbf{v}_G^s-\mathbf{u})\cdot(\mathbf{I}-\mathbf{n}_G\mathbf{n}_G)=(1+4\alpha\beta)\,\nabla\sigma_G^s, \tag{2.13}$$

$$\sigma_G^s=\gamma(\rho_{(0)}^s-\rho_G^s), \tag{2.14}$$

and we note that the stress condition (2.10) may be decomposed into normal and tangential components:

$$-p+\mu\mathbf{n}_G\cdot[\nabla\mathbf{u}+(\nabla\mathbf{u})^T]\cdot\mathbf{n}_G=\sigma_G^s\kappa_G, \tag{2.15}$$

$$\mu\mathbf{n}_G\cdot[\nabla\mathbf{u}+(\nabla\mathbf{u})^T]\cdot(\mathbf{I}-\mathbf{n}_G\mathbf{n}_G)+\nabla\sigma_G^s=0. \tag{2.16}$$

On liquid-solid interfaces we have

$$\mathbf{v}_S^s\cdot\mathbf{n}_S=0, \tag{2.17}$$

$$\mathbf{n}_S\cdot\mathbf{P}\cdot(\mathbf{I}-\mathbf{n}_S\mathbf{n}_S)+\tfrac{1}{2}\nabla\sigma_S^s=\beta\mathbf{u}\cdot(\mathbf{I}-\mathbf{n}_S\mathbf{n}_S), \tag{2.18}$$

$$\rho(\mathbf{u}-\mathbf{v}_S^s)\cdot\mathbf{n}_S=\frac{\rho_S^s-\rho_{Se}^s}{\tau}, \tag{2.19}$$

$$\frac{\partial\rho_S^s}{\partial t}+\nabla\cdot(\rho_S^s\mathbf{v}_S^s)=-\frac{\rho_S^s-\rho_{Se}^s}{\tau}, \tag{2.20}$$

$$\left(\mathbf{v}_S^s-\tfrac{1}{2}\mathbf{u}\right)\cdot(\mathbf{I}-\mathbf{n}_S\mathbf{n}_S)=\alpha\nabla\sigma_S^s, \tag{2.21}$$

$$\sigma_S^s=\gamma(\rho_{(0)}^s-\rho_S^s). \tag{2.22}$$

The surface variables are in the 'surface phase', i.e. physically in a microscopic layer of liquid adjacent to the surface which is subject to intermolecular forces from two bulk phases. In the continuum limit, this microscopic layer becomes a mathematical surface of zero thickness; ρ^s denotes its surface density (mass per unit area) and $\mathbf{v}^s$ is the velocity with which it is transported; α, β, γ, τ and $\rho_{(0)}^s$ are phenomenological material constants

which in the simplest variant of the theory are assumed to take the same value on all interfaces.

The surface tension is considered as a dynamic quantity related to the surface density via the equations of state in the 'surface phase' (2.14) and (2.22) which are taken here in their simplest linear form. The constant γ is associated with the inverse compressibility of the fluid whilst $\rho^s_{(0)}$ is the surface density corresponding to zero surface tension. The equilibrium surface tension itself may be positive or negative; for a liquid-gas interface which is rarefied it will be positive, as for a hydrophobic liquid-solid interface, whilst for a hydrophilic liquid-solid interface it will be negative. Gradients in surface tension influence the flow, firstly, via the stress boundary conditions (2.10) and (2.18), i.e. via the Marangoni effect, and, secondly, in the Darcy type equations[1] (2.13) and (2.21) by forcing the surface velocity $\mathbf{v}^s$ to deviate from that generated in the surface phase by the outer flow. The constants α and β characterize the response of the interface to surface tension gradients and an external torque, respectively; in the simplest variant of the theory both are properties of the fluid. Mass exchange between the bulk and surface phases, caused by the possible deviation of the surface density from its equilibrium value ρ^s_e, is accounted for in the boundary conditions for the normal component of bulk velocity (2.11) and (2.19), and in the surface mass balance equations (2.12) and (2.20). The parameter τ is the surface tension relaxation time.

One would expect a generalized set of boundary conditions to have the classical conditions as their limiting case. For the interface formation model this limiting case follows from the limits $\mu/(\beta L),\ U\tau/L \to 0$, where L and U are characteristic length and velocity scales of the flow. When applied to (2.9)–(2.14) the liquid-gas interface equations are reduced to their classical form (2.6). Notably, if we first apply $U\tau/L \to 0$ to the liquid-solid equations (2.17)–(2.22) we obtain the conventional model (2.7), that is the Navier-slip

[1]The analogy with the Darcy equation is that the tangential surface velocity $\mathbf{v}^s_{||}$ is the average velocity of the interfacial layer and its deviation from that generated by the outer flow is proportional to the gradient of surface tension, which is the negative gradient of surface pressure as $p^s = -\sigma^s$.

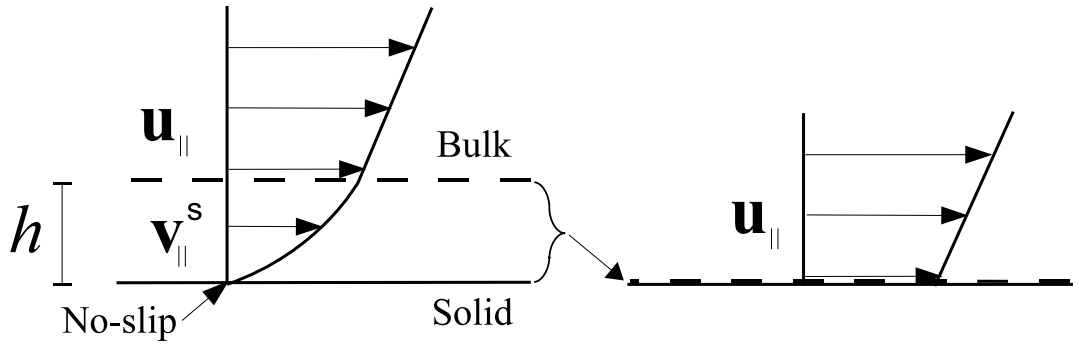

Figure 2.2: Left: an interaction across a microscopic length scale h leads to a non-zero tangential velocity $\mathbf{u}_{||}$ on the liquid facing side of the interface. Right: in the continuum approximation, $h/L \to 0$, this manifests itself as *apparent* slip.

condition combined with impermeability. Then, by further applying $\mu/(\beta L) \to 0$ we obtain the classical equations of no-slip and impermeability (2.5).

It is important to emphasize that in the derivation of the model it is assumed that on the solid-facing side of the liquid-solid interface one has impermeability and no-slip. Furthermore, for an inviscid gas at a constant pressure, on the gas facing side of the liquid-gas interface the only stress is from the atmospheric pressure. However, it is the velocity on the *liquid*-facing side of the interface that is the boundary condition for the Navier-Stokes equations (2.1). In the classical conditions it is assumed that there is no difference in velocity between the solid/gas-facing and liquid-facing side of the interface, whereas in the interface formation model, the velocity on the liquid-facing side of the interface is determined by the interaction occurring in the surface phase and between the surface phase and the bulk. Taking the liquid-solid interface as an example, one can expect effective (or 'apparent') slip, $\mathbf{u}_{||} \neq \mathbf{0}$, that is a difference between the velocity on the liquid-facing side of the interface and the velocity of the solid surface (see Figure 2.2). Additionally, one can expect a non-zero normal component of velocity (a flux in/out of the surface phase), i.e. $\mathbf{u} \cdot \mathbf{n} \neq 0$, if the interface is out of equilibrium (see Figure 2.3).

Where interfaces meet to form a contact line, the surface equations require their own boundary conditions. Consider a liquid-gas-solid contact line with tangent $\mathbf{t}_c = \mathbf{n}_S \times$

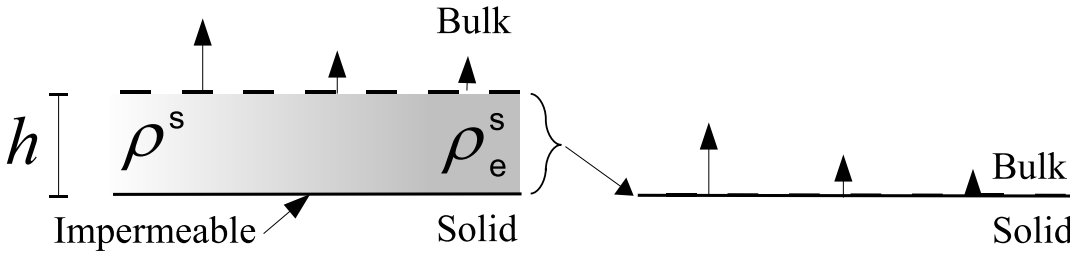

Figure 2.3: Left: when the surface density is above its equilibrium value the interface loses mass to the bulk and produces a non-zero normal velocity $\mathbf{u} \cdot \mathbf{n}$. Right: in the continuum approximation, $h/L \to 0$, this manifests itself as a non-zero normal velocity on the liquid facing side of the substrate.

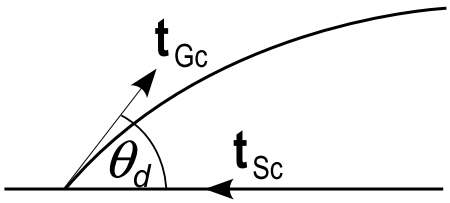

Figure 2.4: Sketch of the contact line region.

$\mathbf{n}_G/|\mathbf{n}_S \times \mathbf{n}_G|$ advancing with speed U_c over a dry solid surface. The tangent to the solid surface pointing towards the contact line is defined by $\mathbf{t}_{Sc} = \mathbf{n}_S \times \mathbf{t}_c$ and a tangent on the free surface pointing away from the contact line defined by $\mathbf{t}_{Gc} = \mathbf{n}_G \times \mathbf{t}_c$, see Figure 2.4. Then continuity of mass flux at the contact line gives

$$\rho_G^s \left(\mathbf{v}_G^s \cdot \mathbf{t}_{Gc} - U_c \mathbf{t}_{Sc} \cdot \mathbf{t}_{Gc} \right) = \rho_S^s \left(\mathbf{v}_S^s \cdot \mathbf{t}_{Sc} - U_c \right), \tag{2.23}$$

The contact angle between the two interfaces $\cos\theta = -\mathbf{t}_{Sc} \cdot \mathbf{t}_{Gc}$ satisfies a force balance, tangential to the liquid-solid interface we have the so-called Young equation:

$$\sigma_S^s + \sigma_G^s \cos\theta_d = 0. \tag{2.24}$$

The surface tension of the solid-gas interface σ_{SG} is taken to be zero. The corresponding normal force balance will not be required.

We can now see that it is the equilibrium surface density that will provide an input for

the wettability of a solid substrate into our model. Applying (2.22) and (2.24) to a drop sitting in equilibrium on a substrate with contact angle θ_e, we have that $\sigma^s_{Se} = \gamma(\rho^s_{(0)} - \rho^s_{Se})$ and $\sigma^s_{Se} = -\sigma^s_{Ge}\cos\theta_e$. Then, for a given liquid, ρ^s_{Se} can be expressed in terms of θ_e, i.e. ρ^s_{Se} is a function of the wettability of a solid substrate. In contrast, in the conventional liquid-solid boundary conditions (2.7), the 'slip' is not linked to the wettability of the substrate.

Receding contact lines and microscopic residual films

The contact line radius of a drop which has impacted and then spreads on a solid surface often reaches a maximum before recoiling and oscillating around its equilibrium position. As a result, the contact line continuously advances and recedes over a portion of the solid substrate. The receding contact line is often observed to leave a microscopic residual film on the solid substrate; a phenomenon which both affects the receding motion of the contact line and alters the properties of what we have referred to as the solid-gas interface (Lam *et al.*, 2001). This pre-wet substrate will subsequently affect the motion of the advancing contact line. In the framework of the interface formation model there is a regular way to incorporate this additional physics into our problem formulation.

The microscopic film has a dual influence on the interface formation equations by (i) contributing a flux of surface mass $\rho^s_{res}U_c$ at the contact line and (ii) creating an additional surface tension contribution σ_{SG} to the force balance . As a result we generalize (2.23) and (2.24) to obtain new contact line equations:

$$\rho^s_G\left(\mathbf{v}^s_G\cdot\mathbf{t}_{Gc} - U_c\mathbf{t}_{Sc}\cdot\mathbf{t}_{Gc}\right) = \rho^s_S\left(\mathbf{v}^s_S\cdot\mathbf{t}_{Sc} - U_c\right) + \rho^s_{res}U_c \tag{2.25}$$

and

$$\sigma^s_S + \sigma^s_G\cos\theta = \sigma_{SG}. \tag{2.26}$$

In the absence of a developed theory for the leaking of microscopic films from moving

contact lines, the parameters ρ^s_{res} and σ_{SG} will be treated as phenomenological parameters.

2.3 Summary

In this chapter have shown how a conventional model is produced by modifying the boundary conditions of the classical model in order to overcome the moving contact-line problem. The physics of interface formation is briefly discussed and the equations which model this process are presented.

In the next chapter we consider a full non-dimensional problem formulation for an axisymmetric drop impact and spreading problem using both the conventional model and the interface formation model.

Chapter 3

Problem formulation for drop impact and spreading phenomena

We consider a spherical drop of liquid with radius a which falls through an inviscid dynamically passive gas with a downward velocity U_0. This drop impacts on a smooth stationary horizontal solid substrate and then spreads; see Figure 3.1. The following motion is assumed to be axisymmetric, which is indeed the case for a wide range of parameters (Bayer & Megaridis, 2006). In particular, this is the case for droplets emitted from ink-jet printers.

We now derive the full non-dimensional formulation of our problem from the bulk

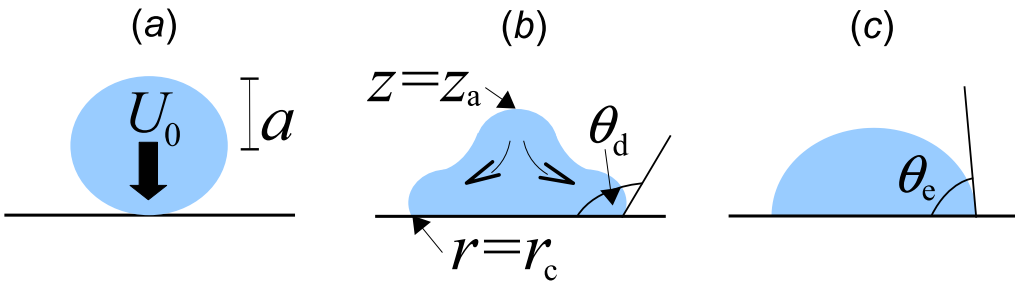

Figure 3.1: a: The initial position of a drop of radius a and impact speed U_0. b: The subsequent spreading with contact line position r_c, apex height z_a and dynamic contact angle θ_d. c: The equilibrium position with contact angle θ_e.

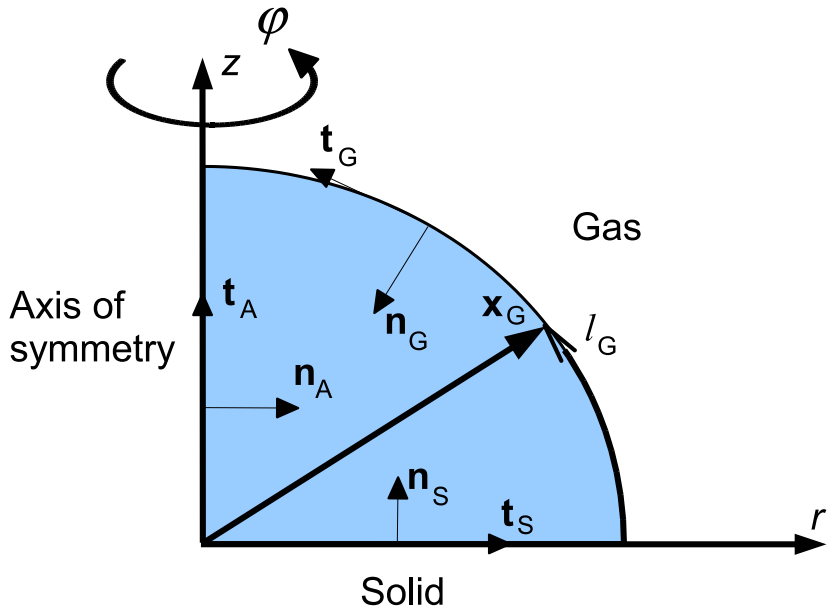

Figure 3.2: The drop's computational domain.

equations (2.1)–(2.2) combined with either the boundary conditions from the conventional model (2.6)–(2.8) or from the interface formation model (2.9)–(2.26). Due to the axisymmetry of the problem, it proves convenient to use cylindrical coordinates $\mathbf{x} = (r, z, \varphi)$, with origin at the intersection of the axis of symmetry and the solid surface, so that all derivatives with respect to φ are zero, see Figure 3.2. The free surface is then parameterized in terms of the arclength l_G and the tangent in this direction is $\mathbf{t}_G$. The distance along the solid surface, from the axis of symmetry is l_S and l_φ is the arclength in the azimuthal direction. Unit vectors in the radial, azimuthal and vertical direction are $\mathbf{e}_r$, $\mathbf{e}_\varphi$ and $\mathbf{e}_z$, respectively,

The boundary $\partial\Omega$ of the domain Ω is comprised of the liquid-solid interface $\partial\Omega_S$ $(0 \leq r_S \leq r_c(t), z = 0)$, the liquid-gas interface $\partial\Omega_G$ $(\mathbf{x}_G = (r_G(l_G, t), z_G(l_G, t)))$ and the axis of symmetry $\partial\Omega_A$ $(r = 0, 0 \leq z_A \leq z_a(t))$, so that $\partial\Omega = \partial\Omega_S \cup \partial\Omega_G \cup \partial\Omega_A$.

It is convenient to use the following scales for length, velocity, pressure and time

$$a, \quad U_0, \quad \frac{\sigma}{a}, \quad \frac{a}{U_0},$$

where $\sigma \equiv \sigma^s_{Ge}$. For the interface formation equations we use the dimensional scales

$$\rho^s_{(0)}, \quad \sigma, \quad U_0,$$

for surface density, surface tension and surface velocity, respectively.

3.1 Bulk equations

In the bulk, from (2.1)–(2.2), we obtain

$$\nabla \cdot \mathbf{u} = 0, \qquad Re\left[\frac{\partial \mathbf{u}}{\partial t} + \mathbf{u} \cdot \nabla \mathbf{u}\right] - \nabla \cdot \mathbf{P} + St\mathbf{e}_z = 0, \tag{3.1}$$

$$\mathbf{P} = -p\mathbf{I}/Ca + 2\mathbf{E}, \qquad \mathbf{E} = \frac{1}{2}\left(\nabla \mathbf{u} + [\nabla \mathbf{u}]^T\right), \tag{3.2}$$

where $Re = (\rho U_0 a)/\mu$, $Ca = (\mu U_0)/\sigma$ and $St = (\rho g a^2)/\mu U_0$ are, respectively, the Reynolds, capillary and Stokes numbers. All quantities are now non-dimensional.

3.2 Boundary conditions

Two different sets of boundary conditions are used in this thesis. First we formulate the equations of the convention model and then after those of the interface formation model.

3.2.1 Conventional equations

From (2.6), on the liquid-gas interface $\mathbf{x} \in \partial\Omega_G$, we obtain

$$\mathbf{n}_G \cdot \mathbf{P} = -\frac{1}{Ca}\left(\frac{\partial \mathbf{t}_G}{\partial l_G} + \frac{\partial \boldsymbol{e}_\varphi}{\partial l_\varphi}\right), \qquad \left(\frac{\partial \mathbf{x}_G}{\partial t} - \mathbf{u}\right) \cdot \mathbf{n}_G = 0. \tag{3.3}$$

From (2.7), on the liquid-solid interface $\mathbf{x} \in \partial\Omega_S$, we have

$$\mathbf{n}_S \cdot \mathbf{P} \cdot \mathbf{t}_S = \bar{\beta}\mathbf{u} \cdot \mathbf{t}_S/Ca, \qquad \mathbf{u} \cdot \mathbf{n}_S = 0, \tag{3.4}$$

where $\bar{\beta} = (\beta U_0 a)/\sigma$ is the non-dimensional coefficient of slip.

On the axis of symmetry $\mathbf{x} \in \partial\Omega_A$, we apply

$$\mathbf{n}_A \cdot \mathbf{P} \cdot \mathbf{t}_A = 0, \qquad \mathbf{u} \cdot \mathbf{n}_A = 0. \tag{3.5}$$

The equations on the free surface (3.3) require their own boundary conditions; this is achieved by imposing constraints on the gradient of the free surface shape. At the apex, $(0, z_a)$, we ensure the free surface remains smooth:

$$\frac{\partial z_G}{\partial l_G} = 0, \tag{3.6}$$

whilst, from (2.8), at the contact line, $(r_c, 0)$, we use the contact angle formula

$$\frac{\cos\theta_e - \cos\theta_d}{\cos\theta_e + 1} = \tanh\left[4.96(CaU_c)^{0.702}\right], \qquad \theta_d = \arctan\left(-\frac{\partial z_G}{\partial r_G}\right). \tag{3.7}$$

At the contact line the kinematic equation becomes

$$\frac{\mathrm{d}r_c}{\mathrm{d}t} = U_c. \tag{3.8}$$

3.2.2 Interface formation equations

The interface formation equations are now presented in a (non-dimensional) form which will prove most convenient for their implementation into the finite element procedure, which is discussed in the next chapter. This involves decomposing the bulk velocity on the surface $\mathbf{u}$ and the surface velocity of the interface $\mathbf{v}^s$ into their normal and tangential

components, denoted with an additional subscript n and t, respectively, and defining surface variables as functions of the arclength coordinates along the solid surface l_S or the free surface l_G, and time. For a surface vector $\mathbf{a}^s$ on the curved free surface, we have $\mathbf{a}^s_G = a^s_{Gn}\mathbf{n}_G + a^s_{Gt}\mathbf{t}_G$, so that the divergence of a surface vector is given by:

$$\nabla \cdot \mathbf{a}^s_G = a^s_{Gn}\nabla \cdot \mathbf{n}_G + \nabla \cdot (a^s_{Gt}\mathbf{t}_G) = a^s_{Gn}\kappa_G + \frac{\partial a^s_{Gt}}{\partial l_G}. \tag{3.9}$$

On the liquid-gas interface, equations (2.9)–(2.14) give

$$\frac{\partial x_{Gn}}{\partial t} = v^s_{Gn}, \tag{3.10}$$

$$\mathbf{n}_G \cdot \mathbf{P} = -\frac{1}{Ca}\left(\frac{\partial\left(\sigma^s_G \mathbf{t}_G\right)}{\partial l_G} + \frac{\partial\left(\sigma^s_G \boldsymbol{e}_\varphi\right)}{\partial l_\varphi}\right), \tag{3.11}$$

$$u_n - v^s_{Gn} = Q\left(\rho^s_G - \rho^s_{Ge}\right), \tag{3.12}$$

$$\frac{\partial \rho^s_G}{\partial t} + \frac{\partial\left(\rho^s_G v^s_{Gt}\right)}{\partial l_G} + \rho^s_G v^s_{Gn}\kappa_G = -\frac{\rho^s_G - \rho^s_{Ge}}{\epsilon}, \tag{3.13}$$

$$v^s_{Gt} - u_t = \left(1 + 4\bar{\alpha}\bar{\beta}\right)\frac{\partial \sigma^s_G}{\partial l_G}, \tag{3.14}$$

$$\sigma^s_G = \lambda(1 - \rho^s_G). \tag{3.15}$$

On the liquid-solid interface, from equations (2.17)–(2.22), we have

$$v^s_n = 0, \tag{3.16}$$

$$Ca\ \mathbf{n}_S \cdot \mathbf{P} \cdot \mathbf{t}_S + \tfrac{1}{2}\frac{\partial \sigma^s_S}{\partial l_S} = \bar{\beta} u_t, \tag{3.17}$$

$$\frac{\partial \rho^s_S}{\partial t} + \frac{\partial\left(\rho^s_S v^s_{St}\right)}{\partial l_S} = -\frac{\rho^s_S - \rho^s_{Se}}{\epsilon}, \tag{3.18}$$

$$u_n = Q\left(\rho^s_S - \rho^s_{Se}\right), \tag{3.19}$$

$$v^s_{St} - \tfrac{1}{2}u_t = \bar{\alpha}\frac{\partial \sigma^s_S}{\partial l_S}, \tag{3.20}$$

$$\sigma_S^s = \lambda(1 - \rho_S^s). \tag{3.21}$$

We have introduced the non-dimensional parameters $\bar{\alpha} = \alpha\sigma/(U_0 a)$, $\bar{\beta} = (\beta U_0 a)/\sigma$, $\epsilon = U_0\tau/a$, $\lambda = \gamma\rho_{(0)}^s/\sigma$ and $Q = \rho_{(0)}^s/(\rho U_0 \tau)$.

On the axis of symmetry, $\mathbf{x} \in \partial\Omega_A$, we formulate the standard conditions of symmetry on the bulk variables:

$$\mathbf{n}_A \cdot \mathbf{P} \cdot \mathbf{t}_A = 0, \qquad \mathbf{u} \cdot \mathbf{n}_A = 0. \tag{3.22}$$

Where the liquid-gas interface and liquid-solid interface intersect the axis of symmetry, the constraints of symmetry on our interface formation variables require that

$$v_{Gt}^s = \frac{\partial \rho_G^s}{\partial l_G} = 0 \quad \text{and} \quad v_{St}^s = \frac{\partial \rho_S^s}{\partial l_S} = 0, \tag{3.23}$$

and on the free surface shape, at the apex, $(0, z_a)$, that

$$\frac{\partial z_G}{\partial l_G} = 0. \tag{3.24}$$

At the liquid-solid-gas contact line, from (2.25), we have continuity of surface mass:

$$\rho_G^s \left(v_{Gt}^s + U_c \cos\theta_d\right) = \rho_S^s \left(v_{St}^s - U_c\right) + \rho_{res}^s U_c. \tag{3.25}$$

The contact line position $(r_c, 0)$, is determined by the contact line evolution equation:

$$\frac{\mathrm{d}r_c}{\mathrm{d}t} = U_c = -v_{Gn}^s / \sin\theta_d, \tag{3.26}$$

and we note that if $Q \neq 0$ then, in general, $U_c \neq \mathbf{u} \cdot \mathbf{t}_S$. Finally, the Young equation, (2.26), becomes

$$\sigma_S^s + \sigma_G^s \cos\theta_d = \sigma_{SG}^s, \qquad \theta_d = \arctan\left(-\frac{\partial z_G}{\partial r_G}\right). \tag{3.27}$$

3.2.3 Initial conditions

The initial position of the drop is chosen so that the dynamic contact angle is $\theta_{d0} = 179°$ and a small portion of the liquid-solid interface exists. Starting from a higher angle was seen to have a negligible influence on the subsequent drop's dynamics. We will assume that the initial velocity field is the same as the flight velocity of the drop, so that the initial conditions are

$$\theta_d = \theta_{d0}, \qquad \mathbf{u} = (0, -1). \tag{3.28}$$

If the interface formation model is being used, then we have

$$\mathbf{v}_G^s = (0, -1), \quad \mathbf{v}_S^s = \mathbf{0}, \quad \rho_G^s = \rho_S^s = \rho_{Ge}^s, \quad \sigma_G^s = \sigma_S^s = 1, \tag{3.29}$$

which reflect the fact that the drop has just touched the solid, so that the liquid-solid surface tension/density is equal to the value it took before impact when it was a liquid-gas interface.

3.3 Parameter range of interest

The impact speed of drops colliding with solids may be as high as $U_0 \sim 10^2$ m s^{-1} in some processes (Lesser & Field, 1983); however, as the drop approaches an equilibrium state, the characteristic speed will be tending to zero. Therefore, although the non-dimensional parameters are based on the impact speed, we would require a range of magnitudes for the non-dimensional parameters to characterize the entire process.

The impact speed and size of drops ejected from ink-jet printers can vary significantly; however, to arrive at estimates for our non-dimensional parameters we consider a drop of radius $a \simeq 25$ μm which impacts a solid at speed $U_0 \simeq 5$ m s^{-1}. Using material constants for water of density $\rho \simeq 10^3$ kg m^{-3}, viscosity $\mu \simeq 10^{-3}$ kg m^{-1} s^{-1}, speed of sound

$c \simeq 1.5 \times 10^3$ m s^{-1} and a liquid-gas equilibrium surface tension of $\sigma \simeq 7 \times 10^{-2}$ N m^{-1} we obtain:

$$Re = \frac{\rho U_0 a}{\mu} \sim 10^2, \quad We = \frac{\rho U_0^2 a}{\sigma} \sim 10, \quad St = \frac{\rho a^2 g}{\mu U_0} \sim 10^{-3}, \quad M = \frac{U_0}{c} \sim 10^{-3},$$

where $We = ReCa$ is the Weber number which in the drop spreading literature is usually used instead of the capillary number. The Mach number M is included to assess the validity of our assumption of incompressibility. When a liquid impacts a solid surface a shock wave is formed which propagates through the drop and creates a pressure jump proportional to M^2 (Lesser & Field, 1983). Due to the smallness of Mach numbers for our problem, we consider our fluid to be incompressible and neglect the effect of this wave as it travels through the drop.

For the solids which we consider, the equilibrium contact angle is in the range $\theta_e \in [10^\circ, 160^\circ]$, with the upper values associated with super-hydrophobic surfaces.

The early stages of spreading are associated with $We, Re \gg 1$ and hence we would expect inertia dominated spreading, which Schiaffino & Sonin (1997) describe as inviscid, impact driven flow. In later stages of spreading, both viscous and capillarity forces will become important and eventually, as the drop tends to its equilibrium shape, will dominate. Therefore, although in the estimates above, the Reynolds number is quite large, the effects of viscosity cannot be neglected. They are important in the boundary layer near the solid after impact and throughout the drop at subsequent stages.

Experimental results from curtain coating, published in Blake & Shikhmurzaev (2002), have been compared to theoretical predictions of the interface formation model. In particular, they showed that $\alpha \sim \beta^{-1}$, and here we will further assume that $\alpha\beta = 1$. The analysis of experiments in Blake & Shikhmurzaev (2002) also provides estimates for the magnitude of phenomenological constants in the interface formation model's equations so

that, with the scales of length and distance used previously, we obtain

$$\epsilon = \frac{U_0\tau}{a} \sim 10^{-3}, \qquad \bar{\beta} = \frac{\beta U_0 a}{\sigma} \sim 10^{3}, \qquad Q = \frac{\rho^s_{(0)}}{\rho U_0 \tau} \sim 10^{-1},$$

Additionally, it is found that $\rho^s_{Ge} \approx 0.6$ and hence, using (3.15) we can see $\lambda \sim 1$. Then, knowing the equilibrium contact angle, from (3.27) we can find the equilibrium surface density on the liquid-solid interface, ρ^s_{Se}, which provides the input of wettability of the solid into the model.

3.4 Summary

A problem is now fully specified by the bulk equations (3.1)–(3.2) combined with either the conventional equations (3.3)–(3.8) or the interface formation equations (3.10)–(3.27) supplemented with initial conditions (3.28)–(3.29). In the next chapter we go on to study how these equations may be solved using numerical methods.

Chapter 4

Numerical procedure

In this chapter, we describe the numerical platform which we have developed to solve the equations of §3 in order to simulate drop impact and spreading phenomena. The platform has been developed so that it may be easily adapted to simulate other capillary problems and in §7 this is demonstrated by using the same code to determine the features of flow over a surface of variable wettability.

4.1 Background

The effects of inertia, viscosity, capillarity and interface formation all contribute to the drop's dynamics. As a consequence, the equations are highly non-linear and hence, if one wishes to proceed without simplifications and the associated limitations on the range of parameters, numerical methods must be used.

The most common numerical methods used for solving free surface flows in a continuum regime are the finite volume, finite difference, finite element and boundary element methods. In each, the aim is to convert a set of PDEs into a set of, often non-linear, algebraic equations which are linearized and then solved using well established methods of linear algebra. This is usually achieved by looking to obtain an approximate solution

to the PDEs at a finite number of positions, called nodes, in the domain. The set of all nodal positions is known as the mesh. The difference between methods is in how the equations are approximated throughout the mesh.

If the solution contains large gradients in certain parts of the domain then it proves necessary to place more nodes in such a region to resolve the physics there correctly. In dynamic wetting problems the most important dynamics to be captured, which occur on a smaller length scale than the bulk flow, appear near the contact line and hence a large number of nodes will be required there.

We shall now describe the numerical methods which have been previously used to simulate drop impact and spreading phenomena, after which we shall outline the finite element method and explain its main advantages over the other methods.

4.1.1 Overview of the numerical methods used to simulate drop impact and spreading phenomena

In the finite difference method equations are formulated at each node, with derivatives calculated using difference formulas. The method has the advantage of being intuitive and reasonably simple to implement in regular geometries. The Marker-and-Cell technique has proved successful for the incorporation of free surfaces into the finite difference methodology and has been used to simulate drops impacting on solids and thin liquid films (Harlow & Shannon, 1967).

Boundary element methods have been used to simulate drop spreading in a Stokes flow regime (Betelú *et al.*, 1997) and for an ideal fluid (Davidson, 2000). In these cases one can reduce the dimensionality of the problem by one; in the case of axisymmetric spreading this leads to a one dimensional problem on the boundary of the domain. This reduction in dimensionality can lead to a significant reduction in the computational demand and complexity of the problem, but is not available when one uses the full Navier-Stokes

equations.

In the finite volume method the domain is split into contiguous cells by a grid which may be structured or unstructured. The conservation laws are then applied in each cell with flux across cell boundaries accounted for. The method has often been applied to free surface flows with the interface cutting through the fixed cells. The interface may then be defined by the fraction of each fluid in a cell (Scardovelli & Zaleksi, 1999). This method has been particularly popular for drop impact problems (Pasandideh-Fard *et al.*, 1996; Bussmann *et al.*, 2000; Yokoi *et al.*, 2009) and is well suited to situations in which the domain undergoes topological transitions, as occurs, for example, if there is splashing after impact.

4.1.2 The finite element method

We use the finite element method (FEM), originally designed for solving structural analysis problems in the 1950's, see the historical review in Gupta & Meek (1996), then later applied to the field of fluid dynamics, and, in particular, successfully applied to free surface flows (e.g. Christodoulou & Scriven, 1989; Fukai *et al.*, 1993; Wilson *et al.*, 2006). This method has the advantage over the other numerical methods of being able to deal with complex geometries without additional complication, by mapping elements in the domain to a *master element* in which analysis is performed. The implementation of stress boundary conditions is achieved in a more natural manner than in other numerical methods where one often has to construct special approximations for such conditions at the boundary.

The simulation of free surface flows using the FEM is well developed with a variety of different approaches successfully implemented. The main differences are in (*i*) how to distribute nodes in the bulk and (*ii*) how to evolve these nodes in time.

The first decision is whether to place the nodes 'by hand' in some predefined manner

(structured meshing), or whether to let the physics of the problems decide where the nodes should be placed (unstructured meshing) in order to capture large gradients in the solution (Mavriplis, 1997).

The second question is which representation to choose, either Eulerian or Lagrangian. In fact a popular choice for free surface flows is the Arbitrary Lagrangian-Eulerian (ALE) approach in which free surface nodes are moved in a Lagrangian manner whilst bulk nodes are evolved in a predefined way. This has the advantage that, as in the Lagrangian approach, the free surface is captured exactly, whilst keeping the main advantage of Eulerian methods that elements are not so easily distorted.

One popular ALE method, known as the *method of spines*, has been successfully applied to many free surface flows (Christodoulou *et al.*, 1997; Heil, 2004; Wilson *et al.*, 2006). This method, described in detail in Kistler & Scriven (1983), builds on the *boundary location method* proposed in Ruschak (1980). In the method, nodes which define the free surface are located at the end of a line on which bulk nodes are attached. These are the so called *spines* of the mesh which usually run from a solid surface to the free surface, with nodes often spaced equally between, see Figure 4.1. As time is stepped forward from t_n to t_{n+1}, all the free surface nodes evolve to new positions and hence the spine, which is attached to the free surface node, moves and drags the bulk nodes to new positions. This choice of parameterization enables simultaneous calculation of the flow field and free surface with the possibility of quadratic convergence.

An alternative method is to decouple the free surface from the bulk flow and look to update its position using either the normal stress condition or the kinematic condition. This method is often used in three-dimensional problems (Cairncross *et al.*, 2000; Baer *et al.*, 2000) where the spine method becomes too computationally intensive.

We anticipate that large gradients in our solution will occur near the contact line and consequently we are able to tailor our mesh accordingly without requiring the power and complexity of unstructured meshing. In this thesis we use the method of spines with

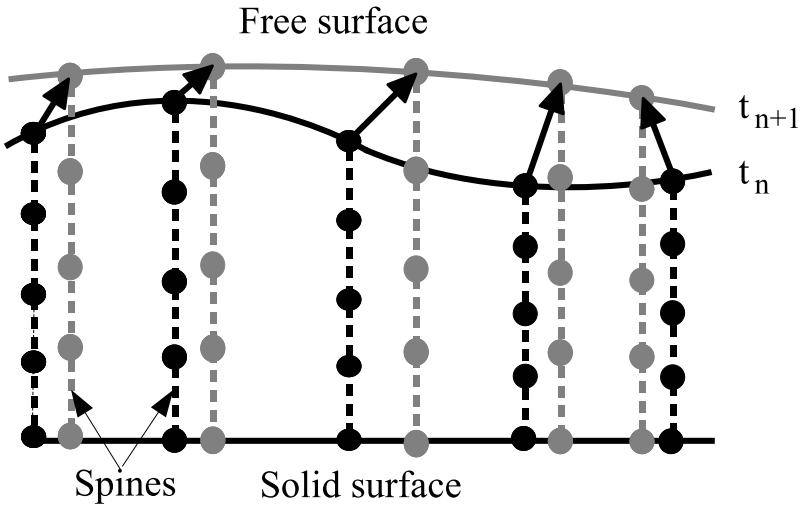

Figure 4.1: Sketch showing how nodes in the bulk lie along spines which run from the solid to the free surface. As time moves from t_n to t_{n+1} nodes in the bulk move with the spine, whose end point defines the new free surface position.

bulk nodes fixed on spines, the motion of which is controlled by the free surface nodal positions. In the following sections we proceed to describe the finite element formulation used for drop impact and spreading simulation.

4.2 Application of the finite element method to drop impact and spreading phenomena

Spines of nodes are distributed over the computational domain and the elements are tessellated around these, see Figure 4.2. At each of the nodes we seek the solution to one or more of the variables in our problem, with the solution approximated by low order polynomials across each element. The global solution is then stitched together using the local element solutions.

Different element types have been used to solve incompressible flow problems (Fortin, 1981); the main variations are in shape, normally either triangular or quadrilateral in two dimensions, and in the number of nodes in each element, or, equivalently, the order of the polynomials across each element. The choice of element for incompressible flow is limited

by the need to satisfy the Ladyzenskaya-Babuska-Brezzi stability condition (Babuska & Aziz, 1972) which, in the primitive formulation of the Navier-Stokes equations, is satisfied when pressure is interpolated with a polynomial of order at least one less than velocity. Such elements are known as mixed elements. The requirement of a lower order approximation of pressure is equivalent to the need for staggered grids in the finite difference method, which ensure that spurious pressure modes are suppressed (Langtangen *et al.*, 2002).

In this thesis, we use triangular elements which approximate the components of velocity quadratically and pressure linearly (Taylor-Hood V6P3 elements) as these elements have been successfully implemented in similar problems (Suckling, 2003; Wilson *et al.*, 2006; Lukyanov & Shikhmurzaev, 2007). In order to keep the free surface smooth we use curved-sided elements. Due to the isoparametric mapping which will be described later, the curved-sided elements are no more difficult to implement than their straight-sided counterparts. Bulk elements contain fifteen unknowns located at six nodes, with each node on the free surface having an additional variable which will determine its location. If the interface formation model is used then four extra variables are present at each node on the liquid-gas interface, whilst three are added to nodes on the liquid-solid interface.

4.2.1 Mesh design

When designing an appropriate numerical scheme to solve drop impact and spreading problems we require a mesh which has the following properties:

(*i*) it is sufficiently fine and refinable near the contact line to capture the appropriate physics there;

(*ii*) the number of nodal points generates a computationally tractable problem;

(*iii*) the elements do not become too distorted as the drop deforms.

To satisfy these constraints we propose a novel way of distributing the spines through the domain. This is based on using the bipolar coordinate system; an idea initially proposed in Suckling (2003) and extended here to deal with problems of large deformation.

In Suckling (2003) the foci of the bipolar system are taken to be $(\pm r_c, 0)$ and the spines, whose lengths determine the shape of the free surface, all emanate from the solid surface, like in Figure 4.1. The problem with this approach is that, although it works well for the majority of the motion, the coordinate system becomes singular as $r_c \to 0$, i.e. as the area of contact between the drop and the solid tends to zero. This is problematic, as, for the drop impact problem, the initial starting position has zero contact between drop and solid; also, if we are to use this platform to model other problems where interface formation is important, such as the breakup of liquid jets or the pinch-off of liquid drops, then it is important that we can obtain the aforementioned limit in a regular way.

Ideally, spines would emanate from both the solid and the axis of symmetry. Thus, initially, all the spines would have a base on the axis of symmetry, but, as the contact line is driven outwards, the mesh would move with the contact line so that the bases of the spines are dragged onto the solid. This may be achieved by using the bipolar coordinate system with foci at the contact line $(r_c, 0)$ and at the apex $(0, z_a)$.

For simplicity, we introduce a new set of Cartesian coordinates, $\mathbf{m} = (m, n)$, which evolve with the mesh and are defined so that the foci of the bipolar coordinate system are located at $(m, n) = (\pm f, 0)$, where $f = \left(\sqrt{r_c^2 + z_A^2}\right)/2$. The transformation back to the original coordinates is given by

$$\begin{pmatrix} r - r_c/2 \\ z - z_a/2 \end{pmatrix} = \begin{pmatrix} \cos(\vartheta) & \sin(\vartheta) \\ -\sin(\vartheta) & \cos(\vartheta) \end{pmatrix} \begin{pmatrix} m \\ n \end{pmatrix}, \tag{4.1}$$

where $\vartheta = \arctan(z_a/r_c)$. The bipolar coordinates (χ, ζ) are related to the new coordinates (m, n) via

$$m = f\frac{\sinh\chi}{\cosh\chi + \cos\zeta}, \quad n = f\frac{\sin\zeta}{\cosh\chi + \cos\zeta}, \tag{4.2}$$

where $\chi \in (-\infty, \infty)$, $\zeta \in (0, \pi)$. Lines of constant χ or ζ are arcs of circles.

Our new mesh is then designed as follows, with the procedure illustrated in Figure 4.2. First we place our spines across the drop by specifying an appropriate function for χ which varies from its value at the contact line, $\chi = \infty$, to its value at the apex of the drop, $\chi = -\infty$. We choose to specify χ in such a way that the distance between adjacent spines increases as a geometric progression as one moves away from the contact line. The nodes are then placed along each spine using a function for ζ which varies from its value at the base ζ_0 to its value at the liquid-gas interface ζ_G, which, for free surface flows, is an unknown of the problem. A linear function $\zeta = \zeta_0 + (\zeta_G - \zeta_0)(j-1)/(j_{max}-1)$ is used to determine the value of ζ at the jth node along a spine containing j_{max} nodes. The elements are then tesselated around the skeleton of the mesh in some appropriate manner.

The mesh design described allows us to have a well resolved region around the contact line whilst far away from the contact line where the dynamics of the drop are controlled by bulk length scales, we can afford to have larger elements and hence lower our computational burden.

A standard parameterization of the free surface is to represent its height as a function of radius or radius as a function of height. Unfortunately this breaks down when the free surface is vertical/horizontal. By using a combination of both representations it is possible to make progress but this approach still contains many drawbacks (Suckling, 2003). In Sprittles (2007) a rather complex method of evolving the spines was designed so as to keep the mesh regular. Here, we propose a more effective and far simpler method: once the spines are distributed according to the contact line position and apex height, the free surface position is determined by the bipolar coordinate ζ_G of a given spine. In this way the spines move with the drop as it evolves and remain equally distributed, without any

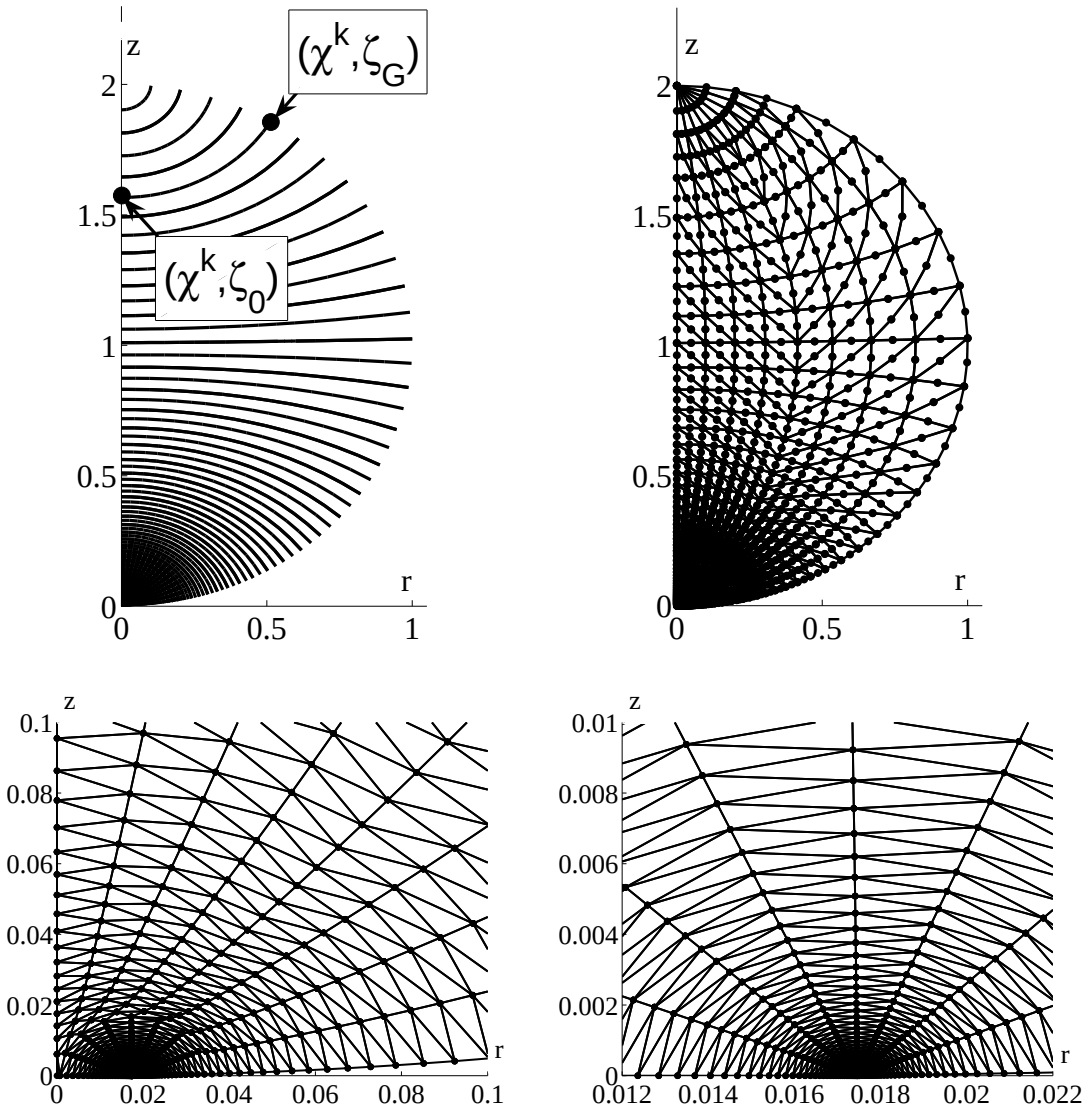

Figure 4.2: Top left: distribution of spines in a drop at its initial position, with the start and end bipolar coordinates of the kth spine shown. Top right: an illustration of how the nodes attach to the spines and the elements are then tessellated around these nodes. Bottom: pictures of increasing resolution showing the density of the mesh as the contact line is approached.

additional complexity.

A consequence of the mesh design is that a node on spine k in the domain becomes dependent on the bipolar coordinate at the end of that spine ζ_G^k, the apex height z_a, and the contact line radius r_c.

The new mesh design works very well for the majority of the motion, see Figure 4.3b-c, but is not ideally suited to meshing the domain when it takes the form of a thin film, which often forms after the inertial stage of spreading as the contact line extends well past its equilibrium radius. Here, we take the foci of the bipolar coordinate system to be at $f = (\pm r_c, 0)$ and $\chi \in (0, \infty)$ which creates a mesh with almost vertical spines for the majority of the film, see Figure 4.3a; the transition requires a full remesh of the domain.

In Figure 4.3 one can observe snapshots of a relatively coarse mesh for the situation in which a drop impacts, spreads and rebounds off a solid substrate. The bipolar coordinate system which determines the mesh generation is, in the first snapshot defined by the foci at $(\pm r_c, 0)$ whilst in the second and third snapshots we can see the newly designed mesh, as used also at the start of the simulation, with foci at $(r_c, 0)$ and $(0, z_a)$: without these mesh alterations there is no way we would be able to simulate such high deformation. In the final image there are actually still over 100 nodes on the liquid-solid interface which are capturing, in this particular case, the interface formation dynamics.

4.2.2 Spatial discretization

For the velocity-pressure formulation of the incompressible Navier-Stokes equations, the *mixed interpolation* should be used (Gresho & Sani, 1999*b*). That is the velocity is approximated across elements with a polynomial of at least one degree higher than pressure. We achieve this by using bi-quadratic interpolating functions ϕ_i for velocity and bi-linear

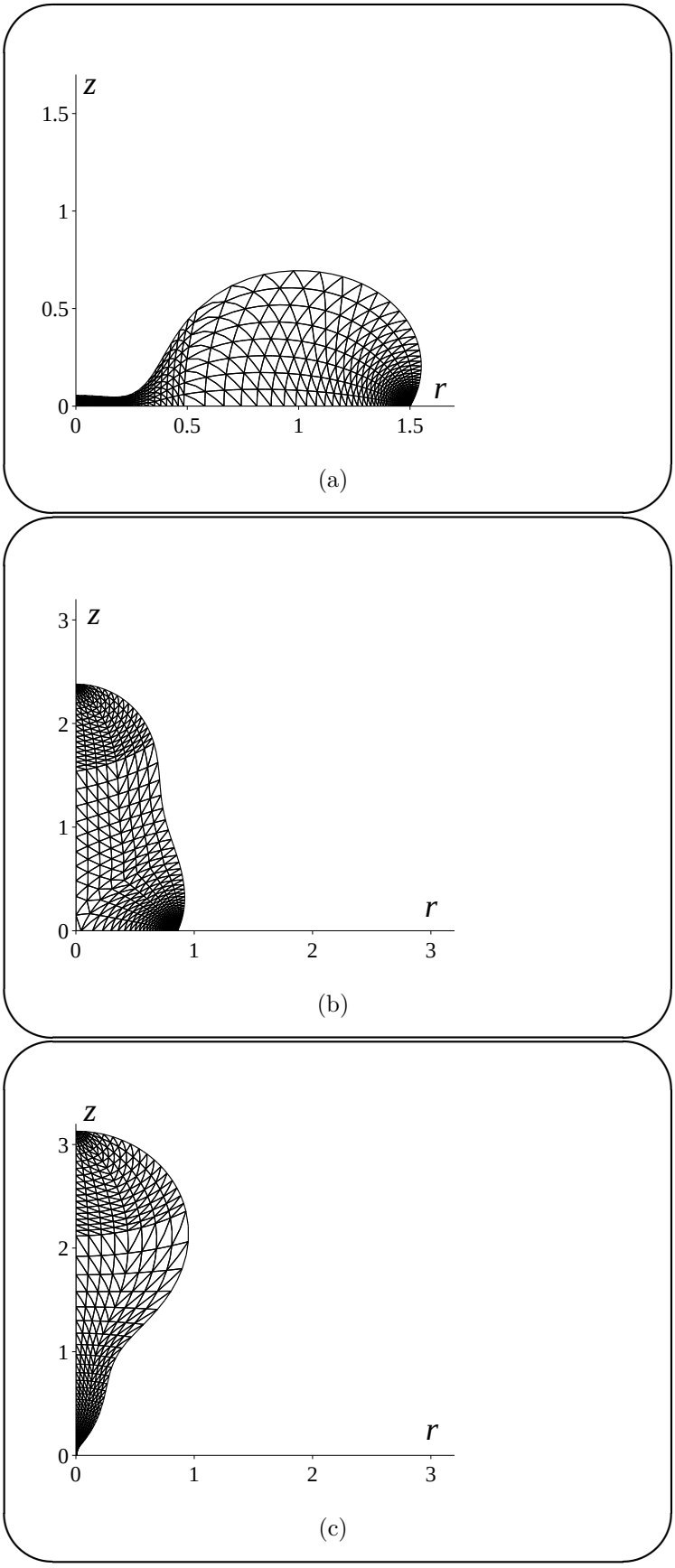

Figure 4.3: Snapshots of a relatively coarse computational mesh for the impact, spreading and rebound of a drop off a hydrophobic substrate.

interpolating functions ψ_j for pressure. Then

$$\mathbf{u} = \sum_{i=1}^{N_u} \mathbf{u}_i \phi_i(\xi, \eta) \ , \qquad p = \sum_{j=1}^{N_p} p_j \psi_j(\xi, \eta), \tag{4.3}$$

where $\mathbf{u}_i$ is the velocity at the ith node and p_j is the pressure at the jth pressure node. There are a total of N_u velocity nodes and N_p pressure nodes. All of the interpolating functions are defined so that each is unity at one node and zero at all the others. These are constructed using local coordinates (ξ, η) over an equilateral triangle called the master element, see Figure 4.4, and are given by

$$\begin{aligned}
&\psi_1 = \frac{1+\eta}{2}, \quad \psi_2 = -\frac{\xi+\eta}{2}, \quad \psi_3 = \frac{1+\xi}{2}, \\
&\phi_1 = 2\psi_1(2\psi_1 - 1), \quad \phi_2 = 2\psi_2(2\psi_2 - 1), \quad \phi_3 = 2\psi_3(2\psi_3 - 1), \\
&\phi_4 = 4\psi_1\psi_3, \quad \phi_5 = 4\psi_2\psi_1, \quad \phi_6 = 4\psi_3\psi_2.
\end{aligned}$$

This triangle is then mapped onto the deformed, curved triangular elements in the computational domain using the mapping

$$r = \sum_{i=1}^{N_u} r_i(r_c, z_a, \zeta_G^k)\phi_i(\xi, \eta) \ , \qquad z = \sum_{i=1}^{N_u} z_i(r_c, z_a, \zeta_G^k)\phi_i(\xi, \eta), \tag{4.4}$$

where (r_i, z_i) are the nodal positions in the global domain. The ability to find the global coordinates of the interior of an element using only its nodal positions and the interpolating functions gives the elements the property of being *isoparametric*. This mapping ensures that the solution to problems in complex domains are of no greater difficulty, as all analysis is performed over the same master element independent of the element's shape in the computational domain.

In (4.4), the dependency of each node on the contact line position, apex position and bipolar coordinate at the end of a spine is shown as, (r_c, z_a, ζ_G^k), but this notation henceforth dropped. The free liquid-gas interface is approximated quadratically and elements

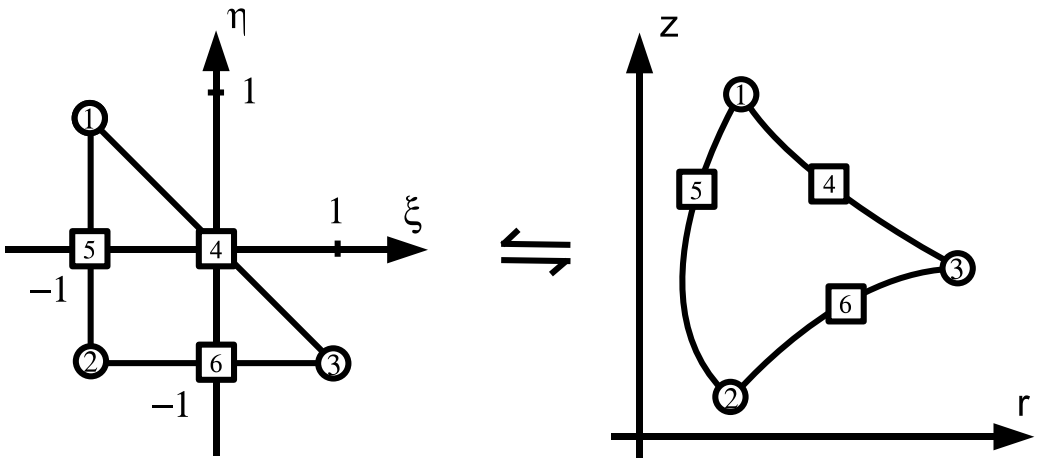

Figure 4.4: The V6P3 master element with local coordinates (ξ, η) which is mapped into the physical (r, z) space via the isoparametric mapping (4.4). The numbered circles represent nodes at which the velocity and pressure are to be found whilst the squares are velocity only nodes.

are orientated to ensure that when the edge of an element defines part of a boundary in the computational domain, the local nodal values associated with that element are always the same on that boundary. We choose the liquid-gas interface to have nodes $2, 6, 3$ associated with it, the liquid-solid interface to have nodes $1, 5, 2$ and the axis-of-symmetry to have $1, 4, 3$. Then, quadratic line elements on the liquid-gas interface and liquid-solid interface are $\phi_m(\xi, -1),\ (m = 1, N_G)$ and $\phi_p(-1, \eta),\ (p = 1, N_S)$, respectively, where N_S and N_G are the number of nodes on that interface. Surface variables may be easily expanded in terms of their nodal values by noting that, for example, on the free surface $\eta = -1$ and hence for a position (r_G, z_G) we have

$$r_G = \sum_{m=1}^{N_G} r_m \phi_m(\xi, -1), \qquad z_G = \sum_{m=1}^{N_G} z_m \phi_m(\xi, -1). \tag{4.5}$$

The interface formation variables are also approximated as an expansion in terms of a

finite number of interpolating functions and, on the free surface, they are

$$\rho_G^s = \sum_{m=1}^{N_G} (\rho_G^s)_m \phi_m(\xi, -1), \quad \sigma_G^s = \sum_{m=1}^{N_G} (\sigma_G^s)_m \phi_m(\xi, -1), \tag{4.6}$$

$$v_{Gt}^s = \sum_{m=1}^{N_G} (v_{Gt}^s)_m \phi_m(\xi, -1), \quad v_{Gn}^s = \sum_{m=1}^{N_G} (v_{Gn}^s)_m \phi_m(\xi, -1), \tag{4.7}$$

whilst on the liquid-solid surface they are

$$\rho_S^s = \sum_{p=1}^{N_S} (\rho_S^s)_p \phi_p(-1, \eta), \quad \sigma_S^s = \sum_{p=1}^{N_S} (\sigma_S^s)_p \phi_p(-1, \eta), \quad v_{St}^s = \sum_{p=1}^{N_S} (v_{St}^s)_p \phi_p(-1, \eta). \tag{4.8}$$

Using the coordinate transformation

$$\frac{\mathrm{d}l_G}{\mathrm{d}\xi} = \sqrt{\left(\frac{\partial r_G}{\partial \xi}\right)^2 + \left(\frac{\partial z_G}{\partial \xi}\right)^2}, \tag{4.9}$$

the unit tangent and normal vectors to the free surface are found locally to be

$$\mathbf{t}_G = \left(\frac{\partial r_G}{\partial \xi}\mathbf{e}_r + \frac{\partial z_G}{\partial \xi}\mathbf{e}_z\right)\frac{\mathrm{d}\xi}{\mathrm{d}l_G}, \qquad \mathbf{n}_G = \left(\frac{\partial z_G}{\partial \xi}\mathbf{e}_r - \frac{\partial r_G}{\partial \xi}\mathbf{e}_z\right)\frac{\mathrm{d}\xi}{\mathrm{d}l_G} \tag{4.10}$$

Also, from the mapping (4.5) we have

$$\frac{\partial r_G}{\partial \xi} = \sum_{m=1}^{N_G} r_m \frac{\partial \phi_m(\xi, -1)}{\partial \xi}, \tag{4.11}$$

$$\frac{\partial z_G}{\partial \xi} = \sum_{m=1}^{N_G} z_m \frac{\partial \phi_m(\xi, -1)}{\partial \xi}. \tag{4.12}$$

Substitution of our approximate solutions into the equations will, in general, result in an error. In the finite element method we require that a *weighted average of the error vanishes over the entire domain.* In the Galerkin method the interpolating functions which were used to discretize our velocity and pressure, are also used as the weighting functions. This gives the *weak form* of our equations.

All equations are weighted with the (bi-)quadratic interpolating functions, apart from the continuity equation which is weighted with the bi-linear pressure interpolating functions. This ensures the same number of equations as unknowns.

The continuity residuals R_C^j are

$$R_C^j = \int_\Omega \psi_j \nabla \cdot \mathbf{u} \; d\Omega, \tag{4.13}$$

whilst the momentum residuals $R_i^{M,\beta}$, where $\beta = (r, \theta, z)$ give

$$R_i^{M,\beta} = \int_\Omega \phi_i \mathbf{e}_\beta \cdot \left[Re \left(\frac{\partial \mathbf{u}}{\partial t} + (\mathbf{u} - \dot{\mathbf{x}}_m) \cdot \nabla \mathbf{u} \right) - \nabla \cdot \mathbf{P} + St \mathbf{e}_z \right] d\Omega, \tag{4.14}$$

where $\dot{\mathbf{x}} = \dfrac{\partial \mathbf{x}}{\partial t}$ is the mesh velocity, as is required in ALE methods as the nodes evolve in time (Jimack & Wathen, 1991). The momentum equations require boundary conditions on every portion of the domain. The application of such conditions can be simplified by using the identity

$$\nabla \cdot (\phi_i \mathbf{e}_\beta \cdot \mathbf{P}) = (\phi_i \mathbf{e}_\beta) \cdot \nabla \cdot \mathbf{P} + (\mathbf{e}_\beta \nabla \phi_i) : \mathbf{P} \tag{4.15}$$

and then by applying the divergence theorem to obtain the *modified Galerkin* (Lewis & Ward, 1991) form of the momentum residuals

$$\mathbf{R}_i^{M,\beta} = \int_\Omega \left[\phi_i \mathbf{e}_\beta \cdot \left[Re \left(\frac{\partial \mathbf{u}}{\partial t} + (\mathbf{u} - \dot{\mathbf{x}}_m) \cdot \nabla \mathbf{u} \right) + St \mathbf{e}_z \right] + (\mathbf{e}_\beta \nabla \phi_i) : \mathbf{P} \right] d\Omega + \oint_\omega \phi_i \mathbf{e}_\beta \cdot \mathbf{P} \cdot \mathbf{n} \; d\omega, \tag{4.16}$$

where $\mathbf{n}$ is the inward normal to the surface $\omega = \partial\Omega$ and in cylindrical coordinates we will have $d\Omega = r dr d\theta dz$ and $d\omega = r d\theta dl$, where l is the arclength along a given boundary for a fixed value of θ.

Boundary conditions of both Dirichlet and stress type are present in our problem formulation. To apply a Dirichlet condition for a given variable we must first identify

which equation is used to determine its value and then replace this equation with the Dirichlet condition at the appropriate node.

Stress conditions are incorporated into the finite element method in a non-intrusive manner by specifying the boundary integral in (4.16). Therefore, the momentum equations will have contributions from the bulk and the boundary so that

$$R_i^{M,\beta} = \left(R_i^{M,\beta}\right)_\Omega + \left(R_i^{M,\beta}\right)_\omega, \tag{4.17}$$

where

$$\left(R_i^{M,\beta}\right)_\omega = \oint_\omega \phi_i \mathbf{e}_\beta \cdot \mathbf{P} \cdot \mathbf{n}\, d\omega. \tag{4.18}$$

Stress conditions are present on all boundaries, so we split our boundary contribution into

$$\left(R_i^{M,\beta}\right)_\omega = \left(R_i^{M,\beta}\right)_{\omega_S} + \left(R_i^{M,\beta}\right)_{\omega_A} + \left(R_i^{M,\beta}\right)_{\omega_G}. \tag{4.19}$$

The individual terms will now be derived for the interface formation equations. The conventional equations may be recovered by setting the surface variables to their equilibrium values and replacing the Young equation with a contact angle formula.

Liquid-gas interface

Using (3.11) we obtain

$$\left(R_i^{M,\beta}\right)_{\omega_G} = -\frac{1}{Ca}\int_{\omega_G} \phi_i \mathbf{e}_\beta \cdot \left[\nabla \cdot \left(\sigma_G^s \left(\mathbf{I} - \mathbf{nn}\right)\right)\right]\, d\omega_G. \tag{4.20}$$

Direct calculation of the integrand will result in second derivatives of our basis functions. This can be circumvented using the approach originally proposed in Ruschak (1980) and later used in three-dimensional problems in, for example, Cairncross *et al.* (2000, p. 400).

First we use the chain rule to obtain

$$\left(R_i^{M,\beta}\right)_{\omega_G} = -\frac{1}{Ca}\int_{\omega_G} \nabla\cdot\left[\left(\phi_i \mathbf{e}_\beta\right)\cdot\left(\sigma_G^s\left(\mathbf{I}-\mathbf{nn}\right)\right)\right] - \left(\sigma_G^s\left(\mathbf{I}-\mathbf{nn}\right)\right) : \nabla\left(\phi_i\mathbf{e}_\beta\right)\ d\omega_G. \quad (4.21)$$

Note that $\nabla_s = (\mathbf{I}-\mathbf{nn})\cdot\nabla$ is the so-called surface gradient operator. Then, using the surface divergence theorem we obtain

$$\left(R_i^{M,\beta}\right)_{\omega_G} = \frac{1}{Ca}\int_{\omega_G} \sigma_G^s\left(\mathbf{I}-\mathbf{nn}\right) : \nabla\left(\phi_i\mathbf{e}_\beta\right)\ d\omega_G - \frac{1}{Ca}\int_C \sigma_G^s\phi_i\mathbf{e}_\beta\cdot\mathbf{m}\ dC \quad (4.22)$$

where $\mathbf{m}$ is the unit vector tangential to the surface and normal to the boundary curve C along the edge of the surface ω_G. Then, in cylindrical axisymmetric coordinates where $\nabla_s = \mathbf{t}\dfrac{\partial}{\partial l_G} + \frac{\mathbf{e}_\theta}{r}\dfrac{\partial}{\partial\theta}$, noting that a 2π obtained after integration over θ is cancelled from every contribution, we have

$$\left(R_i^{M,r}\right)_{\omega_G} = \frac{1}{Ca}\int_{l_G=0}^{l_G=l_a} \sigma_G^s\left[\left(\mathbf{t}_G\cdot\mathbf{e}_r\right)\frac{\partial\phi_i}{\partial r_G} + \frac{\phi_i}{r_G}\right]\ r_G dl_G - \frac{1}{Ca}\left[\left(\mathbf{e}_r\cdot\mathbf{t}_G r_G\right)_a + \left(\mathbf{e}_r\cdot\left(-\mathbf{t}_G\right)r_G\right)_c\right], \quad (4.23)$$

$$\left(R_i^{M,z}\right)_{\omega_G} = \frac{1}{Ca}\int_{l_G=0}^{l_G=l_a} \sigma_G^s\left(\mathbf{t}_G\cdot\mathbf{e}_z\right)\frac{\partial\phi_i}{\partial r_G}\ r_G dl_G - \frac{1}{Ca}\left[\left(\mathbf{e}_z\cdot\mathbf{t}_G r_G\right)_a + \left(\mathbf{e}_z\cdot\left(-\mathbf{t}_G\right)r_G\right)_c\right], \quad (4.24)$$

where subscript a, c demands that the expression be evaluated at the axis of symmetry or contact line, respectively, so that l_a is the arclength along the free surface from the contact line $l_G = 0$ and as $r_G|_a = 0$ there will only be a contribution from the contact line. Now the highest derivatives are of first order. The end point terms could be used to apply boundary conditions on the shape of the free surface at its two ends; however, in this thesis we apply the Young equation (3.27) as a Dirichlet condition. This is because numerical experiments have shown that for high contact angles this equation will not be satisfied in the weak form. This is what Christodoulou & Scriven (1989, p. 333), found in their finite element simulations of slide coating. At the axis of symmetry, condition (3.24) gives that $\mathbf{t}_G|_a = (-1, 0)$.

After using integration by parts and the divergence theorem on the weak form of (3.13), and defining the mesh velocity tangential to the interface to be $\dot{x}_t = \dot{\mathbf{x}}_m \cdot \mathbf{t}$, the interface formation equations on the liquid-gas interface become

$$\left(R_m^{G1}\right)_{\omega_G} = \int_{l_G=0}^{l_G=l_a} \phi_m \left(\frac{\partial x_n}{\partial t} - v_{Gn}^s\right) r_G \, dl_G, \tag{4.25}$$

$$\left(R_m^{G2}\right)_{\omega_G} = \int_{l_G=0}^{l_G=l_a} \phi_m \left[u_n - v_{Gn}^s - Q\left(\rho_G^s - \rho_{Ge}^s\right)\right] r_G \, dl_G, \tag{4.26}$$

$$\left(R_m^{G3}\right)_{\omega_G} = \int_{l_G=0}^{l_G=l_a} \left[\phi_m r_G \left(\frac{\partial \rho_G^s}{\partial t} - \dot{x}_{Gt}\frac{\partial \rho_G^s}{\partial l_G} + \rho_G^s v_{Gn}^s \kappa_G + \frac{\rho_G^s - \rho_{Ge}^s}{\epsilon}\right) - \rho_G^s v_{Gt}^s r_G \frac{\partial \phi_m}{\partial l_G}\right] dl_G - \left[\phi_m \rho_G^s v_{Gt}^s r_G\right]_c, \tag{4.27}$$

$$\left(R_m^{G4}\right) = \int_{l_G=0}^{l_G=l_a} \phi_m \left(v_{Gt}^s - u_t - \left(1 + 4\bar{\alpha}\bar{\beta}\right)\frac{\partial \sigma_G^s}{\partial l_G}\right) r_G \, dl_G, \tag{4.28}$$

$$\left(R_m^{G5}\right)_{\omega_G} = \int_{l_G=0}^{l_G=l_a} \phi_m \left(\sigma_G^s - \lambda(1 - \rho_G^s)\right) r_G \, dl_G. \tag{4.29}$$

At the axis of symmetry, equations (4.27) and (4.28) are replaced by conditions of symmetry $v_{Gt}^s = \dfrac{\partial \rho_G^s}{\partial l_G} = 0$. An alternative approach is to specify the end point conditions in (4.27); this approach was also implemented and made no difference to our results. At the contact line, equation (4.27) is applied and hence the point term at the contact line $\left[\phi_m \rho_G^s v_{Gt}^s r_G\right]_c$ needs to be included; elsewhere the point contributions, which are fluxes of surface mass between elements, have been set to zero to enforce surface mass continuity.

Liquid-solid interface

The generalized Navier equation (3.17) is a stress condition and contributes to the radial momentum equation giving

$$\left(\mathbf{R}_i^M\right)_{\omega_S} = \int_{l_S=0}^{l_S=l_c} \phi_i \mathbf{P} \cdot \mathbf{n}_S \, r_S \, dl_S = \left(\frac{1}{Ca}\int_{\omega_S} \phi_i \left(\bar{\beta}\mathbf{u} \cdot \mathbf{t}_S - \frac{1}{2}\frac{\partial \sigma_S^s}{\partial l_S}\right) r_S \, dl_S, 0\right). \tag{4.30}$$

Additionally, after integrating the weak form of (3.18) by parts and using the divergence theorem, we obtain the surface equations:

$$\left(R_p^{S1}\right)_{\omega_S} = \int_{l_S=0}^{l_S=l_c} \left[\phi_p r_S \left(\frac{\partial \rho_S^s}{\partial t} - \dot{x}_{St}\frac{\partial \rho_S^s}{\partial l_S} + \frac{\rho_S^s - \rho_{Se}^s}{\epsilon}\right) - \rho_S^s v_{St}^s r_S \frac{\partial \phi_p}{\partial l_S}\right] dl_S - \left[\phi_p \rho_S^s v_{St}^s r_S\right]_c, \quad (4.31)$$

$$\left(R_p^{S2}\right)_{\omega_S} = \int_{l_S=0}^{l_S=l_c} \phi_p \left[u_n - Q\left(\rho_S^s - \rho_{Se}^s\right)\right] r_S \, dl_S, \quad (4.32)$$

$$\left(R_p^{S3}\right)_{\omega_S} = \int_{l_S=0}^{l_S=l_c} \phi_p \left(v_{St}^s - \tfrac{1}{2}\left(u_t + U_t\right) - \bar{\alpha}\frac{\partial \sigma_S^s}{\partial l_S}\right) r_S \, dl_S, \quad (4.33)$$

$$\left(R_p^{S4}\right)_{\omega_S} = \int_{l_S=0}^{l_S=l_c} \phi_p \left(\sigma_S^s - \lambda(1-\rho_S^s)\right) r_S \, dl_S. \quad (4.34)$$

Once again, at the axis of symmetry, equations (4.31) and (4.33) are replaced by conditions of symmetry $v_{St}^s = \dfrac{\partial \rho_S^s}{\partial l_S} = 0$. At the contact line (4.31) is replaced by the contact line mass continuity condition (3.25).

Axis of symmetry

Here, we have one stress and one Dirichlet condition (3.22) to apply giving

$$\left(\mathbf{R}_i^M\right)_{\partial\Omega_A} = \mathbf{0}. \quad (4.35)$$

Summary of spatial discretization

Upon substitution of our approximate solution into the weak form of our equations, we will obtain a set of algebraic equations[1] which, when solved, will approximate the actual solution to a required accuracy. The problem are time dependent and we must now consider how to represent the temporal derivatives.

[1]The entire set of local element matrices created by the finite element method are listed in Suckling (2003, Appendix G) for a similar formulation.

4.2.3 Temporal discretization

The result of our spatial discretization is a system of non-linear first order ordinary differential equations (ODEs) in time with a constraint, the continuity condition. Such a system of ODEs that is subject to an algebraic constraint is called a set of Differential Algebraic Equations (DAEs). Our system has Differential Algebraic index 2, which is a measure of the complexity of solving such a system (Gresho & Sani, 1999*b*), with ODEs having index zero. The index is determined by how many times the constraint of a system must be differentiated with respect to time in order to obtain an ODE system. Despite these possible difficulties it has been shown that the same methods that apply to ODEs can be used for DAEs (Lötstedt & Petzold, 1986). For a review of the methods available we refer the reader to Gresho & Sani (1999*b*).

In this thesis, we implement the second-order Backward Differentiation Formula (BDF2) which has been applied successfully to similar problems (Heil, 2004). Here we describe the method applied to a scalar equation $\dot{y} = f(y,t)$, with the extension to the Navier-Stokes equations being a relatively simple task. For a time $(n+1)$ with step $\triangle t$, the method applied to the scalar equation gives

$$\frac{y_{n+1} - y_n}{\triangle t} = \frac{1}{3}\frac{y_n - y_{n-1}}{\triangle t} + \frac{2}{3}\dot{y}_{n+1}, \tag{4.36}$$

where the subscript indicates the time step at which a variable is evaluated and $\dfrac{\mathrm{d}y}{\mathrm{d}t} = \dot{y}$. Alternatively it may be written as

$$\frac{3y_{n+1} - 4y_n + y_{n-1}}{2\triangle t} = \dot{y}_{n+1}, \tag{4.37}$$

which is the second-order accurate one sided Taylor series expansion of y at t_{n+1}.

When a drop impacts and spreads on a solid surface there are different 'stages' of spreading which are characterized by different time scales (Rioboo *et al.*, 2002). Just after

impact the drop will deform rapidly, yet at later times the drop will oscillate relatively slowly around its equilibrium position. It is important that our temporal discretization takes these different scales into account so that the largest possible time step, that enforces a certain accuracy, is chosen automatically. This is achieved by choosing a step size so that the local truncation error $d_n = y_{n+1} - y(t_{n+1})$, where $y(t_{n+1})$ is the exact solution, is maintained below a certain tolerance. By using an explicit second-order Adams-Bashforth method (AB2) (Gresho & Sani, 1999a) to predict the solution y^p_{n+1}, and then comparing the difference between the actual solution and the predicted one, after solving the non-linear equations we are able to deduce this error. For the equation, $\dot{y} = f(y,t)$, having obtained the solution y_{n+1} we follow the analysis of Gresho & Sani (1999a) to obtain a new time step. The BDF2 for variable step size gives

$$\frac{y_{n+1} - y_n}{\triangle t_n} = \frac{\triangle t_n}{2\triangle t_n + \triangle t_{n-1}} \frac{y_n - y_{n-1}}{\triangle t_{n-1}} + \frac{\triangle t_n + \triangle t_{n-1}}{2\triangle t_n + \triangle t_{n-1}} \dot{y}_{n+1}, \tag{4.38}$$

while the predictor gave

$$y^p_{n+1} = y_n + \left(1 + \frac{\triangle t_n}{\triangle t_{n-1}}\right) \triangle t_n \dot{y}_n - (y_n - y_{n-1}) \left(\frac{\triangle t_n}{\triangle t_{n-1}}\right)^2. \tag{4.39}$$

The local truncation error of (4.38) is given by

$$d_n = \frac{(\triangle t_n + \triangle t_{n-1})^2}{\triangle t_n (2\triangle t_n + \triangle t_{n-1})} \frac{\triangle t_n^3 \dddot{y}_n}{6} + \mathrm{O}(\triangle t_n^4) \tag{4.40}$$

whilst the predictor's error is

$$y^p_{n+1} - y(t_{n+1}) = -\left(1 + \frac{\triangle t_n}{\triangle t_{n-1}}\right) \frac{\ddot{y}_n}{6} + \mathrm{O}(\triangle t_n^4). \tag{4.41}$$

We may eliminate the exact solution's contribution $y(t_{n+1})$, which, of course, in general

will not be known, from (4.40) and (4.41) to give

$$d_n = \frac{(1 + \triangle t_{n-1}/\triangle t_n)^2}{1 + 3(\triangle t_{n-1}/\triangle t_n) + 4(\triangle t_{n-1}/\triangle t_n)^2 + 2(\triangle t_{n-1}/\triangle t_n)^3}(y_{n+1} - y^p_{n+1}), \qquad (4.42)$$

so that the error is linearly proportional to the difference between the predicted and actual solution. This error estimate is then used to compute the next step size

$$\triangle t_{n+1} = \triangle t_n(\epsilon/\|d_n\|)^{1/3}, \qquad \|d_n\|^2 = d_n^T d_n/(N y^2_{max}). \qquad (4.43)$$

Here, N is the total number of nodes, y_{max} is an estimate of the maximum value of y in the domain and ϵ is the relative error tolerance parameter. Then the error of the approximate solution is bounded by $\|d_{n+1}\| \leq \epsilon y_{max}$. This allows us to choose the largest possible time step whilst ensuring that the error of the temporal integration remains below a chosen tolerance.

The variable step method outlined above can be extended for use with the Navier-Stokes equations. It is only the velocity solution that is used in the error analysis, as no temporal derivatives of pressure enter the problem. The reader is referred to Gresho & Sani (1999*b*, p. 797), for details. In this book a number of 'rules of thumb' are suggested based on the ratio of the new and previous step sizes, the so-called Delta T Scale Factor, $DTSF = \frac{\triangle t_{n+1}}{\triangle t_n}$. In this code the following constraints are applied.

(*i*) If $DTSF < 0.6$ then the solution is rejected because of the poor correlation between the predicted and actual solution. The time step is repeated with a smaller step size.

(*ii*) If $0.6 \leq DTSF \leq 10$ then the new time step is accepted.

(*iii*) If $DTSF > 10$ then the new time step is set to equal $\triangle t_{n+1} = 10\triangle t_n$. This ensures no large jumps in the time step.

4.2.4 Numerical integration

The coefficients of our nodal unknowns, produced by the finite element procedure, are integrals which must be calculated. A global element E is always mapped onto the master element for integration to be performed, so that we encounter integrals of the form

$$\int_E f(r,z)dE = \int_{\eta=-1}^{-\xi}\int_{\xi=-1}^{1} f(r(\xi,\eta),z(\xi,\eta)) \mid \det(\mathbf{J}_t) \mid r(\xi,\eta)d\xi d\eta, \tag{4.44}$$

to evaluate, where

$$\det(\mathbf{J}_t) = \frac{\partial r}{\partial \xi}\frac{\partial z}{\partial \eta} - \frac{\partial r}{\partial \eta}\frac{\partial z}{\partial \xi} \tag{4.45}$$

is the Jacobian of the isoparametric mapping. Gaussian quadrature allows the integral to be approximated by a weighted sum of the integrand evaluated at n points, called the Gauss points, so that we may evaluate the integrals numerically:

$$\int_{\eta=-1}^{-\xi}\int_{\xi=-1}^{1} f(r(\xi,\eta),z(\xi,\eta)) \mid \det(\mathbf{J}_t) \mid r(\xi,\eta)d\xi d\eta = \tag{4.46}$$

$$\sum_{i=1}^{n} f(\xi_i,\eta_i) \mid (\det \mathbf{J}_t(\xi_i,\eta_i)) \mid r(\xi_i,\eta_i)w_i, \tag{4.47}$$

where w_i is the weight corresponding to Gauss point i. Using n Gauss points allows one to integrate polynomials of degree $2n-1$ exactly (Zienkiewicz & Taylor, 1989).

4.2.5 Remeshing

When elements become so distorted that either the accuracy of the solution is affected or convergence is not possible, then remeshing is the only option. The idea is as follows.

(*i*) Use the current free surface position to generate a new mesh.

(*ii*) Find which old element each new node is contained in.

(*iii*) Use the polynomial approximation across the relevant element to project the old

solution onto the new node.

For incompressible viscous flows this can be problematic, as projecting the solution in this naive manner will in general result in a velocity field which is no longer divergence free (Gresho & Sani, 1999*b*, Appendix 5). Additionally, the process is always associated with a certain loss in accuracy. It is for these reasons that remeshing is an undesirable procedure which we look to circumvent wherever possible.

The need for remeshing is caused by the isoparametric mapping becoming non-invertible. Determining when the distortion of the mesh is such that remeshing is required is an important part of any code, as one wants to maintain the right balance between increasing accuracy by having un-deformed elements and losing accuracy by having to remesh too often. The degeneracy of a straight-sided element may be determined from the internal angles $\alpha_i,\ i = 1, 3$ of the triangle. If $\alpha_i \simeq 0$ or $\alpha_i \simeq \pi$ then the Jacobian of the isoparametric mapping $\det(\mathbf{J}_t)$, defined by (4.45), will become singular and the element is considered degenerate. For curved-sided elements we require a more advanced method and use one suggested in Suckling (2003). He calculates the modulus of the Jacobian normalized by the area of each element, that is

$$D = \left(\frac{\mid \det(\mathbf{J}_t(\xi, \eta)) \mid}{\int_{\eta=-1}^{\eta=-\xi} \int_{\xi=-1}^{\xi=1} \mid \det(\mathbf{J}_t(\xi, \eta)) \mid d\xi d\eta} \right). \tag{4.48}$$

The minimum of D over an element is then taken as an indication of the degeneracy of the element. In reality it proves sufficient to calculate D at a finite number of points inside the element. This check has proved very efficient at identifying degenerate elements and after numerical testing it was found that remeshing should be enforced when $D < 0.25$.

By using a specially designed ALE method, we ensure that regular remeshing of the whole domain is not required. In particular, our design ensures we don't need to remesh the contact line region, which could lead to substantial error generation. Despite the success of this approach, situations do occur when extra resolution is required in a certain

region; this usually occurs due to capillary waves which emanate from the contact line region and travel up the free surface, creating a large curvature in the free surface shape. When these capillary waves reach the axis of symmetry they can often cause the apex to become very close to, and sometimes even touch, the solid surface; these events require a huge amount of resolution in an area of the drop which is usually least resolved. To ensure that the correct outcome is predicted, i.e. the possible formation of a dry-spot, remeshing in this region is essential.

We have implemented a relatively simple remeshing scheme which allows the addition of spines in regions which require them, based on the degeneracy of the elements and the curvature of the free surface. Essentially, if there are not enough elements in an area of high free surface curvature, then two extra spines are added between the existing ones; this creates two rows of elements where previously there was only one. This procedure can be used recursively until the desired accuracy is achieved.

As previously mentioned, the naive projection of variables will invariably lead to a velocity field which does not satisfy the continuity constraint. To overcome these difficulties one may implement more complicated projections. However, a good approximation is to remesh naively and then use two small backward Euler time steps (Gresho & Sani, 1999*b*) in which the velocity field will be adjusted to become divergence-free. In our experience it has been sufficiently accurate to remesh naively when this is necessary and simply continue our implicit time integration with BDF2.

4.2.6 Solution procedure for non-linear algebraic equations

Given the residuals $\mathbf{R}$ evaluated at a point $\boldsymbol{\alpha}^m$, the Newton-Raphson method provides an updated solution $\boldsymbol{\alpha}^{m+1}$ by solving

$$\mathbf{J}\left[\boldsymbol{\alpha}^{m+1} - \boldsymbol{\alpha}^m\right] = -\mathbf{R}(\boldsymbol{\alpha}^m), \qquad \mathbf{J} = \frac{\partial \mathbf{R}(\boldsymbol{\alpha}^m)}{\partial \boldsymbol{\alpha}}. \tag{4.49}$$

The method has quadratic convergence and may be repeated until a sufficient degree of accuracy is achieved. This procedure requires the solution of the linear set of equations (4.49).

To form the Jacobian we can calculate the entries numerically using a difference formula or determine the terms analytically. The dependence of all equations on the free surface unknowns is extremely complicated; however, in terms of speed and accuracy, the advantages gained from making an analytic calculation are significant. In a similar work, on the coalescence of liquid drops, in which the Jacobian was calculated using difference formulas, it took six hours to complete a time step with 1500 elements (Shaw, 2005, p. 186); here, with the Jacobian calculated analytically, such a time step takes only a few seconds. Analytic calculation also improves the convergence of the code, particularly when using small elements where round-off errors in the calculation of the Jacobian can become significant if calculated numerically. The only non-analytic calculation in our code is the dependence of the bulk nodal positions on the free surface position, which can be determined numerically quite quickly as nodes only depend on the contact line position, apex height and nodal position at the end of the spine on which they lie.

In the finite element method many equations are only dependent on unknowns in adjacent elements, so that most entries in the Jacobian are zero. Then, if the equations and unknowns are ordered in a sensible manner, this matrix is sparse and banded. The resulting linearized equations are solved using the MA41 solver provided by the Harwell Subroutine Library.

4.2.7 Geometric wetting

It can be shown that there will be a short period after impact during which the contact angle remains at 180° and the wetting mechanism differs from the subsequent contact-line-driven motion. We refer to this as the *geometric wetting* phase since it is the geometry

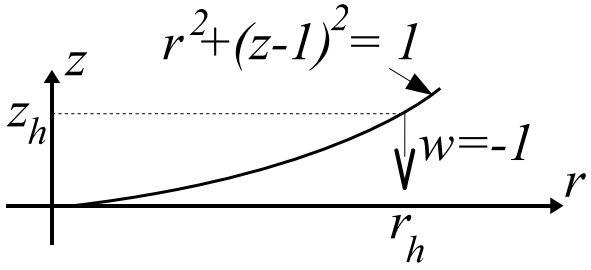

Figure 4.5: Sketch of the contact line region at the point of impact.

of the shapes of the liquid and the solid that determine it.

Just after the moment of impact one has that the area of contact between the liquid and the solid is infinitesimal as $t \to 0$. Hence, to leading order, the downward velocity of the free surface remains the same. For a point (r_h, z_h) on the free surface near to the contact line, it takes a time $t = z_h/|w|$, with $w = -1$, to reach the solid, see Figure 4.5. Using this with the equation of the free surface, $r_h^2+(1-z_h)^2 = 1$, we obtain $r_h^2+t^2-2t = 0$. When this point on the free surface contacts the solid surface it becomes the new contact line position so, for small times, we have $r_c \sim (2t)^{1/2}$. The speed of the contact line, which is $U_c \sim (2t)^{-1/2}$, is then, for early times, often larger than that which is predicted by a wetting model. In this situation, the free surface contacts the solid and performs a rolling type motion with the contact line propagating as a result of the points on the free surface successively touching the solid and the contact angle remaining at 180°.

Computationally, during the geometric wetting period, the contact line node at the start of an iteration does not have a high enough velocity (as ascribed to it by a wetting model) to 'escape' before the free surface ahead of it impacts with the solid (see Figure 4.6). This behaviour is difficult to capture numerically as it involves curved free surface elements being redefined as straight-sided liquid-solid surface elements. Similar computational difficulties are encountered for contact problems in solid mechanics where elastic bodies are pressed into each other; here, sophisticated approaches have been devised to ensure that the free-surfaces of the materials do not overlap (e.g. Kikuchi & Oden, 1988). As an initial approximation, to allow for this type of motion using the finite element method,

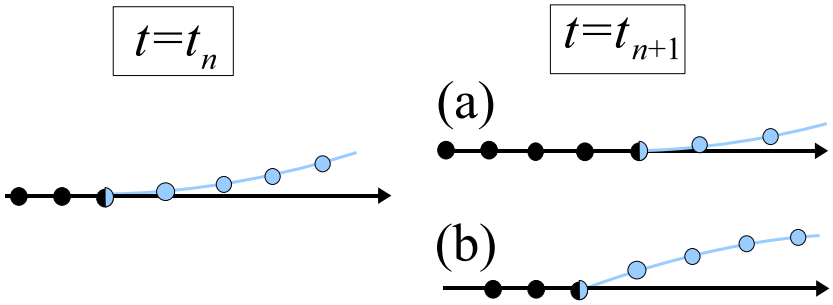

Figure 4.6: Sketch showing how, computationally, the free surface near the contact line evolves from a time t_n (left) to t_{n+1} (right) in (a) geometric wetting, where the free surface nodes (blue) amalgamate with the surface to form solid nodes (black) and (b) the usual contact line driven motion in which the contact angle begins to relax towards its equilibrium value.

we let free surface elements become liquid-solid ones in an element-by-element way. That is, a free surface element is only re-defined as a liquid-solid one once all of its nodes have reached the solid. At this point, the contact line position is redefined. A disadvantage of this approach is that the contact line node moves up what used to be defined as the free surface and hence away from the centre of the mesh, i.e. away from the most resolved region. Consequently, this phase is associated with regular remeshing.

Despite the aforementioned difficulties, our simple method for dealing with the geometric wetting phase provides an accurate description of the early time dynamics.

4.2.8 Pressure behaviour near the contact line

A model using the Navier slip condition predicts an infinite pressure at the contact line (Shikhmurzaev, 2006) and hence we have incorporated special singular elements near the contact line to capture this behaviour: this procedure is described in Suckling (2003), Wilson *et al.* (2006) and Sprittles & Shikhmurzaev (2009*b*). Because the interface formation model predicts a regular pressure (Shikhmurzaev, 2006) such elements are not required.

We have found that when our numerical platform, as well as other standard algorithms, is used to solve dynamic wetting flows, one obtains a spurious multivaluedness and mesh-

dependence in the distribution of the fluid's pressure near to the contact line. This is the case for both the conventional model, using the Navier-slip condition on the liquid-solid interface, and for the interface formation model. To discover the origin of this behaviour we conducted a special investigation and considered a simple problem which is representative of flow local to the contact line, namely that of two-dimensional viscous flow in a corner region with the boundary conditions for the tangential to the sides of the corners components of bulk velocity, formulated in terms of stresses. This investigation is described in the Appendix.

To summarize the results presented in the Appendix, the origin of the difficulty is that, near a corner formed by smooth parts of the boundary, in addition to the solution of the formulated inhomogeneous problem, there also exists an eigensolution. For obtuse corner angles this eigensolution (a) becomes dominant and (b) has a singular radial derivative of velocity at the corner. Despite the bulk pressure in the eigensolution being constant, when the derivatives of the velocity are singular, numerical errors in the calculation of the velocity near the corner give rise to pressure spikes, whose magnitude increases as the mesh is refined. A method is developed that uses the knowledge about the eigensolution to remove the artifacts in the pressure distribution. The method is first explained in the simple case of a Stokes flow in a corner region and then generalized for the Navier-Stokes equations applied to describe steady and unsteady free-surface flows encountered in problems of dynamic wetting (see Appendix).

The developed method, which removes the spurious pressure behaviour has been incorporated into our numerical platform. This has allowed, for the first time, testing of the affect which the spuriousness in pressure has on the results of a drop impact and spreading simulation and hence when its inclusion is critical. We have found that, in the parameter range of interest, the pressure artifacts have a negligible effect on the position of the free surface as a function of time. This is not surprising because, when the standard numerical approach is used, although the pressure distribution is multivalued as the contact line is

approached, it remains integrable so that the free surface shape may be obtained. The velocity distribution is not affected by whether the pressure artifacts are removed or not and hence neither are the interface formation equations.

4.3 Summary

In this chapter, we have proposed a procedure for solving the equations of §3 using the finite element method for the spatial discretization with the spine method to represent the free surface. Evolving the free surface nodes in a novel manner enables us to bypass difficulties associated with regularly remeshing the entire domain. Temporally our scheme is second-order accurate and, by bounding the error, the code automatically chooses the appropriate time step for the physics of the problem. The resulting system of non-linear equations is solved using the Newton-Raphson method. Notably, our code is developed to be able to simulate a geometric wetting phase at the start of a simulation. Spurious pressure behaviour has been identified and determined to have a negligible influence on the drop's bulk dynamics.

Chapter 5

Validation of the numerical platform

To be confident in the new results which our numerical platform will produce, we first check that it is able to reproduce existing published results. Initially, we consider the oscillations of liquid drops, using the classical surface equations, and find excellent agreement with previous numerical studies. Then we consider the implementation of the unsteady interface formation equations, which have never previously been incorporated into a numerical code. Therefore, to ensure our numerical code is accurate, we first use it in a parameter regime where asymptotic analysis provides explicit formulae for the interface formation variables and, most notably, a speed-angle relationship. We are then able to confirm that a straightforward implementation of the interface formation equations into our code is inadequate for the description of dynamic wetting flows. After several critical alterations to the standard approach, we show that our code approximates well both steady and unsteady flows.

5.1 Oscillating liquid drops

In Sprittles (2007), our numerical platform was used to simulate small amplitude capillary-gravity waves. The analysis of our results confirmed that the code was able to accurately

simulate unsteady free surface flows in the case where the deformation of the free surface is small. Drops that impact and spread on solid surfaces may undergo severe deformation, and in this section we show that our platform can handle such motion without any alteration. The classical equations of fluid mechanics (3.1)–(3.3),(3.5),(3.6) are used in the simulations of this section.

We consider a 'benchmark' problem for free surface flows: that of freely oscillating liquid drops in zero gravity. This is an interesting problem in its own right with many applications, e.g. to name one, in the calibration of remote sensing rainfall devices (Beard *et al.*, 1989). Also, in the future, we will consider the dynamics of an oscillating drop which falls through a viscous gas before impacting and then spreading on a solid surface.

When the amplitude of the oscillations are small, analytic results exist (Rayleigh, 1879). However, for drops of arbitrary viscosity and deformation computational methods are the only option. Our parameters are chosen so that we can compare our results to the numerical studies of Basaran (1992) and Meradji *et al.* (2001).

Consider the axisymmetric oscillation of a viscous liquid droplet in zero gravity. The initial shape is most naturally represented in spherical polar coordinates (R, α, φ), with the origin located at the centre of the drop, see Figure 5.1, so that the drop surface $\mathbf{x}_G$ is

$$\mathbf{x}_G = f(\alpha, t)\mathbf{e}_R, \tag{5.1}$$

where $\mathbf{e}_R$ is a unit vector in the radial direction. In the benchmark test case, the drop is released from a shape whose deviation from a sphere is proportional to the nth spherical harmonic, so that

$$f(\alpha, 0) = \gamma_n[1 + f_n P_n(\cos\alpha)], \tag{5.2}$$

where f_n is the amplitude of the initial deviation and γ_n is a normalising factor which ensures that the droplet has the correct non-dimensional volume, in our case $4\pi/3$. The

Re=10	Basaran	Meradji	Present Work
T_1	2.660	2.640	2.656
$(a/b)_{T_1}$	1.434	1.432	1.432
Re=100			
T_1	2.905	2.930	2.936
$(a/b)_{T_1}$	2.331	2.304	2.305

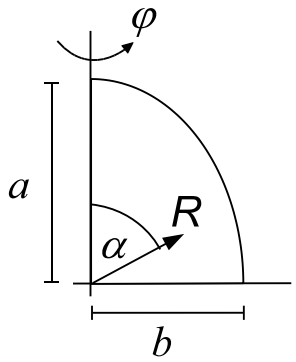

Figure 5.1: Table comparing current results to previous published data and a sketch showing the setup for the oscillating drops.

$n = 0$ mode observes changes in volume whilst the $n = 1$ mode moves the centre of mass of the drop, so the chosen mode for comparison is $n = 2$. A measure of the deformation of the drop is its aspect ratio a/b, where $a = f(0, t)$ is the length of the semi-major axis and $b = f(\pi/2, t)$ is the length of the semi-minor axis, see Figure 5.1.

5.1.1 Results

Due to symmetry, we may consider the domain $\alpha \in (0, \pi/2)$ in axisymmetric coordinates with symmetry conditions applied along the boundaries $\alpha = 0$ and $\alpha = \pi/2$.

We record the time T_1, and aspect ratio of the drop after one period $(a/b)_{T_1}$, for $f_2 = 0.9$, $Re = 10, 100$ and $We = 1$ in order to validate our code against the previous studies. For the results which are presented, a mesh of 630 elements was used with a fixed time step of $\delta t = 0.001$. Doubling the number of elements or reducing the time step by a factor of ten resulted in a change of less than 0.1%. Significantly, the results in Basaran (1992) were for 128 elements whilst Meradji *et al.* (2001) use an order of magnitude more elements.

Our results in the table are seen to be in good agreement with both studies. The values align most closely with those of Meradji *et al.* (2001), which is reassuring given the greater mesh resolution associated with this study. The decay of the aspect ratio is

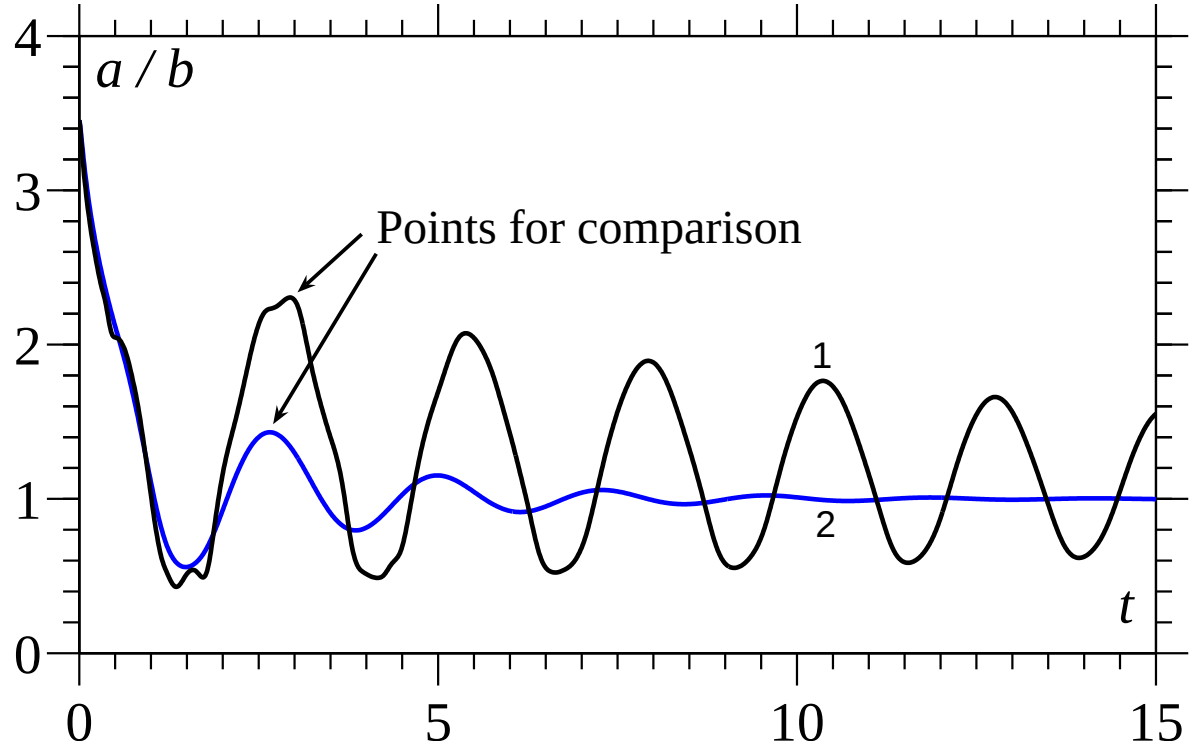

Figure 5.2: Aspect ratio a/b of two drops, released from $f_2 = 0.9$, over a number of periods. Curve 1 is obtained using Re=100, We=1 whilst Curve 2 is for Re=10, We=1.

plotted in Figure 5.2. It should be pointed out that the kinks in Curve 1 of Figure 5.2 are not numerical artifacts; they are associated with the high deformation regime and can be seen in the previous studies.

In Figure 5.3 we show snapshots from the first period of the drop's evolution for the $Re = 100$ case. The effect of viscous damping on the high deformation simulation can be seen by comparing the drop shape at $t = 0$ and $t = 2.93$.

Having shown that our numerical platform provides excellent results when used to simulate high deformation free surface flows with the classical fluid mechanical equations, we now ensure that the interface formation equations are also correctly implemented.

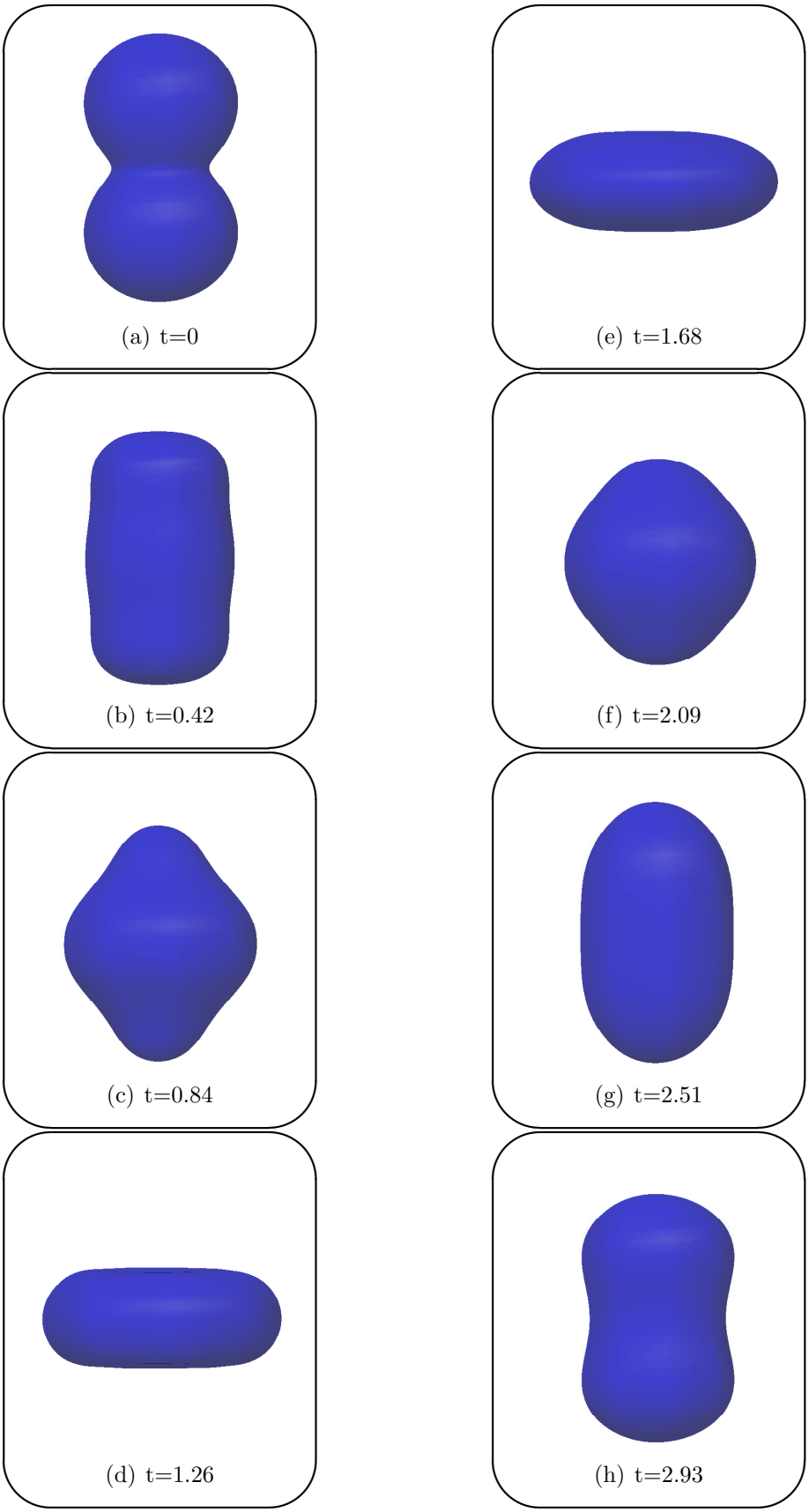

Figure 5.3: Evolution of a liquid drop, released from $f_2 = 0.9$, over one period with Re=100 and We=1.

5.2 Interface formation equations: comparison of numerical and asymptotic results

When the interface formation equations are used to model dynamic wetting flows, asymptotic results can be obtained at small capillary and Reynolds numbers, in the absence of the hydrodynamic assist of dynamic wetting. In this parameter regime, explicit formulae may be obtained for the surface variables and an asymptotic speed-angle relationship can be derived.

We consider three problems of increasing complexity. First, we compare the explicit formulae obtained from the asymptotics to numerical results obtained for the case in which the liquid-gas interface is fixed as planar and we have flow in a wedge. Second, we perform the same comparison but with the liquid-gas interface genuinely free. Third, we consider the position of the contact line and contact angle as a function of time for the unsteady spreading of a liquid drop, which involves using the speed-angle relationship with a spherical cap approximation for the free-surface shape. Because this is the first attempt to implement the time-dependent interface formation equations into a numerical code, this methodical approach has proved necessary to elucidate, and fix, a number of unforeseeable computational problems.

A full derivation of the results we use may be found in Shikhmurzaev (2007), here we shall just outline the main assumptions and the general analytic procedure.

5.2.1 Derivation of asymptotic results

Consider the steady propagation of a liquid-gas free surface over a solid substrate. The length scale of the interface formation process, characterized by the surface tension relaxation length $l = U\tau$ is assumed to be much smaller than the bulk length scale L; this means that the non-dimensional parameter $\epsilon \ll 1$. To further simplify the problem it is

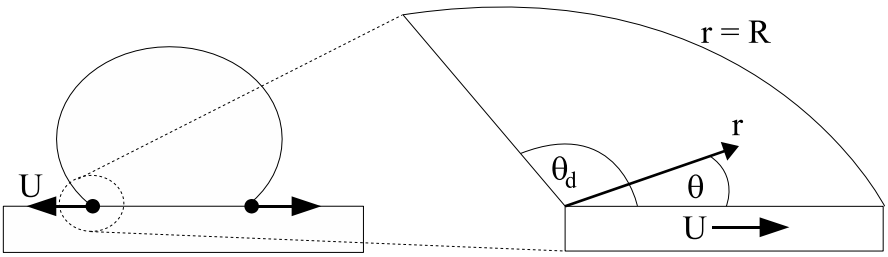

Figure 5.4: Sketch showing how we obtain a local problem in a wedge, from the full dynamic wetting problem, in the limit $Ca \ll 1$.

reasonable to consider small capillary numbers. Then, to leading order in Ca the normal stress boundary condition (3.11) gives that the free surface is planar, so that the problem may be considered locally in a wedge shaped domain, in a frame moving with the contact line, as shown in Figure 5.4. In the double limit of $Ca, \epsilon \to 0$, asymptotic progress is possible and, assuming that the deviation of the surface density ρ^s from equilibrium is small, we can obtain simple explicit formulae for the surface distributions. These can then be used for comparison to our numerical results.

The problem splits into two main asymptotic regions, an inner region where the interface formation dynamics 'kick in' and an outer region where the interface is in equilibrium. We may consider flow in the wedge's outer region to be determined by a moving impermeable no-slip boundary and a flat impermeable zero tangential stress 'free' surface. The solution to this problem is known and given in Moffatt (1964). The streamfunction in polar coordinates (r, θ) centred at the corner of a wedge of angle θ_d is given by

$$\psi = \frac{r}{\sin\theta_d \cos\theta_d - \theta_d} \left[(\theta - \theta_d) \sin\theta - \theta \sin(\theta - \theta_d) \cos\theta_d \right]. \tag{5.3}$$

In the inner region, at leading order, the surface density takes its equilibrium value on the liquid-gas interface so that the surface mass flux all the way along the interface, and hence into the contact line, is given by $u(\theta_d)\rho^s_{Ge}$. Here, $u(\theta_d)$ is the radial velocity of the bulk flow in the far field on the liquid-gas interface. Using (5.3), with $ru = \dfrac{\partial \psi}{\partial \theta}$, for

an angle $\theta = \theta_d$ we obtain

$$u(\theta_d) = \frac{\sin\theta_d - \theta_d \cos\theta_d}{\sin\theta_d \cos\theta_d - \theta_d}. \tag{5.4}$$

Then, knowing the surface mass flux into the contact line, one may determine how the surface variables relax to their equilibrium values along the liquid-solid interface and hence determine the dynamic contact angle. One finds that

$$\rho^s_S = \rho^s_{Se} - C\exp(-ks), \qquad v^s_{St} = 1 - \frac{Ck}{4V^2}\exp(-ks), \tag{5.5}$$

where $s = r/\epsilon$ is the scaled distance from the contact line,

$$k = 2V(\rho^s_{Se})^{-1}\left[\left(V^2 + \rho^s_{Se}\right)^{1/2} - V\right], \qquad C = \frac{2V\left(\rho^s_{Se} + \rho^s_{Ge}u(\theta_d)\right)}{\left(V^2 + \rho^s_{2e}\right)^{1/2} + V}, \tag{5.6}$$

and $V = U[\bar{\beta}\epsilon/((1 + 4\bar{\alpha}\bar{\beta})\lambda)]^{1/2}$. Finally, the dynamic contact angle is given by the expression

$$\cos\theta_e - \cos\theta_d = \frac{2V\left[\cos\theta_e + \left(1 - \rho^s_{Ge}\right)^{-1}\left(1 + \rho^s_{Ge}u(\theta_d)\right)\right]}{V + \left[V^2 + 1 + \cos\theta_e\left(1 - \rho^s_{Ge}\right)\right]^{1/2}}. \tag{5.7}$$

Alternatively, given the dynamic contact angle, this expression may be inverted for the non-dimensional speed of the contact line V. The presence of $u(\theta_d)$ in (5.7) shows there is a connection between the flow in the outer asymptotic region and the value of the dynamic contact angle. In the case considered here, the flow in the outer region is fully determined by the contact line speed and the contact angle; i.e. it may be calculated by using Moffat's solution for Stokes flow in a wedge shaped domain. This is the case considered in Shikhmurzaev (1997*b*) where the theory shows excellent agreement with experiments of relatively large drops spreading from rest. However, with the microdrop impact and spreading phenomena we are ultimately interested in, the asymptotic approach is not available as (*i*) at high impact speed inertial effects are significant and (*ii*) in the early stages of spreading there is the presence of a nearby boundary (the axis-of-symmetry): the dynamics of the flow in the vicinity of the contact line will then have

to be computed and the speed-angle relationship will be problem-specific (Lukyanov & Shikhmurzaev, 2007).

5.2.2 Comparison between numerical and asymptotic results

The asymptotic results presented in the previous section are now used to validate our numerical code in a certain range of parameter values. All results were obtained for $\theta_e = 60°, \rho^s_{Ge} = 0.95, Re = 0$ and the other parameters which were varied are listed where appropriate.

Flow in a wedge

In these simulations the far field $r = R$ must be a sufficient distance from the contact line to ensure that its presence doesn't affect the inner region's dynamics; we have set it to be at a distance $R = 10^5\epsilon$, that is $s = 10^5$.

Surprisingly, while testing the code implemented in terms of the surface variable ρ^s and $\mathbf{v}^s$, over a wide range of parameter values, we found that convergence was often unobtainable for small capillary numbers, for approximately $Ca \leq 0.001$. It turns out that a computationally favourable approach is to introduce the surface flux vector $\mathbf{J}^s = \rho^s\mathbf{v}^s$ and use this to eliminate $\mathbf{v}^s$ from equations (3.10)–(3.29). This has the effect of making the surface mass continuity equations linear (3.13), (3.18) at the expense of the Darcy type equations (3.14), (3.20). As a result of this alteration, the code is able to accurately approximate flows at small capillary numbers. Quite why this is the case is yet to be ascertained, but it appears to be preferable to have a linear surface-mass-flux contribution to the surface-mass continuity condition (3.25) at the contact line.

With our new setup, we choose the same parameter values as those used in Lukyanov & Shikhmurzaev (2007) in order to compare the performance of our code to the only previous numerical code, which used the streamfunction-vorticity formulation, to solve

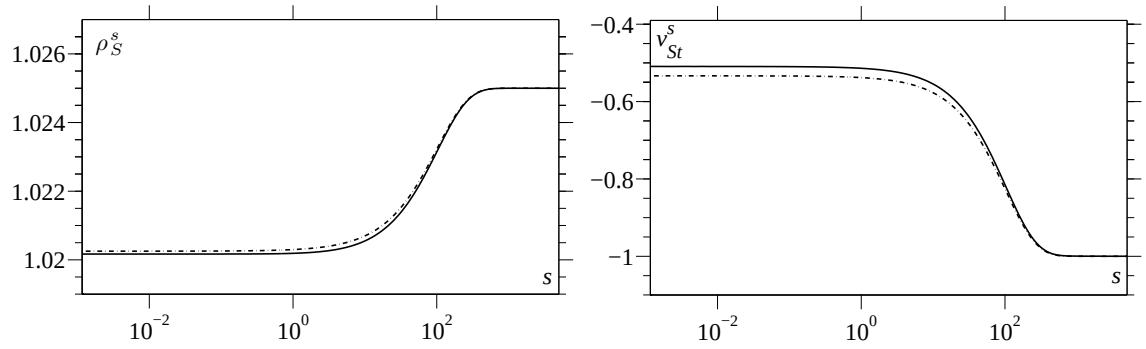

Figure 5.5: Comparison of computed interface formation variables with the asymptotic prediction (dashed line) a distance s along the liquid-solid interface from the contact line. Parameter values $Ca = 10^{-3}, \epsilon = 10^{-4}, \bar{\beta} = 25, Q = 0.4$. The dynamic contact angle was computed to be 66.25° with an asymptotic value of 66.1°.

these equations.

In Figure 5.5, we show the computed surface distributions and the asymptotic predictions along the liquid-solid interface for $Ca = 10^{-3}, \epsilon = 10^{-4}, \bar{\beta} = 25, Q = 0.4$. The agreement is seen to be excellent and the computed dynamic contact angle $\theta_d = 66.25°$ is only 0.15° away from the predicted asymptotic value.

In Figure 5.6, we see a similarly good agreement, with the difference between the asymptotic angle of 102.22° and numerically calculated angle of 102.15° only 0.07° for the parameter values $Ca = 10^{-2}, \epsilon = 10^{-3}, \bar{\beta} = 250, Q = 0.04$, which are associated with a factor of ten increase in the characteristic speed.

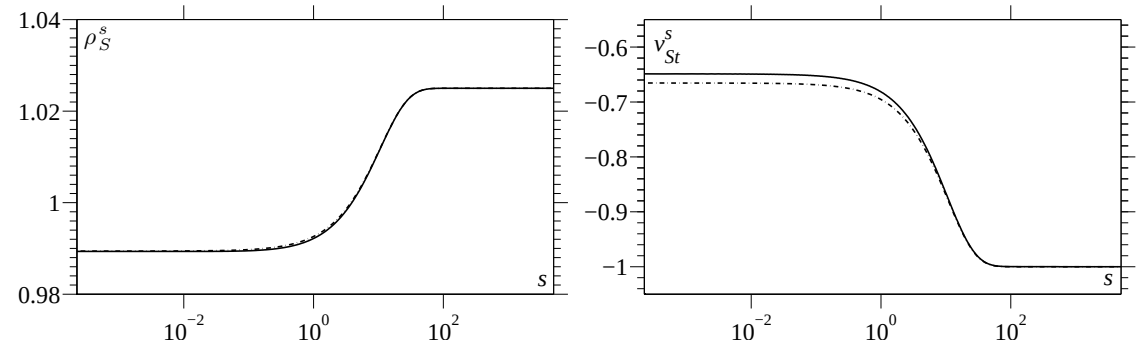

Figure 5.6: Comparison of computed interface formation variables with the asymptotic prediction (dashed line) a distance s along the liquid-solid interface from the contact line. Parameter values $Ca = 10^{-2}, \epsilon = 10^{-3}, \bar{\beta} = 250, Q = 0.04$. The dynamic contact angle was computed to be 102.15° with an asymptotic value of 102.22°.

The agreement between asymptotics and computation for both sets of parameters is better than seen in Lukyanov & Shikhmurzaev (2007, p. 17,18); this is probably due to the higher degree of approximation and the greater resolution which we have used. In these simulations we used 2495 elements with the smallest element having size 10^{-7}. It was found that it is important not to increase the element size too fast as one moves away from the contact line. We used a 4% increase in size: any larger increase was seen to noticeably lower the accuracy of the approximation.

Steady drop evolution

To ensure that the free surface terms are working correctly, we consider an inwardly moving substrate and check that the drop attains the correct dynamic contact angle (see Figure 5.7). This situation is somewhat artificial as the substrate moves radially inwards from all directions, raising the question of, physically, where the substrate is actually going. However, we are interested in the region near the contact line which, in general, will not be affected by any unphysical problems which may occur on the liquid-solid interface near the axis of symmetry.

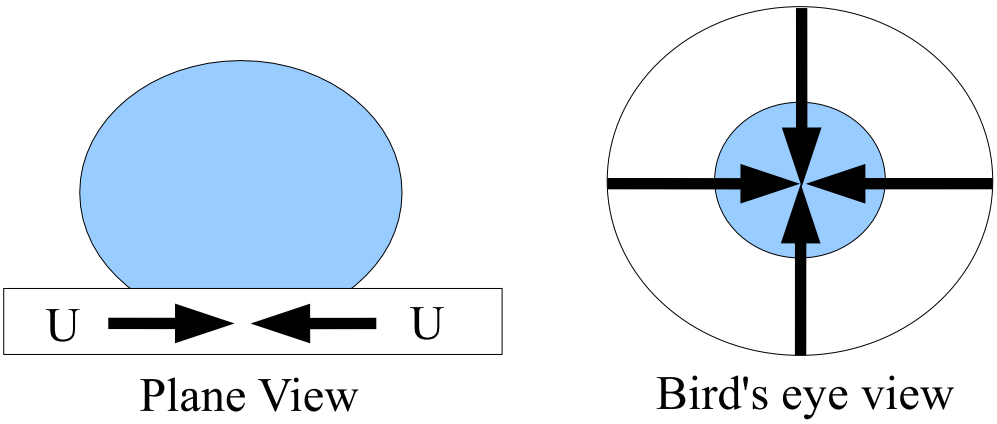

Figure 5.7: Setup to test the implementation of the interface formation equations in a steady free surface flow by moving the substrate radially inwards.

The results of this testing were surprising: we obtained very poor agreement with the

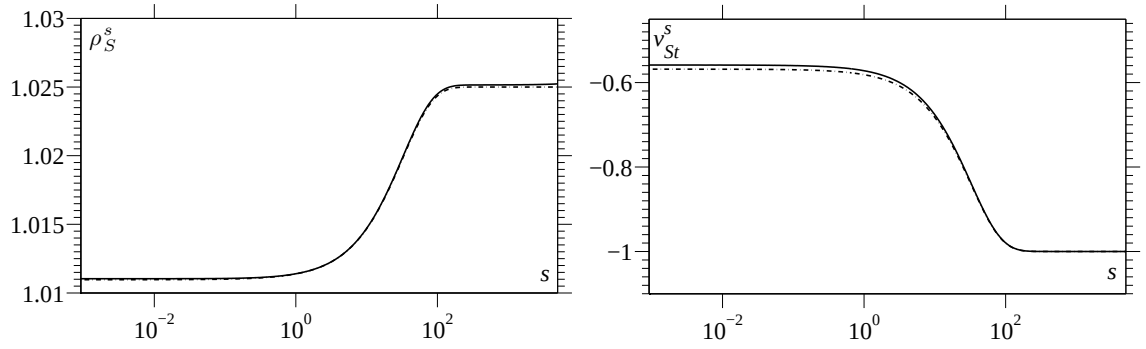

Figure 5.8: Computed interface formation variables, for the steady drop evolution problem, compared to the asymptotic prediction (dashed line) a distance s along the surface from the contact line. Parameter values $Ca = 10^{-3}, \epsilon = 10^{-4}, \bar{\beta} = 250, Q = 0.04$. The dynamic contact angle was computed to be 77.29° with an asymptotic value of 77.33°.

asymptotics and the code often failed even to produce a converged solution. The cause of this problem was found to be in the mesh design. Initially, the mesh was designed by increasing the distance between spines by a certain amount, roughly 4%, as one moves away from the contact line. Consequently, the mid-point of a quadratic free surface element was not quite in the centre of that element. This had absolutely no effect when using the conventional model, or when the free surface was planar (as in the previous examples), but it drastically affected the accuracy of the interface formation equations' approximation when a surface is curved. Once discovered, this was easily rectified by relocating the spines associated with these nodes, i.e. every other spine, so that mid-point nodes on the free surface are always located in the centre of the free surface element.

In Figure 5.8, we see that when the aforementioned procedure is used, we obtain excellent agreement with the asymptotics: without this procedure, with the spines less than 4% off centre, no convergence was possible. The difference between the computed angle of 77.29° and the asymptotic contact angle was only 0.04° for the parameter values used of $Ca = 10^{-2}, \epsilon = 10^{-3}, \bar{\beta} = 250, Q = 0.04$.

Spreading of drops

As a final test, we consider the spreading of axisymmetric drops in the same parameter regime. As shown in Shikhmurzaev (1997*b*), analytically this involves coupling the contact angle formula (5.7) with a spherical cap approximation for the drop's free surface shape. The iterative procedure to determine the free surface evolution is, having been given the initial free surface shape and hence the contact angle, to:

(*i*) find the contact-line speed V, given the contact angle, using (5.7);

(*ii*) step forward in time using $\dfrac{\mathrm{d}r_c}{\mathrm{d}t} = V$ to determine the new contact line position r_c;

(*ii*) find the new contact angle using a spherical cap approximation with volume conservation, that is, given r_c, solve

$$r_c^3 = \frac{4(\sin\theta_d)^3}{2 + (\cos\theta_d)^3 - 3\cos\theta_d}$$

for θ_d;

(*iv*) repeat.

In Shikhmurzaev (1997*b*), it is noted that there will be a short period after $t = 0$ before the flow reaches the quasi-static regime in which the temporal derivatives in the Navier-Stokes and interface formation equations may be neglected. Such a 'boundary layer' is indeed observed in the first few time steps of the computed results but does not significantly affect the agreement between the asymptotics and the numerics.

Simulations start with the contact angle at $\theta_0 = 120^\circ$ and continue until the drop evolves to its equilibrium angle of $\theta_e = 60^\circ$, with parameter values taken to be $Ca = 10^{-3}, \epsilon = 10^{-4}, \bar{\beta} = 250, Q = 0.04$. We set $Re = 0$ and consequently there are no oscillations around the equilibrium state. The time step is fixed at $\triangle t = 0.01$ for all simulations.

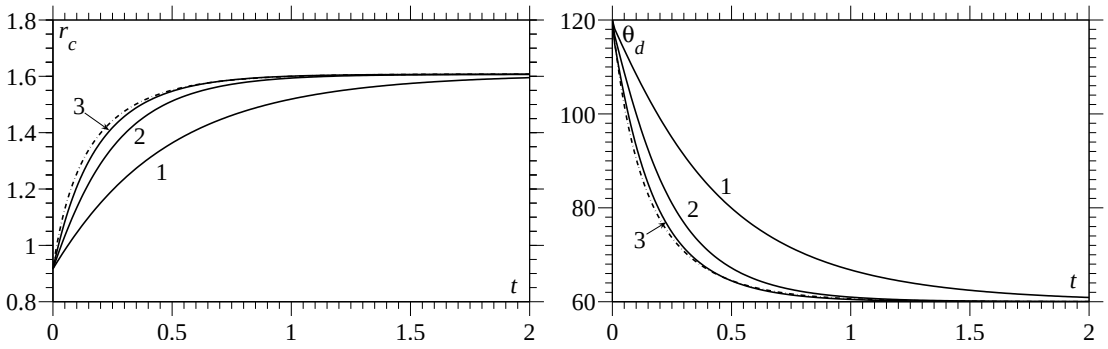

Figure 5.9: Contact line position r_c and dynamic contact angle θ_d at time t of a drop spreading towards equilibrium. The computed solution on three meshes of increasing resolution (1-3) is compared to the asymptotic prediction (dashed line). Parameter values $Ca = 10^{-3}, \epsilon = 10^{-4}, \bar{\beta} = 250, Q = 0.04$.

By using three meshes of increasing resolution we demonstrate the convergence of the full code towards the asymptotic prediction as the mesh is refined. The number of spines (total elements) in the meshes $1-3$ are $251(1985), 301(2385)$ and $351(2785)$, which correspond to a smallest element size of $8 \times 10^{-6}, 1 \times 10^{-6}$ and 2×10^{-7}, respectively.

From our results, shown in Figure 5.9, it can be seen that 351 spines are sufficient to accurately resolve the interface formation dynamics and provide good agreement with the asymptotics. The parameter values encountered here are computationally the worst case scenario because, when we consider impacting microdrops, both Ca and ϵ will be much larger and hence not as much resolution/computational power will be required to resolve the smallest scales which are of $O(\epsilon Ca)$. The complexity for impacting drops will come from the huge deformation which the free surface will undergo.

5.3 Summary

We were able to reproduce published numerical results on oscillating liquid drops and hence ensure that our approximation of the bulk equations combined with the classical surface equations is accurate. When we considered our implementation of the interface formation equations, the slow, methodical testing of all terms proved invaluable. Numer-

ical tests, guided by analytic results, have taught us that in order to accurately approximate the equations of interface formation, in addition to the standard implementation we should:

(*i*) use the flux variable $\mathbf{J}^s$ instead of the surface velocity $\mathbf{v}^s$;

(*ii*) ensure that the mid-point node in elements on the free surface is located at the centre of that element;

(*iii*) increase the element size slowly, with jumps in size of no more than 4%, as we move away from the contact line.

Without these alterations to our initial (standard) approach, our code failed to converge in many cases. The reason for the larger-than-expected effect of these points is still somewhat unclear and deserves further attention.

Chapter 6

Drop impact and spreading on solid surfaces of constant wettability

In this chapter, we present the results of our investigation into microdrop impact and spreading on surfaces of constant wettability. First, we consider two simulations which allow us to identify some general features of the flows we shall encounter. These simulations will be used as reference points. The results from this show that the interface formation model is able to predict the experimentally observed non-uniqueness of the speed-angle relationship, and we proceed to investigate this phenomenon in further depth. It is then shown that our results are in qualitative agreement with experimental findings and that our model is able to recover information which is hidden in the experiments. Then, by varying the model's parameters around a base state, we identify their influence on the drop's evolution.

To acquire a base state, we consider a drop of water of radius $a = 25$ μm with viscosity $\mu = 1$ mPa s and density $\rho = 10^3$ kg m^{-3}. The liquid-gas interface is assumed to have equilibrium surface tension $\sigma = 70$ mN m^{-1}. The estimates for the interface formation model's parameters come from Blake & Shikhmurzaev (2002), where it is assumed that $\beta = 1/\alpha = \mu/h$, $\rho^s_{(0)} = \rho h$ and $\tau = \hat{\tau}\mu h^2$, where h is a microscopic length scale associated

with the thickness of the interfacial layer (a reasonable estimate is 2 nm (Rowlinson & Widom, 1982)) and $\hat{\tau}$ is a coefficient of proportionality. It is found by comparing theoretical predictions to the experimental data that $\rho^s_{Ge} \simeq 0.6$, $\hat{\tau} \simeq 1.9\times10^{12}$ s^2 kg^{-1} m^{-1} and $\sigma_{SG} \simeq 0$. Initially, we shall use these values in all of our simulations before, later in the chapter, considering their individual influence on the drop's dynamics. The reason we specify a base state in terms of dimensional parameters corresponding to a particular physical system, as opposed to just setting some values for the non-dimensional groups, is that in reality the system's parameters cannot be varied independently: a change in the fluid leads to variations of several dimensional and hence dimensionless parameters. Therefore, it is instructive to have a base state specified as above and then vary it in a way that would correspond to a possible experiment.

We take the base impact speed to be $U_0 = 5$ m s^{-1} so that $Re = 1.3 \times 10^2$, $We = 8.9$, $St = 1 \times 10^{-3}$, $\epsilon = 1.4 \times 10^{-3}$, $\rho^s_{Ge} = 0.6$, $\bar{\beta} = 8.9 \times 10^3$ and $Q = 6 \times 10^{-2}$. If the drop is released from rest, then we use instead $U = \sigma/\mu$ as a characteristic scale for velocity, which gives $Re = We = 1.8 \times 10^3$, $St = 9 \times 10^{-5}$, $\epsilon = 2 \times 10^{-2}$, $\rho^s_{Ge} = 0.6$, $\bar{\beta} = 12.5 \times 10^4$ and $Q = 4.1 \times 10^{-3}$. We shall see in the next section that when the drop is released from rest, the contact line velocity is small so that the Reynolds and Weber numbers based on this velocity are considerably smaller than their characteristic values.

6.1 Base state simulations

Initially, we consider the features of drops which start spreading from rest, before studying the influence of a non-zero impact speed on the subsequent evolution of the drop. Simulations are run using both the conventional and the interface formation model.

6.1.1 Spreading from rest

The drops' evolutions, obtained using both the conventional model and the interface formation model, are shown in Figure 6.1. There are no observable differences between the two motions, so that a general discussion of the dynamics will apply for either case.

From the snapshots in Figure 6.1, we can see that initially, in $t = 0 - 40$, the contact line is driven radially outwards as the contact angle relaxes towards its equilibrium value: this is a capillary-driven wetting phase. Most of the drop remains motionless until around $t = 60$, when the apex falls and squeezes fluid from near the axis of symmetry towards the contact line region. At $t = 120$ the drop appears to have slightly overshot its equilibrium position, which is achieved at around $t = 200$.

In Figure 6.2 one can see that during the capillary-driven wetting phase the dynamic contact angle varies quickly, reducing by approximately 80° during the period $t = 0 - 5$. From the velocity fields shown in Figure 6.3, we can see that, as a result of the contact line motion, fluid is being pulled from the bulk of the drop towards the contact line region. The disturbance to the free surface, caused by the contact angle's variation, creates a capillary wave, see $t = 10$ in Figure 6.3, which travels up the free surface and finally reaches the apex region at around $t = 40$. Until this time, the apex region has not felt the motion of the contact line and has a spherical cap shape. Counter-intuitively, one can see from Figure 6.3 and Figure 6.4 that the first movement of the apex is up, at around $t = 40$; however, capillarity effects soon force the apex downwards, relatively quickly, in the period $t = 50 - 100$.

At around $t = 80$, one can see from Figure 6.2 that the contact angle is beginning to approach its equilibrium value and, from Figure 6.4, we can see that this corresponds to a slowing of the contact line. However, the motion of the apex leads to a second phase of spreading, from $t = 80 - 110$, which is driven by the inertia of the fluid arriving from near to the axis of symmetry, which pushes the contact line slightly past its equilibrium radius

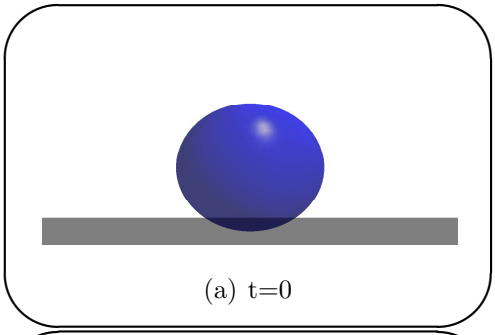

(a) t=0

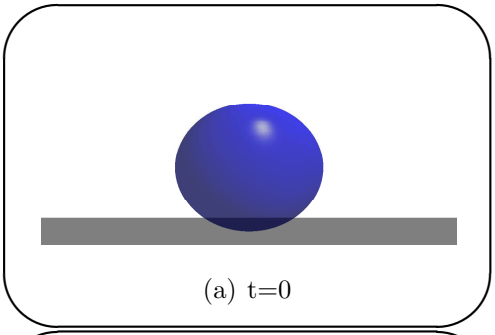

(a) t=0

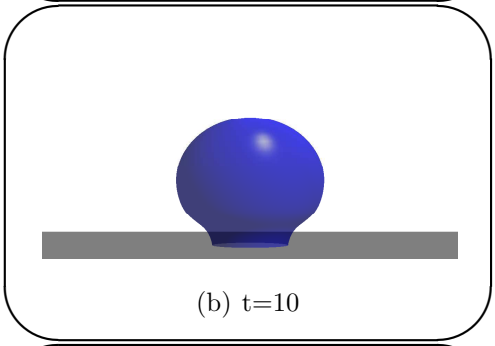

(b) t=10

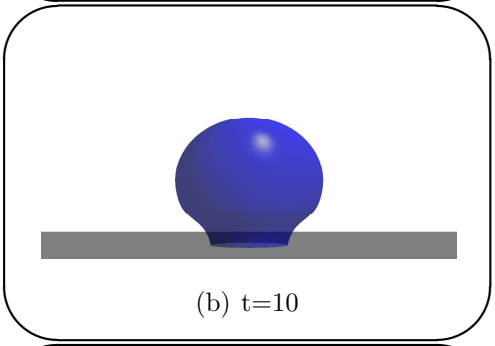

(b) t=10

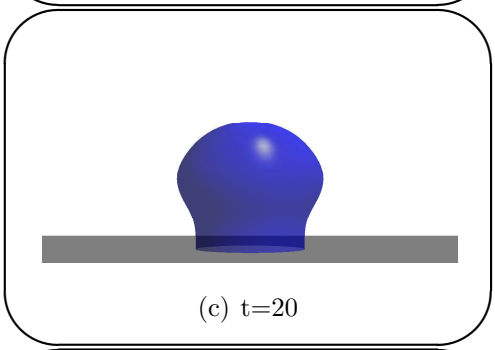

(c) t=20

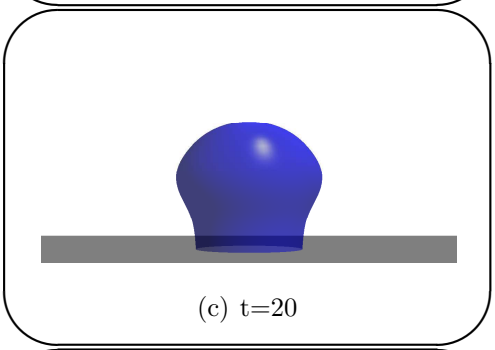

(c) t=20

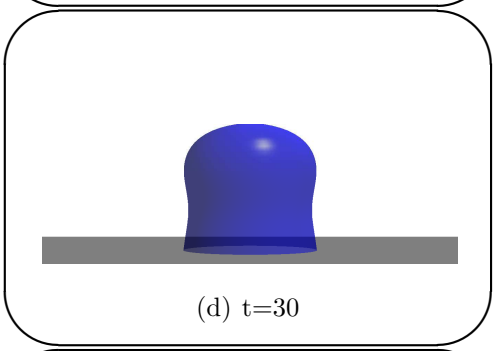

(d) t=30

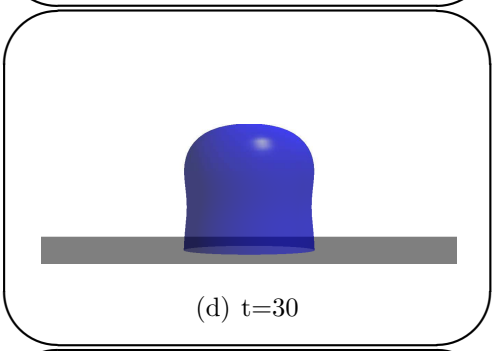

(d) t=30

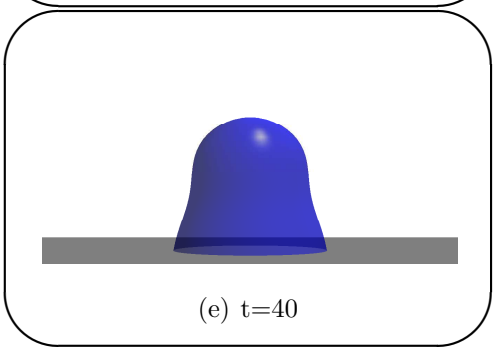

(e) t=40

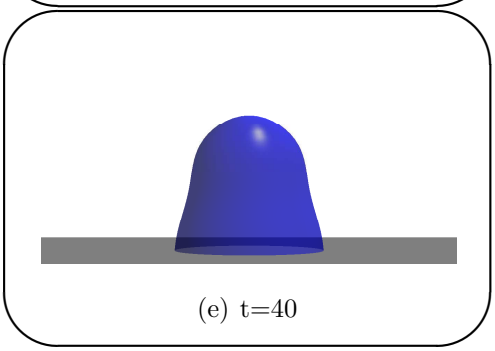

(e) t=40

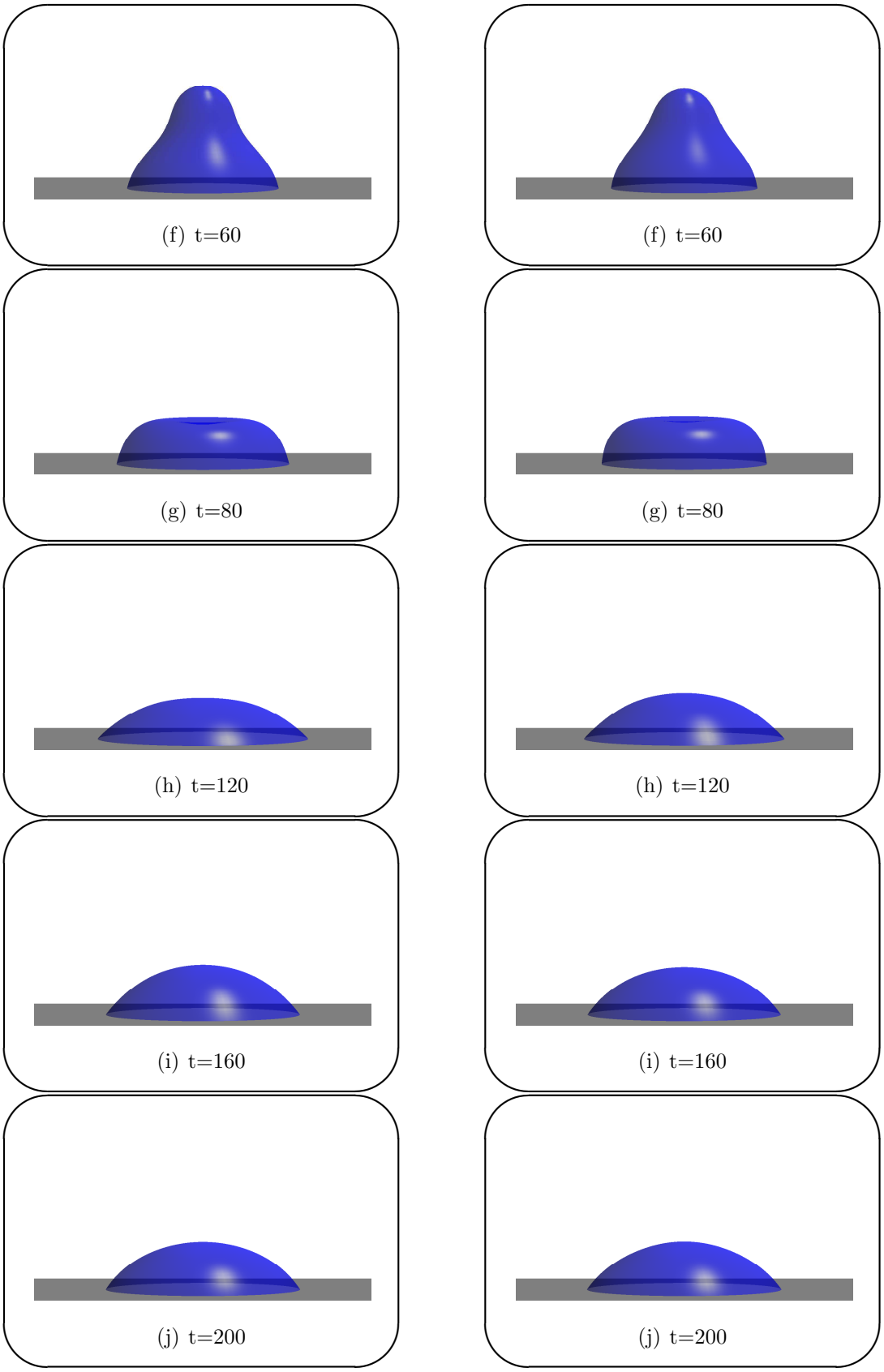

Figure 6.1: Evolution of our base state drop, using the interface formation model (left) and conventional model (right), after it has been released from rest on a surface characterized by $\theta_e = 60°$.

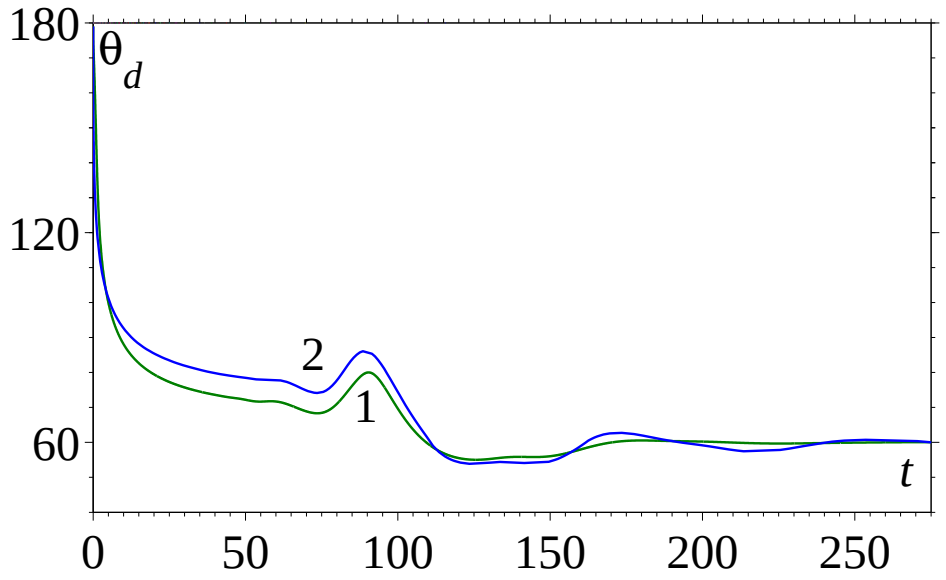

Figure 6.2: The dynamic contact angle θ_d as a function of time t for the case in which our base state drop is released from rest on a surface characterized by $\theta_e = 60°$. Curve 1 is obtained using the interface formation model whilst Curve 2 is obtained using the conventional model.

of $r_c = 1.61$. One can see from Figure 6.5 that this coincides with the free surface area reaching a minimum, at around $t = 70$, when the drop is approximately a spherical cap, before increasing rapidly as inertial forces cause the drop to overshoot its equilibrium position. Then, the free surface area achieves a local maximum and surface tension forces begin to dominate; acting to return the drop to the shape of a spherical cap. The subsequent interplay between the surface tension forces and inertial ones causes the drop to oscillate slightly around its equilibrium position, compare $t = 70$ and $t = 110$ in Figure 6.3, with viscous forces acting to damp this motion. In this case, the oscillations are damped quite quickly and by $t = 250$, the amplitude of the oscillation in the contact line position is only $\triangle r_c = 0.002$.

Quantitatively comparing the results obtained from the two models, we can see from Figure 6.4 that the conventional model (Curve 2) predicts a greater maximum spread of approximately 5%, with the contact line overshooting its equilibrium value of 1.61, whilst the interface formation model (Curve 1) predicts that the contact line will be arrested earlier and, consequently, that more energy is dissipated by larger oscillations of the apex

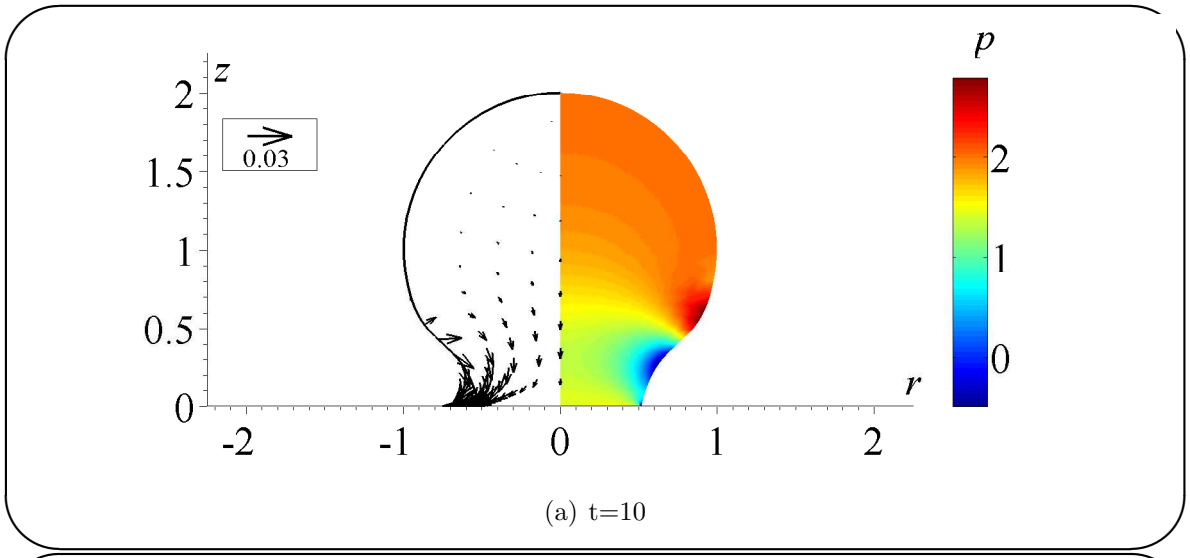

(a) t=10

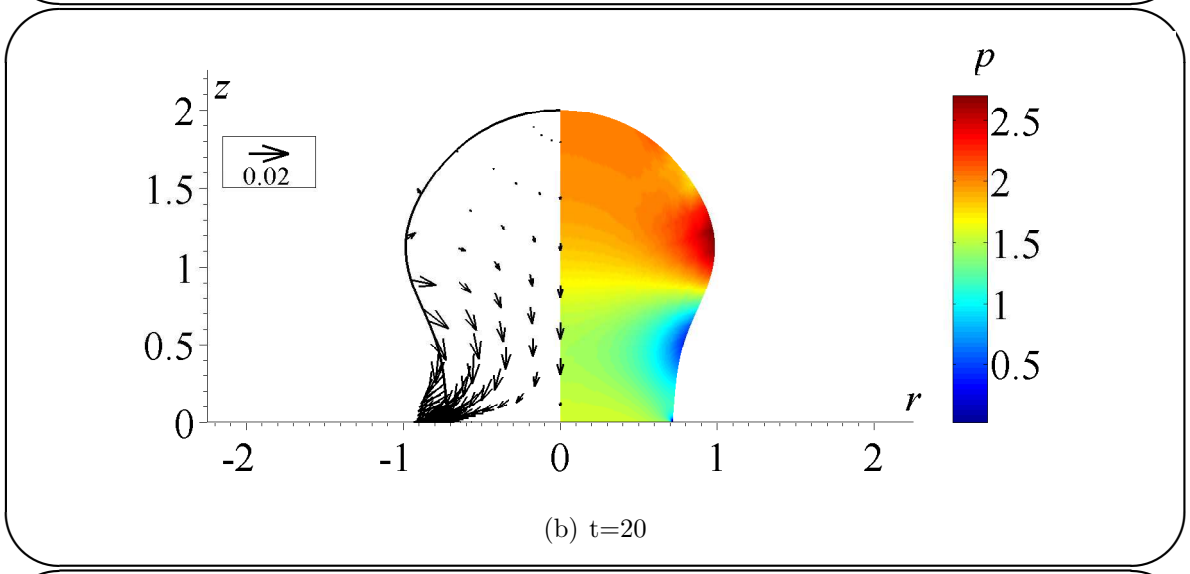

(b) t=20

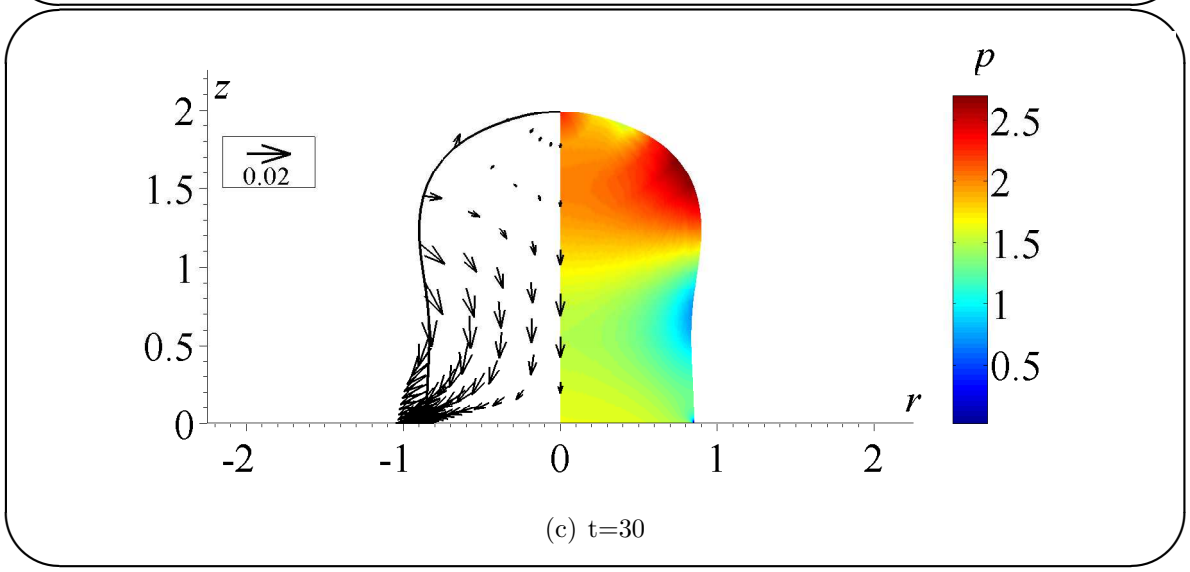

(c) t=30

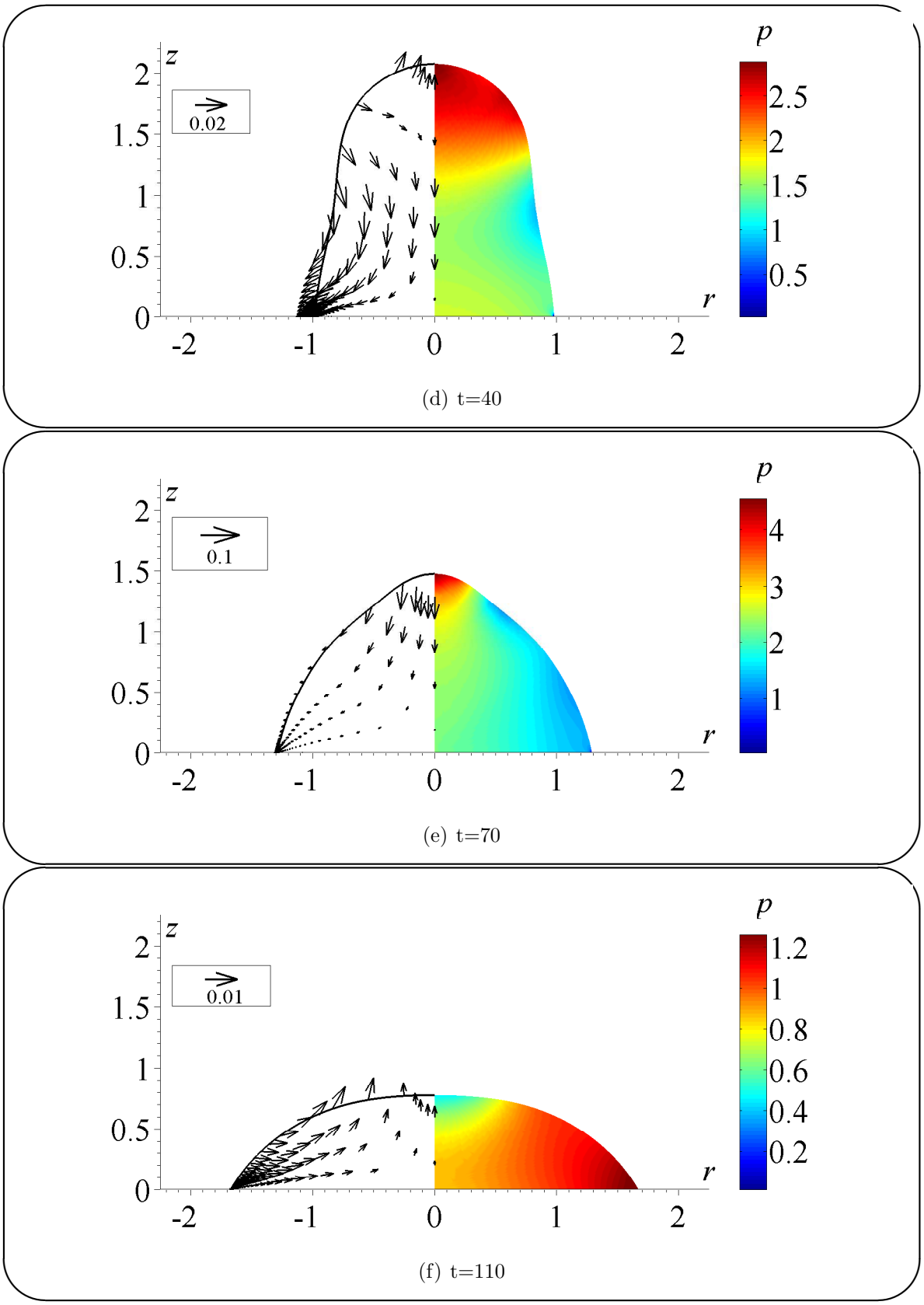

Figure 6.3: Velocity and pressure distributions inside our base state drop after it has been released from rest on a surface characterized by $\theta_e = 60°$.

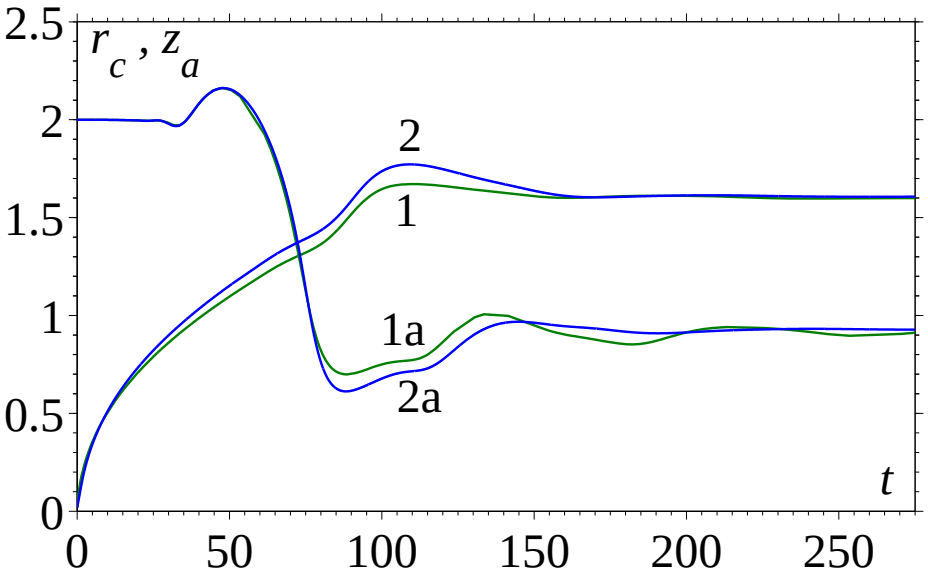

Figure 6.4: Curves 1,2 are the radius of the contact line r_c whilst Curves 1a,2a are the apex height z_a, both as a function of time t for the case in which our base state drop is released from rest on a surface characterized by $\theta_e = 60°$. Curves 1 and 1a are obtained using the interface formation model whilst Curves 2 and 2a are obtained using the conventional model.

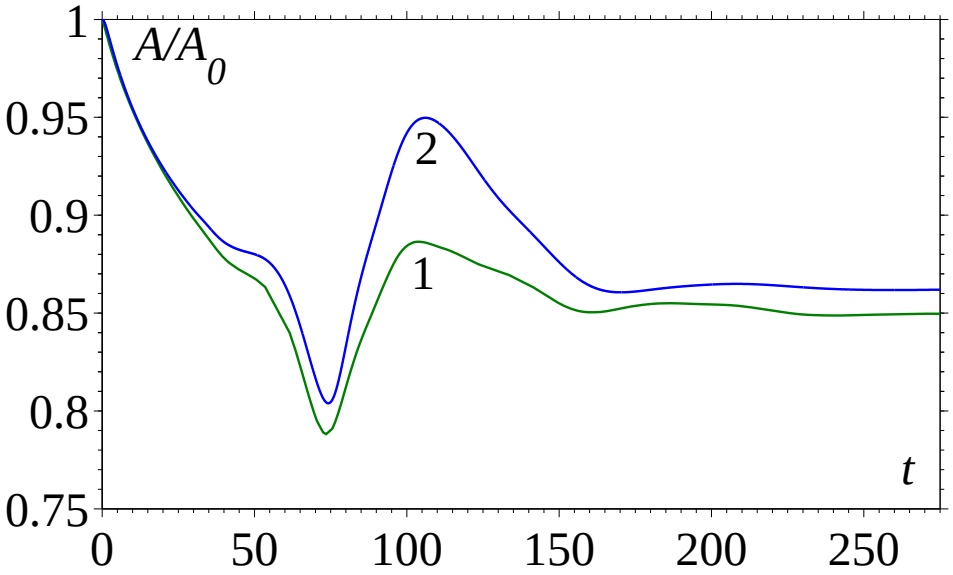

Figure 6.5: The free surface area A normalized by its initial value $A_0 = 4\pi$ as a function of time t for the case in which our base state drop is released from rest on a surface characterized by $\theta_e = 60°$. Curve 1 is obtained using the interface formation model whilst Curve 2 is obtained using the conventional model.

height, see Curve 1a in Figure 6.4.

We have shown that a drop which starts from rest is initially driven by the non-equilibrium position of the contact line. We proceed now to consider how the same drop's motion is altered by a non-zero impact speed.

6.1.2 Impact and spreading

We now consider a drop impact and spreading simulation where the impact speed is taken to be its base value of $U_0 = 5$ m s^{-1}. Once again, it is difficult to observe any qualitative differences between the snapshots in Figure 6.6 obtained by using the two different wetting models, and hence the discussion about the drop's general dynamics is valid for either simulation.

From Figure 6.6, we can see that the initial stages of motion are entirely different from those previously obtained for a drop spreading from rest. The descending bulk of the drop now forces fluid near the solid radially outwards, which creates a rim of fluid near the contact line: this initial phase is inertia-driven spreading. The small rim of fluid around the contact line region is observable at $t = 0.4$ and, in the subsequent images, is seen to grow in time. Above this rim, until about $t = 1.4$, the free surface appears to be completely unaffected by the contact line motion and maintains a spherical cap shape. The apex continues to fall for so long that at $t = 3$ it almost touches the solid surface, before finally recoiling. This change in direction of the apex appears to roughly correspond with the start of a dewetting phase, in which the contact line begins to retreat. Oscillations follow but are relatively soon damped by viscous forces, so that by $t = 10$ the drop is close to its equilibrium position.

From $t = 0.5$ in Figure 6.7, we can see that the small rim of fluid near the contact line creates a capillary wave in the free surface which travels towards the apex region in the subsequent images $t = 1, 2, 3$. The position of this free surface disturbance appears

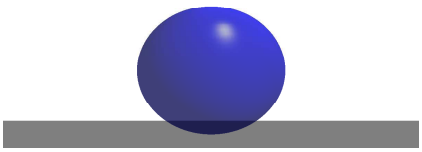

(a) t=0

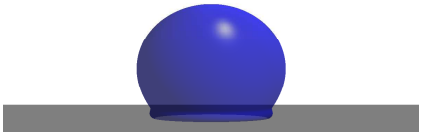

(b) t=0.2

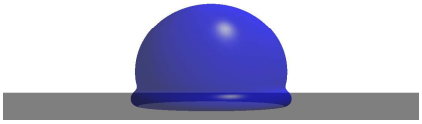

(c) t=0.4

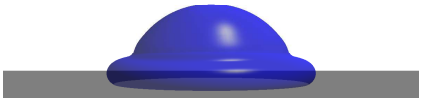

(d) t=0.8

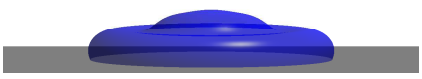

(e) t=1.4

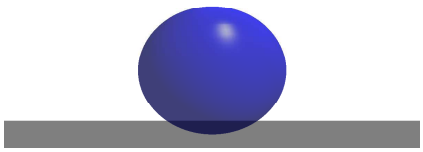

(a) t=0

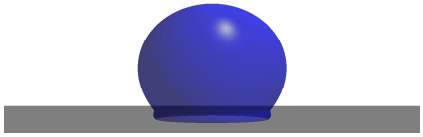

(b) t=0.2

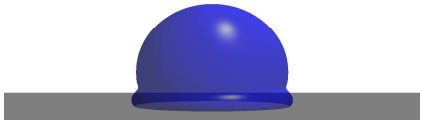

(c) t=0.4

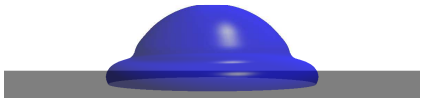

(d) t=0.8

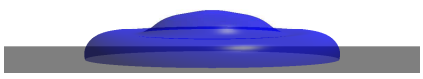

(e) t=1.4

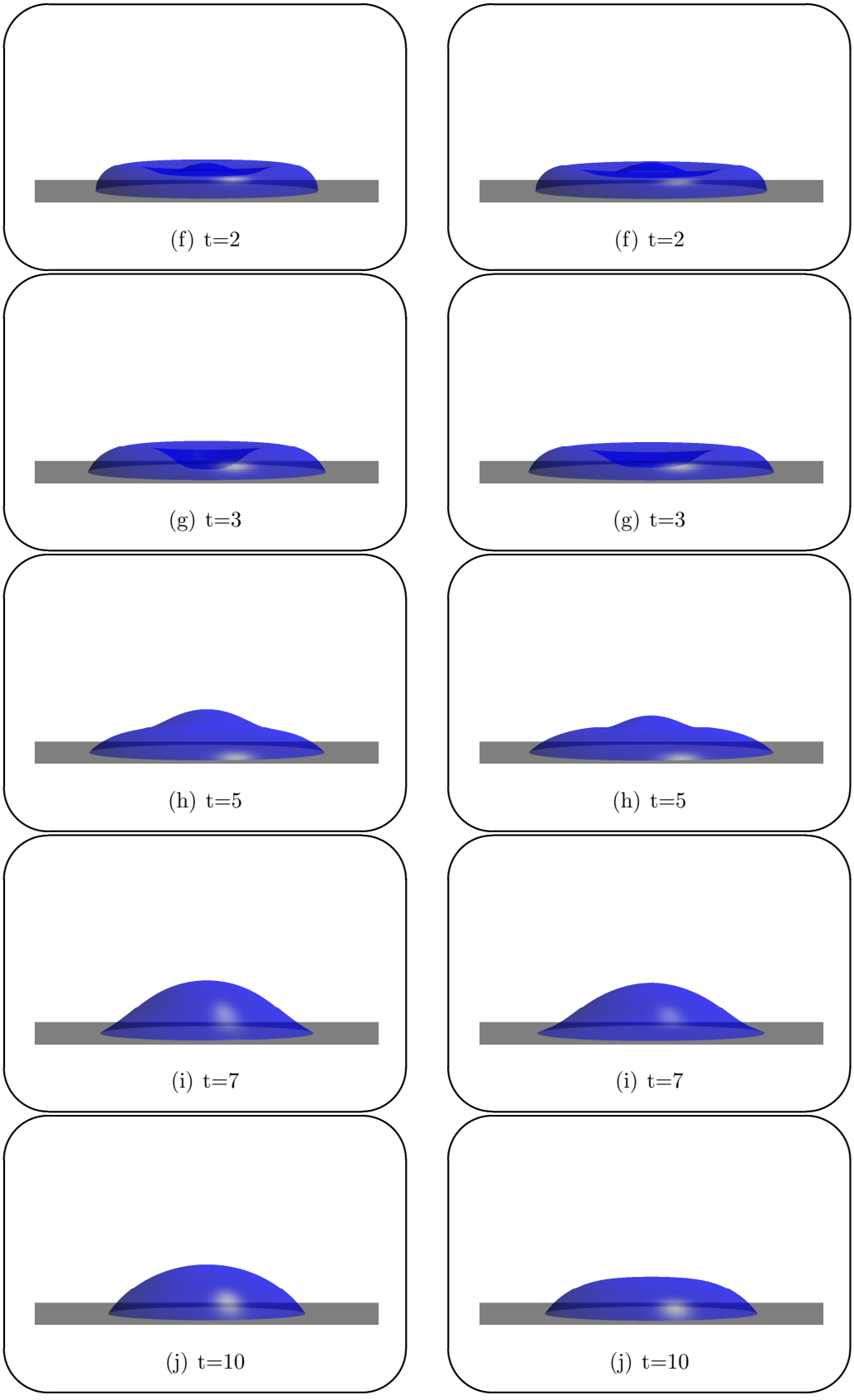

Figure 6.6: Evolution of our base state drop after impact, using the interface formation model (left) and conventional model (right), on a surface characterized by $\theta_e = 60°$.

to roughly determine the radius at which the velocity changes from radial, in the contact line region, to vertically downwards in the rest of the drop.

At $t = 2$ and $t = 3$ in Figure 6.7 one can see that the most violent flow is near the apex, which is being forced towards the solid. From Figure 6.10 we can see that this coincides with the free surface area reaching a maximum, so that surface tension effects begin to dominate and, consequently the contact line begins to recede, see Figure 6.8. The motion of fluid towards the axis of symmetry forces the apex to recoil just before it touches the solid: it reaches a minimum of $z_a = 0.02$. From Figure 6.8, we can see that the drop then proceeds to perform small oscillations around it equilibrium position. This can also be observed by looking at $t = 5$ and $t = 8$ in Figure 6.7.

We now consider the quantitative differences of the two models' predictions and, in Figure 6.8, we can see that for $t = 0 - 2$ there is very little difference between the curves obtained using each model. This is what one should expect during the inertia-driven phase of the drop's motion where the wettability of the substrate is known to play a negligible role (Rioboo *et al.*, 2002). Again, there is approximately a 5% difference in the maximum spread predicted by the two models and it can be seen that there is a similar deviation in the predicted apex height. From Figure 6.9, we can observe that the contact angle as a function of time differs for the two drops, with the contact angle relaxing much faster when the conventional model is used. It appears that this greater acceleration of the contact line drives it further and increases the subsequent oscillations of the contact line radius.

An extended geometric wetting phase

In our simulations on drop impact, as opposed to the drop spreading from rest, we have observed that the geometric stage of wetting extends well past the first few time iterations of our scheme where it was expected to be present, as described in §4. During this stage, the free surface contacts the solid and the contact line propagates as a result of the points

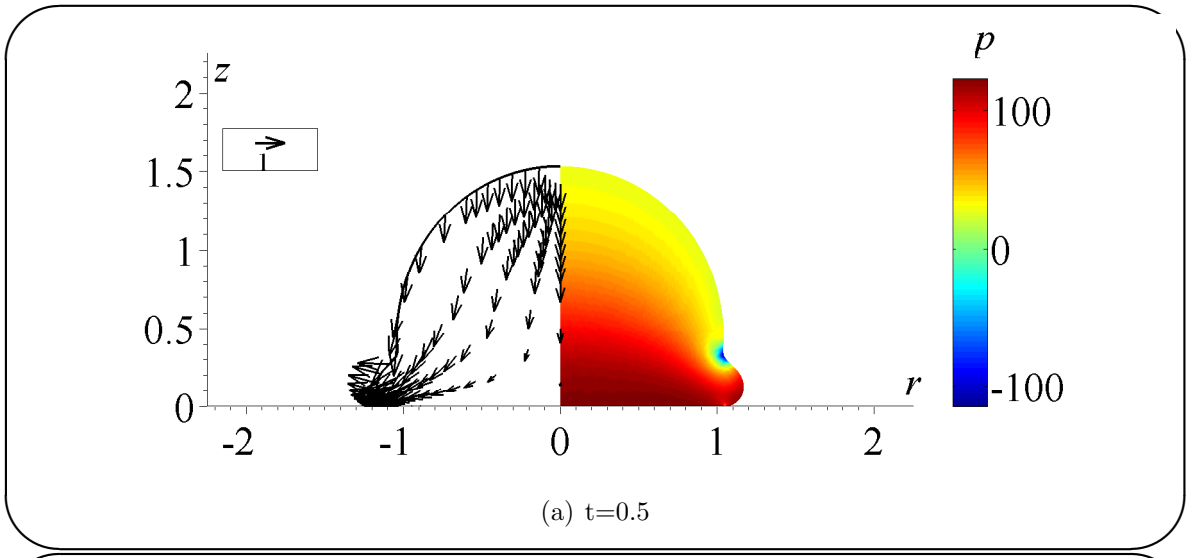
z
p
100
0
-100
r
2
1.5
1
0.5
0
-2
-1
0
1
2

(a) t=0.5

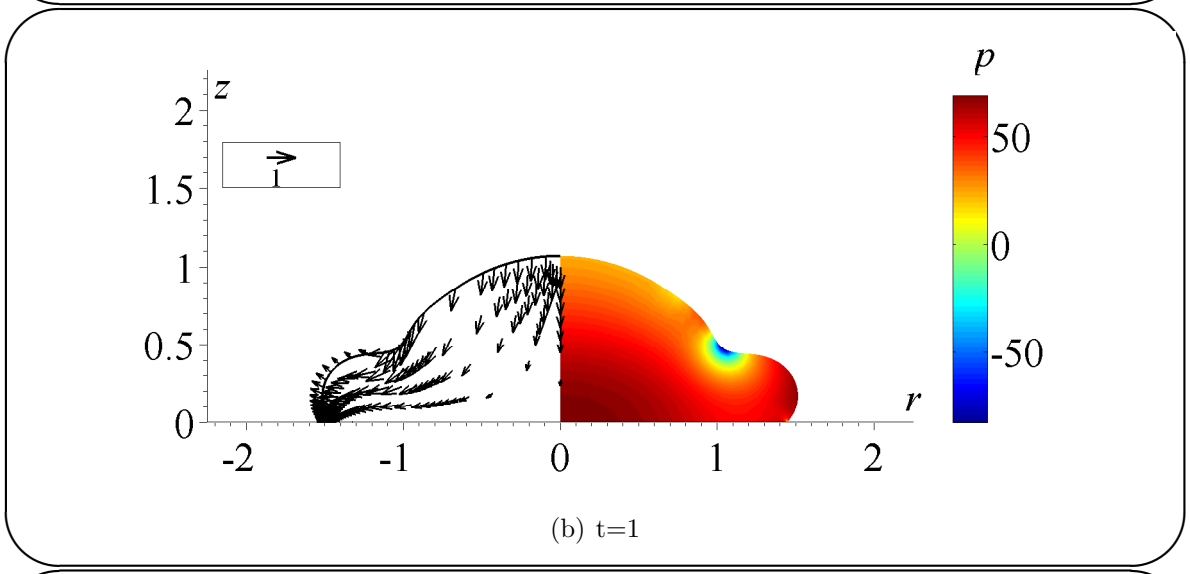
z
p
50
0
-50
r
2
1.5
1
0.5
0
-2
-1
0
1
2

(b) t=1

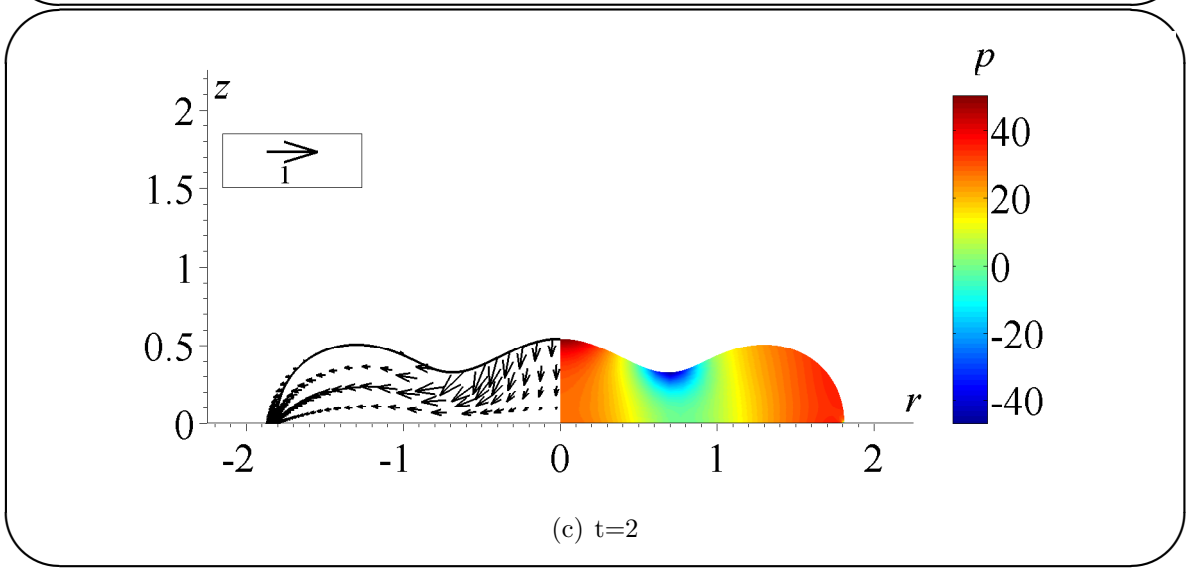
z
p
40
20
0
-20
-40
r
2
1.5
1
0.5
0
-2
-1
0
1
2

(c) t=2

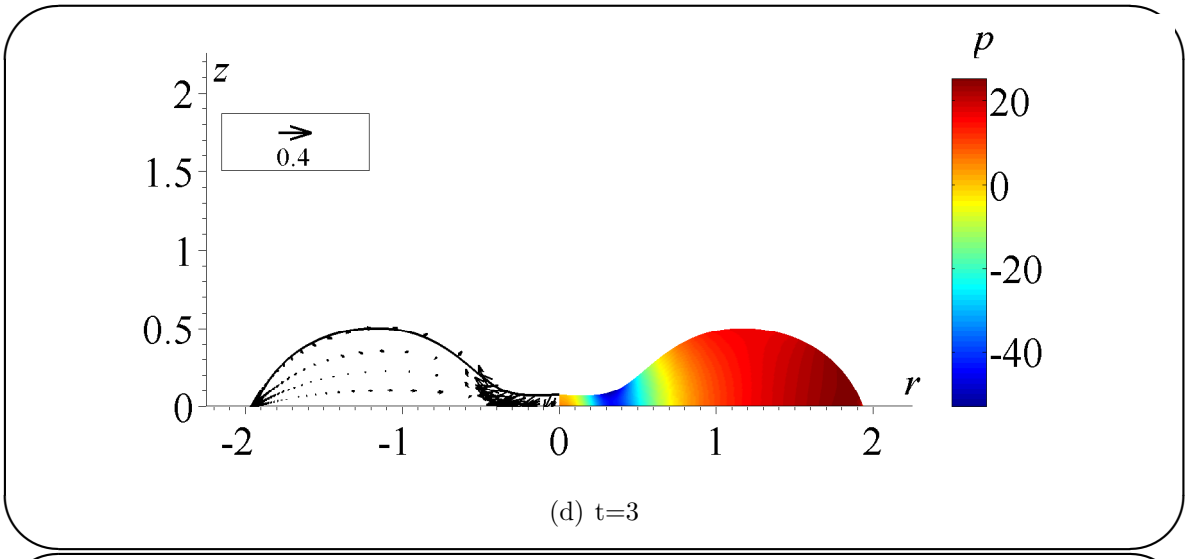

(d) t=3

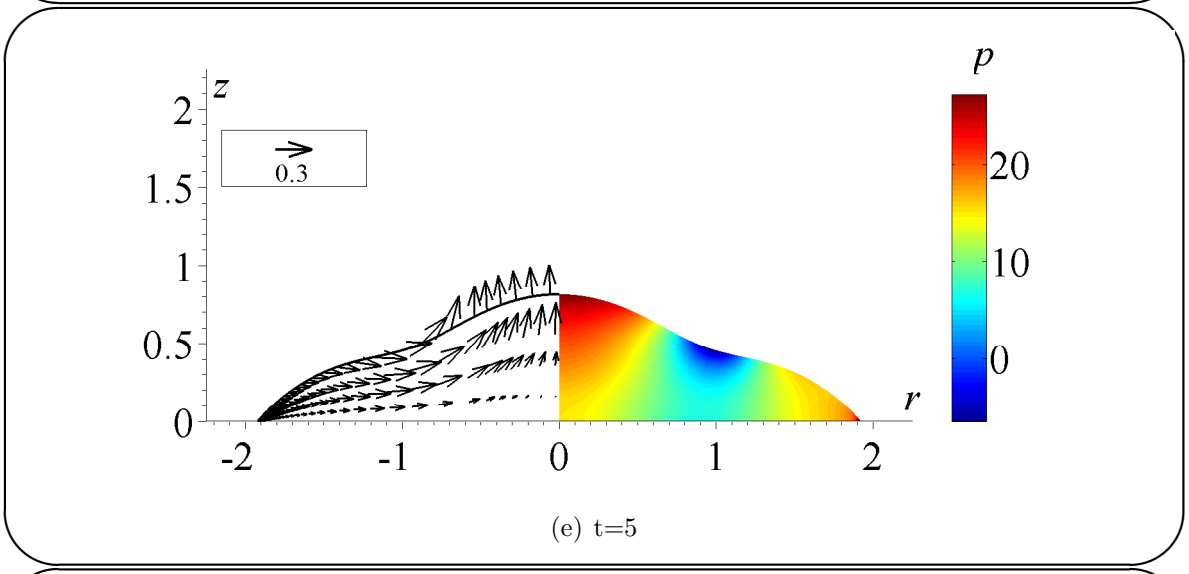

(e) t=5

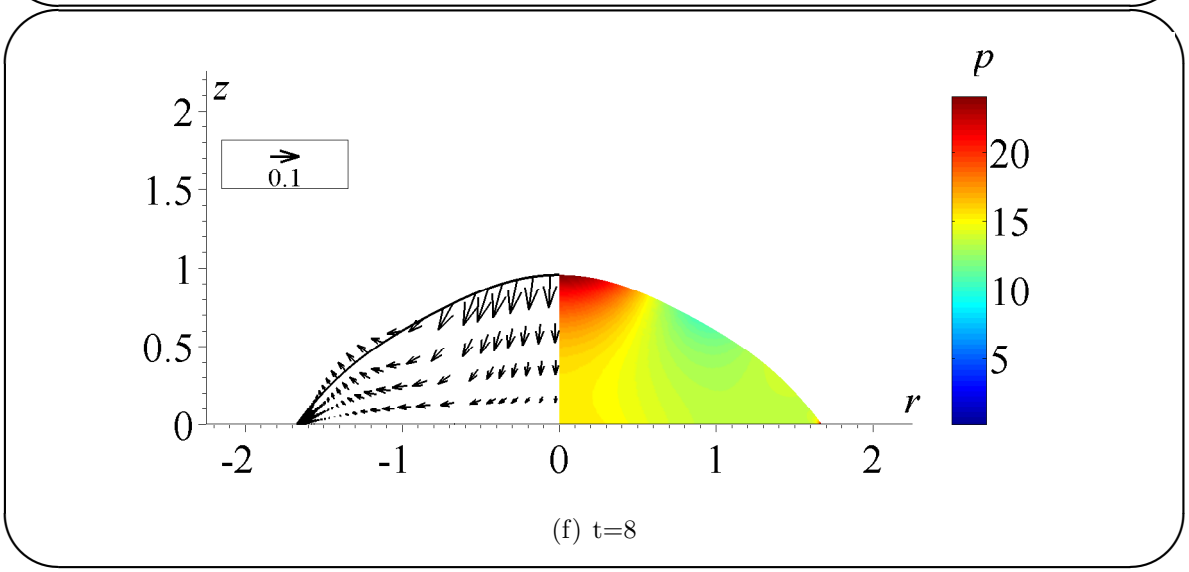

(f) t=8

Figure 6.7: Velocity and pressure distributions inside our base state drop after impact on a surface characterized by $\theta_e = 60°$.

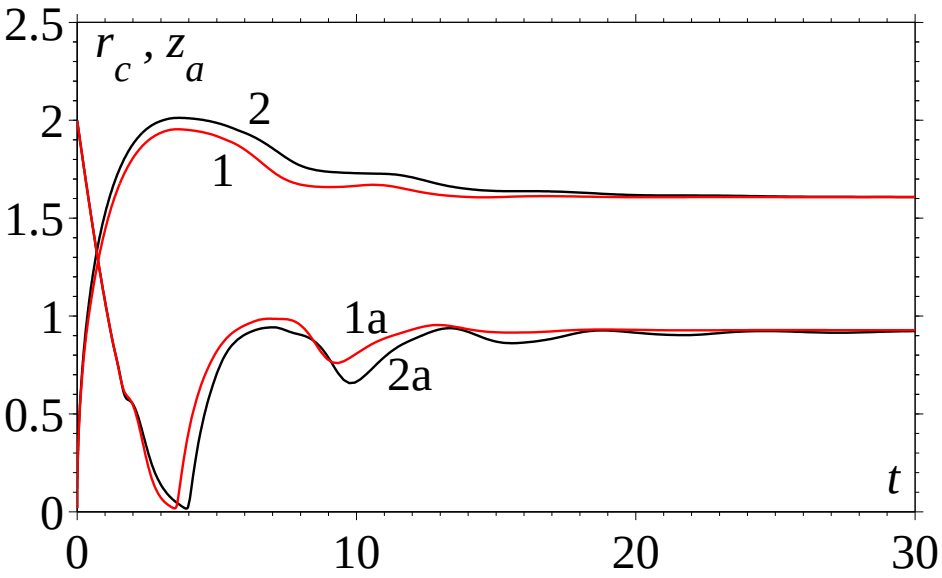

Figure 6.8: Curves 1,2 are the radius of the contact line r_c whilst Curves 1a,2a are the apex height z_a, both as a function of time t for the impact and spreading of our base state drop on a surface characterized by $\theta_e = 60°$. Curves 1 and 1a are obtained using the interface formation model whilst Curves 2 and 2a are obtained using the conventional model.

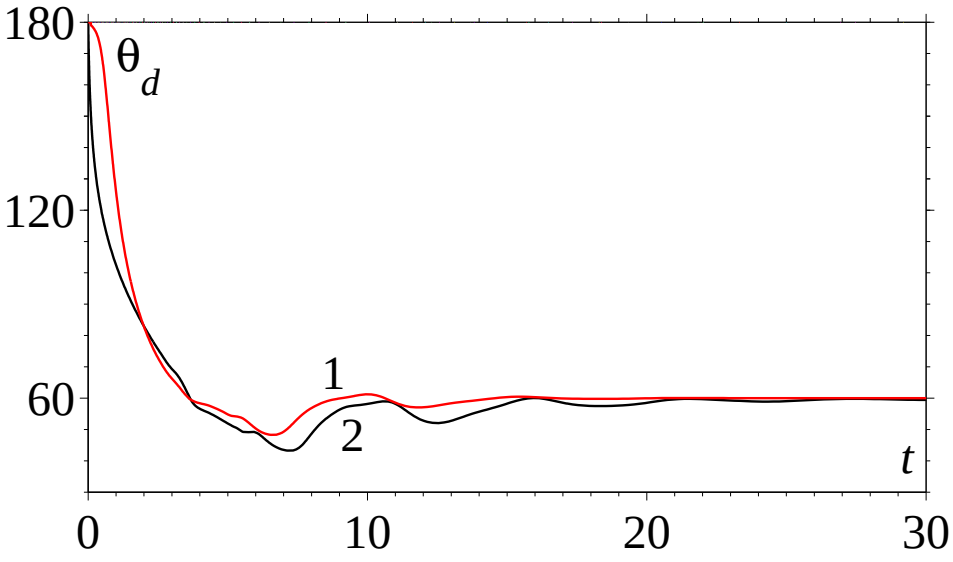

Figure 6.9: The dynamic contact angle θ_d as a function of time t for the impact and spreading of our base state drop on a surface characterized by $\theta_e = 60°$. Curve 1 is obtained using the interface formation model whilst Curve 2 is obtained using the conventional model.

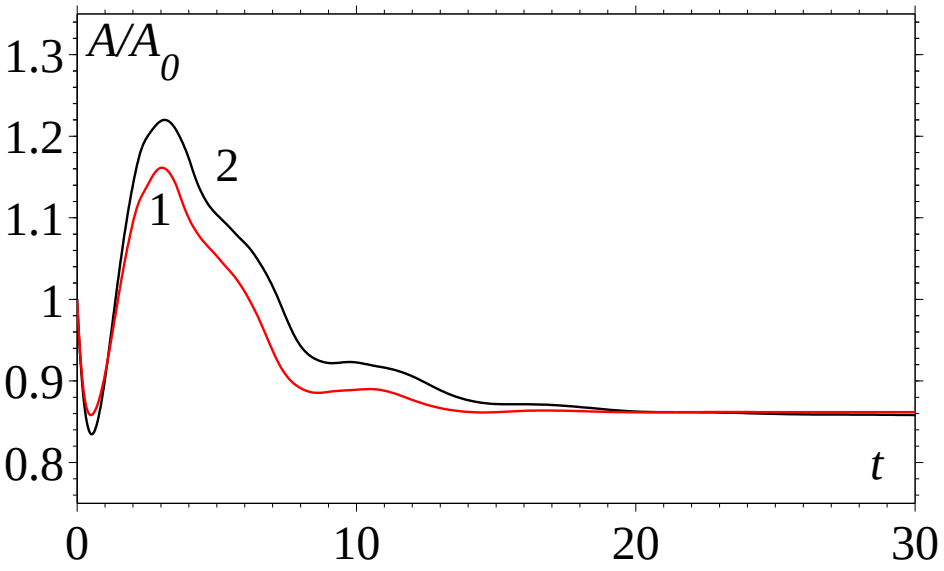

Figure 6.10: The free surface area A normalized by its initial value $A_0 = 4\pi$ as a function of time t for the impact and spreading of our base state drop on a surface characterized by $\theta_e = 60°$. Curve 1 is obtained using the interface formation model whilst Curve 2 is obtained using the conventional model.

on the free surface successively touching the solid, whilst the contact angle remains at 180°. For the base state, this period lasts until $t = 8 \times 10^{-3}$ when the conventional model is used whilst for the interface formation model it continues until $t = 9 \times 10^{-2}$. In the latter case, this means that the contact line is at $r_c \sim 0.5$ when the geometric wetting finally finishes, so that the length of the liquid-solid interface cannot be considered small, as in §4 where we showed that geometric wetting would occur immediately after impact due to the negligible influence of the solid base on the flow field near the free surface.

Notably, in our test runs, we have observed that the higher the Reynolds number, the longer this period lasts and, for high Reynolds numbers, we can show the influence of the solid base on the flow field actually enhances geometric wetting. We can consider the effect of the solid on the drop's flow field to be analogous to the effect of a plate of finite size on a flow normal to it. In this situation, for the ideal fluid one has an infinite velocity at the edges (Sedov, 1965). In the case of drop impact, this analogy implies a velocity on the free surface near the contact line region higher than the initial downwards

one. Then, at high Reynolds numbers, the contact line velocity predicted by a wetting model is not sufficient to allow the contact line to escape before the free surface ahead of it impacts the solid. Conversely, this suggests that at low Reynolds numbers, where viscous forces influence the whole flow and slow the initial downwards velocity on the free surface, geometric wetting will only briefly occur, if at all, and indeed this is exactly what is observed in our simulations.

To give some physical perspective on the geometric wetting phase, the maximum speed of the contact line, which occurs immediately after impact, is $U_c = 197$ and the geometric phase lasts until $t = 0.09$ when the contact-line-driven motion, predicted by the interface formation model, takes over. To re-dimensionalize these results, using the parameter values we chose to create the base state, the maximum speed is $\sim 10^3$ m s^{-1} and the geometric wetting lasts for a time $\sim 10^{-1}$ μs.

6.1.3 Speed-angle relationships obtained from the base state simulations

We now consider the speed-angle relationships obtained, for the two base state situations, from both the interface formation model and the conventional model. More precisely, we consider the relationship between the capillary number based on the contact-line speed $Ca_c = \mu U_c/\sigma$ and the contact angle; however, as the fluid is considered to be the same in each simulation, it is equally valid to speak of a speed-angle relationship.

Curves 1c and 1i in Figure 6.11 were obtained using the conventional model and the interface formation model, respectively, for the case in which the drop spreads from rest. The most notable difference between the two curves is near $\theta_d = 179°$, that is at the start of the simulation. The first point, corresponding to the initial conditions, has been omitted so that one can most easily observe that, after the first time step, the conventional model immediately predicts a value $Ca_c \sim 1$. This value is independent of the time step so, as

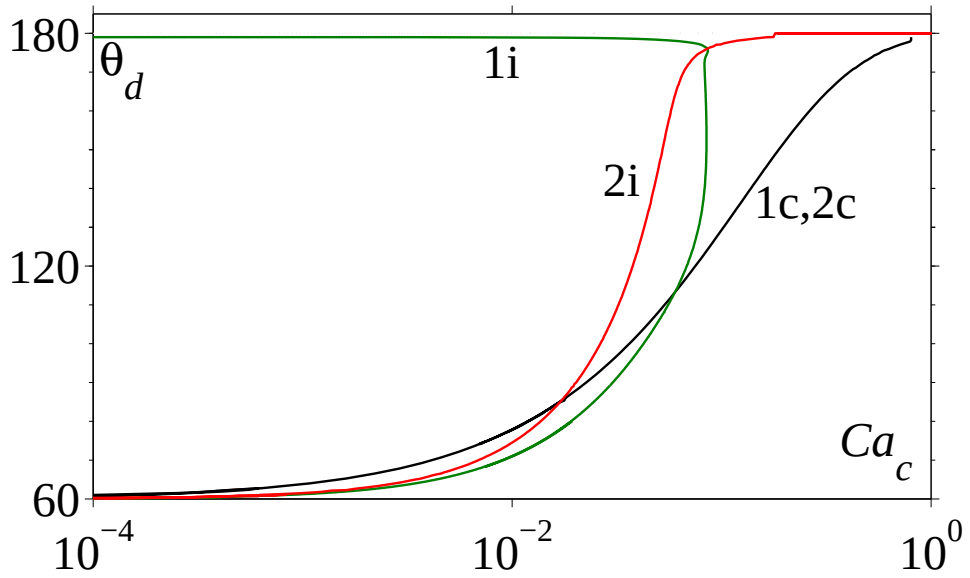

Figure 6.11: Comparison of the relationship between the capillary number based on contact-line speed Ca_c and the dynamic contact angle θ_d for four simulations. Curves 1c and 2c were obtained from the base state runs using the conventional model for spreading from rest and with impact, respectively, whilst Curves 1i and 2i were obtained using the interface formation model for spreading from rest and with impact, respectively.

one decreases the initial time step, the acceleration becomes unbounded. Consequently, for the initial time steps, a numerical solution obtained using the conventional model will not converge as the time step is reduced. From Curve 1i, we can see that when the interface formation model is used, the behaviour of the contact line is entirely different. The contact-line speed is now reaching a maximum of around $Ca_c \sim 0.1$ in a finite time, and independently of the time steps. After this initial period, both curves are qualitatively similar as the contact angle relaxes towards its equilibrium value and hence the contact-line speed goes down. Thus, for the interface formation model we have (i) a physically-realistic gradual acceleration of the contact line after the initial contact of the drop with the solid and (ii) a non-unique correspondence between the contact-line speed and the dynamic contact angle.

We now consider the case in which our base state is the drop impacting and spreading on a solid surface. For this case, Curves 2c and 2i in Figure 6.11 were obtained using the conventional model and the interface formation model, respectively. Both simulations

begin with a period of geometric wetting where the contact angle remains at $\theta_d = 180°$. Curve 2c exits this phase at $Ca_c \sim 1$ and, as expected, proceeds to follow exactly the same path as Curve 1c since the speed-angle relationship is explicitly built into the model. From Curve 2i, we can see that the interface formation model predicts that the geometric wetting phase will last longer.

Comparing Curves 1i and 2i in Figure 6.11, it is clear that, in contrast to the predictions of any conventional model, there is no unique speed-angle curve obtained when using the interface formation model. Curve 1i is particularly incredible, as each value in $0 < Ca_c < 0.1$ corresponds to two contact angles. For example, for $Ca_c = 0.01$, there are two angles which are over 100° apart! As previously pointed out, this behaviour is critical as it allows the contact-line speed to steadily increase, as opposed to jumping onto a prescribed curve independently of the initial contact-line speed. For $Ca_c < 0.01$, the lower branch of Curve 1i and Curve 2i are close, which suggests that this is an asymptotic regime where there is a unique speed-angle relationship and in the next section we will investigate this effect further.

6.1.4 Summary of the results from our base state simulations

We have seen that for the base state simulations, the free surface shapes obtained using the interface formation model and the conventional model are qualitatively similar but that there are quantitative differences of approximately 5%. This is a reassuring result as the conventional model is based on an empirical relationship for the speed-angle relationship which one could expect to roughly approximate the dynamics in this particular flow.

The most notable difference between the results obtained from the two models is that when a drop is released from rest the conventional model predicts an infinite acceleration of the contact line whereas the interface formation model allows a large speed to be attained in a finite time. Also, only the interface formation model was able to predict

the experimentally observed non-uniqueness of the speed-angle relationship, which was sometimes achieved even in a single simulation.

As the conventional model predicts unphysical behaviour and is unable, even in principle, to predict the non-uniqueness of the speed-angle relationship, we now use only the interface formation model and begin by investigating the non-uniqueness of the speed-angle relationship in more detail.

6.2 Non-uniqueness of the speed-angle relationship

We have seen from our base state simulations that the interface formation model predicts a non-uniqueness of the speed-angle relationship. This non-uniqueness means that it is the flow field in the bulk and geometric constraints on the flow that influence the contact angle. Here, we consider this phenomenon in more detail by determining the effect of the drop size and its impact speed on the speed-angle relationship. To allow the contact angle a large range in which to vary, we consider a more wettable surface characterized by $\theta_e = 30°$. The speed-angle relationships are now compared to the asymptotic small capillary number relationship (5.7).

6.2.1 A novel prediction: different sized drops produce different speed-angle relationships

Having observed that there is a non-uniqueness in the speed-angle relationship obtained for a single drop spreading towards an equilibrium value, we now consider what influence the size of the drop has on this relationship. To do so, we consider drop sizes over three orders of magnitude. Specifically, we consider three drops of radii $1, 10, 100$ μm with all other dimensional parameters the same as for our base state drop.

Figure 6.12 shows snapshots from the spreading of the three drops. Although all the

drops are initially in a capillary-driven wetting phase, the evolution of each drop is very different, with the smallest drop remaining approximately as a spherical cap throughout motion whilst the largest drop undergoes severe deformation caused by the dominance of inertial effects after the capillary-driven wetting phase. The rather strange shapes seen for the largest drop, from $t = 120 - 200$ in Figure 6.12, have been observed experimentally and can be seen in Figure 6 and Figure 8 of Schiaffino & Sonin (1997) for the low speed impact of millimetre-sized drops. This behaviour occurs because, at higher Reynolds and Weber numbers, it takes a long time for the apex region of the drop to feel that the contact line is moving radially outwards and by this time a volume of liquid near the apex has been left behind. The simulation is terminated when the large curvature near the apex causes too much element distortion: it could be that the small drop at the apex is about to pinch-off and detach from the bulk of the drop, but without special numerical treatment there we cannot be certain.

In Figure 6.13, we show the speed-angle relationships for these three numerical simulations. As previously discussed, the drops start from rest and accelerate to a large contact line speed in a finite time. Subsequently, three visibly different speed-angle relationships are obtained. It is interesting to consider whether the speed-angle relationship will approach the asymptotic one as the drop becomes larger or smaller. As the drop becomes larger, the region in which the interface formation variables are out of equilibrium becomes relatively small compared to the bulk length scales, as in the asymptotics. However, this coincides with an increase in the capillary number, which is assumed to be small in the asymptotic result. In Figure 6.13, we see that as Curves 1-3 approach the asymptotic region, $Ca_c \ll 1$, the larger the drop, the closer its curve is to the asymptotic prediction. As one would expect, all three curves coincide with the small capillary number speed-angle relationship (5.7) for very low capillary numbers based on the contact-line speed, but it is the smallest drop, see Curve 1, which approaches the asymptotic prediction most slowly. Surprisingly, the smallest drop's speed actually increases slightly as the contact angle decreases to around 150°. This is against the general trend of all speed-angle rela-

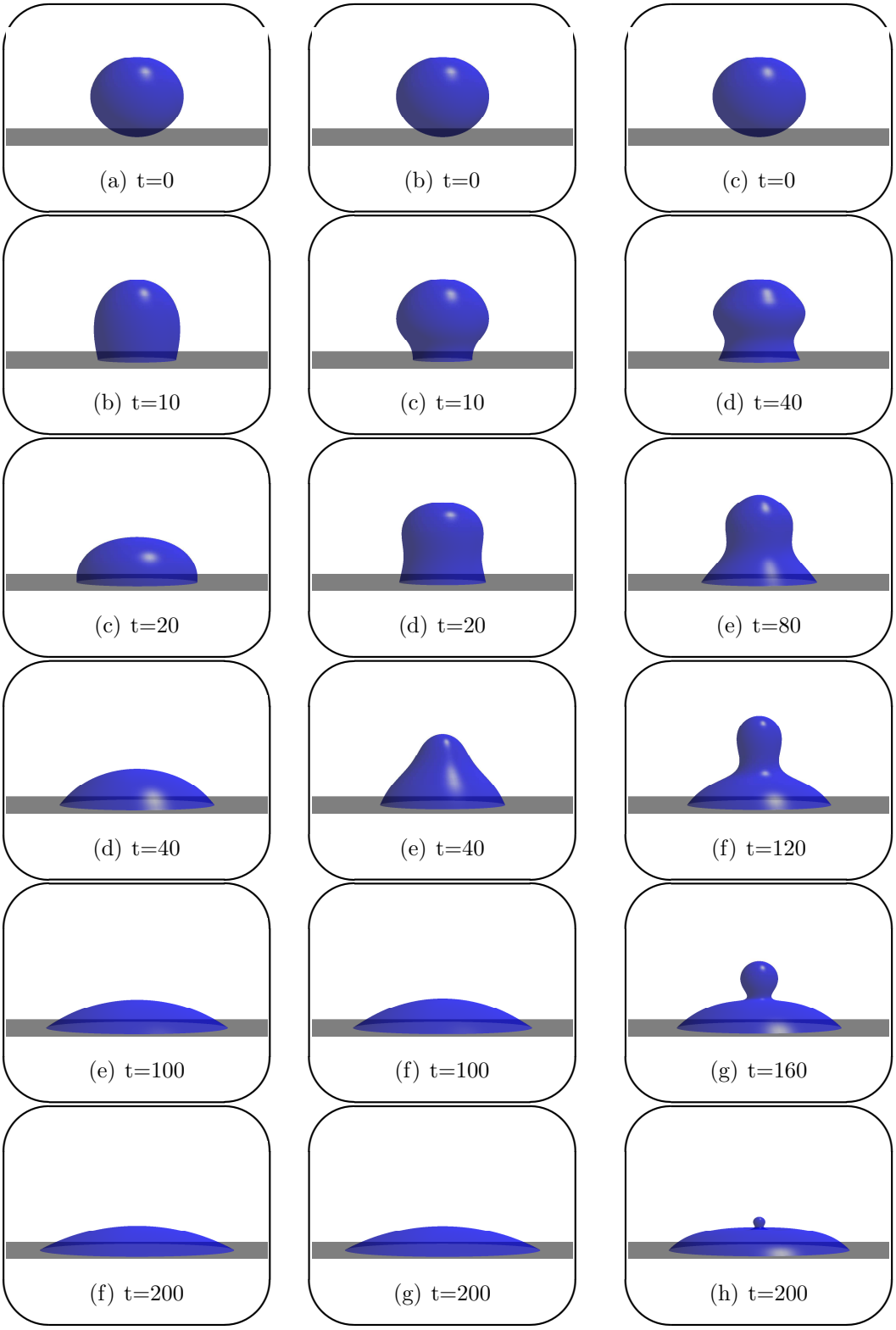

Figure 6.12: Left to right: spreading from rest of liquid drops of radii $1, 10, 100\mu$m towards an equilibrium angle $\theta_e = 30°$.

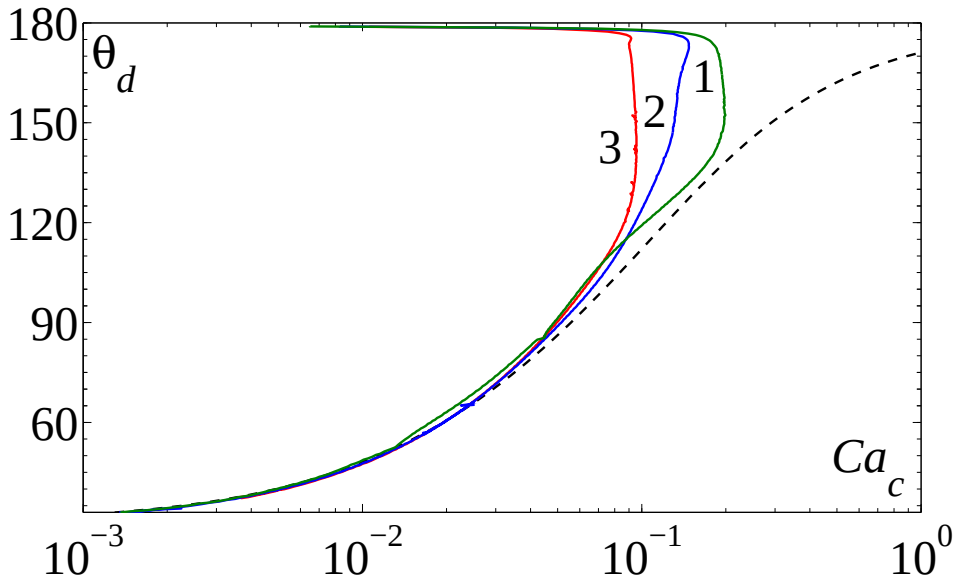

Figure 6.13: Comparison of the contact-line speed-angle relationship as drops 1-3 of radii $1, 10, 100\mu m$, respectively, spread towards an equilibrium angle of $\theta_e = 30°$. The dashed line is the small capillary number speed-angle relationship.

tionships previously proposed. This rather strange result, and the fact that the smallest drop approaches the asymptotic speed-angle relationship slowest, are due to the size of interface formation region being comparable to the length of the liquid-solid base, so that the whole interface is out of equilibrium and the usual trends do not apply.

We now proceed to consider if different impact speeds can also produce different speed-angle relationships, as has been observed in the experiments of Šikalo *et al.* (2005) and Bayer & Megaridis (2006).

6.2.2 The influence of impact speed

We consider impact speeds of $U_0 = 1, 4, 8$ m s^{-1} on a surface characterized by $\theta_e = 30°$. In Figure 6.14 we can see that the dynamics of the three drops are very different. In particular, at the lowest speed of impact, we can recognize capillary-driven wetting in the early stages, whilst for the highest impact speed it is clear that the initial spreading is inertia-driven.

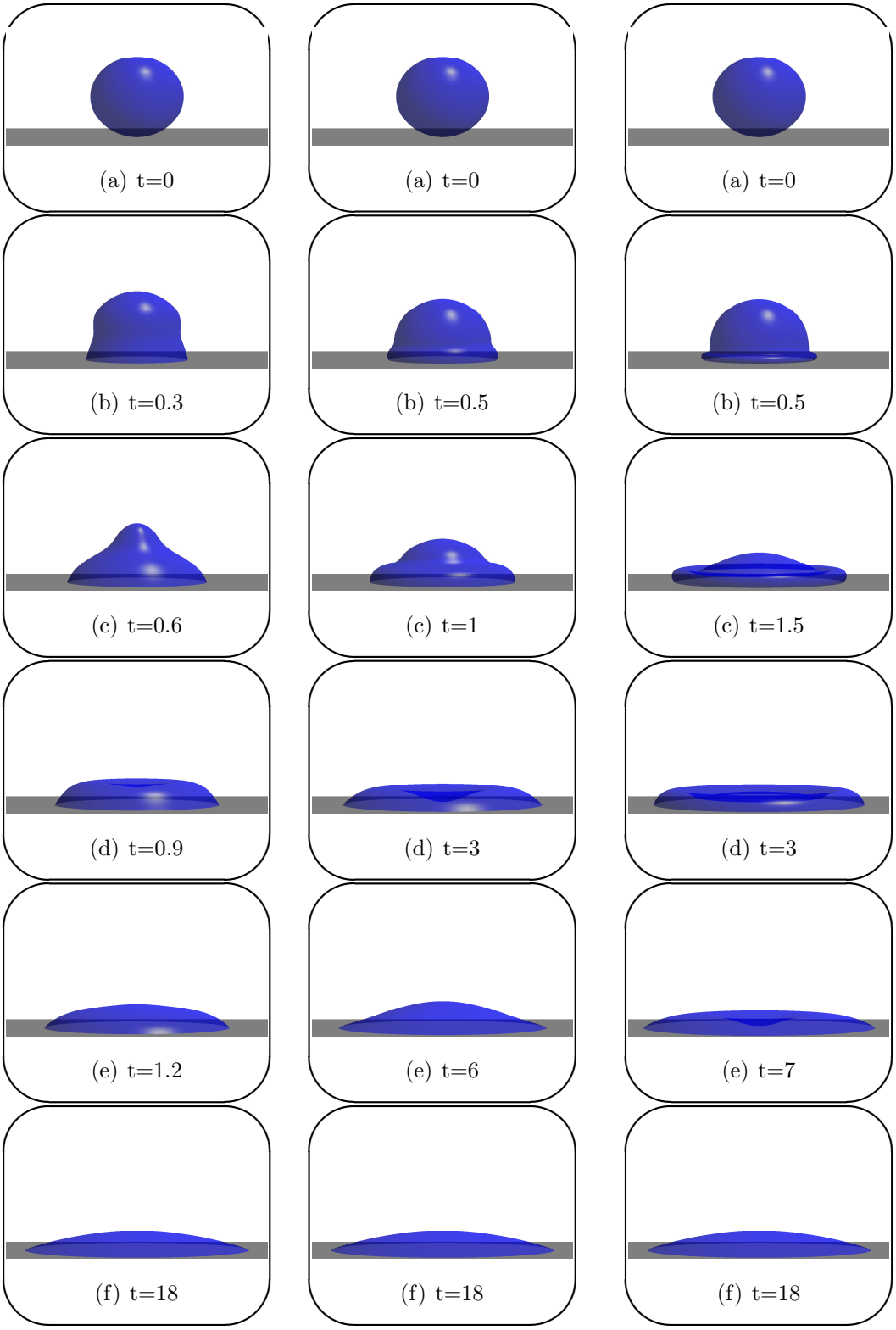

Figure 6.14: Left to right: spreading of three identical drops with impact speeds $U_0 = 1, 4, 8$ m s^{-1} towards an equilibrium angle $\theta_e = 30°$.

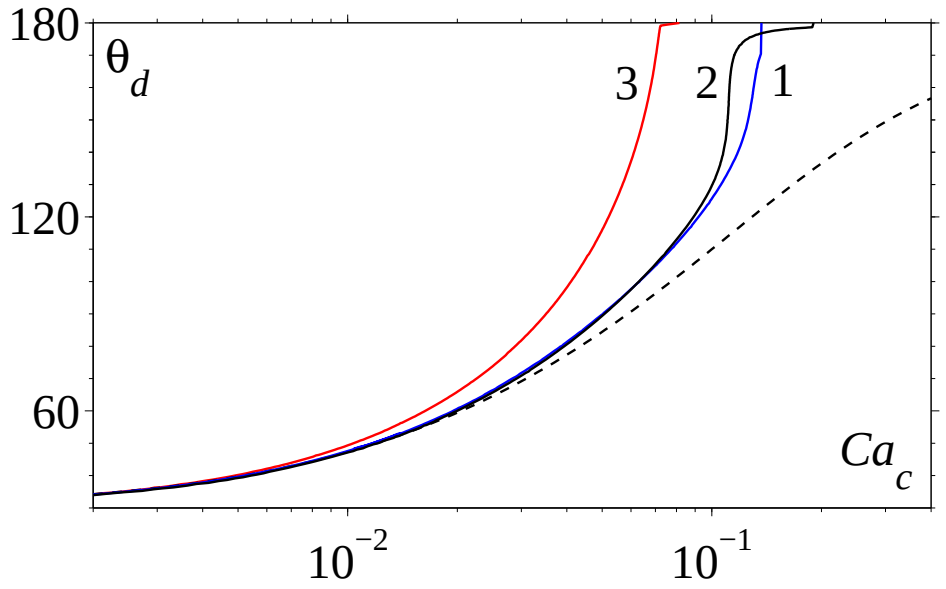

Figure 6.15: Comparison of the speed-angle relationship for three identical drops (1-3) with impact speeds $U_0 = 1, 4, 8$ m s^{-1}, respectively, spreading on a surface characterized by $\theta_e = 30°$.

In Figure 6.15 we see that the different drop dynamics produce different speed-angle relationships, with the highest impact speed deviating most from the asymptotic prediction. Notably, taking $Ca_c = 0.05$, there is a difference of 40° between the angle associated with the slowest impact speed compared to the fastest one. So, where a conventional model would suggest a unique contact angle for this contact-line speed, the interface formation model predicts a deviation of 40° simply by changing the drop's impact speed for a given liquid-solid system. Such a large effect may be outside the range of experimental error, even for the relatively small drops considered here, and hence could be detected experimentally.

The drop with the highest impact speed is in the geometric wetting phase for considerably longer than the other two drops, a time 0.8 compared to $0.01, 0.06$ for the $U_0 = 1, 4$ m s^{-1} speed impacts, respectively. Consequently, when the highest impact speed drop exits the geometric wetting phase, it does so at a smaller capillary number based on the contact-line speed. This accounts for the large initial deviation from the asymptotic prediction which predicts that as $\theta_d \to 180°$, we have $Ca_c \to \infty$.

6.2.3 Discussion of the observed non-uniqueness of the speed-angle relationship

Some general conclusions may be drawn from the speed-angle relationships obtained. In all cases, as one would expect, the asymptotic speed-angle relationship agreed very well with the computed results for small Ca_c, in practice for $Ca_c < 0.01$. Surprisingly, none of the simulations were able to reach $Ca_c > 0.5$ at an angle $\theta_d < 180°$, i.e. the drop was always in the geometric wetting phase for $Ca_c > 0.5$. In the range $0.01 < Ca_c < 0.5$ one observes significant non-uniqueness of the dynamic contact angle. It appears that the deviation from the asymptotic prediction is roughly linear with respect to the size of the drop and more than linear in the impact speed. We now show why this is the case.

A rough estimate for when the non-uniqueness is likely to occur can be obtained by considering the ratio of the relaxation length $U_c\tau$ to the radius r_s of the Stokes region, that is the zone near the contact line region where inertial effects become negligible and the assumptions of the asymptotics hold. For this ratio we use the notation $N = U_c\tau/r_s$. We can approximate the size of the Stokes region by setting $Re = \rho U_c r_s/\mu = 10^{-2}$ so that, for drops of water, we have $r_s = 10^{-8}U_c^{-1}$ m. Then, for the parameters used, we obtain $N \simeq U_c^2 \simeq 10^3 Ca_c^2$. For a deviation from the asymptotic, i.e. unique, speed-angle relationship to be large we need $N \gg 1$ and, if we take as an estimate $N > 10$, we have $Ca_c > 0.1$. Indeed, from the results we have obtained this estimate is very reasonable. It is also interesting to see that the effect is quadratically dependent on the contact line velocity, which is in agreement with our observations.

6.3 Recovering information which is missing from the results of microdrop experiments

We now show that our simulations are able to capture features which are not observable from experiments, namely the shape of the free surface near the contact line and the behaviour of the apex region when it is not the highest point of the drop and hence is hidden below the outer free surface. To do so, we compare the snapshots from our simulations to the experimental images in Dong *et al.* (2007) for the impact and spreading of water microdrops. First, in Figure 6.16 we show that our results are in qualitative agreement with the experimental images of a drop of radius 24 μm impacting at 4.4 m s^{-1} on a surface characterized by $\theta_e = 108^\circ$.

Having established that our simulation agrees with the observable features of the microdrop experiment, we use our results to uncover information which is missing in the experimental images, beginning by looking at the initial stages of wetting.

6.3.1 Overcoming poor experimental spatio-temporal resolution

After impact, from roughly $t_d = 0 - 6$ μs, one can see from Figure 6.16 that the top of the drop remains spherical in both the experiment and the simulation. However, from the experimental images, one cannot accurately determine the shape of the free surface near the contact line.

This is a situation in which we can use our code to recover information which is unobtainable in the experiments. In Figure 6.17 we show the shape of the drop near the contact line at a non-dimensional time $t = 0.25$ for the three impact speeds considered in Dong *et al.* (2007) of $U_0 = 2.2$ m s^{-1}, 4.4 m s^{-1} and 12.2 m s^{-1}. Dimensionally, these images are at times $t_d = 2.4$ μs, $t_d = 1.8$ μs and $t_d = 0.5$ μs, respectively. In each image one can observe the formation of a rim of fluid around the contact line; however, the size

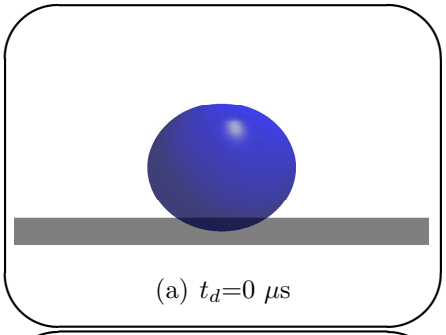

(a) t_d=0 μs

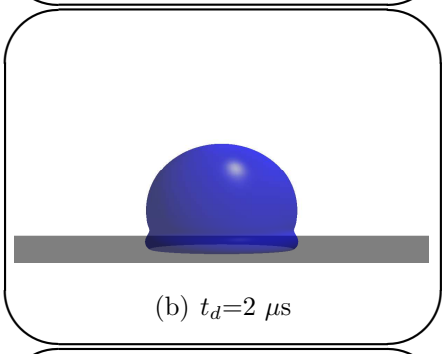

(b) t_d=2 μs

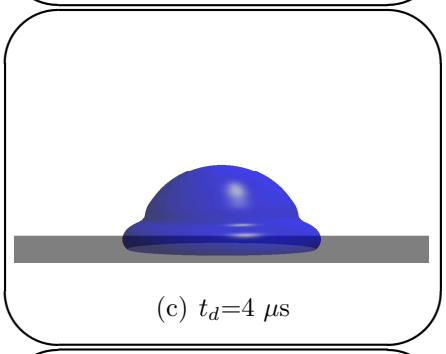

(c) t_d=4 μs

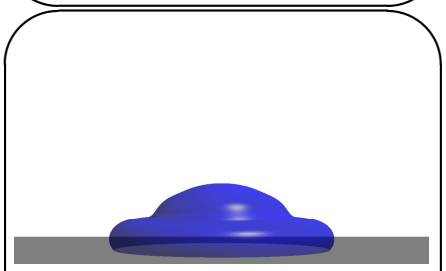

(d) t_d=6 μs

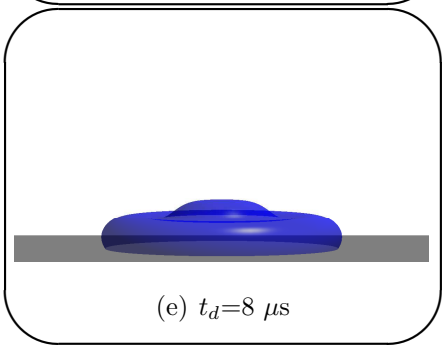

(e) t_d=8 μs

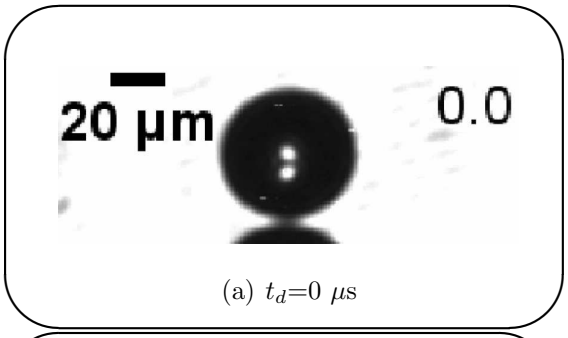

(a) t_d=0 μs

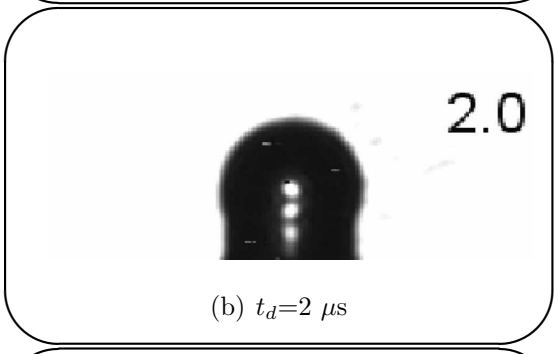

(b) t_d=2 μs

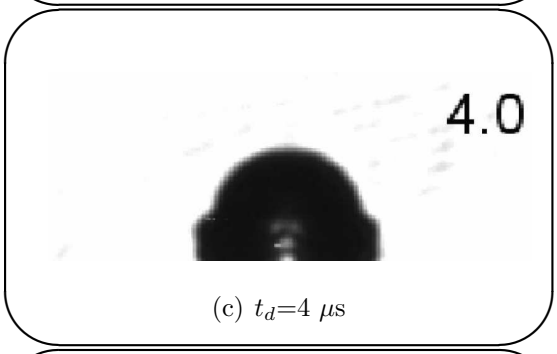

(c) t_d=4 μs

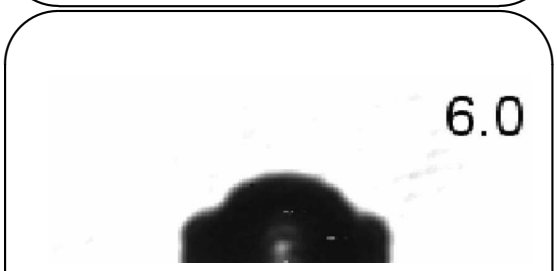

(d) t_d=6 μs

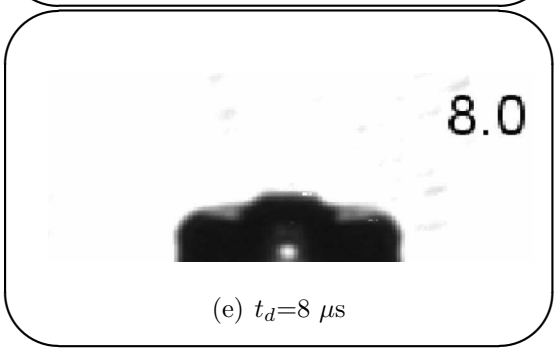

(e) t_d=8 μs

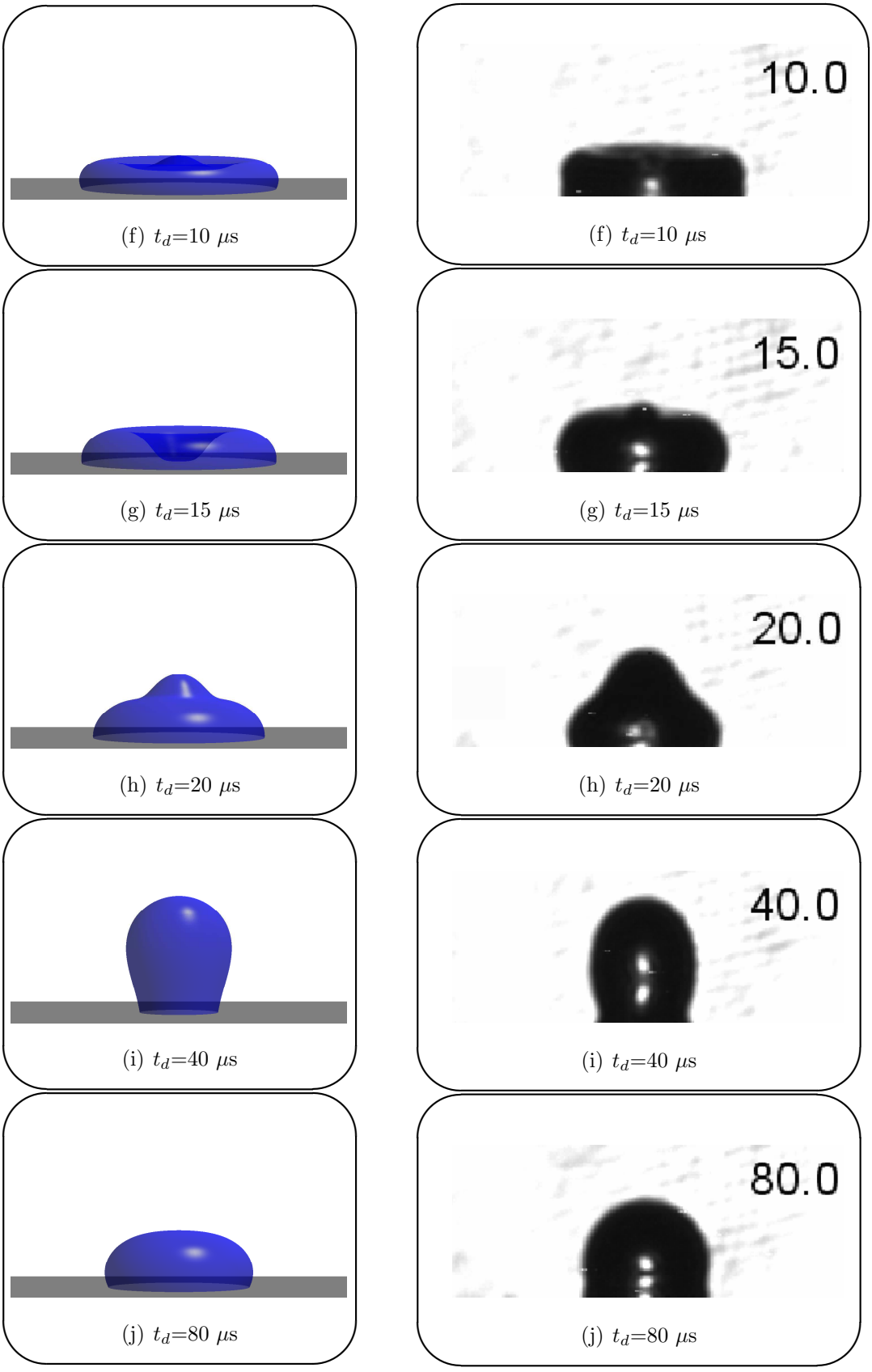

(f) t_d=10 μs (f) t_d=10 μs

(g) t_d=15 μs (g) t_d=15 μs

(h) t_d=20 μs (h) t_d=20 μs

(i) t_d=40 μs (i) t_d=40 μs

(j) t_d=80 μs (j) t_d=80 μs

Figure 6.16: Comparison of images from our simulation (left) to the experiments of Dong *et al.* (2007) (right) for a drop of radius 24 μm impacting at 4.4 m s^{-1} on a surface characterized by $\theta_e = 108°$.

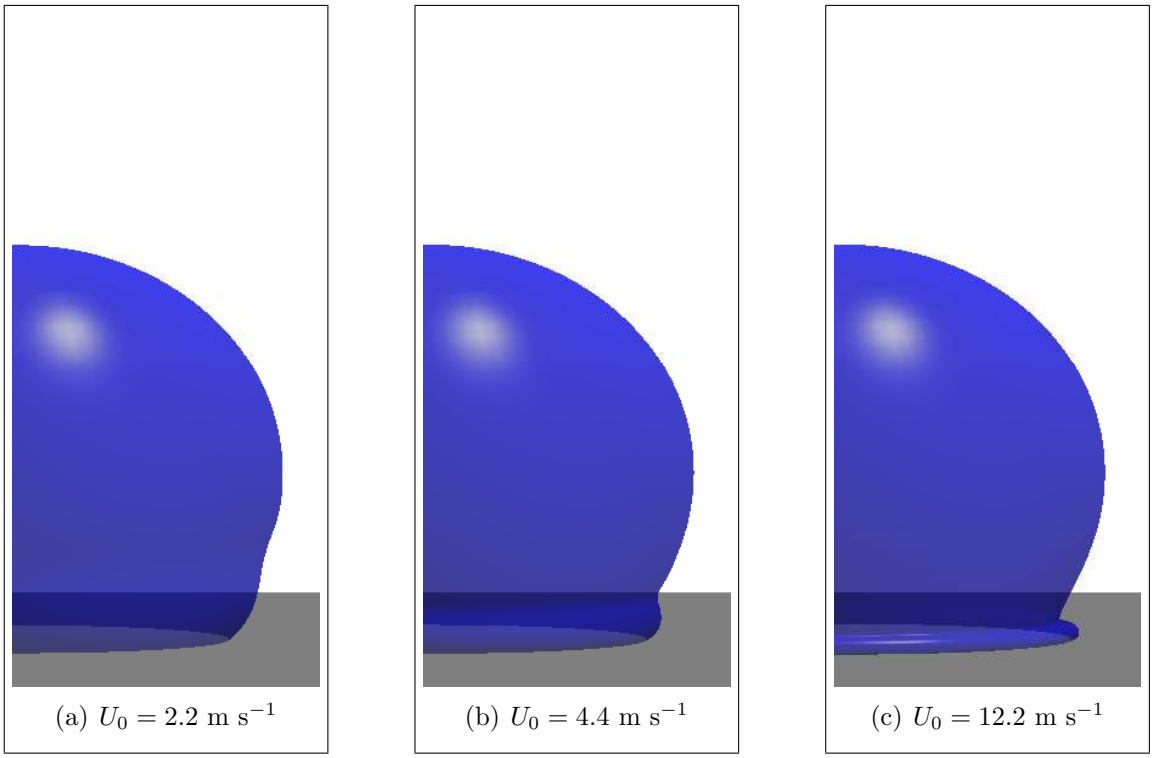

(a) $U_0 = 2.2$ m s^{-1} (b) $U_0 = 4.4$ m s^{-1} (c) $U_0 = 12.2$ m s^{-1}

Figure 6.17: The drop's shape at a (non-dimensional) time $t = 0.25$.

of this rim differs significantly, with the highest speed of impact creating the smallest rim of fluid and virtually no deformation to the free surface above. This is in qualitative agreement with results obtained for millimetre-sized drops, see for example experimental images in Rioboo *et al.* (2002), but is here predicted in a regime where a lack of spatial resolution makes it impossible to achieve unambiguous conclusions from the experimental images.

We now consider a case where the main problem is not a lack of spatial and temporal resolution, but that the dynamics of interest are completely hidden.

6.3.2 Recovering hidden dynamics

In the experimental images in Figure 6.16, at around $t = 10$, we can no longer observe the apex region because it disappears below the free surface which is closer to the camera. In larger drops, see for example Renardy *et al.* (2003), the transparency of the free surface

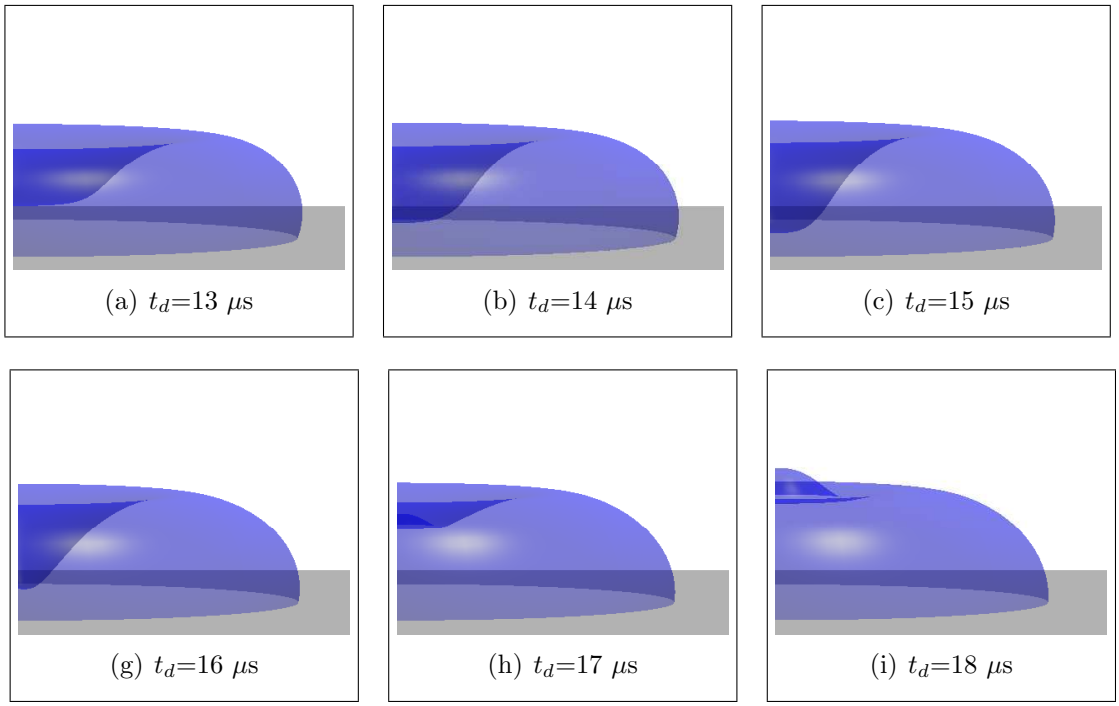

Figure 6.18: Snapshots from a simulation for the 4.4 m s^{-1} impact showing the behaviour of the apex region as it becomes unsighted in the experiment.

in the experiments allows the apex behaviour to be monitored, but this does not seem possible in microdrop experiments. In Figure 6.18, we can see that the simulation provides the missing information. The observable height of the drop hardly changes for a whole 5 μs, whilst the apex almost contacts the solid ($t_d = 15$ μs), before being driven upwards with a great speed (notice the distance travelled between $t_d = 16$ μs and $t_d = 17$ μs) after which it finally becomes the highest point of the drop again.

6.3.3 Concluding remarks

We showed that our model predicts observable features of microdrop experiments. Then, we established that in situations where the experimental results failed to let us draw unambiguous conclusions about the drop's dynamics; the model allowed us to. Having demonstrated the usefulness of the code in the early stages of wetting, we now use it to determine the accuracy of a number of analytic predictions proposed in the literature for the drop's evolution during this stage.

6.4 Early stage of wetting

We now use our code to identify when analytic power-laws proposed for the contact line radius as a function of time, in the initial stages of wetting, accurately approximate microdrop impact and spreading. We consider two such laws, both proposed for the early stages of inertia-driven drop impact and spreading phenomena. First, we have $r_c \sim (2t)^{1/2}$, which, as described in §4, occurs when the velocity near the contact line on the free surface has not been affected by the impact. This is certainly the case in the moments after impact, but here we consider how long its assumptions may be valid for. Second, we consider a law proposed in Kim *et al.* (2000), where the early stages of a drop's motion are considered analogous to that of a drop falling through a plane, with the mass loss added back on to the drop, so that the shape is a spherical cap with a cylindrical base to which the lost mass is added. This results in the prediction $r_c = (-\frac{1}{16}(3(t^2 - \frac{10}{3}t + 1)^{1/2} + 1 - 3t)^2 + 1)^{1/2}$.

Interestingly, in Figure 6.19, we can see that the majority of the curves fall between $r_c \sim (2t)^{1/2}$ and the formula of Kim *et al.* (2000). The power laws are based on the assumption that the wettability of the solid substrate has no influence and, indeed, in Figure 6.19 the wettability is seen to have no affect on the motion of the base state drop with Curve 0 and Curve 2, obtained for surfaces characterized by $\theta_e = 60^\circ$ and $\theta_e = 30^\circ$, respectively, being almost graphically indistinguishable. This confirms that the initial wetting phase of our base state drop is indeed inertia-driven, i.e. capillarity has no influence. Consequently, the choice of conventional or interface formation model in this phase has no affect on the dynamics of the drop. When the drop size is decreased, one can see from the Curve 3 in Figure 6.19, the spreading is slower. This is because the Reynolds and Weber numbers are smaller and the limit of zero Reynolds and Weber number corresponds to a drop evolving from rest, so that the initial spreading is entirely capillary-driven, i.e. none of the above arguments for inertia-driven flow will hold. Surprisingly, an increase in the speed of impact to $U_0 = 8$ m s^{-1} leads to the simulation predicting a faster spread

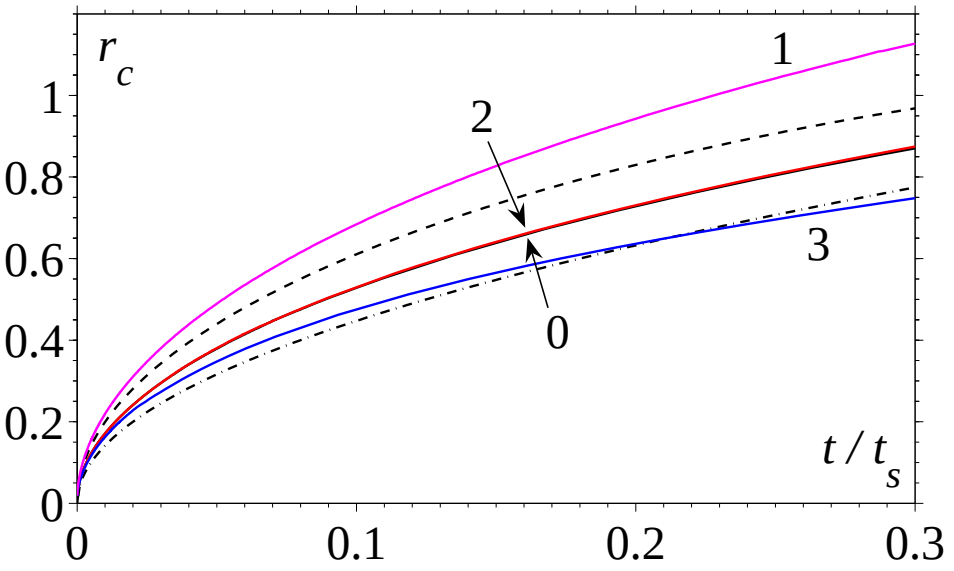

Figure 6.19: Plot of contact line radius r_c against time t, with $t_s = 5 \times 10^{-6} U_0 a^{-1}$ a scaling factor which is unity for the base state. The top dashed line is the prediction from Kim *et al.* (2000) whilst the bottom dash-dot line is for $r_c = (2t)^{0.5}$. The unbroken curves are, 0: base state, 1: $U = 8$ m s^{-1}, 2: $\theta_e = 30°$, and 3: $a = 5$ μm.

than that obtained from either early-time model. This is caused by the formation of a small rim of fluid, see Figure 6.17, so that the shape is not well approximated by a spherical cap truncated by a cylindrical base as assumed in Kim *et al.* (2000). In fact the additional fluid is not added to a cylindrical base which supports a spherical cap, but instead is squeezed out into a toroidal rim of fluid which protrudes from a spherical cap. Consequently, for high impact speeds, it appears that both models underestimate the contact line position as a function of time during the period in which inertia dominates.

We have seen that the proposed power laws only provide estimations that are accurate in a small range of parameter space. For our base state drop, in the early stages of wetting, the wettability of the substrate has no influence on the drop's evolution; however, the size of the drop and its impact speed are observed to significantly alter the initial spreading phase and now we shall consider their full influence on a drop's dynamics.

6.5 Influence of dimensional parameters

We shall now consider how an impacting drop's evolution is influenced by, firstly, its size and, secondly, its impact speed.

6.5.1 Drop size

We consider droplets of size 1 μm, 5 μm and 25 μm, respectively. The only parameters which depend (linearly) on size are Re, We, ϵ^{-1} and $\bar{\beta}$, so that, for larger droplets, one can expect greater deformation of the free surface as inertial forces dominate capillary and viscous ones. From Figure 6.20 we can see that this is indeed the case: the smallest drop approximately maintains a spherical cap shape whilst the largest drop's free surface is heavily deformed, particularly in the contact line region for early times.

In Figure 6.21 we show the contact line radii and apex heights of the spreading drops as a function of time. One may expect that all the drops would pass their equilibrium position, by differing amounts, before recoiling and approaching, or oscillating around, their equilibrium position. This is not the case. Both of the smallest drops appear never to extend past their equilibrium radius. To understand this surprising behaviour it is insightful to study the dynamics of the apex region. As can be seen from the curves in Figure 6.21, and the snapshots from the simulation in Figure 6.20, in all cases, the liquid near the apex initially falls with its impact speed and the free surface there remains spherical; meanwhile, the contact line is being driven radially outwards. The duration of this type of motion greatly affects the drop's dynamics: the larger the drop, the longer this period lasts, with the apex of the largest drop falling for so long that it almost contacts the substrate. For the two smaller drops, the apex recoils, due to the more dominant influence of capillary forces, much earlier and, as liquid is pulled towards the axis of symmetry, the outward radial motion of the contact line is curtailed. In Curve 2a of Figure 6.21, one can see that at around $t = 2$ (see lower arrow), the apex recoils and soon after, see Curve

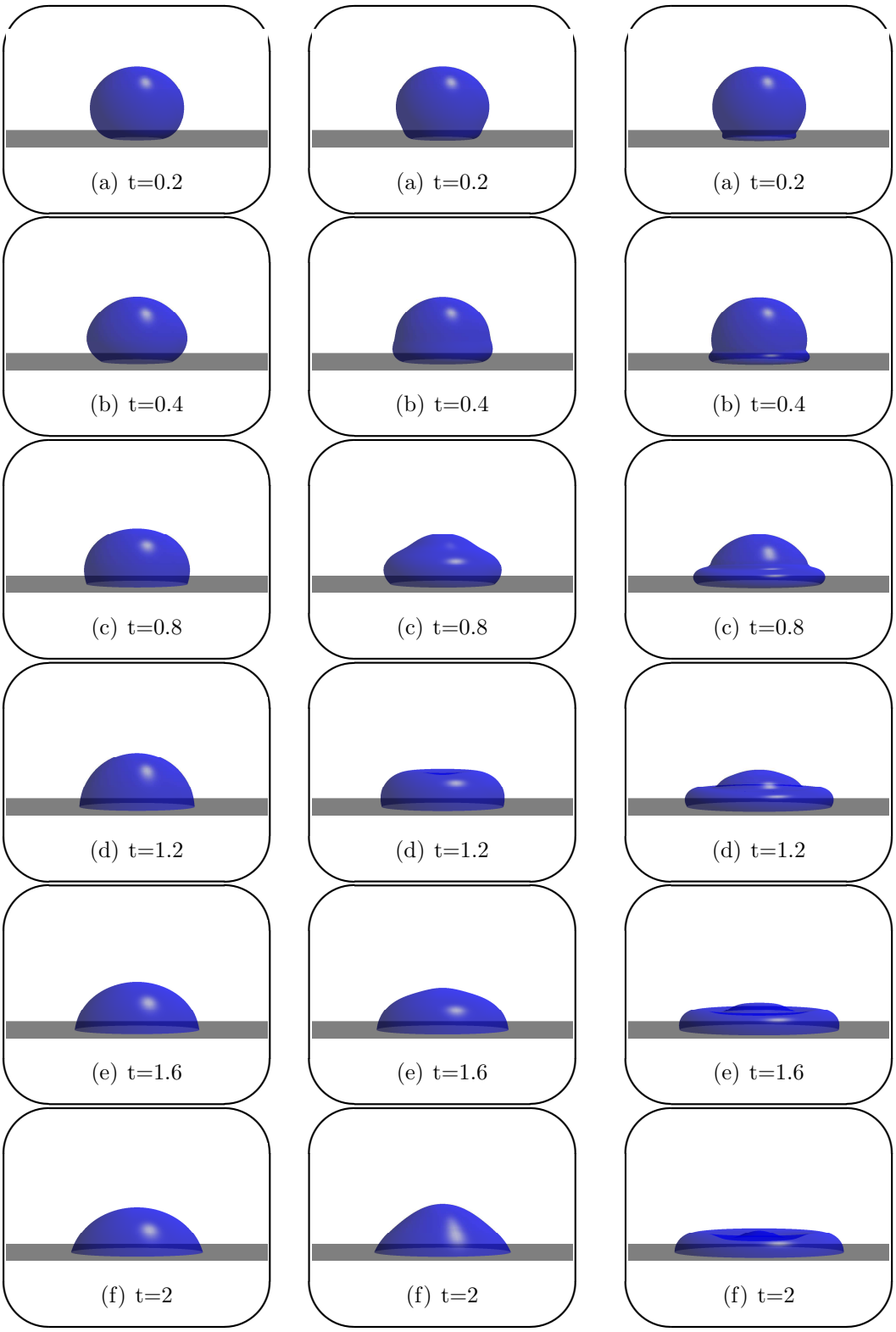

Figure 6.20: Left to right: impact and spreading of $1, 5, 25$ μm liquid drops towards an equilibrium angle $\theta_e = 60°$.

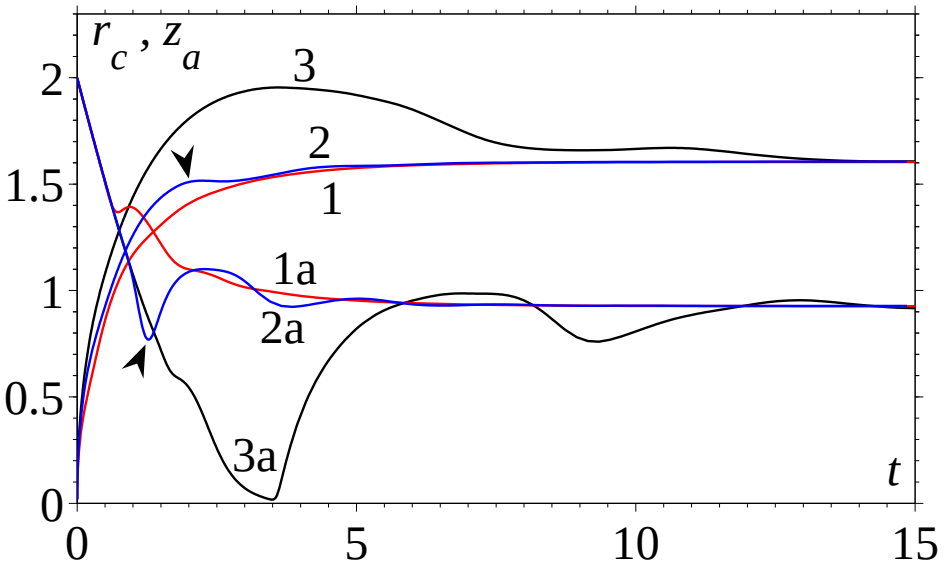

Figure 6.21: The contact line position, Curves 1-3, and apex height, Curves 1a-3a, for the impact and spreading of drops of size 1: 1 μm; 2: 5 μm; 3: 25 μm towards an equilibrium angle $\theta_e = 60°$.

2, the contact line is momentarily arrested (see upper arrow), and retreats a little, before slowly asymptoting to its equilibrium position unlike the largest drop which overshoots the position before oscillating around it.

Having considered the influence of a drop's size on its evolution we now proceed to consider the other dimensional parameter which may be easily varied for a given liquid-solid combination, namely the impact speed.

6.5.2 Impact speed

We now consider our base state drop impacting at speeds $U_0 = 3, 5, 7$ m s^{-1}. It is interesting to see from Figure 6.22 that the evolution of each drop is significantly different, despite the relatively small changes in the impact speed. This suggests that we are in a parameter regime where the influence of inertial, viscous and capillarity forces are all important, so that a relatively small change in parameter values will lead to a significant alteration in the balance of forces and have a noticeable affect on a drop's dynamics.

From Figure 6.23, as may be expected, we can see that the higher the impact speed, the larger the maximum spread and the longer it takes to reach this position. Having attained a maximum spread, the time taken for the contact line to reach its equilibrium radius, which is a slow capillary-driven motion, is roughly proportional to the distance with which the drop initially overshoots its equilibrium value.

From Curve 1a in Figure 6.23, we can see that at the lowest impact speed the apex height reaches a minimum of $z_a = 0.35$ whilst from Curve 2a we can see that an increase in impact speed of 2 m s^{-1} leads to the apex almost touching the substrate, reaching a minimum of $z_a = 0.02$. Then, one may expect that a further increase of 2 m s^{-1} in impact speed will certainly mean that the free surface will contact the solid at the apex. This is not the case. Surprisingly, the minimum apex height actually increases to $z_a = 0.03$ and occurs at a much later time, around $t = 5.5$ compared to $t = 3.5$ for the mid-speed impact. Also, in contrast to the other two lower speed impacts, the contact line achieves a maximum before the apex height reaches its minimum. It is rather strange that the further increase in impact speed does not force the apex to contact the solid. It could be that when the apex approaches the solid, the curvature in this region becomes so large that surface tension forces act to pull the free surface back upwards; but this does not seem to explain why for two different simulations the apex reaches almost the same height. A more likely explanation is that it is the bulk flow which is preventing the touching. This is certainly a subject which deserves further attention in our future work.

Having established the influence of the drop size and impact speed on the evolution of a drop, we now consider the role of various physical mechanisms by studying variations in the non-dimensional parameters.

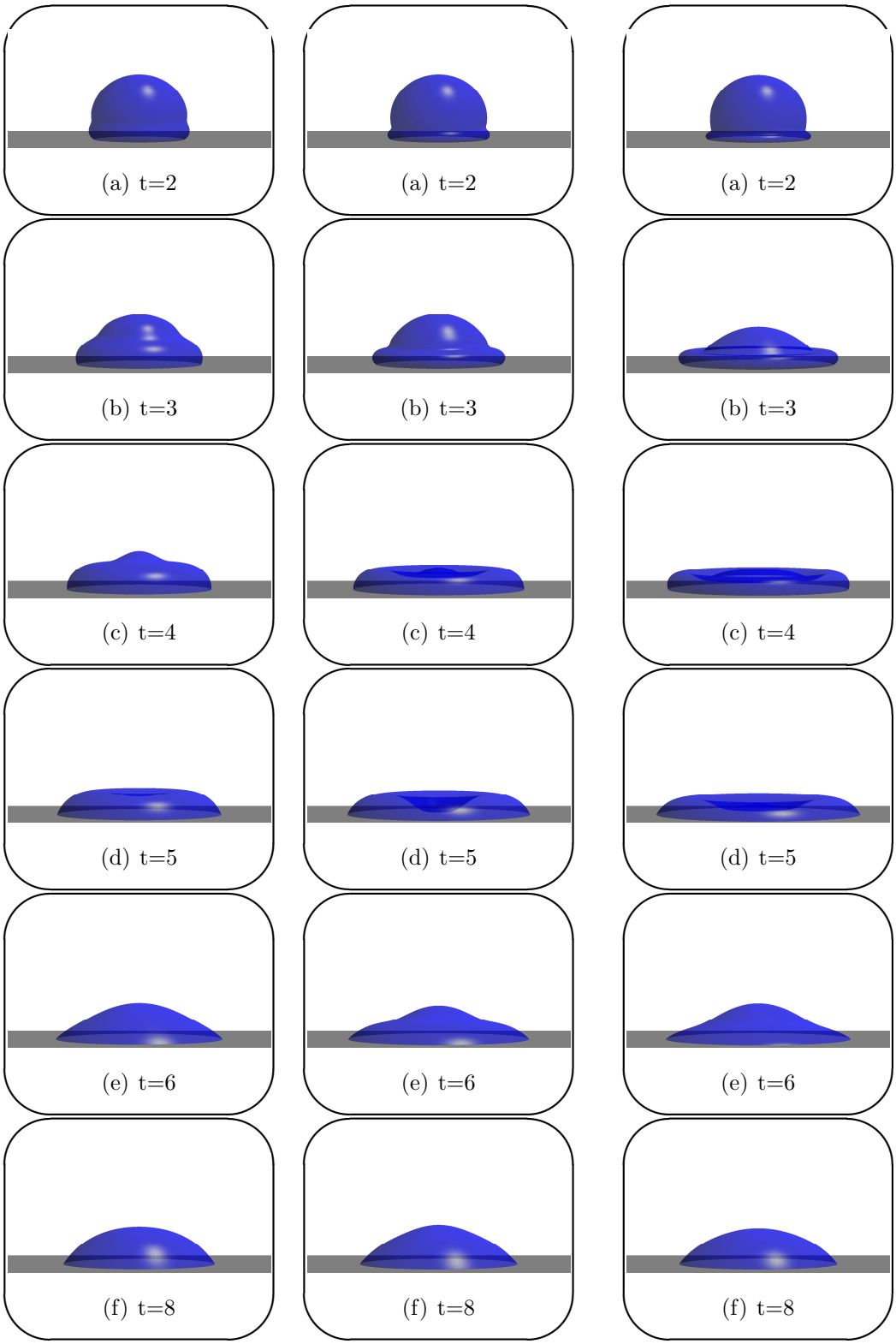

Figure 6.22: Spreading of our base state drop after impacting at $U_0 = 3,\ 5,\ 7$ m s^{-1} (left to right) on a surface characterized by $\theta_e = 60°$.

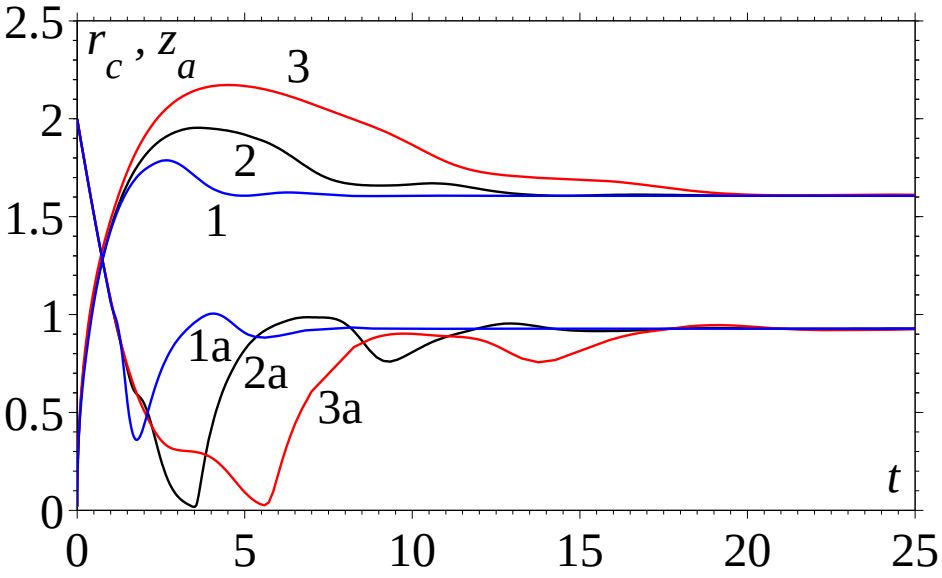

Figure 6.23: The contact line position, Curves 1-3, and apex height, Curves 1a-3a, for a drop impacting with speeds $U_0 = 3,\ 5,\ 7$ m s^{-1} ,respectively, as a function of time, on a surface characterized by $\theta_e = 60°$.

6.6 The role of the similarity parameters Re and We

The simulations so far have considered the variation of dimensional parameters so that the similarity parameters characterizing the bulk flow, namely the Weber and Reynolds numbers, have not been fixed. Here, by varying the size of the drop and its impact speed so that, firstly the Weber number remains fixed at its base value $We_b = 9$, and secondly the Reynolds number remains fixed at $Re_b = 125$, we are able to isolate their influence on a drop's dynamics and identify the importance of inertial, viscous and capillarity effects. Specifically, we consider our usual base state and compare it to a case in which the drop size is halved. Then, to obtain a fixed Weber number we need $U \to \sqrt{2}U$ so that $Re = \sqrt{2}Re_b$, whilst to fix the Reynolds number we require $U \to 2U$ and hence $We = 2We_b$.

From Figure 6.24 we see the curves of the contact line radius and apex height for the three simulations all differ. As one may expect, when inertial effects are more dominant, as is the case for higher Reynolds and Weber numbers, there is a larger spread. In

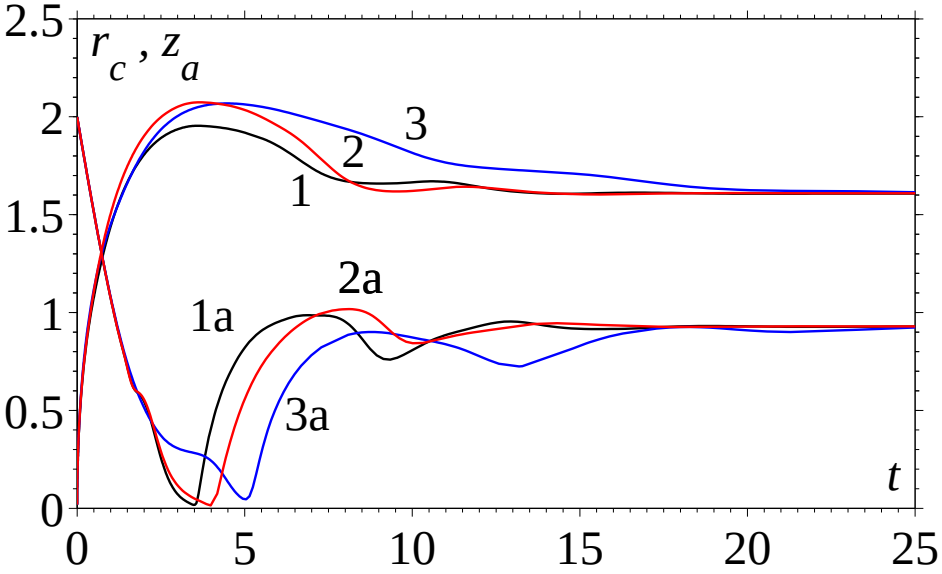

Figure 6.24: The contact line radius, Curves 1-3, and apex height, Curves 1a-3a, of three drops with $(Re, We) = 1 : (125, 9),\ 2 : (177, 9),\ 3 : (125, 18)$ as a function of time, for the base state drop landing on a surface characterized by 60°.

particular, one can see from Curve 3 in Figure 6.25 that for the higher Weber number simulation, where inertial effects become more dominant compared to capillarity ones, the free surface area is, at certain times, considerably larger than in the base state simulation, Curve 1. This is because the drop is allowed to create more free surface area, and thus spread further, before surface tension effects finally dominate and pull the drop back into a spherical cap shape.

Comparing the base state simulation, Curve 1 in Figure 6.24, to the other curves, one can see that the change in the Reynolds number, see Curve 2, begins to influence the contact line radius much sooner than the change in Weber number, see Curve 3, which only begins to affect the motion after the drop has extended past its equilibrium radius of $r_c = 1.61$. The maximum spread for the increased Weber and Reynolds numbers is similar, so we can conclude that both viscous effects, which force the drop out of its inertia-driven phase sooner, and capillarity effects, which prevent large increases in the free surface area, have a critical influence on the maximum spread of a microdrop.

Our results suggest that energy balance models for microdrop impact and spreading

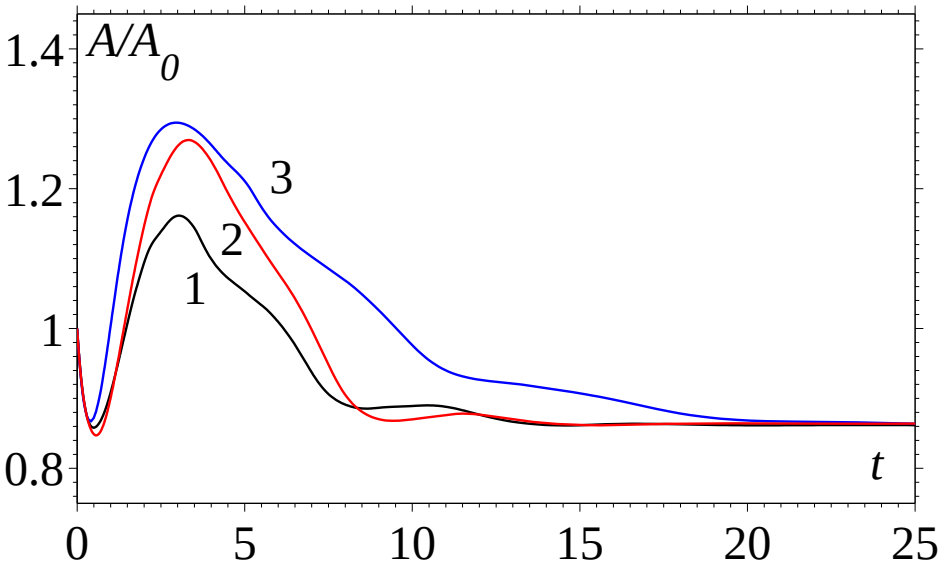

Figure 6.25: The free surface area A normalized by its initial value $A_0 = 4\pi$ as a function of time t for the impact and spreading of three drops with $1 : (Re, We) = (125, 9),\ 2 : (177, 9),\ 3 : (125, 18)$ on a surface characterized by $\theta_e = 60°$.

are unlikely to provide accurate predictions of the maximum spread of a drop. Specifically, we have shown that the balance of inertial, capillarity and viscous forces is critical to the maximum spread and hence, amongst other things, energy balance models will be hindered by a crude approximation of the viscous dissipation between impact and maximum spread.

Having determined how the bulk parameters affect a drop's evolution, we now consider the solid surface's influence.

6.7 Influence of wettability

The wettability was seen to have no influence on the early stages of our base state drop's spreading; however, it determines the final shape of the drop and hence must become dominant at least during the latter stages of spreading. We consider the impact and spreading of our base state drop on three surfaces, characterized by the equilibrium contact angle which a free surface forms with them, and we shall refer to them as a wetting surface ($\theta_e = 10°$), a partial wetting surface ($\theta_e = 60°$) and a hydrophobic surface ($\theta_e = 110°$).

In Figure 6.26 one can see that, as expected, during the initial phase of spreading, roughly until $t = 1.2$, the drop shapes are graphically indistinguishable. Noticeably, as can be seen in both Figure 6.26 and Figure 6.27, although the wettability of the substrate eventually begins to alter the position of the contact line; this is not felt by the apex until a much later time. In fact, the initial fall of the apexes are very similar and it is only upon recoil of the apex, around $t = 4$, that their paths begins to differ. When the drops begin to recoil, their motions differ quite significantly; notably, only the contact line of the drop on the hydrophobic substrate, see Curve 3, recoils past its equilibrium radius and performs significant oscillations. The same drop also manages to attain a greater height on recoil than its initial position, suggesting that on a slightly more hydrophobic surface, the drop may rebound.

The drop on the wetting surface takes the longest to reach the position of maximum spread: one can see from Curve 1 in Figure 6.27 that the contact line is momentarily arrested around $t = 10$, after which the drop's evolution enters a new, capillary-driven, phase of wetting which occurs on a much longer time scale. This behaviour is in qualitative agreement with experimental findings (e.g. Dong *et al.*, 2007). Interestingly, it is the drop on the partially wetting surface which attains its equilibrium position first.

6.7.1 Rebound of a drop off a solid surface

In Figure 6.28 we can see that on a surface characterized by $\theta_e = 130°$, the base state drop impacts, spreads and then rebounds off the substrate.

The radius of the contact line and the apex height are Curve 4 and Curve 4a, respectively, in Figure 6.26, which are seen to be similar to Curves 3,3a for the $\theta_e = 110°$ case until the position of maximum spread, at which point the drop on the more hydrophobic substrate dewets the solid much faster. By comparing the images at $t = 3$ and $t = 4$ in Figure 6.28 one can see that this is caused by a jet emanating from the apex region

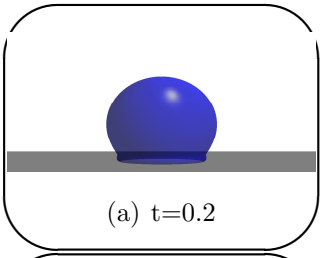

(a) t=0.2

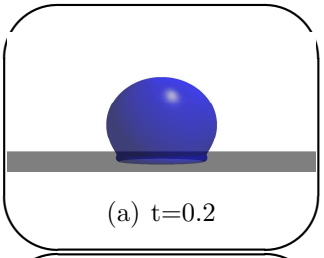

(a) t=0.2

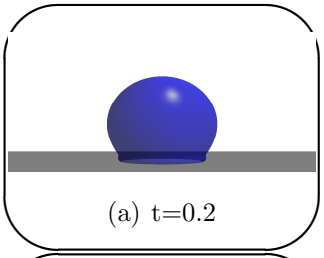

(a) t=0.2

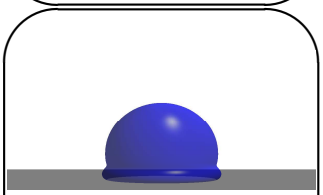

(b) t=0.4

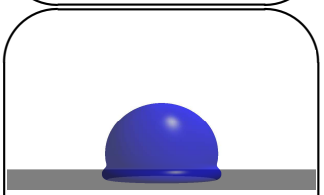

(b) t=0.4

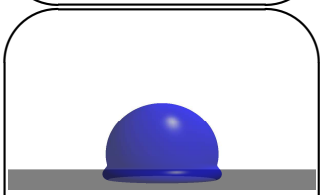

(b) t=0.4

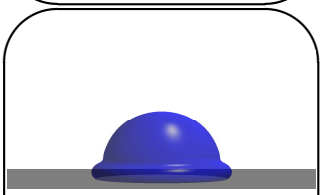

(c) t=0.6

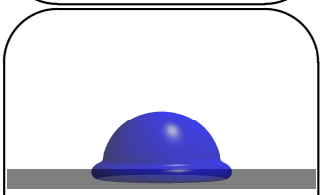

(c) t=0.6

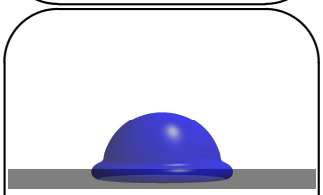

(c) t=0.6

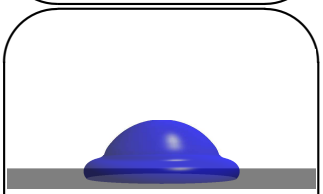

(d) t=0.8

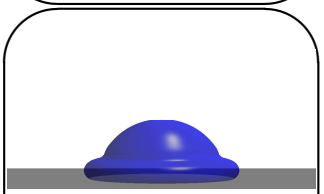

(d) t=0.8

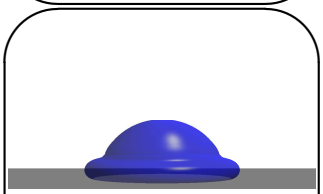

(d) t=0.8

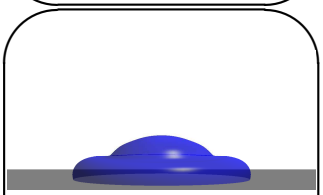

(e) t=1.2

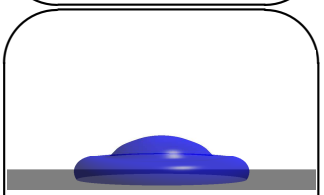

(e) t=1.2

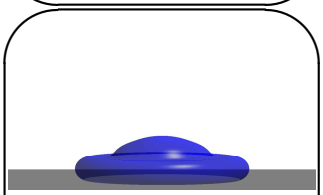

(e) t=1.2

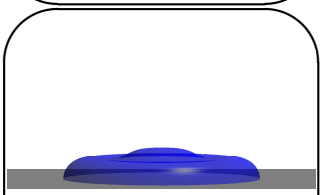

(f) t=1.6

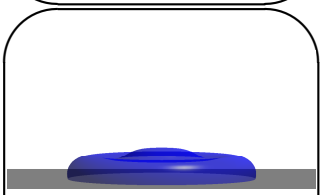

(f) t=1.6

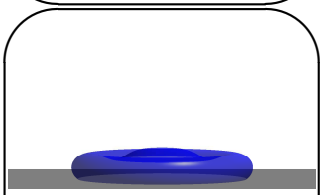

(f) t=1.6

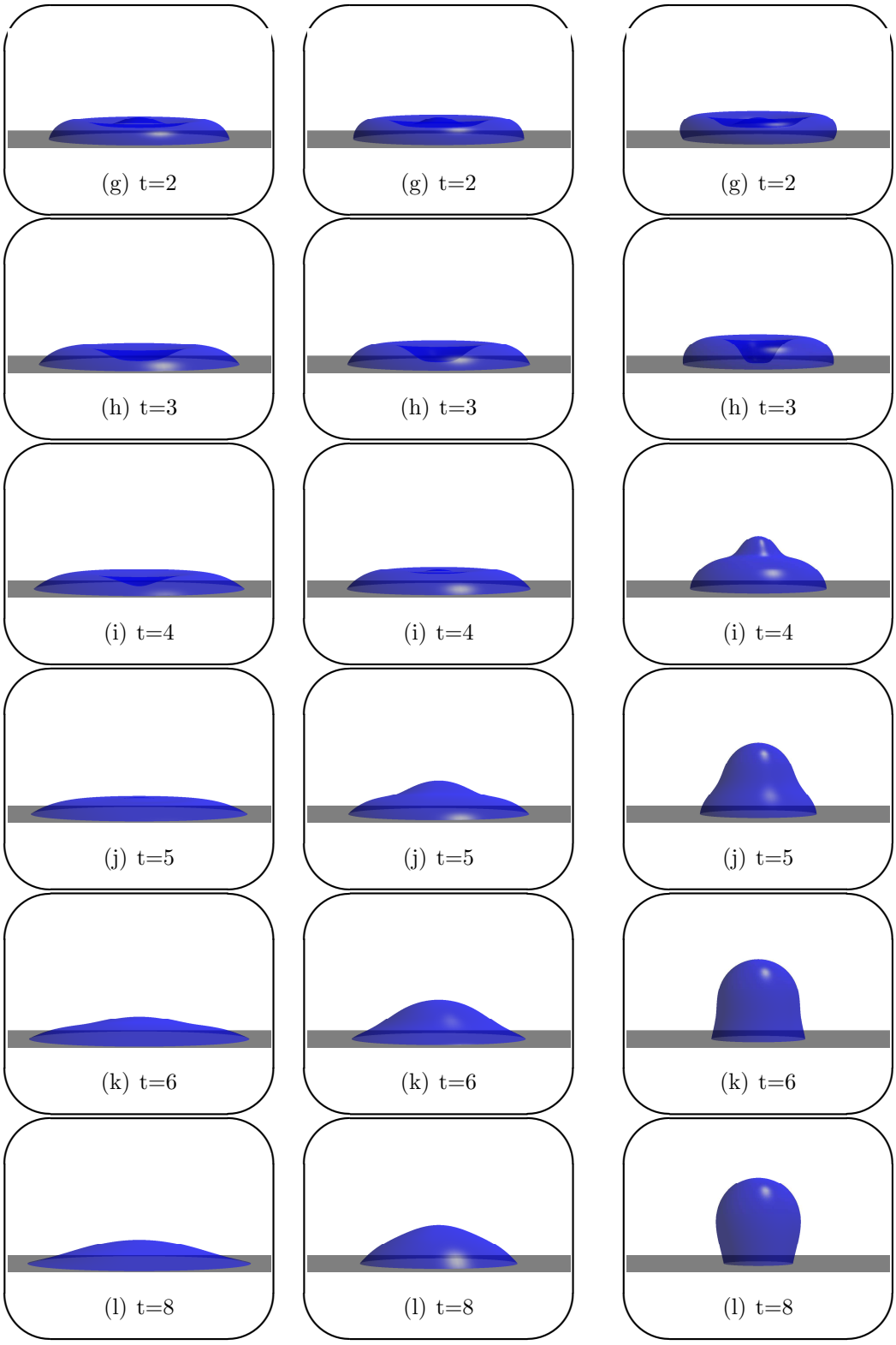

Figure 6.26: Impact and spreading of our base state drop on three surfaces characterized by (left to right) $\theta_e = 10°, 60°, 110°$.

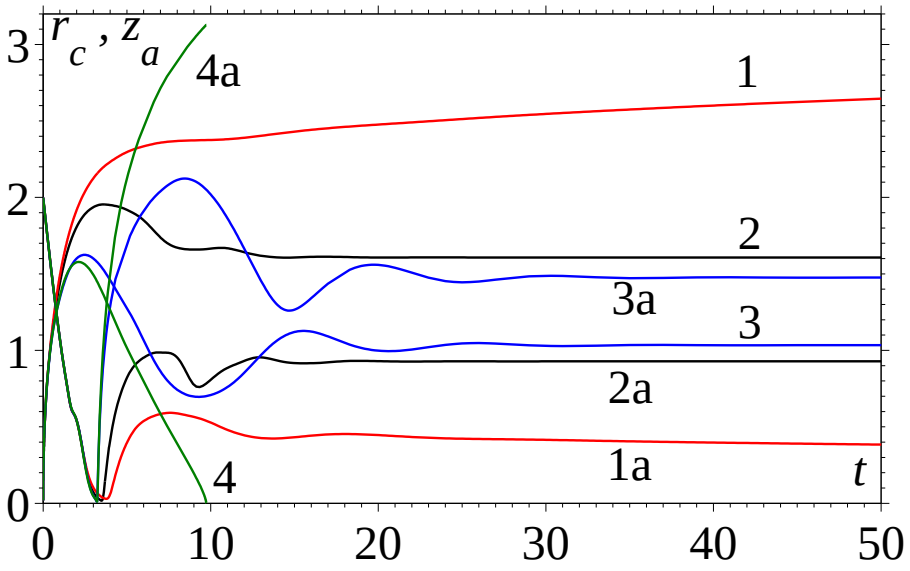

Figure 6.27: The contact line radius, Curves 1-4, and apex height, Curves 1a-4a, of the drop as a function of time, for the base state drop landing on surfaces 1-4 characterized by $\theta_e = 10°, 60°, 110°, 130°$.

which pulls fluid towards the axis of symmetry. The simulation has to be terminated as the drop is about to leave the substrate; extending the numerical platform to account for such behaviour is certainly viable. It is of interest to see that the drop's final shape is pear shaped and, indeed, this shape has been observed experimentally (Mao *et al.*, 1997) and is seen to lead to the pinch-off of the bottom section and/or large oscillations after rebound.

6.7.2 Summary of the influence of wettability

We have shown that the wettability of a substrate has a huge influence on a drop's dynamics after the early, inertia-driven, stages of wetting and that microdrop impact, spreading and rebound can occur on moderately hydrophobic surfaces. Having shown that the effects of capillarity dominate in the latter stages of spreading, we proceed to investigate the role of the interface formation parameters on a drop's dynamics.

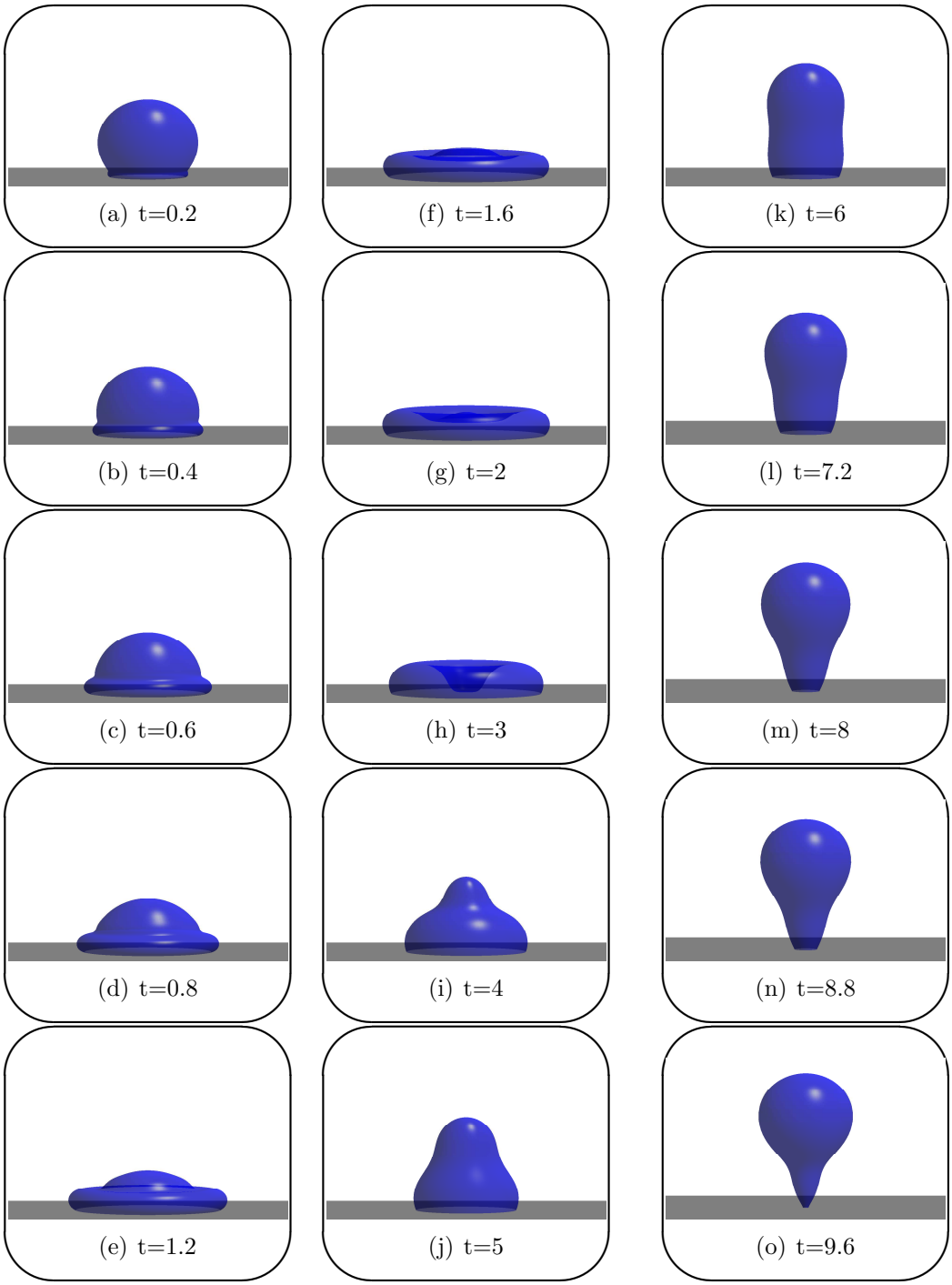

Figure 6.28: Impact, spreading and rebound of our base state drop on a surface characterized by $\theta_e = 130°$.

6.8 The role of the interface formation model's parameters

So far, we have used the estimates obtained in Blake & Shikhmurzaev (2002) for the values of the interface formation model's parameters. However, experiments on drop impact and spreading could themselves be used to provide accurate estimates for these parameters. Here we shall develop this idea. Rather than attempt to vary all the parameters in the model, we make the same assumptions used in Blake & Shikhmurzaev (2002), which, for a particular liquid-solid-gas combination, leaves the relaxation time τ and the (dimensional) equilibrium surface density on the liquid-gas interface $\hat{\rho}^s_{Ge}$, to vary. The non-dimensional parameters Q and ϵ are linearly dependent on the value of τ whilst the dimensional value $\hat{\rho}^s_{Ge}$ is used to determine ρ^s_{Ge} and hence $\lambda = 1/(1 - \rho^s_{Ge})$. The liquid-gas interface is rarefied so that it is only useful to consider $\rho^s_{Ge} < 1$, whilst the value of the relaxation time is not as clearly limited and has been estimated by experiments using the oscillating jet method to be as high as $\tau = 6 \times 10^{-4}$ (Kochurova & Rusanov, 1981), so that it is certainly reasonable to consider at least a factor of ten increase/decrease in its value.

The curves in Figure 6.29 demonstrate the significant effect which varying the relaxation time, and hence ϵ and Q, by a factor of ten has on the drop's dynamics. The smaller the relaxation time, the further the drop will spread. This can be understood by noting that as $\epsilon \to 0$, the interface tends to an equilibrium state quicker and hence, from the Young equation, the contact angle takes its equilibrium value sooner. Then we can see that our findings are in agreement with the results of previous studies which have shown that by setting $\theta_d = \theta_e$ rather than using a contact angle formula, which is simply a limiting case of what we have considered here, leads to a larger prediction of the spread factor (Pasandideh-Fard *et al.*, 1996). Conversely, a larger relaxation time results in a smaller maximum spread but an enhancement in the oscillations of the apex. Such large deviations in the contact line radius and apex height obtained for different parameter

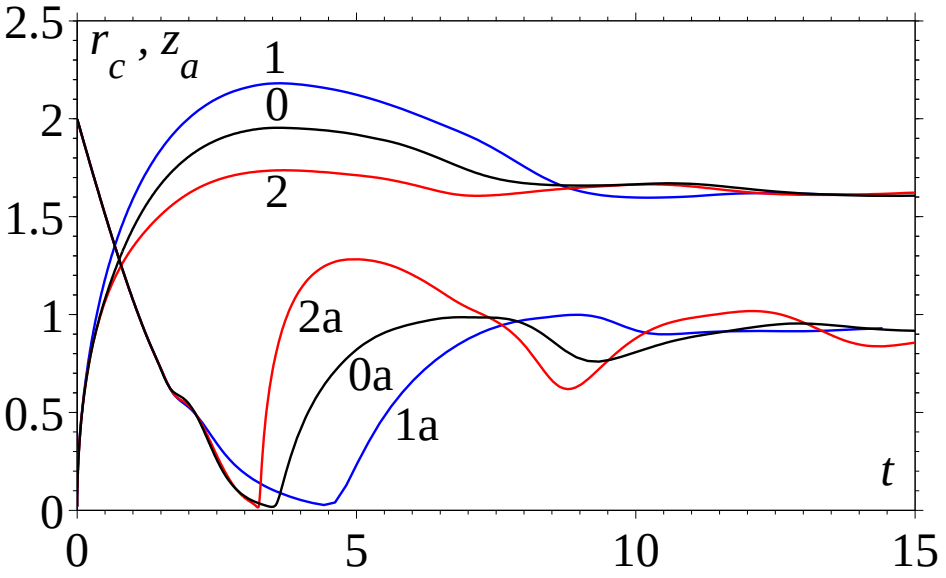

Figure 6.29: Effect of varying the relaxation time about its base state on the radius of the contact line, Curves 1-3, and the apex height, Curves 1a-3a, as a function of time. 0: base state ($\tau = \tau_b$), 1: $0.1\tau_b$, 2: $10\tau_b$.

values suggest that drop impact and spreading phenomena provide a good situation from which to gain accurate estimates on the relaxation time.

We now vary the equilibrium surface density on the liquid-gas interface around its base state of $\rho^s_{Ge} = 0.6$. We can see in Figure 6.30, from Curve 3 and Curve 4, that taking values of $\rho^s_{Ge} = 0.4, 0.8$ does slightly alter the drop's motion. An alternative approach is to look to vary the parameter λ by a factor of ten, so that $\rho^s_{Ge} = 0.96$, and, from Curves 5, 5a we can see that this creates a much larger deviation in the drop's motion, to such an extent that the apex of the drop touches the solid surface and the simulation halts. Although our code cannot currently simulate the subsequent behaviour, it has been observed experimentally (Renardy *et al.*, 2003) that the dry out of the centre can lead to a bubble becoming entrapped upon recoil. This qualitative prediction could be checked experimentally and would enable bounds on the parameter ρ^s_{Ge} to be established *independently* of the parameter τ. This result is rather intriguing and deserves further attention, as it goes against the prediction of the small capillary number speed-angle relationship (5.7) that varying λ will have the same effect as varying ϵ^{-1}.

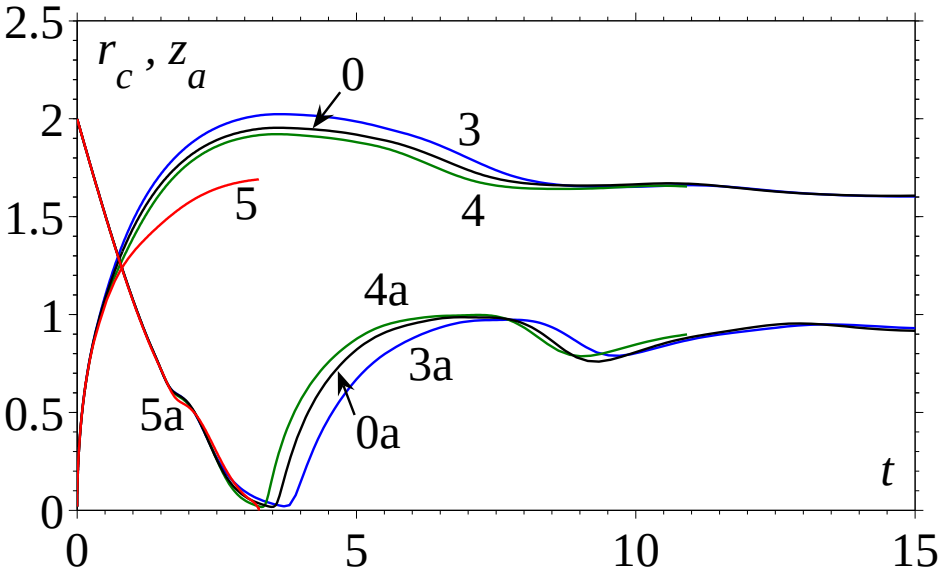

Figure 6.30: Effect of varying the parameter ρ^s_{Ge} about its base state on the radius of the contact line (Curves 0, 3-5) and the apex height (Curves 0a, 3a-5a) as a function of time. 0: base state (ρ^s_{Ge}=0.6), 3: ρ^s_{Ge}=0.4, 4: ρ^s_{Ge}=0.8, 5: ρ^s_{Ge}=0.96 ($\lambda = 10\lambda_b$).

Having established the influence of some of the parameters of the interface formation model on a drop's evolution, we now show how our model may be extended to incorporate additional physical phenomena.

6.9 Hysteresis of the dynamic contact angle

Experimentally, it has been established that the angle at which a contact line begins to advance may differ significantly from the angle at which it starts to recede: i.e. the contact angle exhibits hysteretic behaviour (Petrov *et al.*, 2003). This effect can be used to pin the contact line in its position of maximum spread and hence inhibit the subsequent oscillations, which may be detrimental in a particular application. Various physical phenomena may create this hysteresis (Shikhmurzaev, 2007): here we consider it to be caused by the appearance of a microscopic residual film which is created when the contact line begins to recede. This phenomenon has been experimentally observed when the contact line dewets a partially wettable surface, for example in Lam *et al.* (2001).

In the absence of a residual film, the contact line immediately begins to retreat after reaching its maximum spread and, hence, its equilibrium contact angle. However, when the influence of the residual film is included, the contact line will not begin to retreat until its receding contact angle $\theta_r < \theta_e$ is attained. The value of θ_r is determined by the surface tension of the residual film σ_{SG}, which enters the Young equation (3.27). When the contact line finally begins to retreat, there is a mass flux $-\rho^s_{res}U_c$ out of the contact line to form the microscopic film.

The residual film has a second affect on the drop's evolution. The contact line will usually oscillate around an equilibrium radius and, as a result, the contact line may advance over a pre-wet substrate. Then, it will encounter an additional surface tension σ_{SG} and a flux of surface mass into the contact line which we shall assume is equal to $\rho^s_{res}U_c$.

During the period in which the contact angle is changing from the value at which it advances to the one at which it will recede, or vice-versa, the Young equation (3.27) is replaced with a condition which pins the contact line. When the critical value of the contact angle required for the contact line to become unpinned is achieved, the Young equation is re-instated and the contact line begins to move.

In Figure 6.31 we show the radius of the contact line and the apex height as a function of time for three different sets of parameter values: $(\sigma_{SG}, \rho^s_{res}) = (0.24, 0.24)$, $(0.48, 0.24)$ and $(0.24, 0.48)$, with $\sigma_{SG} = 0.24, 0.48$ corresponding to $\theta_r = 42°, 12°$. These are compared to the usual base state for which $\theta_r = \theta_e$ and $\rho^s_{res} = 0$. There are three qualitatively different curves, with the value of ρ^s_{res} seen to have a negligible influence. In the case of the smallest receding contact angle, see Curve 2, the drop's contact angle never attains the critical value required to recede and hence remains pinned in its position of maximum spread. It is interesting to note that in this case, because the contact line is pinned so that the region dissipates less energy than usual, more energy becomes available to power the oscillations in the apex height, which become more pronounced than in the base state.

This allows the possibility of determining bounds of hysteresis on a given substrate by measuring the height of the drop as a function of time. For the $\theta_r = 42°$ case, after being pinned for a short period of time, the drop's contact angle passes the critical receding value so that the contact line retreats. The contact line never reaches the dry substrate again ($r > 1.98$) and spreads to a larger equilibrium radius than usual as there is now an additional contribution to the Young equation from the surface tension of the pre-wet liquid-gas interface.

In Figure 6.31 the speed-angle relationships near to the origin are shown. During the initial advance of the contact line, all four curves approach $Ca_c = 0$ along the same path. However, at this point the curves bifurcate with only the base state curve returning along its original path. One can see that in the case of $\theta_r = 12°$ the contact angle only drops to around $\theta_d = 15°$ so that the contact line remains pinned, whilst for the $\theta_r = 42°$ cases the contact line eventually begins to move, although this is now along a new path which is slightly affected by the value of ρ^s_{res}.

In this section we have demonstrated that additional physical phenomena may be incorporated into the interface formation model in a regular way and that effects such as the hysteresis of the dynamic contact angle can be predicted. Notably, a method for determining the critical values for the properties of a microscopic residual film, that cause a contact line to become pinned at a position of maximum spread, has been established.

6.10 Summary

We have used our numerical platform to probe the dynamics of microdrops which impact and spread on surfaces of constant wettability. It was shown that the interface formation model does not predict unphysical effects, such as the infinite acceleration of a drop placed on a solid surface, which are inherent in the conventional model. Using the interface formation model, we have observed non-uniqueness of the speed-angle relationship and

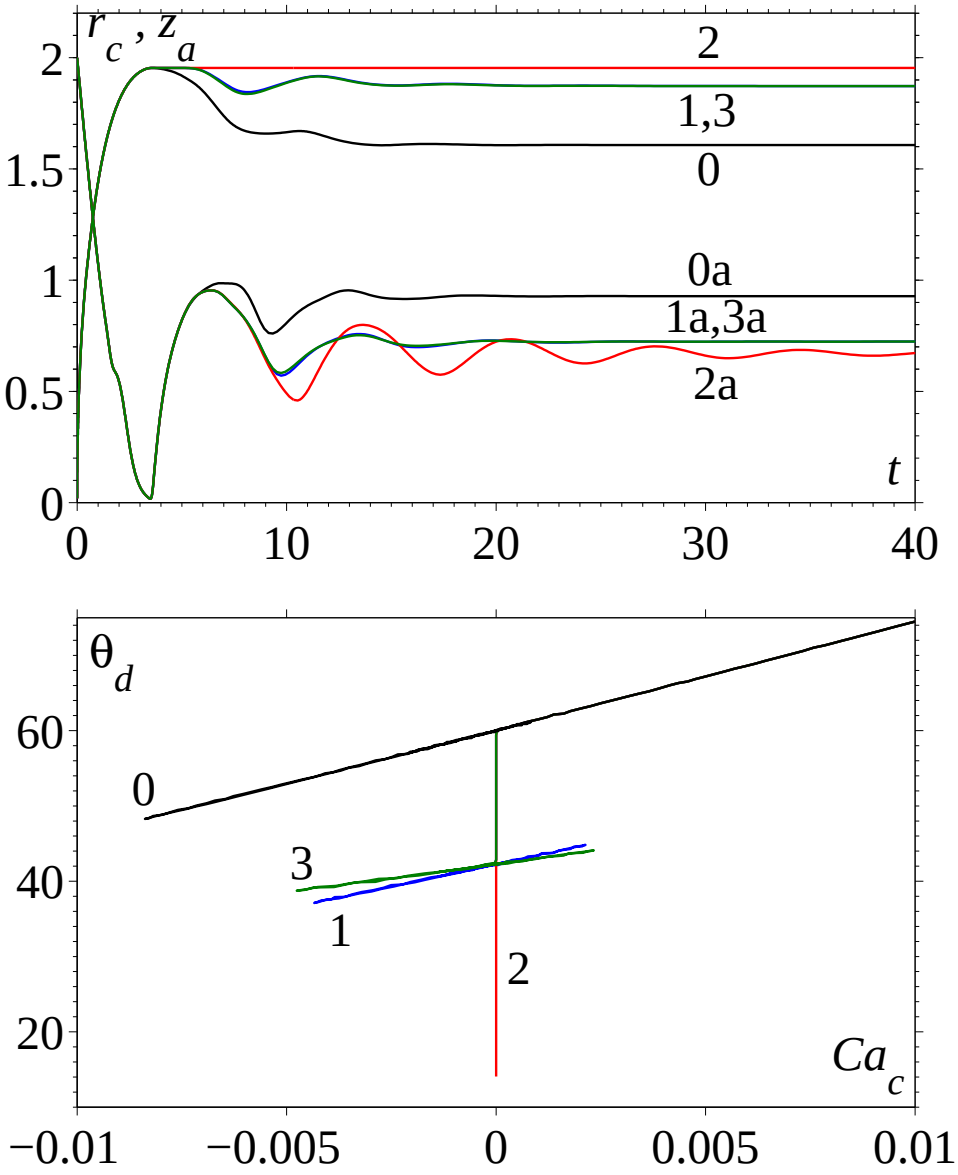

Figure 6.31: Top: plot showing the radius of the contact line, Curves 0-3, and the apex height, Curves 0a-3a, as a function of time with 0: $(\sigma_{SG}, \rho^s_{res})$= (0,0), 1: (0.24,0.24), 2: (0.48,0.24), 3: (0.24,0.48). Bottom: plot showing the relationship between the capillary number based on the contact-line speed and the dynamic contact angle for the four simulations.

have found that geometric wetting occurs for a longer period than previously assumed. The role of a range of parameters was investigated and their effect on physical phenomena, such as maximum spread or possible rebound, has been established. This leaves other additional parameters, perhaps most notably the viscosity of the fluid and the surface tension of the liquid-gas interface, as the subject for future work.

Our next aim is to simulate the impact and spreading of drops on surfaces of variable wettability, but, before doing so, we must consider how the concept of wettability is incorporated into a model. We consider this in the next chapter by looking at a simplified problem of shear flow over a surface of varying wettability before, in the chapter after that, considering microdrop impact and spreading on such a surface.

Chapter 7

Flow over surfaces of varying wettability

Having shown that our numerical platform produces significant new results for the impact and spreading of microdrops on homogeneous substrates, our attention turns to spreading on surfaces of variable wettability. Before tackling the full problem of drop impact and spreading on such a surface, we first have to consider how variations in wettability can be incorporated into a continuum model. To do so, we study the far simpler problem of shear flow over a solid of variable wettability. We apply the interface formation model to this situation without any ad-hoc changes and show that it describes well the results of molecular dynamics simulations. Having established this, we will be able to incorporate transitions in wettability into our model for spreading drops without any additional complexity.

First we consider a plane-parallel shear flow over a smooth solid surface that encounters a change in wettability, see Figure 7.1. After, we simulate flow over a substrate which is intermittently patterned with different wettabilities; the case considered by molecular dynamics simulations (Priezjev *et al.*, 2005; Qian *et al.*, 2005).

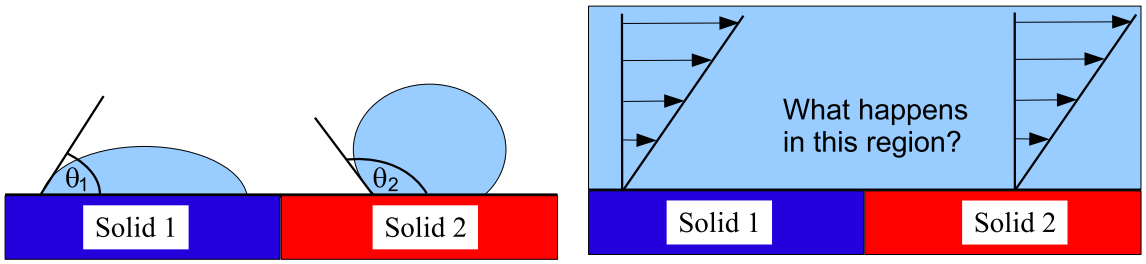

Figure 7.1: Left: Solid 1 is considered more wettable than Solid 2. Right: how will the change in wettability of the substrate affect the shear flow?

7.1 Flow over a surface with a single transition in wettability

Consider the steady flow of an incompressible Newtonian liquid passing over a stationary flat solid surface. The liquid is driven over the solid by a plane-parallel shear of magnitude S in the far field. We consider the bulk flow to be described by the steady Navier-Stokes equations (2.1)–(2.2) with the boundary conditions on a solid surface from the interface formation theory (2.17)–(2.22). The interface formation equations were derived for solid surfaces of uniform wettability, i.e. for a constant value of the equilibrium surface density ρ^s_{Se}. As previously discussed in §2, this constant is related to the wettability of the substrate and can be expressed in terms of the equilibrium contact angle that a liquid drop's free surface would form on it (see (7.12) below).

In order to model variable wettability, we allow the equilibrium surface density to be a smooth function of position on a solid surface. In particular, we consider a transition region in which the equilibrium surface density varies smoothly, from its value ρ^s_{1e} on solid 1 to value ρ^s_{2e} on solid 2, across a finite distance l. Then we may consider the equilibrium surface density to take the form

$$\rho^s_{Se} = \tfrac{1}{2}\left(\rho^s_{1e} + \rho^s_{2e}\right) + \tfrac{1}{2}\left(\rho^s_{2e} - \rho^s_{1e}\right)\tanh\left(x/l\right), \tag{7.1}$$

where x is a Cartesian coordinate in the plane of the solid surface.

To account for a solid of variable wettability, we have to modify the generalized Navier condition (2.17) and the Darcy type equation (2.21) by replacing

$$\nabla\sigma_S^s \to \nabla\sigma_S^s + \rho_S^s F^s, \quad \text{where} \quad F^s = \frac{\gamma\nabla\rho_{Se}^s}{\rho_{Se}^s}. \tag{7.2}$$

The reaction force F^s acts on the liquid-solid interfacial layer from the solid surface and by balancing gradients of the equilibrium surface tension $\sigma_{Se}^s = \sigma_S^s\left(\rho_{Se}^s\right)$, ensures the existence of a state of equilibrium.

The flow is plane-parallel in the (x, y)-plane of a Cartesian coordinate system, the origin of which is at the centre of the transition region, and the constant shear of magnitude S in the far field gives

$$\mathbf{u} \to S\ \mathbf{ij}\cdot\mathbf{r} \quad \text{as} \quad \mathbf{r} \to \infty, \tag{7.3}$$

where $\mathbf{i}$ and $\mathbf{j}$ are unit vectors in the x and y directions and $\mathbf{r}$ is the radius-vector.

For this problem it is convenient to non-dimensionalize our equations using

$$U = \mu^{-1}\sigma, \quad L = US^{-1}, \quad P = \mu S, \quad \sigma, \quad \rho_{(0)}^s$$

as the scales for velocities, length, pressure, surface tension and surface density. Then in the bulk one has

$$\nabla\cdot\mathbf{u} = 0, \qquad Re\left(\mathbf{u}\cdot\nabla\mathbf{u}\right) = -\nabla p + \nabla^2\mathbf{u}, \tag{7.4}$$

whilst on the surface, where we use the notation u and v for tangential and normal components of velocity,

$$\left(\frac{\partial u}{\partial y} + \frac{\partial v}{\partial x}\right) + \frac{1}{2}\left(\frac{d\sigma_S^s}{dx} + \frac{\lambda\rho_S^s}{\rho_{Se}^s}\frac{d\rho_{Se}^s}{dx}\right) = \bar{\beta}u, \tag{7.5}$$

$$v = Q\left(\rho_S^s - \rho_{Se}^s\right), \tag{7.6}$$

$$\epsilon\frac{d\left(\rho_S^s v_{St}^s\right)}{dx} = -\left(\rho_S^s - \rho_{Se}^s\right), \tag{7.7}$$

$$v^s_{St} = \tfrac{1}{2}u + \bar{\alpha}\left(\frac{d\sigma^s_S}{dx} + \frac{\lambda\rho^s_S}{\rho^s_{Se}}\frac{d\rho^s_{Se}}{dx}\right), \tag{7.8}$$

$$\sigma^s_S = \lambda(1-\rho^s_S), \tag{7.9}$$

$$\rho^s_{Se} = \tfrac{1}{2}\left(\bar{\rho}^s_{1e} + \bar{\rho}^s_{2e}\right) + \tfrac{1}{2}\left(\bar{\rho}^s_{2e} - \bar{\rho}^s_{1e}\right)\tanh\left(x/\bar{l}\right), \tag{7.10}$$

and in the far field

$$u \to 1\ , v \to 0 \ \text{ as } \ x^2+y^2 \to \infty. \tag{7.11}$$

Here

$$Re = \frac{\rho\sigma^2}{S\mu^3},\ \epsilon = S\tau,\ \bar{\beta} = \frac{\beta\sigma}{\mu^2 S},\ Q = \frac{\rho^s_{(0)}\mu}{\rho\tau\sigma},\ \bar{\alpha} = \frac{\alpha S\mu^2}{\sigma},$$

$$\bar{l} = \frac{\mu S l}{\sigma},\ \lambda = \frac{\gamma\rho^s_{(0)}}{\sigma},\ \bar{\rho}^s_{ie} = \frac{\rho^s_{ie}}{\rho^s_{(0)}} \qquad (i=1,2).$$

Given that the equilibrium contact angle θ is used as a measure of the wettability of a solid substrate, it is convenient to eliminate $\bar{\rho}^s_{ie}$ in favour of θ_i using the Young equation (2.24) and (7.9):

$$\bar{\rho}^s_{ie} = 1 + \lambda^{-1}\cos\theta_i \qquad (i=1,2). \tag{7.12}$$

Hereafter we will refer to the portion of the solid substrate with equilibrium contact angle θ_1 and θ_2 as 'solid 1' and 'solid 2', respectively.

The analysis of experiments in Blake & Shikhmurzaev (2002) provide estimates for the magnitude of phenomenological constants in the interface formation model's equations. Using these estimates and taking $\rho \sim 10^3$ kg m^{-3}, $\mu \sim 10^{-2} - 10$ kg m^{-1} s^{-1}, $\sigma \sim 10^{-2} - 10^{-1}$ N m^{-1}, $S \sim 10^3 - 10^5$ s^{-1} and $l \sim 10^{-8} - 10^{-7}$ m one arrives at a typical

range of values for the magnitudes of the non-dimensional groups

$$Re \sim 10^{-9} - 10^{3}, \qquad \epsilon \sim 10^{-6} - 10^{-2}, \qquad \bar{\beta} \sim 10^{1} - 10^{7},$$
$$Q \sim 10^{-3} - 10^{3}, \qquad \bar{l} \sim 10^{-6} - 10^{1}, \qquad \lambda \sim 2 - 10^{2},$$
$$\theta_i \in [0^\circ, 180^\circ] \qquad (i = 1, 2).$$

As mentioned earlier, it is the double limit $\bar{\beta}^{-1} \to 0,\ \epsilon \to 0$ applied to equations (7.5)–(7.9) that results in the no-slip condition and hence all effects associated with deviation from the classical no-slip are at leading order in these parameters.

7.1.1 Results

Problem (7.4)–(7.11) was solved numerically using the finite element method. The code used has been previously described in §4 for a more complex problem and hence the details of the numerics are omitted. A full parametric investigation may be found in Sprittles & Shikhmurzaev (2007); here we outline a few of the main results.

Figure 7.2 shows the streamlines of the flow for the case where solid 1 is more hydrophillic than solid 2; the values of the dimensionless constants are given in the figure caption. As one can see, when the outer flow drives the fluid from a hydrophillic to a hydrophobic zone, there appears a normal flux from the surface phase into the bulk. It is noteworthy that, as shown in Figure 7.2, the vertical component of the bulk velocity is nonzero at $y = 0$, whereas for the classical Navier condition with different coefficients of sliding friction one has $v = 0$ at $y = 0$ and the normal component of velocity away from the solid appears solely due to the disturbance of the tangential flow at $y = 0$. This occurs due to fluid particles forming the interface being driven by the outer flow towards the region of lower equilibrium surface density, so that one has $\rho_S^s > \rho_{Se}^s$ in the disturbed equilibrium, and hence, according to (7.6), $v > 0$.

Importantly, it can be seen in Figure 7.2 that the flux out of the surface phase occurs

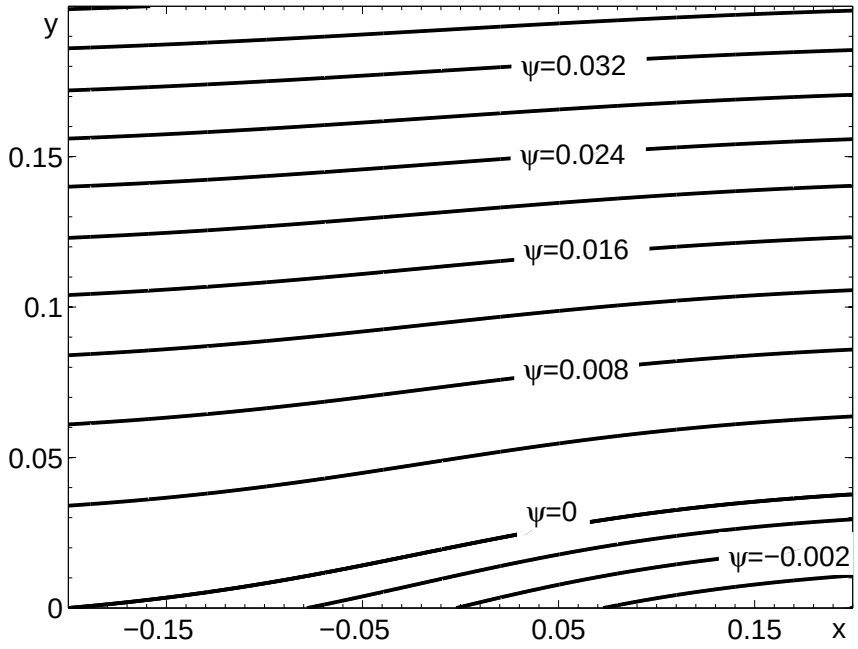

Figure 7.2: Streamlines for flow over a single transition in wettability, centred at $x = 0$, in which values of the streamfunction ψ are given. Parameter values $Re = 0.01$, $\epsilon = 0.01$, $\bar{\beta} = 10$, $Q = 100$, $\bar{l} = 0.1$, $\lambda = 10$, $\theta_1 = 10^\circ$ and $\theta_2 = 100^\circ$.

both in the hydrophillic ($x < 0$) and hydrophobic ($x > 0$) regions of the solid and extends itself well outside the transition zone. When solid 1 is more hydrophobic than solid 2 one observes the reverse effect, with the normal component of velocity directed towards the surface, corresponding to a flux into the surface phase. Once again this occurs on both sides of the transition region.

It is interesting to consider what causes the slip on the solid surface to vary. In other words, do the main variations in the terms on the left hand side of the generalized Navier condition (7.5), come from gradients in surface tension or from changes in the shear stress acting on the interface? Curve 1 in Figure 7.3 shows the distribution of the deviation of the tangential stress (the first term on the left-hand side in (7.5)) from that generated by the far field $T = [\partial u/\partial y + \partial v/\partial x - 1]$, across this region. Importantly, there are now contributions to the tangential stress from both $\partial u/\partial y$ and $\partial v/\partial x$ since the latter becomes nonzero due to variation in the normal velocity along the surface as a result of the

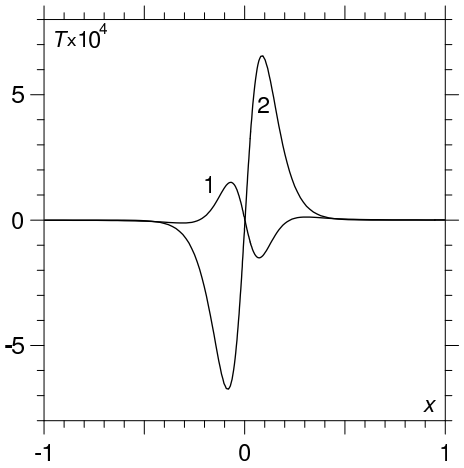

Figure 7.3: Variation of the 'generators' of slip (the terms on the left hand side of the generalized Navier condition (7.5)) in response to a variation in the solid surface wettability. In curve 1, $T = [\partial u/\partial y + \partial v/\partial x - 1]$ whilst in Curve 2, T=$[d\sigma_S^s/dx + (\lambda\rho_S^s/\rho_{Se}^s)\, d\rho_{Se}^s/dx]\,/2$. Results are obtained for parameter values $Re = 0.01$, $\epsilon = 0.01$, $\bar{\beta} = 100$, $Q = 1$, $\bar{l} = 0.1$, $\lambda = 20$, $\theta_1 = 10°$, $\theta_2 = 100°$.

spatially nonuniform desorption (adsorption) process caused by the deviation of ρ_S^s from its local equilibrium value. As discussed earlier, this effect could follow neither from the standard Navier condition nor from any of its generalizations if the interface formation process and the associated mass exchange between the interface and the bulk are not taken into account. The deviation of the second term on the left-hand side of (7.5) from zero is shown as Curve 2 in Figure 7.3. One can see that it is the variation in this second term in (7.5) that dominates and hence it is the imbalance between the surface tension gradient and the tangential surface force caused by shear flow that is mainly responsible for a variation in slip on the surface as its wettability changes.

To determine the magnitude of the effect we calculate the integral of the normal velocity, i.e. the total flux out of the surface phase per unit time

$$J = \int_{-\infty}^{\infty} v\, dx, \tag{7.13}$$

which we consider as a measure of the influence that a patterned surface has on an adjacent flow. The value of J is a sensible choice of measure as we have seen that it is the normal

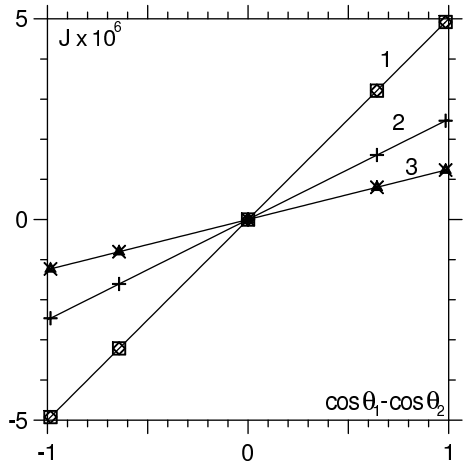

Figure 7.4: Dependence of flux on parameters Q, ϵ, $\bar{\beta}$ and λ. Parameters are varied around a base state, the results of which are represented by vertical crosses, of: $\bar{\beta} = 100$, $Q = 1$, $\epsilon = 0.01$, $\lambda = 20$. Then, diamonds: $\epsilon = 0.02$; squares: $Q = 2$; triangles: $\bar{\beta} = 200$; diagonal crosses: $\lambda = 40$. For all curves $\theta_1 = 90^\circ$ whilst θ_2 is varied, and $Re = 0.01$. Curves $1 - 3$ represent the predicted flux given by (21).

component of velocity that causes the noticeable deviation from plane-parallel shear flow.

Given that the change in solid does indeed alter the flow of an adjacent liquid, consider how the magnitude of the effect is dependent on the choice of solids. Our results suggest that the normal flux per unit time is proportional to the difference $\cos\theta_1 - \cos\theta_2$. The numerical analysis of the problem made it possible to advance and then verify the following approximate formula for J:

$$J = \frac{\epsilon Q}{2\bar{\beta}\lambda}\left(\cos\theta_1 - \cos\theta_2\right). \tag{7.14}$$

The accuracy with which this equation represents J is illustrated in Figure 7.4.

Order of magnitude arguments for the phenomenological parameters and the analysis of experiments on dynamic wetting (Blake & Shikhmurzaev, 2002) suggest that $\beta \sim \mu/h$, where h is the thickness of the interfacial layer (modelled here as an 'interface' of zero thickness). Using this estimate, for the dimensional flux per unit time out of the surface

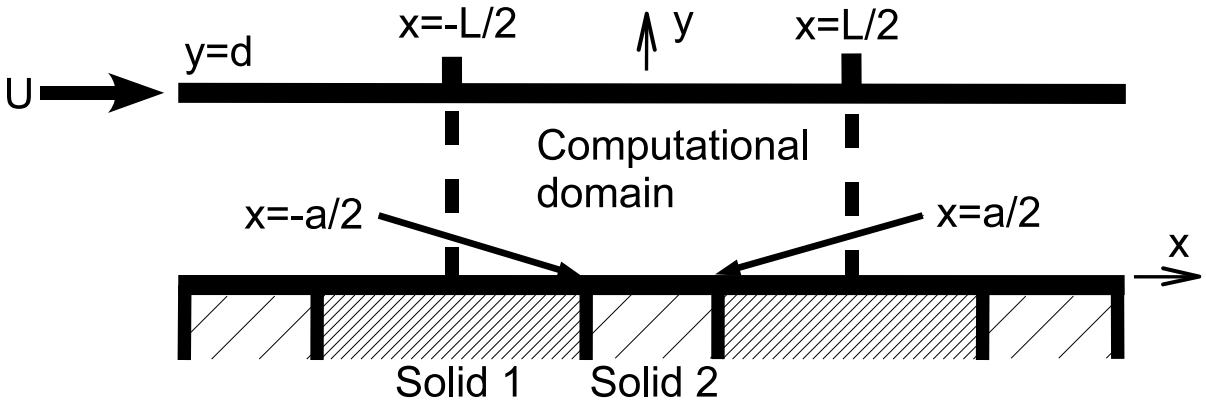

Figure 7.5: Problem setup.

phase in a liquid/solid/solid system one has

$$J_{dim} \sim \frac{Sh\sigma}{\rho\gamma} \left(\cos\theta_1 - \cos\theta_2\right). \tag{7.15}$$

Given that h is typically very small (a few nanometres for simple fluids (Rowlinson & Widom, 1982)), the above estimate highlights the subtle nature of the effects that we have described.

7.2 Flow of thin films over an intermittently patterned surface

We now extend our analysis to consider the case of an intermittently patterned surface (see Figure 7.5) where the upper surface has homogenous wettability and moves in its own plane with velocity $\mathbf{u} = (u, v) = (U, 0)$, whilst the lower surface is patterned with a variable wettability and remains stationary. The pattern on the lower surface consists of intermittent stripes of solid 1, with width $L - a$, and solid 2, with width a. It is assumed that both surfaces are perfectly smooth. This case is considered in more detail in Sprittles & Shikhmurzaev (2009*a*).

For the intermittently patterned surface, equation (7.1) is replaced by the following

expression which prescribes the wettability of the lower surface:

$$\rho^s_{Se} = \rho^s_{1e} + \tfrac{1}{2}\left(\rho^s_{2e} - \rho^s_{1e}\right)\left\{\tanh[(a/2+x)/l] + \tanh[(a/2-x)/l]\right\}, \tag{7.16}$$

whilst on the upper solid we assume $\rho^s_{Se} \equiv \rho^s_{1e}$. Additionally, due to the periodicity of the problem we apply

$$\mathbf{u}\,|_{x=-L/2} = \mathbf{u}\,|_{x=L/2}, \quad \left.\frac{\partial \mathbf{u}}{\partial x}\right|_{x=-L/2} = \left.\frac{\partial \mathbf{u}}{\partial x}\right|_{x=L/2}, \tag{7.17}$$

$$\rho^s_S\,|_{x=-L/2} = \rho^s_S\,|_{x=L/2}, \quad v^s_{St}\,|_{x=-L/2} = v^s_{St}\,|_{x=L/2}\,. \tag{7.18}$$

We consider each stripe of solid to have equal width and the aspect ratio to be unity (L=d). Then, without loss of generality, we may consider solid 1 to be more hydrophilic than solid 2. The upper wall is at $d = 10^{-1}$ μm and moves with speed $U = 10^{-1}$ m s^{-1}; other dimensional values are the same as for the single transition in wettability. Streamlines for $\theta_1 = 10°$, $\theta_2 = 80°$ are shown in Figure 7.6 and compare favourably to the molecular dynamics snapshot from Priezjev *et al.* (2005). Both show that the less hydrophilic substrate appears to act as an obstacle to motion with streamlines coming out of the interfacial layer as the solid becomes less hydrophilic, at $x = -0.25$, and entering again as the solid becomes more hydrophilic again, at $x = 0.25$. This effect can be seen clearly by looking at the normal velocity on the liquid facing side of the liquid-solid interface in Figure 7.6. One can see that the components of velocity are trying to relax to their equilibrium values, $\mathbf{u}_e = (9.8 \times 10^{-3}, 0)$ but are unable to obtain them before the next transition in wettability. This means that the distance between transitions is of the same order as the relaxation length, which is the distance that it takes for surface properties to relax to their equilibrium values. The width of the transition region $\bar{l}$ is far smaller than the relaxation length and, as in the single transition case, its exact size has very little effect on the overall flow field.

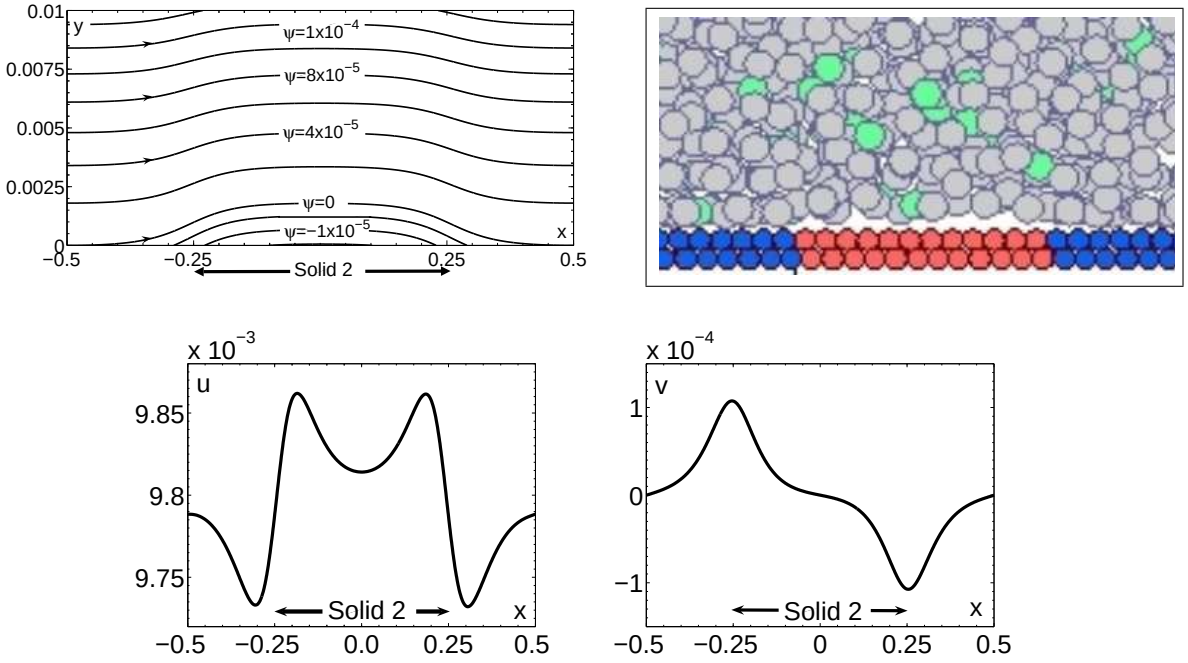

Figure 7.6: Streamlines and the corresponding components of velocity on the substrate for flow over a intermittently patterned surface, in which values of the streamfunction ψ are given, compared to a snapshot from a molecular dynamics simulation. Parameters are at their typical values with $\theta_1 = 10°$ and $\theta_2 = 80°$.

7.3 Concluding remarks

As was shown, the interface formation model applied to the flow over a solid surface of variable wettability allows us to describe the main features of this flow as observed in molecular dynamics simulations, most notably the nonzero component of the bulk velocity normal to the solid surface. A natural link between 'wettability' interpreted in terms of the concept of the 'contact angle' featuring in the spreading of liquids on solid surfaces and a viscous flow over solids of variable wettability with no free surface present has been established. Importantly, the interface formation model deals with these phenomena entirely within the approach of continuum mechanics with no artificial inclusion of intermolecular forces in its framework. An interesting feature that follows from the results is that slip, i.e. the difference between the tangential component of the fluid's velocity and the corresponding component of the velocity of the solid surface, results primarily from the disturbance of the force balance in the 'surface phase' and not from

the tangential stress, as follows from the standard Navier condition. This has significant consequences when attempting to interpret the results of molecular dynamics simulations and experiments in terms of a continuum theory.

Notably, in contrast to studies of slip on super hydrophobic substrates, where the presence of nanobubbles leads to the effective slip length of the system becoming a relevant measure of the effects of variable wettability of the substrate (Lauga & Stone, 2003; Priezjev *et al.*, 2005), here the slip coefficient β remains the same on both solids.

In this chapter, we have established that the interface formation model accounts for the affect which variations in the wettability of a solid have on an adjacent flow. Now, we may use this model, without any ad-hoc changes, to consider more complex flows such as the dynamic wetting of surfaces of variable wettability.

Chapter 8

Impact and spreading of drops on custom-made surfaces

We now consider the impact of drops on solid surfaces whose wettability has been modified in order to manipulate the spreading of liquids over them. First, we show how microdrop impact and spreading may be controlled by patterning an otherwise hydrophillic substrate with regions of hydrophobicity. Then, we consider the dynamics of drops which impact and spread on super-hydrophobic substrates, before finally considering whether a super-hydrophobic substrate can be patterned with areas of hydrophillicity in order to stop microdrops which impact on such a solid rebounding back off.

8.1 Impact and spreading on surfaces of variable wettability

We study microdrops impacting in the centre of a disc or annulus shaped region of wettability which differs from the rest of the surface. Specifically, we consider a smooth solid surface of wettability $\theta_e = 60°$, which has been patterned so that regions of the surface

become more hydrophobic, but remain smooth.

First, we consider the simplest case in which a drop lands in the centre of a disc which is more hydrophobic than the rest of the surface.

8.1.1 A disc of hydrophobic substrate

Consider a disc, $r < 1.52$, with wettability $\theta_e = 110°$ on a solid which elsewhere has wettability characterized by $\theta_e = 60°$. We will show that this patterning allows one to choose between two final equilibrium drop shapes by using only the initial impact speed as a controlling parameter.

From Figure 8.1 and Figure 8.2 we see how this is achievable: on the patterned surface the equilibrium radius which is wet by a drop impacting at 4 m s^{-1} is $r_c = 1.03$, whilst for a 5 m s^{-1} impact it is $r_c = 1.61$. This occurs because the lower speed drop is unable to reach the edge of the hydrophobic surface and hence behaves as if it is on a homogeneous surface with wettability defined by $\theta_e = 110°$. The higher speed impact is able to reach the edge of the disc, at which point it encounters the more wettable surface, that, as can be seen by looking at Curve 2 in Figure 8.1 at $t = 2$, results in an increase in the wetting speed and causes the contact line to advance further. This is no guarantee that the drop's contact line will remain on the more wettable surface as the contact line could return to the hydrophobic solid, which would enhance the dewetting process, again on recoil. However, from Curve 2 in Figure 8.1, we can see that the contact line's recoil is relatively shallow and the contact line approaches an equilibrium position without ever encountering the hydrophobic disc again.

Although we were able to choose different final contact-line radii by varying the impact speed, once the solid had been chosen, we had no control over what this radii was to be. Using an annulus of hydrophobic surface opens up the possibility of using the impact speed to control the final wetted area, and now we consider if this is possible.

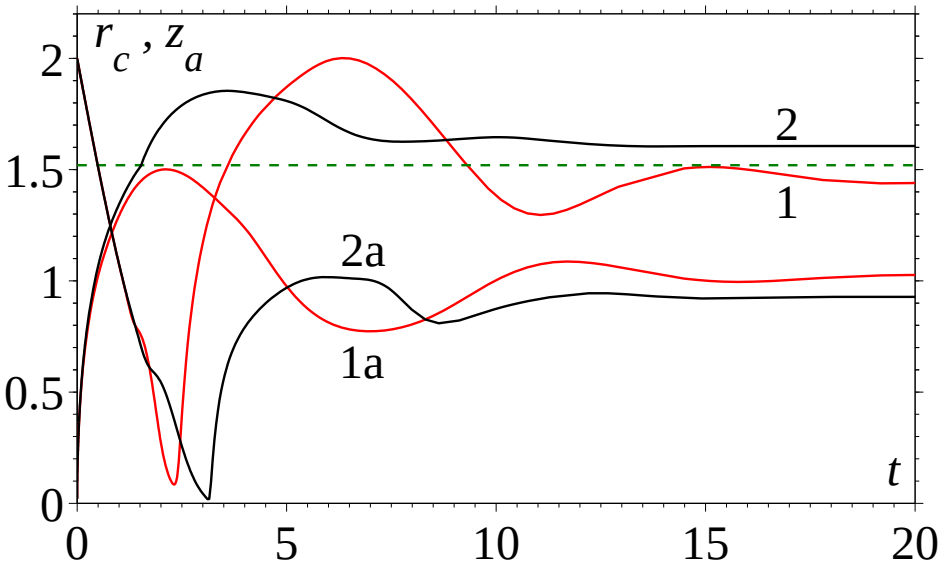

Figure 8.1: Radius of the contact line (1,2) and apex height (1a,2a) as a function of time for two drops impacting a patterned surface at 1: $U_0 = 4$ m s^{-1} and 2: $U_0 = 5$ m s^{-1}, respectively. The boundary between the surface characterized by $\theta_e = 110°$ ($r < 1.52$) and that defined by $\theta_e = 60°$ ($r > 1.52$) is marked with a dashed line.

8.1.2 An annulus of hydrophobic substrate

We now show that it is possible, by patterning the substrate with an annulus of hydrophobicity, to ensure the drop wets an equilibrium radius of $r_c = 1.2$ or $r_c = 1.61$, using only the impact speed as the controlling parameter. This is achieved by patterning a surface otherwise characterized by $\theta_e = 60°$ with an annulus $1.2 < r < 1.52$ of surface characterized by $\theta_e = 110°$ and, again, considering the dynamics of a drop impacting this surface with speeds $U_0 = 4$ m s^{-1} and $U_0 = 5$ m s^{-1}.

We can see from Figure 8.3 and Figure 8.4, that the drop with the highest impact speed is able to attain an equilibrium position of $r_c = 1.61$ whilst, as hoped, due to the surface patterning the drop with the lower impact speed is unable to cross the annulus of hydrophobic substrate and it gets driven back towards the inner disc of hydrophilic substrate. Once there, the radius of the contact line oscillates around $r_c = 1.2$, as the equilibrium radius on the hydrophobic surface is $r_c = 1.03$ whilst it is $r_c = 1.61$ on the hydrophilic one. One can see from Curve 1 in Figure 8.3, that the oscillations of the

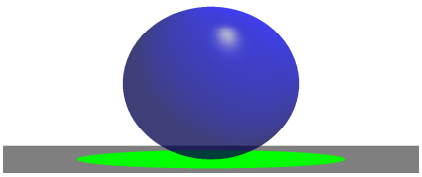

(a) t =0

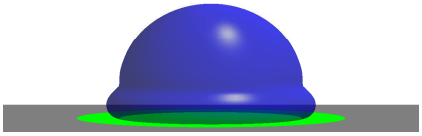

(b) t =0.5

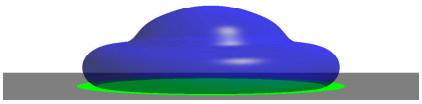

(c) t =1

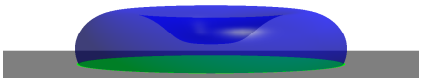

(d) t =2

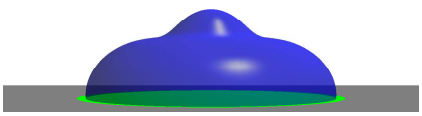

(e) t =3

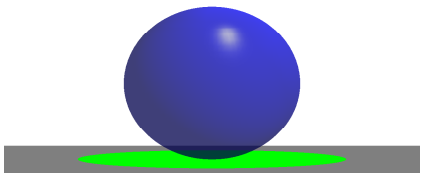

(a) t =0

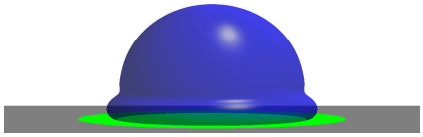

(b) t =0.5

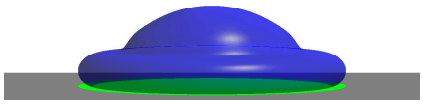

(c) t =1

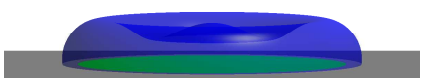

(d) t =2

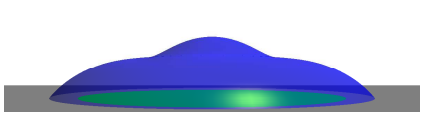

(e) t =3

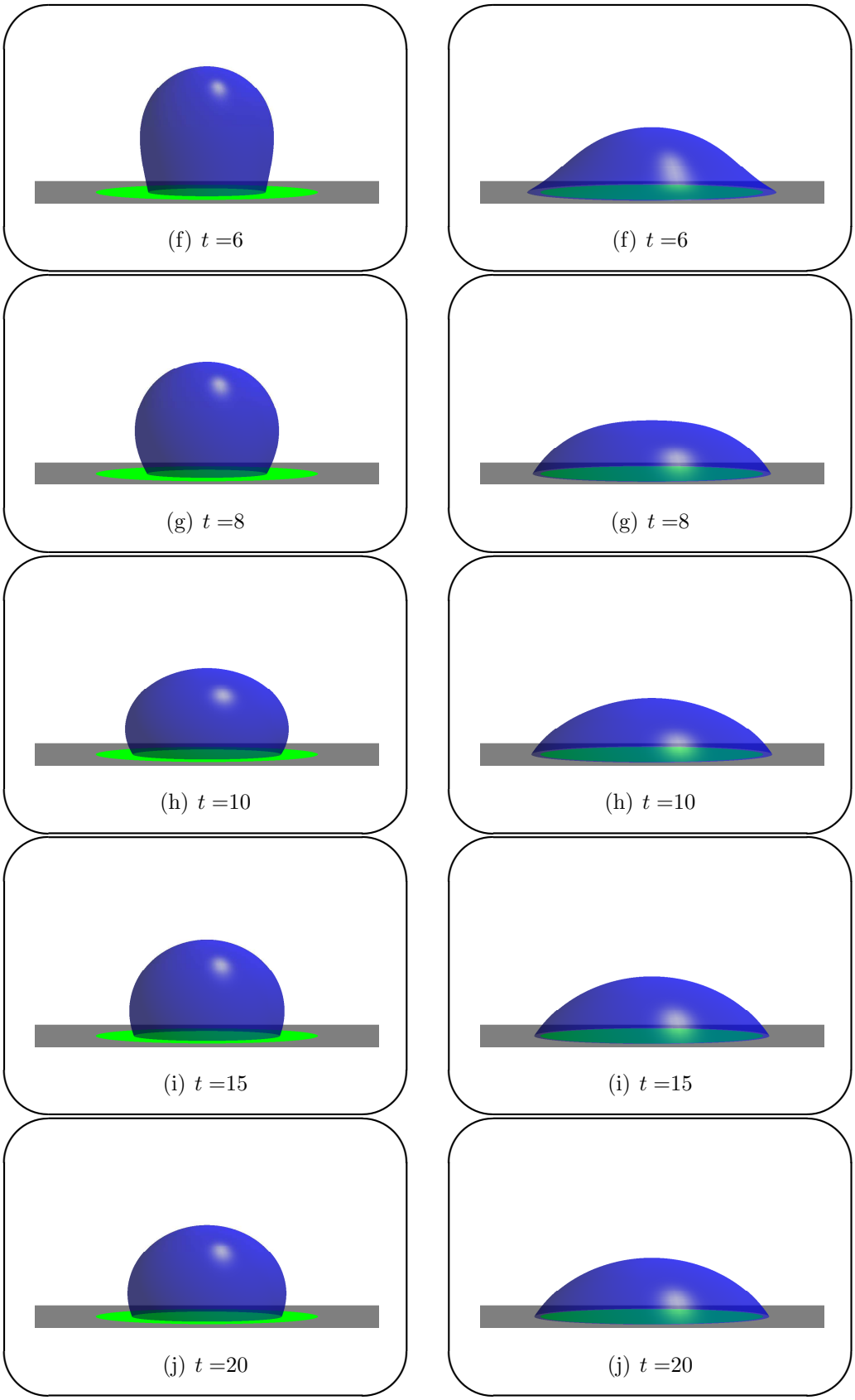

Figure 8.2: Evolution of two drops impacting a patterned surface at (left) $U_0 = 4$ m s^{-1} and (right) $U_0 = 5$ m s^{-1}. The hydrophobic surface patterning, characterized by $\theta_e = 110°$ is marked in green whilst the grey corresponds to $\theta_e = 60°$.

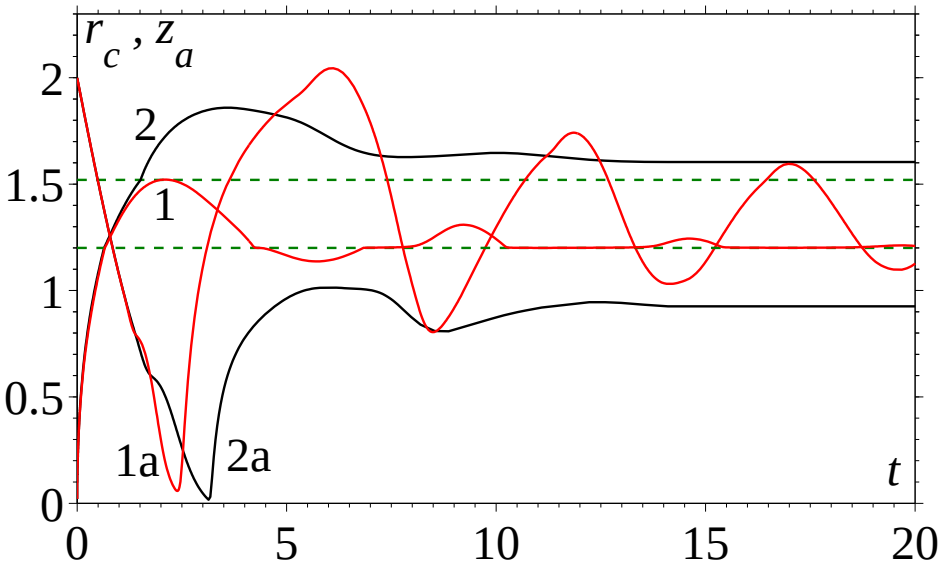

Figure 8.3: Position of the contact line (1,2) and apex height (1a,2a) as a function of time for two drops impacting a patterned surface at 1: $U_0 = 4$ m s^{-1} and 2: $U_0 = 5$ m s^{-1}. The boundary between the surface characterized by $\theta_e = 110°$ ($1.2 < r < 1.52$) and that defined by $\theta_e = 60°$ is marked with a dashed line.

contact line radius are relatively small in magnitude and, consequently, the apex height's oscillations are much larger than usual, see Curve 1a, as energy is now mainly dissipated there.

Having considered drop impact and spreading on a surface patterned with regions of hydrophobic surface, we would now like to consider how a super-hydrophobic surface can be used to manipulated the drop's dynamics. First, we consider how a drop behaves when it impacts on a surface of homogeneous super-hydrophobicity.

8.2 Impact and spreading on a super-hydrophobic surface

Initially, we consider the impact of a millimetre-sized drop on a super-hydrophobic surface, for which there are experimental images which we may compare to. Then, we consider microdrop impact and spreading on such as surface where, until now, no experimental or

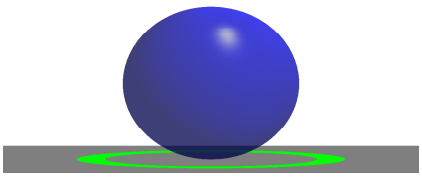

(a) t =0

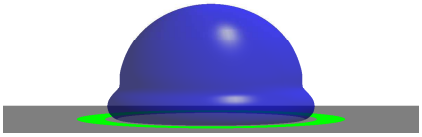

(b) t =0.5

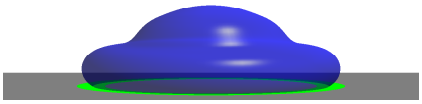

(c) t =1

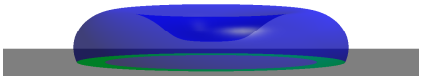

(d) t =2

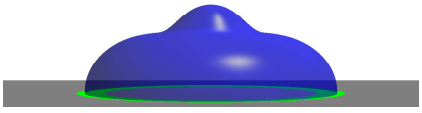

(e) t =3

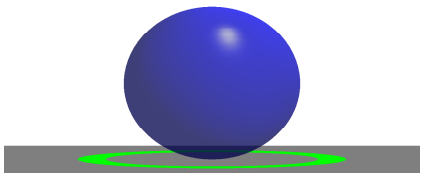

(a) t =0

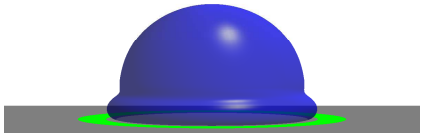

(b) t =0.5

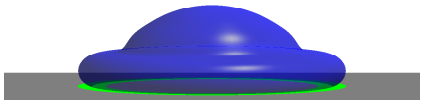

(c) t =1

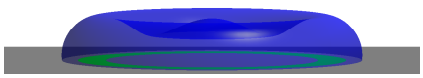

(d) t =2

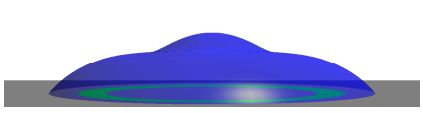

(e) t =3

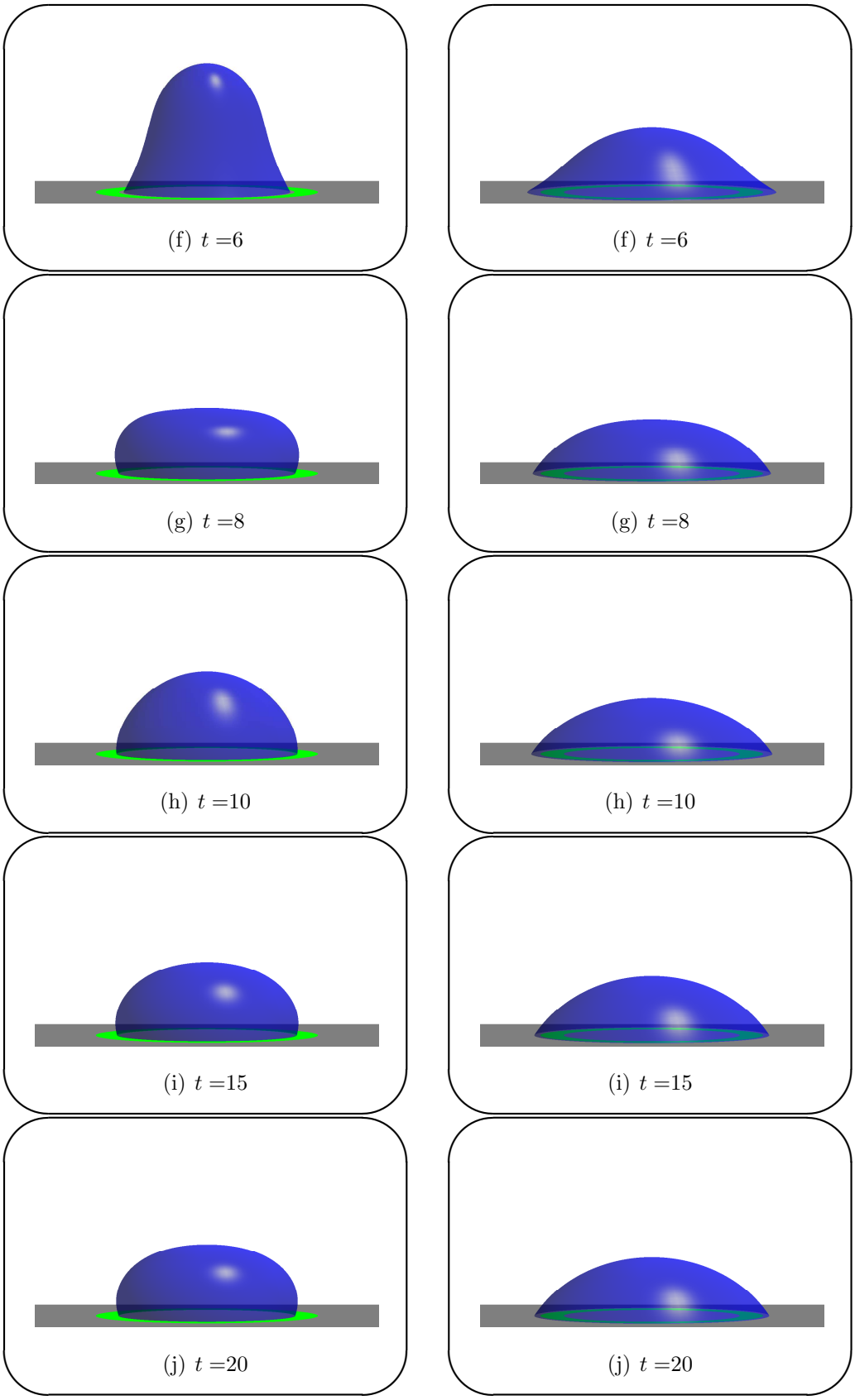

Figure 8.4: Evolution of two drops impacting a patterned surface at (left) $U_0 = 4$ m s^{-1} and (right) $U_0 = 5$ m s^{-1}. The hydrophobic surface patterning, characterized by $\theta_e = 110°$ is marked in green whilst the grey corresponds to $\theta_e = 60°$.

theoretical results have been presented.

8.2.1 Millimetre-sized drop impact

The experimental images of a millimetre-sized drop impacting a super-hydrophobic surface published in Renardy *et al.* (2003) show a drop which has oscillated through flight and hence impacts in a non-spherical shape. The authors suggest this initial shape may be approximated by a mode 2 spherical harmonic, see §5.1, with the amplitude of the initial deviation from a sphere being $f_n = 0.29$. We adopt this initial position in our simulations and, for a water droplet of radius 1.75 mm impacting at 0.41 m s^{-1}, we have that $Re = 718$, $We = 4$, $St = 73$. Because of the size of the drop, we have been unable to accurately use the interface formation model for this situation, so we have used the conventional model, which may be used when the surface has constant wettability, with $\theta_e = 160°$.

A comparison between snapshots from our numerical simulation and the experimental images in Renardy *et al.* (2003) is shown in Figure 8.5. The simulation captures the main features seen in the experiment: the formation of a series of pyramidal shapes, which are seen to be caused by capillary waves which emanate from the contact line and travel up the free surface towards the apex. This causes the apex to oscillate above and below the observable free surface and eventually get thrown downward with such force that it touches the solid, at which point the drop becomes toroidal and the simulation terminates. Throughout the simulation the free surface near the centre of the drop disappears below the height of the outer rim of fluid so that in the experiment one is left un-sighted. In such situations the simulation allows us to follow the free surface with ease and, significantly, see how that the apex contacts the solid.

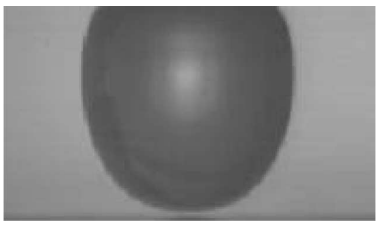

(a) t_d =0 ms

(b) t_d =2.7 ms

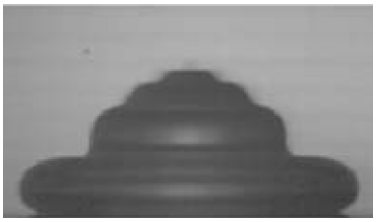

(c) t_d =4.5 ms

(d) t_d =4.9 ms

(e) t_d =5.9 ms

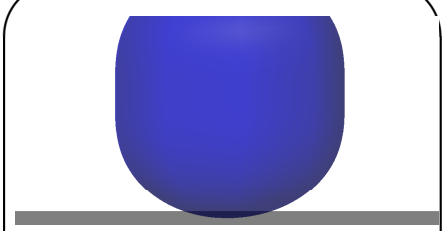

(a) t_d =0 ms

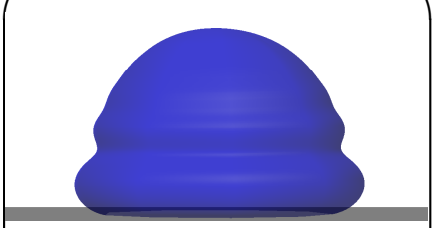

(b) t_d =2.7 ms

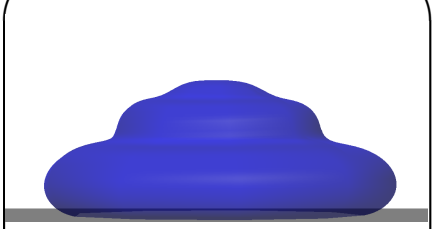

(c) t_d =4.5 ms

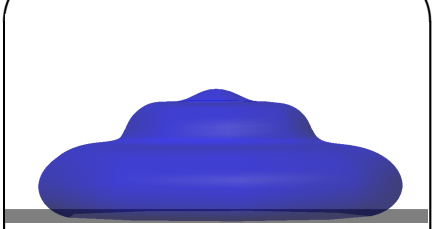

(d) t_d =4.9 ms

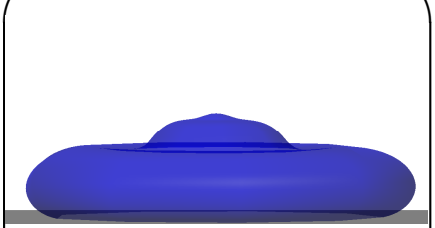

(e) t_d =5.9 ms

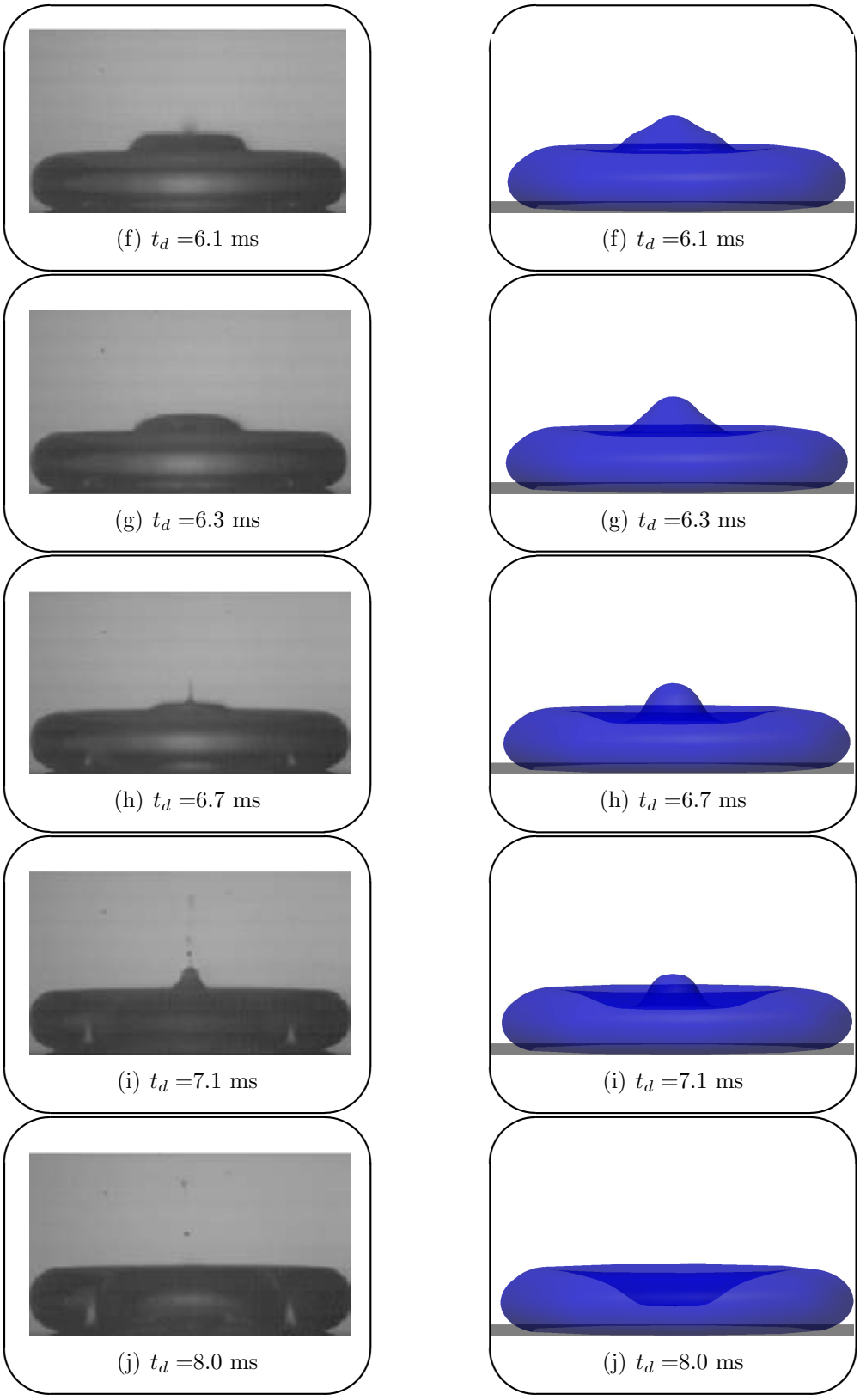

Figure 8.5: Comparison of a simulation using the conventional model to the experiments in Renardy *et al.* (2003).

8.2.2 Microdrop impact

We now consider the impact and spreading of our base state microdrop on a super-hydrophobic solid, characterized by $\theta_e = 160°$, of constant wettability and on a solid containing a disc of hydrophillicity, characterized by $\theta_e = 60°$. Given the results in §6, we may expect a drop to rebound off the surface of constant super-hydrophobicity and, consequently, we are interested in seeing if it is possible to inhibit this rebound through surface patterning. As previously, for microdrop simulations we use the interface formation model which has the advantage that, when we come to consider impact on a substrate patterned with areas of variable wettability, we will not need to make any ad-hoc alterations to our model.

One can see in Figure 8.6 that the drop which impacts the surface of constant super-hydrophobicity does indeed rebound; however, by using a disc of hydrophillicity $r < 1.3$ this rebound is prevented. The initial evolutions of the two drops are seen to be similar until around $t = 3$, at which point the contact line begins to dewet the solid, see Figure 8.7. While the drops are recoiling, a powerful jet emanates from the centre of the drop which, for the surface of constant super-hydrophobicity, forces the drop off the substrate. In Figure 8.8, one can see just how quickly the apex region, which forms the jet, rises. For the drop on the patterned surface, when the contact line reaches the hydrophilic substrate again it no longer has the will to dewet the solid and becomes almost pinned, see Figure 8.7. Then, eventually the apex is pulled downwards by surface tension forces, and it is their subsequent interplay with inertial forces that determines the dynamics of the large oscillations, seen in Figure 8.7, which are damped by viscous forces. Therefore, the surface patterning has indeed prevented the rebound of a drop off an otherwise super-hydrophobic solid.

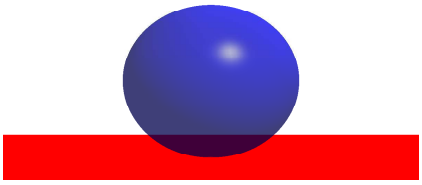

(a) t =0

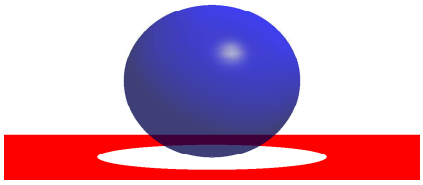

(a) t =0

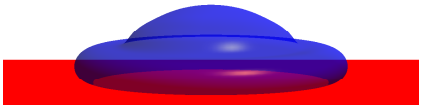

(b) t =1

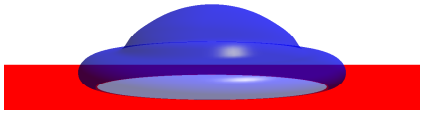

(b) t =1

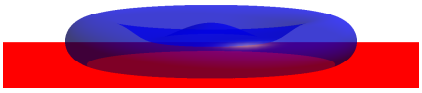

(c) t =2

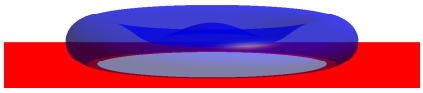

(c) t =2

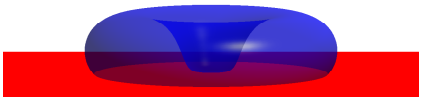

(d) t =3

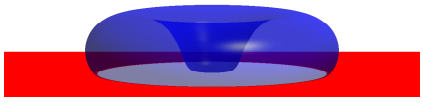

(d) t =3

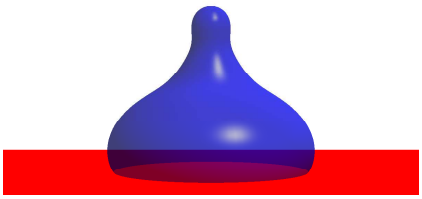

(e) t =4

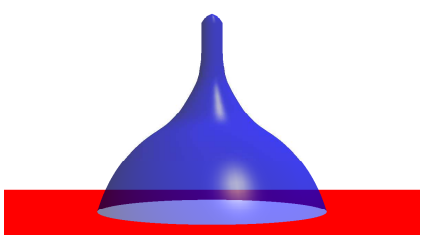

(e) t =4

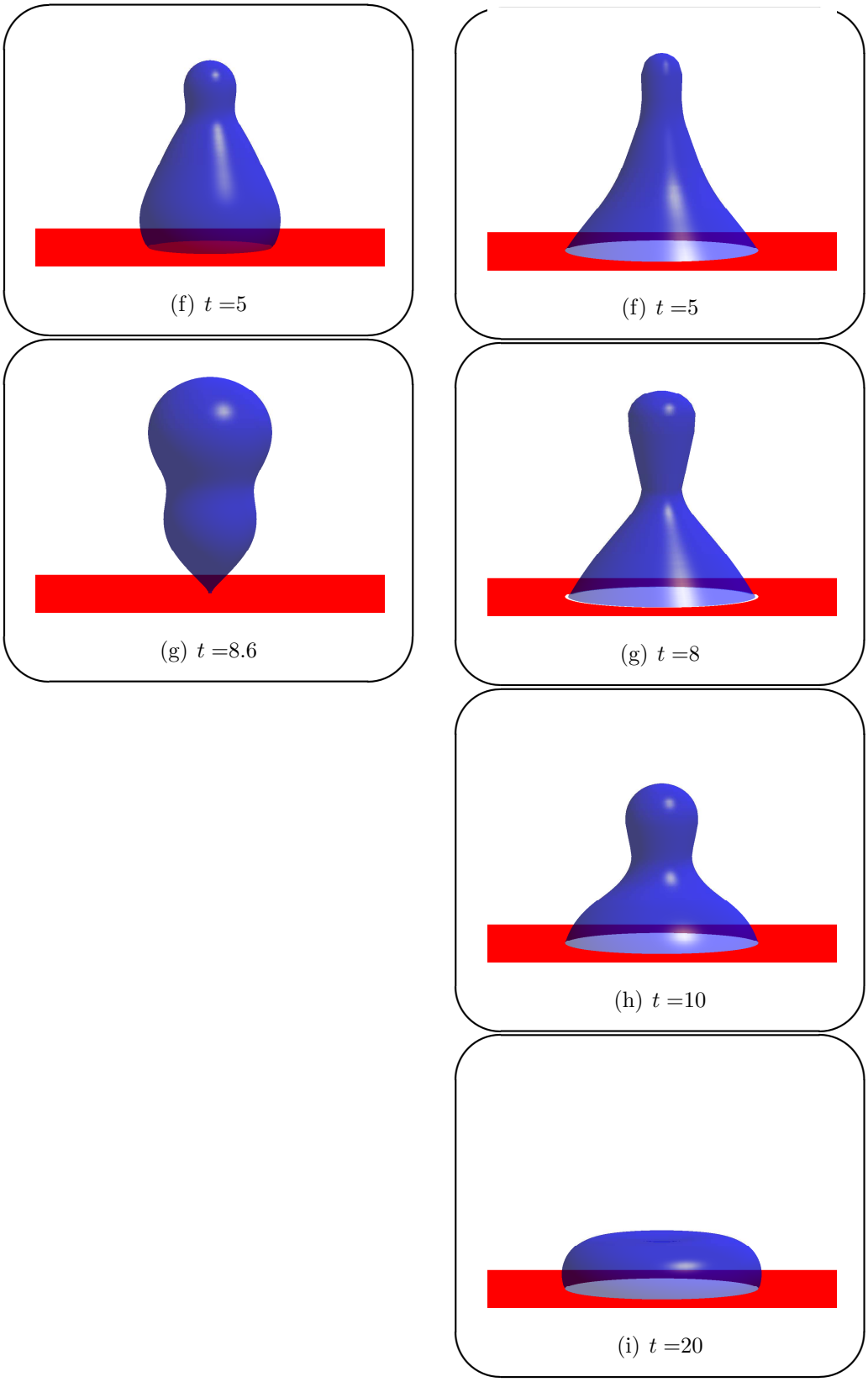

Figure 8.6: Evolution of a drop impacting on a super-hydrophobic surface (left) compared to the same drop impacting on a surface patterned with a disc, $r < 1.3$, of hydrophilic surface (right). The super-hydrophobic surface is in red and is characterized by $\theta_e = 160°$ whilst the hydrophilic one is in white and is characterized by $\theta_e = 60°$.

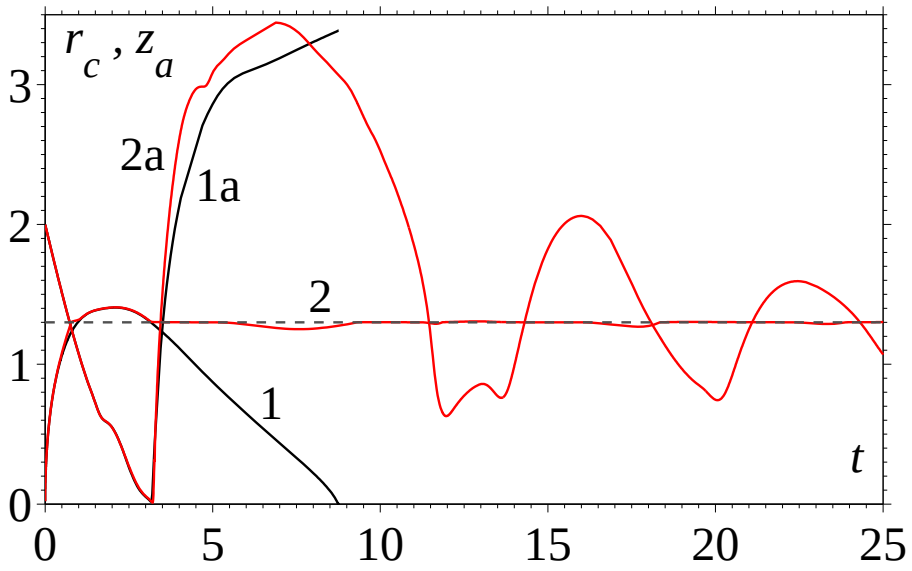

Figure 8.7: Radius of the contact line (1,2) and apex height (1a,2a) of drops impacting on a super-hydrophobic surface (1,1a) characterized by $\theta_e = 160°$ and the same surface patterned with a disc ($r < 1.3$) of hydrophilic surface (2,2a), characterized by ($\theta_e = 60°$). The boundary between the two surfaces is marked with a dashed line.

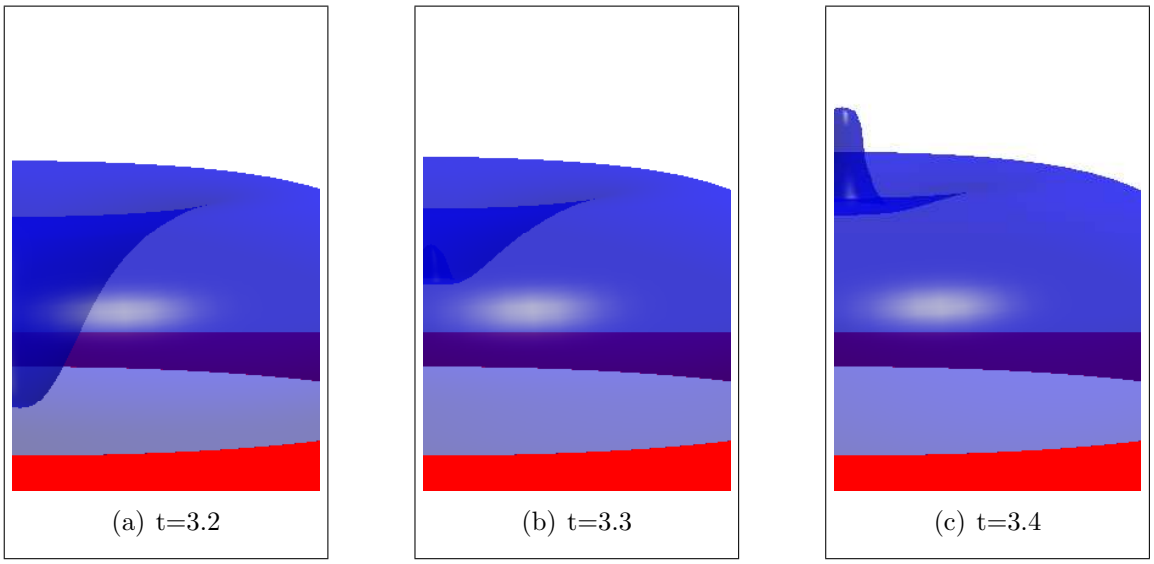

(a) t=3.2 (b) t=3.3 (c) t=3.4

Figure 8.8: Formation of a powerful jet during spreading on a surface characterized by $\theta_e = 160°$ with hydrophilic patterning characterized by $\theta_e = 60°$ for $r < 1.3$.

8.3 Summary

We have shown how microdrop spreading can be hugely influenced by variations in the wettability of a substrate and how this effect may be utilised to manipulate a drop's dynamics after deposition. Notably, by patterning the substrate, one can gain control of the final position of a droplet by varying only the impact speed. An interesting question to consider for the case in which a higher speed impact drop was able to pass an annulus of less wettable substrate, is whether at an even higher impact speed, where the recoil may be larger, the drop will return to the annulus and dewet part of the solid again.

We have shown that by patterning a super-hydrophobic substrate with a hydrophilic disc, one is able to prevent the rebound of a drop, a phenomenon which is detrimental to controlled deposition of liquid drops on a solid. It would be of interest to consider how large the area of hydrophillicity must be in order to prevent the rebound. Then, for example, by covering a super-hydrophobic surface with small patches of hydrophillicity, is one able to inhibit rebound of drops landing on the substrate and yet still obtain a large equilibrium contact angle? Preliminary tests show that rebound can be prevented with a relatively small disc of hydrophillicity, down to around $r < 0.5$.

Chapter 9

Directions of future research

In this thesis, we have demonstrated some of the capabilities of the model which we have developed. In the future, we intend to use our numerical platform to investigate a wider range of parameter values and look to see how the interface formation model's predictions compare to both the conventional model and to experiments. Are there new, experimentally verifiable, predictions which the interface formation model makes that distinguish it from those predicted by a conventional model? It is important to remember that the conventional model has become conventional because it allows one to incorporate empirical data from auxiliary experiments for the speed-angle relationship, so that finding discriminating cases means determining the flow conditions where this empiricism does not work. Ideally, we will run our code for larger drops, on the scale of millimetres, where experiments already exist which show the non-uniqueness of the speed-angle relationship (Šikalo *et al.*, 2005; Bayer & Megaridis, 2006). Computationally, these larger drops are more challenging to simulate as (*i*) at higher Weber and Reynolds numbers the drop undergoes larger deformation, and (*ii*) there is a larger disparity between the characteristic length scale on which the bulk flow operates compared to the length scale of interface formation.

We now consider possible extensions to the work presented in this thesis. We concen-

trate on effects which can be incorporated into the existing numerical platform as opposed to those, such as the simulation of non-axisymmetric three-dimensional phenomena, which would require significant, albeit technical, alterations to the current approach.

9.1 Wetting of imperfect solid surfaces

Often, dynamic wetting occurs on a solid substrate which cannot be considered smooth, chemically homogeneous and impermeable, i.e. a solid where the imperfections are on a scale where their influence can no longer be accounted for by effective coefficients for the interfacial equations. In particular, the spreading of drops on rough or porous substrates are relevant for a wide range of industrial processes. In both cases the complexity is in the modelling as opposed to the computation: one must consider how the imperfect substrate affects the boundary conditions at the liquid-solid interface and in what way the dynamic contact angle should be interpreted and then determined.

Jansons (1987) showed that the macroscopic boundary condition for a surface with microscopic regions of no-slip and free slip is the Navier-slip boundary condition . The effect of surface imperfections on the dynamic contact angle can also be important, most noticeably by causing contact angle hysteresis (e.g. Ramos *et al.*, 2003). In Jansons (1985), the deviation of the effective contact angle (on the bulk length scale) from its fixed actual value (on the scale of the roughness) was considered for a contact line moving over a solid containing disperse patches of roughness. On the scale of the roughness, the contact angle was fixed to its equilibrium value $\theta_d = \theta_e$. An interesting direction of research would be to use a dynamic contact angle on the scale of the roughness and determine what effect the patches have on the effective contact angle.

If the solid is porous, one has to couple the effects of spreading with the imbibition of fluid into the base. Preliminary work on this topic has involved using a bundle-of-tubes model for flow through the porous media (Washburn, 1921) coupled with a spherical cap

approximation for the drop shape. Either a constant contact angle (Davis & Hocking, 1999, 2000) or a dynamic contact angle formula (Clarke *et al.*, 2002) derived for spreading on an impermeable substrate, has been used to find the contact line position.

The aforementioned approaches all consider the influence which imperfections of the solid have on an adjacent flow using the classical or conventional model. However, as we have already discussed, for surfaces containing no imperfections, the classical model has no solution and the conventional model makes unacceptable predictions. Ideally, we would start with the interface formation model, which has been shown to resolve the paradoxes of previous models, and build into it the additional physical effect of surface imperfections. So far, this has not been considered, but it could be the subject of future work.

9.2 Impact and spreading in a viscous gas

The effect of a surrounding viscous gas on a drop's dynamics is a fascinating area of research with many unanswered questions. The air cushion formed as a drop approaches a solid substrate can severely deform the drop's shape, to such an extent that air bubbles are subsequently observed in the centre of spreading drops (Chandra & Avedisian, 1991; Van Dam & Le Clerc, 2004). Thus an interesting question is, what is the initial shape of an impacting drop? Also, why does reducing the air pressure of the surrounding gas suppress splashing (Xu *et al.*, 2005)?

To model such flows, we must be careful what boundary condition are applied at the solid-gas interface in order to avoid encountering the moving contact-line problem in the viscous gas. One option is to apply the Navier-slip condition, which could crudely model the slip of gas past an adjacent solid substrate (Shikhmurzaev, 2007).

Numerically, it seems viable to continue using the spine method, but now to run the spines past the free surface and through the gas. This may only be necessary near the

contact line and the base of the drop where the air cushion influences the free surface shape. Mathematically, this poses a problem of how to describe only the lubricating effect of the gas under the drop and avoid computing the gas flow everywhere around the drop, which would be both physically irrelevant and computationally inefficient.

9.3 Extension of the numerical platform

In this thesis, we opted to use structured meshing. We designed two meshes, based on the bipolar coordinate system, and were able to simulate the majority of flows of interest. Unfortunately, certain circumstances have arisen where our approach has failed. In some of these cases, when the spines become tangential to the free surface, the spine method could still be used if all the spines are re-orientated; alternatively, the constant tampering with the spine orientations could be avoided if we used an unstructured mesh. This approach has already been successfully used to simulate drop impact and spreading phenomena in Ganesan (2006); however, this code did not attempt to resolve the dynamics near the contact line. A sensible approach therefore would be to design a hybrid mesh that is structured around the contact line region, ensuring that the interfacial dynamics are sufficiently well resolved there, and unstructured in the rest of the drop, where more mesh flexibility is needed.

9.4 Ubiquity of flows which can be simulated

The numerical platform can easily simulate other dynamic wetting flows, such as, for example, the propagation of a meniscus through a capillary tube or channel, where non-uniqueness of the speed-angle relationship has already been observed experimentally (Ngan & Dussan V, 1982). Additionally, as considered in Saha & Mitra (2009), we could consider the effect which walls of variable wettability will have on the propagation of a

meniscus through a microchannel.

Our platform can also be easily adapted to model a number of other capillary flows. In particular, we can consider other phenomena where the interface formation model resolves the paradoxes associated with a classical fluid mechanical approach. Such situations include the coalescence of liquid drops, the breakup of liquid threads, the rupture of thin films and the formation of free surface cusps (Shikhmurzaev, 2007). Thus far, the model has only been applied to these problems in particular limits where analytic progress was possible: with our numerical platform we are free to investigate the whole parameter space of interest.

Chapter 10

Summary

Our investigation into the impact and spreading of microdrops on smooth surfaces of constant wettability has resulted in an increased understanding of the dynamics of such droplets. The model which we have developed has allowed us to determine the role which particular parameters play in the evolution of a droplet and understand the associated physical mechanisms. This paves the way for optimization of the process. By considering the dynamics of microdrops on surfaces of variable wettability it was shown how to alter the final position of a droplet using only the impact speed as a controlling parameter.

To achieve these results, we developed a numerical platform which was specifically tailored for the simulation of dynamic wetting flows. The spine method allowed us to capture the free surface precisely whilst ensuring that bulk nodes evolved with the drop and did not create overly distorted elements. This was combined with the second-order Backward Differentiation Formula for integration in time which, when combined with an predictor-corrector scheme, allowed for the automatic choice of time step, by bounding the discretization error. The novel achievements from this development are now listed.

- The mesh design, using the bipolar coordinate system, allowed for the simulation to begin from an angle as close to 180° as required and, in contrast to all previously developed codes for drop impact and spreading, provided enough resolution

to capture the small-scale physics (of both the conventional model and the interface formation model) near the contact line.

- The cause of the spurious pressure behaviour near the contact line, usually not noticed due to a lack of spatial resolution in previous codes, was identified and a method for its removal was developed, in the Appendix. This allowed us to determine that, in the parameter range considered in this thesis, it has a negligible affect on the drop's evolution.

- The unsteady interface formation model was fully implemented into the numerical platform, for the first time, and it was found that to provide accurate results one must (*i*) use the surface mass flux variable at low capillary numbers, (*ii*) not increase distance between spines too quickly as one moves away from the contact line and (*iii*) ensure that the middle node of each free-surface quadratic element is central.

The numerical platform was thoroughly validated and was seen to provide results which were in agreement with previous numerical results for the oscillation of liquid drops in a regime where inertial, capillarity and viscous forces are all present. We then showed that the interface formation equations were correctly implemented by producing numerical results which were in excellent agreement with previous asymptotic results. In the most complex case we considered the axisymmetric spreading of a liquid drop at a small capillary number.

Having established the accuracy of the code, we studied the impact and spreading of microdrops on solid surfaces. The new results from this were as follows.

- For early time, there is a geometric wetting phase in which the contact angle remains at 180° and the wetting mechanism is different from that which is usually observed in standard dynamic wetting experiments and associated theoretical studies.

- The experimentally observed non-uniqueness of the speed-angle relationship can be predicted by using the interface formation model and may even be observed in a

single simulation. It is shown that for the same liquid-solid combination, different speed-angle relationships can be obtained by varying the impact speed of the drop, or, as never previously considered, the size of the drop.

- Drop impact and spreading provides an ideal situation from which to accurately determine values for the interface formation model's parameters as relatively small changes in their values can lead to significant qualitative changes in the drop's dynamics.

Our attention then focused on how wettability manifests itself in the boundary conditions on the liquid-solid interface. The conventional model predicts that variations in wettability will not alter an adjacent shear flow, but, using the interface formation model, we were able to make the following deductions.

- A single change in wettability, occurring where solid 1 meets solid 2, disturbs a shear flow and leads to an effect whose magnitude is proportional to $\cos\theta_1 - \cos\theta_2$, where θ_i is the contact angle which a free surface makes with solid $i = 1, 2$.

- The streamlines obtained for flow over an intermittently patterned surface are qualitatively in agreement with molecular dynamics simulations.

The ability of the interface formation model to account for variations in the wettability of the solid substrate allowed us to consider drop impact and spreading on such surfaces without any ad-hoc alterations to our model. The main conclusions from our investigation into drops impacting on such custom-made surface were as follows.

- Once a surface has been patterned with areas of differing wettabilities, it is possible to switch between different equilibrium positions by varying only the impact speed.

- Our model is able to predict the experimentally observed pyramidal and toroidal free surface shapes formed by drops which impact and spread on super-hydrophobic surfaces.

- Rebound of a microdrop off a super-hydrophobic surface can be prevented by using small patches of hydrophillic patterning.

Finally, we have discussed the possible directions for future research, some of which are modelling challenges and others which require extensions to our numerical scheme.

Appendix A

Viscous flows in domains with corners

In dynamic wetting problems, it is necessary to consider domains in which two parts of a piecewise smooth boundary locally form a two-dimensional wedge (Figure A.1). The value of the contact angle can vary, depending on the wetting speed and the overall flow (Hoffman, 1975; Blake *et al.*, 1999; Wilson *et al.*, 2006; Shikhmurzaev, 2007), so that, to describe the process, one has to be able to solve equations of fluid mechanics in domains where two parts of the boundary locally form wedges of different angles.

In most practically relevant situations, the resulting free-boundary problems are un-

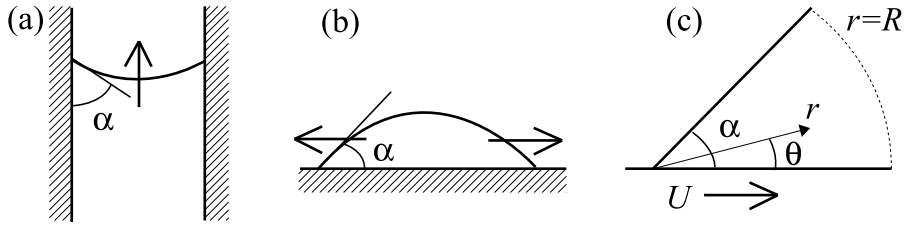

Figure A.1: Sketches of (a) a rising meniscus and (b) a spreading drop as examples of steady and unsteady flows involving dynamic wetting, i.e. the process of spreading of a liquid over a solid substrate. The free surface forms a 'contact angle' α with the solid boundary so that locally, in a frame moving with the contact-line speed U, to leading order as the distance to the contact line goes down, one has a flow in a corner (c).

tractable analytically and have to be solved numerically. The main difficulty in the numerics of dynamic wetting is the handling of the flow in the immediate vicinity of the contact line, where the obstacles are two-fold. Firstly, given that the region, where the no-slip boundary condition is relaxed to avoid the moving contact-line problem, is extremely small, one has to ensure that the computational mesh there is sufficiently refined for the slip region to be well resolved. Otherwise, the global effect of the under-resolved corner region could be quite dramatic, as has been emphasized in several recent works (Afkhami *et al.*, 2009; Schönfeld & Hardt, 2009; Weinstein & Pismen, 2008). At the same time, away from the contact line, where only bulk length scales need to be resolved, the meshing should not be excessive, for the computations to still be feasible.

In dynamic wetting, one arrives at a mathematical problem, locally in a wedge region (Figure A.1c), with different boundary conditions on the two sides. Both sets of boundary conditions involve first-order differential operators applied to the tangential component of the bulk velocity and linear homogeneous algebraic conditions for the normal component; that is, on each interface, boundary conditions formulated in terms of the tangential stress and the condition of impermeability. As always, it is important to ensure that the numerical code does not give rise to numerical artifacts, which in this case might arise as a result of the boundary being not smooth. This is the second and more severe difficulty one faces in numerically solving problems of dynamic wetting, and a necessary condition to ensure the absence of artifacts is that the numerical solution becomes mesh-independent as the mesh size goes down. If this is not the case, there is obviously no convergence of the numerical solution to the one it is supposed to approximate.

It is important to note that the two difficulties inherent in solving fluid mechanical problems in corners 'interact': if the code gives rise to an artifact so that the numerical solution is mesh-dependent, then the more one resolves the mesh near the contact line, the more pronounced and unacceptable the artifact becomes.

We will show that an attempt to apply well-tested standard numerical methods to

the moving contact-line problem in a straightforward way can lead to a numerical artifact which is exacerbated as the mesh is refined. By stripping the moving contact-line problem of 'additional' difficulties, we show that even in the simplest case of a steady Stokes flow in a corner region, irrespective of a particular numerical implementation, in a certain range of corner angles the computed bulk pressure is mesh-dependent, as the code attempts to approximate a function which is multivalued at the corner. If the pressure multivaluedness is suppressed using numerical means, then the pressure and velocity fields no longer satisfy the original equations in the bulk. Neither of these options is satisfactory, and the persistent nature of the problem makes it necessary to handle it robustly, beginning by determining its origin.

In order to identify the origin of this behaviour of the numerical solution, we consider an even simpler case of the flow in a wedge formed by zero-tangential-stress boundaries, where an exact analytic solution is available. A comparison of the numerical results with this exact solution, which has a globally constant pressure, shows that the observed 'multivaluedness' of pressure is indeed a numerical artifact. Once the zero-tangential-stress boundary condition on one of the boundaries is replaced with the original inhomogeneous Robin-type condition, like the Navier-slip condition, the nature of the artifacts does not change, thus indicating that the artifact is the result of superposition of the spurious solution to the homogeneous (zero-tangential-stress) problem and the solution of the inhomogeneous problem.

The considered cases suggest that the conventional application of the standard numerical methods will lead to numerical artifacts not only in the modelling of dynamic wetting that uses the Navier-slip condition but also in its generalizations (see, for example, Thompson & Troian, 1997; Qian *et al.*, 2003), most notably for us, the interface formation model (Shikhmurzaev, 2007). Additionally, the artifacts will occur in other free-surface flows, like coalescence of liquid volumes (Shikhmurzaev, 2007) and the cusps/corners in the free surface generated by convergent flows (Joseph *et al.*, 1991; Shikhmurzaev, 2005), where

one has a corner flow with the boundary conditions of the same type. The method of removing numerical artifacts developed in the present work applies to all these flows in a straightforward way.

A.1 Problem formulation

Consider the two-dimensional steady viscous flow of an incompressible Newtonian fluid, with density ρ and viscosity μ, in a corner confined by straight boundaries located at $\theta = 0$ and $\theta = \alpha$ of a polar coordinate system (r, θ) in the plane of flow and the 'far field' boundary on an arc of a sufficiently large radius $r = R$ (Figure A.1c). Conventionally, we will refer to the $\theta = 0$ and $\theta = \alpha$ boundaries as the 'solid boundary' and the 'free surface', respectively. Finding the free-surface shape, which is planar only to leading order as $r \to 0$, is an additional, though rather standard, element of difficulty, not essential to the problem we are going to consider initially. The 'free surface' will be made genuinely free, with its shape to be determined, in §A.5.2. Here we are interested in the flow in a corner formed between a prescribed planar free surface and a solid boundary, so that the normal-stress boundary condition, used to find the free surface shape, is not required.

The flow is driven by the motion of a solid at $\theta = 0$, which slides with speed U parallel to itself, and, possibly, also by the far-field conditions. The speed U will be used as a scale for the fluid's velocity. For simplicity, we will assume that the velocity and length scales that characterize the flow are such that the Reynolds number Re based on these scales is small. Then as $Re \to 0$, to leading order in Re we may consider the Stokes flow. It should be emphasized that all essential results remain valid for the full Navier-Stokes equations since they come from the asymptotic behaviour of the solution as $r \to 0$. Considering the Stokes flow allows us to demonstrate the method we use to handle the pressure multivaluedness more clearly, without additional but nonessential details associated with handling nonlinear convective terms. These details are described

in §A.5.2.

For the problem in question, the non-dimensional Stokes equations for the bulk pressure p and the radial and azimuthal components of velocity (u, v) take the form

$$\frac{1}{r}\frac{\partial(ru)}{\partial r} + \frac{1}{r}\frac{\partial v}{\partial \theta} = 0, \qquad (0 < r < R,\ 0 < \theta < \alpha), \tag{A.1}$$

$$\frac{\partial p}{\partial r} = \Delta u - \frac{u}{r^2} - \frac{2}{r^2}\frac{\partial v}{\partial \theta}, \qquad \frac{1}{r}\frac{\partial p}{\partial \theta} = \Delta v - \frac{v}{r^2} + \frac{2}{r^2}\frac{\partial u}{\partial \theta}, \tag{A.2a,b}$$

where

$$\Delta = \frac{\partial^2}{\partial r^2} + \frac{1}{r}\frac{\partial}{\partial r} + \frac{1}{r^2}\frac{\partial^2}{\partial \theta^2}.$$

On the solid surface, for a solution not to have a multivalued velocity at the corner (Dussan V & Davis, 1974; Shikhmurzaev, 2007), we use the Navier slip condition (Navier, 1823), as opposed to the no-slip condition of classical fluid mechanics, and keep intact the impermeability condition for the normal component of velocity to the surface:

$$\frac{\partial u}{\partial \theta} = r\bar{\beta}(u - 1), \quad v = 0, \qquad (0 < r < R,\ \theta = 0). \tag{A.3a,b}$$

Here $\bar{\beta}$ is the dimensionless 'coefficient of sliding friction' (Lamb, 1932). In the limits $\bar{\beta} \to 0$ and $\bar{\beta} \to \infty$, one recovers the conditions of zero tangential stress (free slip) and no-slip, respectively. The value of $1/\bar{\beta}$ is proportional to a (non-dimensional) 'slip length' that characterizes the region where the velocity field specified with the help of the Navier condition (A.3a) deviates from the velocity field which would have been specified by no-slip.

On the free surface, we have the standard boundary conditions of zero tangential stress and impermeability:

$$\frac{\partial u}{\partial \theta} = 0, \quad v = 0, \qquad (0 < r < R,\ \theta = \alpha). \tag{A.4a,b}$$

The boundary conditions in the far field can be imposed in different ways. For simplicity, we will make the far-field conditions 'passive' and assume that

$$\frac{\partial u}{\partial r} = \frac{\partial v}{\partial r} = 0, \qquad (r = R,\ 0 < \theta < \alpha). \tag{A.5}$$

This condition is an adaptation for a finite domain of a boundary condition that would specify the asymptotic behaviour of the flow field at infinity. As is known (Moffatt, 1964), this condition is satisfied if the Navier slip condition (A.3a) is replace by no-slip (i.e. for $\bar{\beta} = \infty$ in (A.3a)), so that (A.5) can be seen as a condition that the disturbance caused by finiteness of $\bar{\beta}$ attenuates in the far field. In computations, for the far-field to have a negligible effect on the near-field flow, it is sufficient to put $R \geq 100/\bar{\beta}$.

Equations (A.1)–(A.5) fully specify the problem of interest.

A.2 Local asymptotics

The defining feature of our problem is the angle formed by two parts of the boundary and, for future references, it is useful to reproduce the leading-order asymptotics for the solution of (A.1)–(A.5) as $r \to 0$ (Shikhmurzaev, 2006, 2007). After introducing the stream function ψ by

$$u = \frac{1}{r}\frac{\partial \psi}{\partial \theta}, \quad v = -\frac{\partial \psi}{\partial r}, \tag{A.6a,b}$$

equations (A.1)–(A.2) are reduced to a biharmonic equation $\Delta^2 \psi = 0$ with boundary conditions (A.3)–(A.4) taking the form

$$\frac{\partial^2 \psi}{\partial \theta^2} = r\bar{\beta}\left(\frac{\partial \psi}{\partial \theta} - r\right), \quad \psi = 0, \qquad (\theta = 0,\ 0 < r < R), \tag{A.7a,b}$$

$$\frac{\partial^2 \psi}{\partial \theta^2} = 0, \quad \psi = 0, \qquad\qquad (\theta = \alpha,\ 0 < r < R). \qquad\qquad (A.8a,b)$$

Condition (A.7a), which is the only inhomogeneous boundary condition in the problem (i.e. the condition that drives the flow), suggests looking for the leading-order term of the local asymptotics in the form $\psi = r^2 F(\theta)$, which is one of a family of separable solutions to the biharmonic equation of the form $\psi = r^\lambda F(\theta)$. After substituting ψ into the biharmonic equation and boundary conditions (A.7)–(A.8), we have that

$$\psi = r^2 \left(B_1 + B_2 \theta + B_3 \sin 2\theta + B_4 \cos 2\theta \right), \qquad (A.9)$$

where the constants of integration B_i $(i = 1, \ldots, 4)$ are: $B_1 = -B_4 = -\bar{\beta}/4$, $B_2 = -B_1/\alpha$, $B_3 = B_1 \cot 2\alpha$.

The pressure field obtained from (A.2) using (A.6) and (A.9) has the form

$$p = \frac{\bar{\beta}}{\alpha} \ln r + p_0. \qquad (A.10)$$

where p_0 is a constant which sets the pressure level.

The most notable characteristics of the flow are that, as $r \to 0$, the velocity scales *linearly* with r whilst the pressure is *logarithmically* singular at the corner and does not depend on the angular coordinate θ. These simple features provide a quick test to determine whether there are any major issues with a numerical result.

A.3 Numerical results

The problem formulated in the previous section was solved using our numerical platform: flow in a wedge shaped domain is just a special, simple, case of the implementation described in §4.

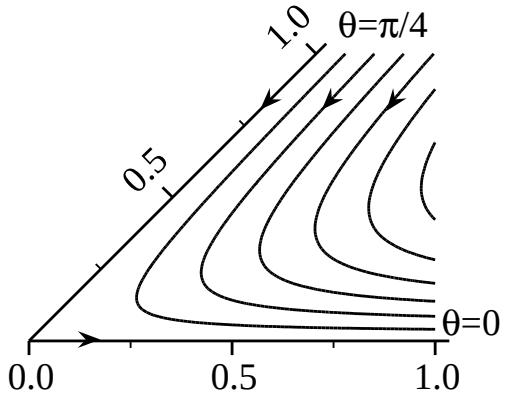

Figure A.2: Streamlines for $\alpha = \pi/4$ in increments of $\psi = 0.02$ with the boundaries at $\theta = 0$ and at $\theta = \alpha$ corresponding to $\psi = 0$.

As an additional test of the robustness of our numerical results and the ubiquity of the emerging numerical artifacts (described below) for the flows in the corner regions that we are examining here, these results have been verified for test cases using a commercially available code, COMSOL Multiphysics. All computations presented below correspond to $\bar{\beta} = 10$, $R = 10$; the runs in the process of investigation covered a wide range of parameters to ensure that the features described below are invariant with respect to variations of these parameters.

A.3.1 Acute wedge angles

First, we consider the case of $\alpha < \pi/2$ and show that our numerical results are in excellent agreement with the local asymptotics described earlier.

The streamlines in Figure A.2 illustrate the general features of the flow: motion is created by the relative movement of the solid surface with respect to the corner, and the fluid near the solid is pulled out of the corner by the moving substrate and, by continuity, it is replenished there by an inflow from the far field.

The pressure distribution near the corner in the form of isobars and, to make it easier to envisage, a 3-dimensional plot are shown in Figure A.3. As predicted by equation

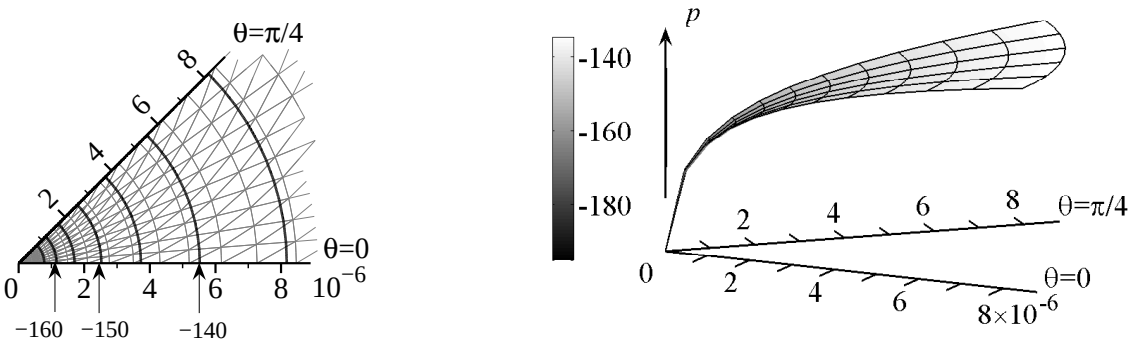

Figure A.3: Pressure distributions in the vicinity of the corner for $\alpha = \pi/4$. Left: pressure contours in steps of size 5, as the corner is approached with the underlying finite element mesh visible. Right: surface plot of pressure.

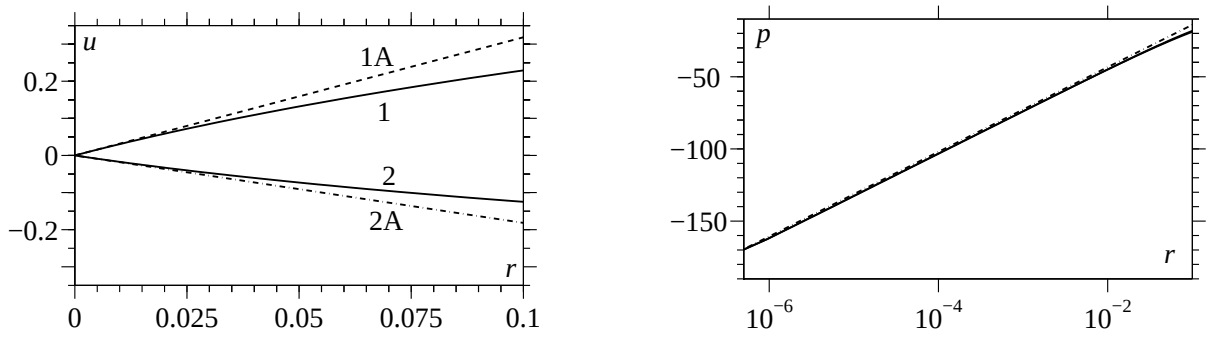

Figure A.4: Left: comparison of the computed radial velocity u along the liquid-solid interface 1 and liquid-gas interface 2 with the corresponding asymptotic results $1A$ and $2A$, respectively. Right: comparison of the computed pressure along the interfaces to the asymptotic result (dashed line).

(A.10) of the local asymptotics, the pressure in the vicinity of the corner is independent of θ.

The quantitative comparison of the computed velocity and pressure with those given by the asymptotics is shown in Figure A.4. As one can see, the agreement between numerical and analytic results for the distribution of velocity and pressure is excellent. The velocity is linear whilst the pressure, which is plotted in a semi-logarithmic frame, is logarithmic with the expected gradient. The pressure constant p_0 in (A.10) has been chosen to provide the best fit, but does not in any way determine the shape or gradient of the curve.

A.3.2 Obtuse angles: multivaluedness of pressure

In the previous subsection, we have shown that our algorithm gives excellent results for $\alpha < \pi/2$. However, for the angles $\alpha > \pi/2$ the situation changes. The same code, as well as COMSOL Multiphysics, that we used for comparison, produce results that are markedly mesh-dependent. This means that, at least, the numerical solution cannot be regarded as a uniformly valid approximation of the exact one, and, possibly, that it is completely spurious.

Figure A.5 shows the picture of streamlines near the corner. The flow is faster than that obtained for acute angles but, at first sight, there is no indication of any particular abnormality, at least on a qualitative level. However, when we examine the plots of the pressure distribution near the corner shown in Figure A.6, it becomes immediately clear that there are severe numerical issues. The smooth θ-independent pressure obtained for acute angles is now replaced by two huge spikes of differing signs at the nodes adjacent to the corner. The more we refine the mesh, the larger the spikes become. The distributions of velocity and pressure along the boundaries near the corner shown in Figure A.7 confirm that we have a problem to resolve. The numerical method implies single-valuedness for both velocity components and the pressure at the corner, and computations confirm single-valuedness of velocity[1] (Figure A.7). However, as one can see in Figure A.7, the velocity differs drastically from what is predicted by the asymptotics, most noticeably by not behaving linearly with radius. Furthermore, the asymptotics predicts that near the corner the flow along the free surface is in the upstream direction as the radial component of velocity along the free surface is positive. This is in stark contrast to the streamline pattern observed in Figure A.5, which shows a regular downstream flow with the velocity on the free surface directed towards the corner, as one may intuitively expect.

Although the problem with the computed velocity distribution is worrying, the situa-

[1]Its single-valuedness is ensured by the slip boundary condition (Dussan V & Davis, 1974; Dussan, 1979), whereas, numerically, once we assume all functions to be single-valued, the impermeability conditions make the corner a stagnation point.

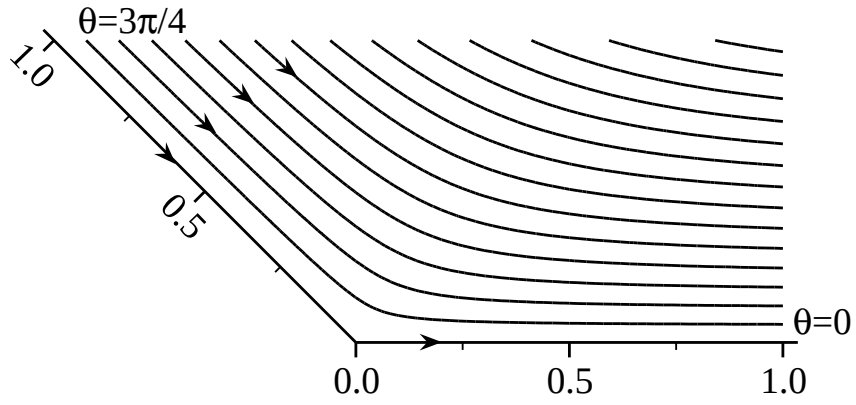

Figure A.5: Streamlines for $\alpha = 3\pi/4$ in increments of $\psi = 0.04$ with the boundaries at $\theta = 0$ and at $\theta = \alpha$ corresponding to $\psi = 0$.

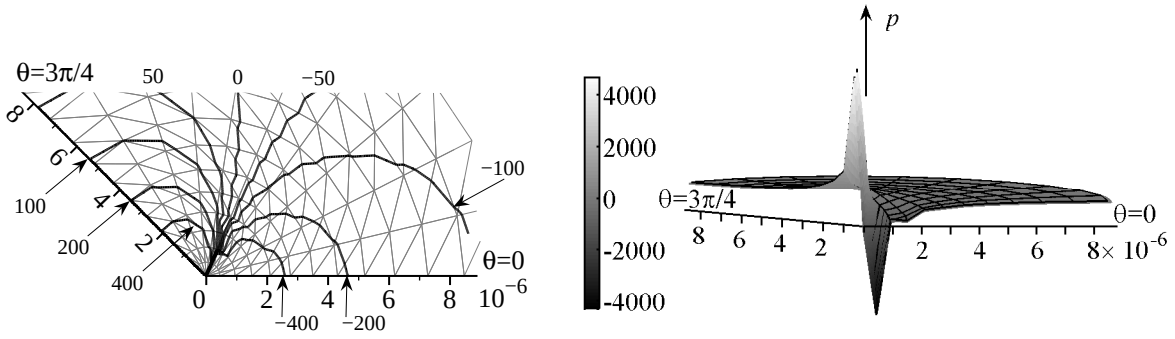

Figure A.6: Pressure distributions in the vicinity of the corner for $\alpha = 3\pi/4$. Left: pressure contours as the corner is approached with the underlying finite element mesh visible. Right: surface plot of pressure.

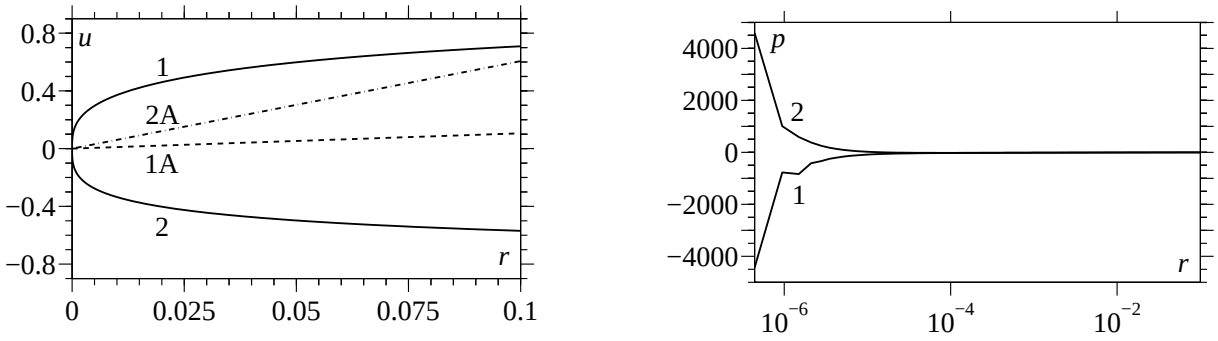

Figure A.7: Left: comparison of the computed radial velocity u along the liquid-solid interface 1 and liquid-gas interface 2 with the corresponding asymptotic results $1A$ and $2A$, respectively. Right: computed pressure along the interfaces.

tion with the pressure is even more severe. As one can see from Figure A.6 and Figure A.7, the numerical scheme is attempting to approximate a function which is both singular and multivalued at the corner. As one approaches the corner along different radii, the pressure behaves differently and tends to plus infinity along the radii closer to the free surface and to minus infinity along those closer to the solid boundary. Since the numerical scheme imposes (artificial) single-valuedness at the corner by stating that pressure has one value at the corner node, the code tries to reconcile the calculated pressure with this requirement over the first row of elements, thus creating the cliffs shown in Figure A.6. The numerical results are mesh-dependent: the smaller one makes the size of the first row of elements, the nearer the multivalued solution approaches the corner, and the higher the cliffs of pressure become. Obviously, the mesh-dependent numerical results cannot be regarded as a uniformly valid approximation of the actual solution to (A.1)–(A.5) and hence have to be rejected. As shown by the semi-logarithmic plot in Figure A.7, the singularity of pressure at the corner is also stronger than logarithmic (by plotting the pressure in the log-log frame one can show that it is actually algebraic with the exponent dependent on α).

It should be emphasized that the difficulties we are describing are above the level of a particular numerical implementation of a particular algorithm. It is not only that the code we used has been thoroughly validated (see the previous section); additionally, the commercially available code COMSOL Multiphysics has also been applied to the wedge flow problem for both acute and obtuse angles, and in all cases identical results have been recorded.

A.3.3 Remedies described in the literature

The encountered problem is resilient to standard approaches which have been described in the literature as successful remedies to spurious numerical effects. The first approach to be tried is to incorporate the asymptotic results described earlier in the numerical scheme

to 'come out' of the corner, thus bypassing any spurious effects that might have been caused by the geometry. The asymptotics can be matched with the numerical solution outside a given radius in a variety of ways. This approach has proved successful in similar situations in which corner singularities exist (see Shi *et al.*, 2004). However, it has been found that for our problem such an alteration of the scheme merely shifts the pressure cliff to the arc at the radius where the asymptotics has been applied. This is of no help whatsoever, since the results have all the deficiencies listed above.

Another standard approach is to impose penalties of various forms, similar to those used with equal-order interpolation to circumvent the LBB condition (see Baer *et al.*, 2000), but such a method simply fails to drive the code into a mesh-independent solution. The extent to which the penalties flatten the pressure cliffs is exactly the extent to which the numerical solution (to the 'penalized problem') departs from that which would satisfy the original problem discretized using the standard FEM. In other words, instead of driving the code to the 'right' solution, the penalty becomes part of the differential equations the code is solving, i.e. the method effectively replaces the original problem with a different one.

The pressure behaviour which we have described has previously been observed, suspected of being spurious and designated as the subject of future research in a paper on the finite element simulation of curtain coating (Wilson *et al.*, 2001). As is pointed out in this paper, a reason that the problem may have not been treated in other investigations is a lack of computational resolution. A rough indication of the region which must be resolved by any numerical scheme is the slip length, given by $1/\bar{\beta}$. Tests show that at least 100 nodes should be used along each radial-ray within this region. With the graded mesh we have used and for modern computers this requirement causes no problem. For a mesh with a single element size, achieving this is more difficult, as the numerical cost of having every element of size $0.01/\bar{\beta}$ could render the computational task untractable. It may be that this is the case in a number of older publications in which computational

power proved a major problem (see Kistler & Scriven, 1983; Christodoulou & Scriven, 1989). In our calculations presented here, the smallest element has the size of 4×10^{-7}, and we have 206 nodes inside the slip length along each radial-ray.

A.4 Origin of the pressure multivaluedness: a model situation with an analytic solution

At this stage, the question is whether the difficulty, albeit resilient to conventional alterations of the algorithm, is a numerical artifact, or whether at $\alpha > \pi/2$ the computed features are a genuine property of the mathematical problem. The robustness of the velocity distribution and the fact that, contrary to the asymptotics, its radial dependence is strongly nonlinear, with a singular radial derivative at the corner, suggest that here we might be dealing with an eigensolution, i.e. a solution satisfying homogeneous boundary conditions, $v = \partial u/\partial\theta = 0$ $(\theta = 0, \alpha)$, that superimposes on the one described by the asymptotics. Then, if the eigensolution for the velocity has indeed singular radial derivatives at the corner, the computed pressure behaviour could result from numerical errors in calculating the velocity field corresponding to this eigensolution.

An eigensolution to our problem has been known for a long time (see Moffatt, 1964, p. 14). In terms of the stream function, it has the same separable form as the asymptotic solution described in Section A.2:

$$\psi_e = Ar^{\lambda}\sin(\lambda\theta), \qquad \lambda = \pi/\alpha, \tag{A.11}$$

where A is an arbitrary constant.

This solution is promising for two reasons. Firstly, it is only for $\alpha > \pi/2$ that we have $\lambda < 2$ and hence this solution can dominate the one described by the local asymptotics (A.9) in the near field. Secondly, it exhibits the numerically computed non-linear radial

dependence of velocity. Note that, although the velocity of the eigensolution tends to zero at the corner, its radial dependence scales like $r^{\lambda-1}$, and hence for $\pi/2 < \alpha < \pi$ the derivatives of velocity in the radial direction are singular at the corner.

Surprisingly, the eigensolution (A.11) produces a *globally constant* pressure. This simplicity allows an ideal opportunity to check whether the spikes associated with the multivaluedness of pressure computed earlier are indeed numerical artifacts. In order to do this, we consider the flow in a corner region with the Navier slip condition replaced with zero tangential stress, i.e. with $\partial u/\partial\theta = 0$ and $v = 0$ on both boundaries $\theta = 0$ and $\theta = \alpha$. The flow can then be generated only by the boundary conditions in the far field which we set using the eigensolution (A.11), where, for simplicity, we use $A = 1/\lambda$:

$$u = r^{\lambda-1}\cos(\lambda\theta), \quad v = -r^{\lambda-1}\sin(\lambda\theta) \qquad (r = R,\ 0 < \theta < \alpha). \tag{A.12}$$

Then the eigensolution is the exact global solution to our test problem. As for the pressure distribution, once the pressure level has been set, say, to zero, then one will have $p \equiv 0$ in the whole domain.

Once this problem is computed numerically, the situation becomes clear. Figure A.9 shows the isobars and a 3-dimensional plot obtained using our code. The isobars and the 3-dimensional plot resemble those which we have already seen for the Navier condition in the previous section, with the same cliffs in the pressure profile at the nodes nearest to the corner. This is a remarkable result given that we know the global solution is in fact $p \equiv 0$! Thus, we may now conclude that the pressure cliffs are spurious and have a numerical origin.

The conclusion we arrived at is important: the spurious pressure spikes we described above have been reported in the literature — and they have been interpreted as a physical effect (e.g. Tilton, 1988). A thorough testing of the numerics near the corner, in particular a test for mesh-independence, would have allowed this error to be identified and make

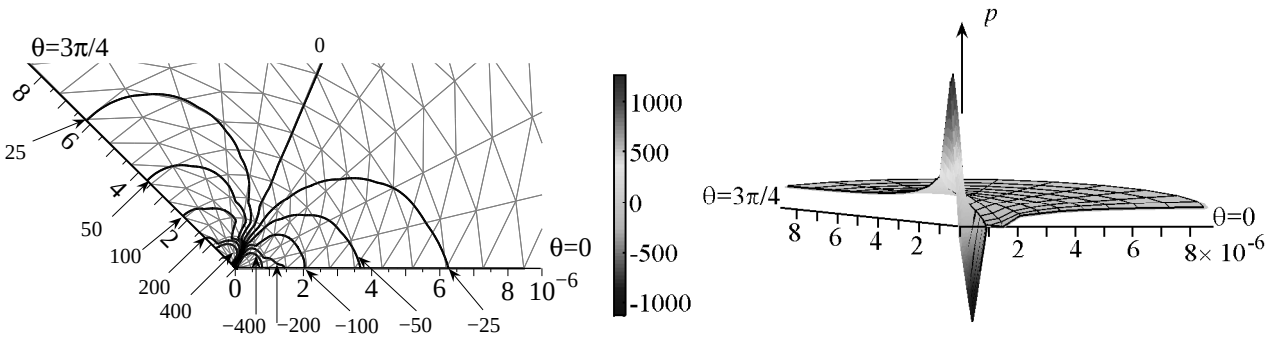

Figure A.8: Pressure distributions in the vicinity of the corner for $\alpha = 3\pi/4$ using our numerical code. The underlying finite element mesh is visible in both plots. Left: pressure contours as the corner is approached. Right: surface plot of pressure.

one consider the problem we are dealing with here.

A.4.1 Persistence of the problem

Exactly the same computational problem was solved using COMSOL Multiphysics. Here, the condition of impermeability and zero tangential stress is selected as a boundary condition by choosing boundary 'wall' and then choosing the type 'slip'. Once again, the V6P3 element is used, but now the mesh, visible for both plots in Figure A.9, has been generated by COMSOL using adaptive grid refinement techniques, and it is unstructured. At the end of the refinement procedure the mesh had $24,343$ elements and convergence was achieved when all of the residuals fell below 10^{-12}.

Figure A.9 shows the isobars and a 3-dimensional plot obtained using COMSOL Multiphysics. These results are in perfect quantitative agreement in the far field with what was obtained using our code and are seen to be similar in the near field (compare to Figure A.8); there is little point in comparing specific values in the near field as the results are seen to be mesh dependent for both codes.

The same spurious features of the numerical solution have been encountered for both the unstructured mesh of COMSOL and the structured mesh of our numerical code, thus suggesting that any alternative mesh design would not allow a route out of the problem.

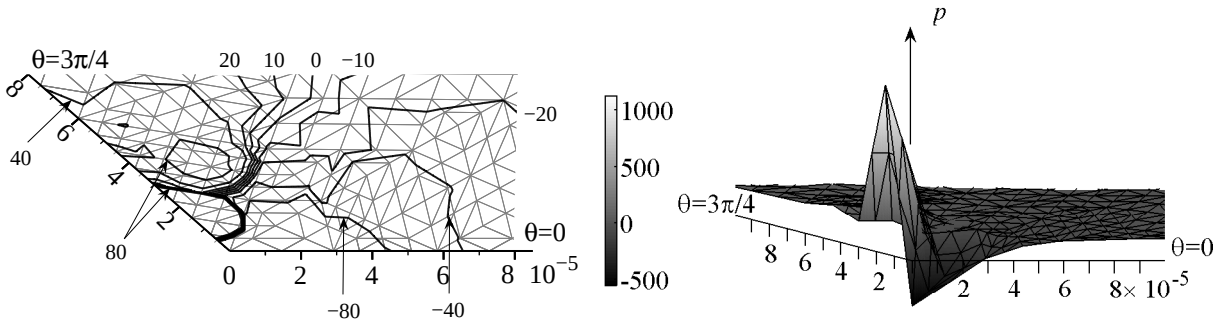

Figure A.9: Pressure distributions in the vicinity of the corner for $\alpha = 3\pi/4$ as calculated by COMSOL Multiphysics. The underlying finite element mesh is visible in both plots. Left: pressure contours as the corner is approached. Right: surface plot of pressure. The numerical artifacts are of the same nature as those shown in Figure A.8, although the mesh is completely different.

Additionally, COMSOL offers the choice of ten different elements, and, as we have tested, the choice of any of these elements does not affect the overall picture.

In the next section, we will show how the information we have about the eigensolution as the underlying cause of the problem can be used to resolve it.

A.5 Removal of pressure multivaluedness

First, we will describe the method of removing the pressure multivaluedness from the numerical solution of the problem formulated in Section 2, i.e. for the Stokes flow in a wedge region, and then show how the method can be 'localized' to apply to general 2-dimensional Navier-Stokes flows, both steady and unsteady, where an angle formed with the solid surface by *a priori* unknown free boundaries is but one element.

The key idea of the method is very simple. In the situation where, as in our case, the eigensolution is *the* cause of the pressure multivaluedness, we can subtract this solution from the problem and use the degree of freedom it offers, i.e. arbitrariness of A in (A.11), to ensure single-valuedness of pressure at the corner. Once the supplementary (to the eigensolution) velocity and pressure fields are computed, we can put the eigensolution,

i.e. the velocity field described by (A.11) and uniformly zero pressure, back. The resulting solution will have the analytically known eigencomponent of the velocity field superimposed on the numerically computed 'supplementary' flow and single-valued pressure, and it will satisfy the original equations and boundary conditions.

A.5.1 Simplest case: Stokes flow in a corner region

For the problem formulated in Section A.1, consider the velocity and pressure as sums of the eigensolution:

$$u_e = A\lambda r^{\lambda-1}\cos(\lambda\theta), \quad v_e = -A\lambda r^{\lambda-1}\sin(\lambda\theta), \quad p_e = 0, \qquad \text{(A.13}a,b,c\text{)}$$

where $\lambda = \pi/\alpha$, and the components to be computed (hereafter these are marked with a tilde):

$$(u, v, p) = (u_e, v_e, p_e) + (\tilde{u}, \tilde{v}, \tilde{p}). \qquad \text{(A.14)}$$

The constant A in (A.13a,b) is yet to be specified.

Since the eigensolution satisfies the Stokes equations (A.1)–(A.2) and the free surface boundary conditions (A.4) exactly, one has that $\tilde{u}$, $\tilde{v}$ and $\tilde{p}$ have to satisfy the unaltered Stokes equations (A.1)–(A.2) and boundary conditions (A.4), whereas the boundary conditions on the solid surface and in the far field for these variables will take the form

$$\frac{\partial\tilde{u}}{\partial\theta} = r\bar{\beta}\left(A\lambda r^{\lambda-1} + \tilde{u} - 1\right), \qquad \tilde{v} = 0, \qquad (0 < r < R, \theta = 0), \qquad \text{(A.15}a,b\text{)}$$

$$\frac{\partial\tilde{u}}{\partial r} = -A\lambda(\lambda-1)r^{\lambda-2}\cos(\lambda\theta), \quad \frac{\partial\tilde{v}}{\partial r} = A\lambda(\lambda-1)r^{\lambda-2}\sin(\lambda\theta),$$
$$(r = R,\ 0 < \theta < \alpha). \qquad \text{(A.16}a,b\text{)}$$

To complete the problem formulation for $\tilde{u}$, $\tilde{v}$ and $\tilde{p}$, we must add an equation to account

for the additional unknown constant A. To do so, we impose a condition that the pressure is single valued at the corner:

$$\lim_{r\to 0} \frac{\partial \tilde{p}}{\partial \theta} = 0. \tag{A.17}$$

Qualitatively, this condition can be explained as follows. The method is based on taking the eigensolution out of the total and hence ensuring that $(\tilde{u}, \tilde{v})$ do not have the singularity of the radial derivatives at the corner, and the numerical error in their computation will not give rise to the errors in computations of the pressure which result in its multivaluedness. By imposing (A.17), we are effectively ensuring that the eigensolution is taken out *fully* from the viewpoint of what this subtraction is aimed at achieving. In other words, out of a one-parametric family of eigensolutions, parameterised by the constant A, condition (A.17) selects the one that underpins the flow we are considering.

A simple way for us to impose (A.17) numerically is to demand that the pressures at the nodes nearest to the corner on the free surface and on the solid boundary are equal, as in our mesh they are equidistant from the corner.

Equations (A.1)–(A.2), (A.4), (A.15)–(A.17) have been solved using our numerical code with the same solution procedure as before. The streamlines of the supplementary flow obtained from the computation are shown in Figure A.10 alongside the streamlines to our original problem formulated in Section 2, obtained using (A.14). Although the underlying asymptotic solution predicts that there must be flow *reversal* near the corner, which is replicated in our numerical solution for $(\tilde{u}, \tilde{v})$, this feature is blown away by the strength of the eigensolution when it is superimposed on top.

The pressure plots in Figure A.11 show a qualitative transformation from those observed in previous sections: the pressure is now single valued, smooth and exhibits no mesh-dependence. Both the isobars and the 3D surface plot are now similar to those obtained earlier for acute angles (Figure A.3).

The comparison with the asymptotics of Section 3 is shown in Figure A.12 and A.13.

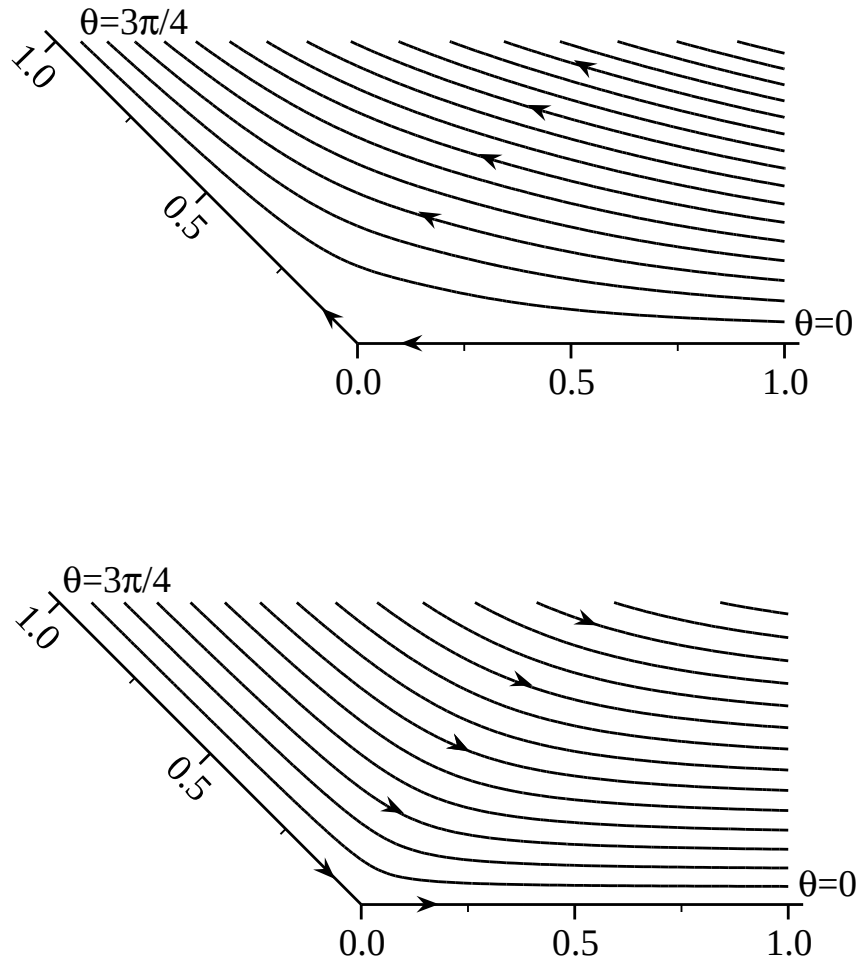

Figure A.10: Top: the computed streamlines in increments of $\psi = -0.04$. Bottom: the streamlines with the eigensolution superimposed to produce the full solution with increments of $\psi = 0.04$. In both plots $\alpha = 3\pi/4$ with the boundaries at $\theta = 0$ and at $\theta = \alpha$ corresponding to $\psi = 0$. The constant $A = 1.3026$.

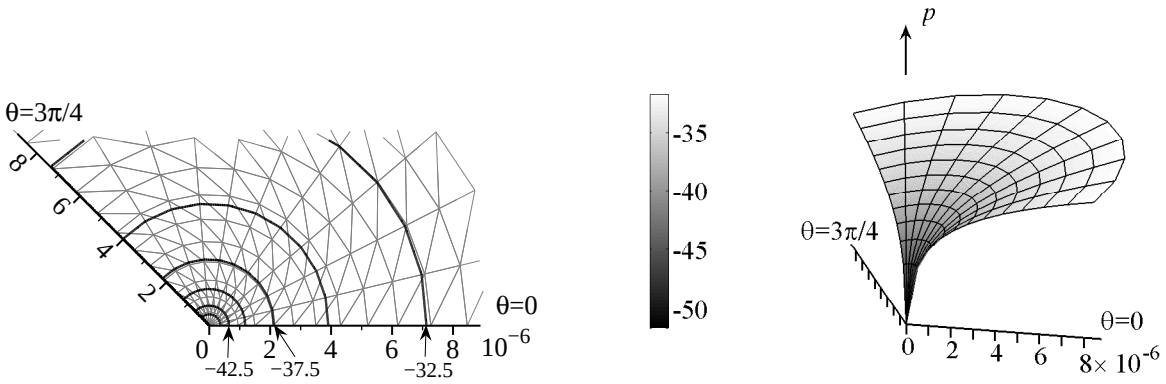

Figure A.11: Pressure distributions in the vicinity of the corner for $\alpha = 3\pi/4$ using our numerical platform with the eigensolution removed and $A = 1.3026$. Left: pressure contours in steps of size 2.5 as the corner is approached, with the underlying finite element mesh visible. Right: surface plot of pressure.

The agreement of pressure is visibly excellent. One can also observe that the radial velocity along the interfaces $\tilde{u}$ and its asymptotic prediction only coincide in a much smaller region than previously observed for acute angles. This is no surprise, given that the eigensolution now enters the Navier condition (A.15a), where the first term in brackets on the right-hand side becomes small compared to the last term only very close to the corner.

Interestingly, the dominance of the eigensolution in the combined solution for obtuse angles ensures that the velocity field near the corner is almost anti-symmetric about the centre line $\theta = \alpha/2$, whereas for acute angles this is not the case.

Thus, for the present problem of flow in a corner, we have fully resolved the situation. However, when considering more complicated flows, which involve a corner only as an element, the method of removing the eigensolution from the problem formulation throughout the entire domain could become unnecessarily complicated; the eigensolution is only important near one corner and yet it will make artificial contributions to equations and boundary conditions in the whole domain. A more reasonable approach would be to design a 'local' variant of the method to remove the eigensolution only near the corner, where its presence creates the unwanted numerical artifacts, leaving the rest of the flow

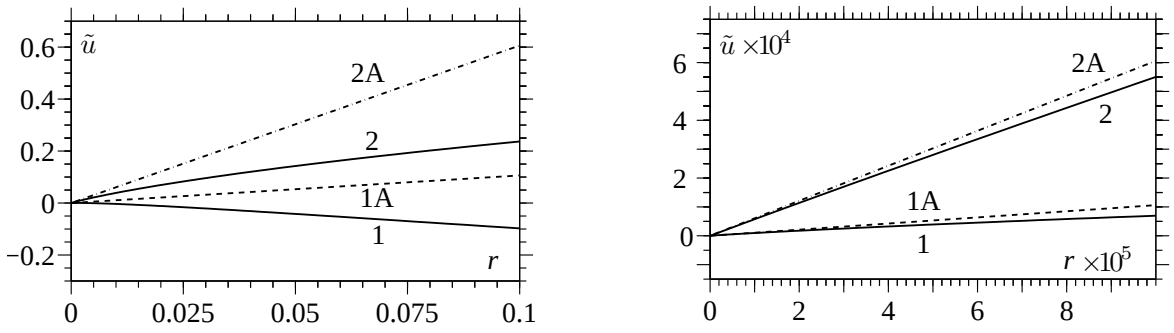

Figure A.12: Comparison of the computed radial velocity $\tilde{u}$ along the liquid-solid interface (1) and liquid-gas interface (2) with the asymptotic results (1A) and (2A), respectively, on the scale of the previous plots (left) and at a higher resolution (right).

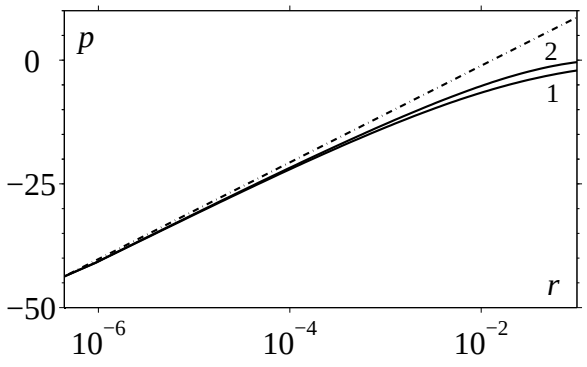

Figure A.13: Comparison of the computed ('actual') pressure along the liquid-solid (1) and liquid-gas (2) interface to the asymptotics (dashed line).

domain intact. This variant of the method is considered below.

A.5.2 General case: Navier-Stokes equations in domains with curvilinear free boundaries

We will begin by describing the pressure regularization method in its generic form and then illustrate it by considering two test problems: (a) a steady propagation of a meniscus in a channel with plane-parallel walls (Figure A.1a) and (b) an unsteady spreading of a (2-dimensional) liquid drop over a solid surface (Figure A.1b). Now, we have that the bulk flow is described by the full Navier-Stokes equations up to the corner (which, in accordance with the literature, we will now call the 'contact line') and the position of the curved free surface is *a priori* unknown.

After non-dimensionalizing the problem using characteristic length L and velocity U scales from the global flow the incompressible Navier-Stokes equations in the bulk are

$$\nabla \cdot \boldsymbol{u} = 0, \qquad Re\left[\tfrac{\partial \boldsymbol{u}}{\partial t} + \boldsymbol{u} \cdot \nabla \boldsymbol{u}\right] = \nabla \cdot \boldsymbol{P} + St\,\hat{\boldsymbol{g}},$$
$$\boldsymbol{P} = -p\boldsymbol{I} + \left[\nabla \boldsymbol{u} + (\nabla \boldsymbol{u})^T\right], \qquad \text{(A.18}a,b,c\text{)}$$

where $\boldsymbol{P}$ is the stress tensor; $\boldsymbol{I}$ is the metric tensor; $St = \rho L^2 g/(\mu U)$ is the Stokes number based on the acceleration due to gravity g and $\hat{\boldsymbol{g}}$ is a unit vector in the direction of the gravitational force.

On the flat solid surface, which moves at non-dimensional speed $\boldsymbol{U}_w$, we have the same Navier-slip and impermeability conditions as in §A.5.1:

$$\boldsymbol{n} \cdot \boldsymbol{P} \cdot (\boldsymbol{I} - \boldsymbol{nn}) = \bar{\beta}\,(\boldsymbol{u} - \boldsymbol{U}_w) \cdot (\boldsymbol{I} - \boldsymbol{nn}), \qquad (\boldsymbol{u} - \boldsymbol{U}_w) \cdot \boldsymbol{n} = 0, \qquad \text{(A.19}a,b\text{)}$$

where $\boldsymbol{n}$ is always the internal normal to an interface, so that the tensor $(\boldsymbol{I} - \boldsymbol{nn})$ extracts the tangential component of a vector.

On the free surface, which is defined by $f(\boldsymbol{x}, t) = 0$, where $\boldsymbol{x}$ is the position vector and the function f is to be found, we have the standard dynamic and kinematic conditions:

$$Ca\, \boldsymbol{n} \cdot \boldsymbol{P} = \boldsymbol{n} \nabla \cdot \boldsymbol{n}, \qquad \frac{\partial f}{\partial t} + \boldsymbol{u} \cdot \nabla f = 0, \tag{A.20a,b}$$

where $Ca = \mu U / \sigma$ is the capillary number based on the constant surface tension coefficient σ of the liquid-gas interface.

Both test problems may be slightly simplified by using that, in the plane of flow, both flow configurations are symmetric about a line perpendicular to the centre of the free surface.

On this line, we apply conditions of symmetry i.e. zero-tangential stress and impermeability:

$$\boldsymbol{n} \cdot \boldsymbol{P} \cdot (\boldsymbol{I} - \boldsymbol{n}\boldsymbol{n}) = 0, \qquad \boldsymbol{u} \cdot \boldsymbol{n} = 0. \tag{A.21a,b}$$

In each of the test problems, the free surface is bounded by the solid surface at one end, where, to avoid deviating from the main aspects of this paper, the dynamic contact angle is simply prescribed as a constant[2] α, and an axis of symmetry at the other end where we apply a condition ensuring the free surface remains smooth there.

In the case of the steadily propagating meniscus, we also have conditions in the far field which reflect the fact that the flow is fully developed there:

$$\frac{\partial \boldsymbol{u}}{\partial x} = 0. \tag{A.22a,b}$$

In order to 'localize' the pressure regularization method, we now introduce an artificial 'internal boundary' that will separate the 'inner' region near the contact line where the

[2]Our approach has been extended to the case in which the contact angle varies with time. Here we do not consider this as it is an additional aspect that interferes with the main issue.

regularization procedure will be used from the rest of the flow domain (the 'outer region'). Inside the inner region, we remove the eigensolution prior to computing the supplementary components of the velocity and pressure, and then superimpose it back, as we did in the previous subsection: this prevents the spurious pressure behaviour described in Sections 4 and 5. In the outer region, there is no need to alter the standard numerical approach to solving the appropriate equations (A.18)–(A.21). Solutions in both the inner and the outer region are computed simultaneously and have to be matched at the internal boundary.

Thus, after decomposing the solution in the inner region into the sum of the eigensolution and the supplementary part to be computed,

$$(\boldsymbol{u}, p) = (\boldsymbol{u}_e, 0) + (\tilde{\boldsymbol{u}}, \tilde{p}), \tag{A.23}$$

in the inner region we need to:

(i) Take into account the contribution of the eigensolution to the bulk equations (A.18) for $\tilde{\boldsymbol{u}}$ and $\tilde{p}$ arising from the fact that the eigensolution satisfies the Stokes equations, i.e. $\nabla \cdot \boldsymbol{u}_e = \nabla \cdot \boldsymbol{P}_e = 0$, where

$$\boldsymbol{P}_e = \left[\nabla \boldsymbol{u}_e + (\nabla \boldsymbol{u}_e)^T\right], \tag{A.24}$$

is the stress tensor of the eigensolution, but not the Navier-Stokes equations. Then we have:

$$\nabla \cdot \tilde{\boldsymbol{u}} = 0,$$
$$Re\left[\tfrac{\partial(\tilde{\boldsymbol{u}}+\boldsymbol{u}_e)}{\partial t} + (\tilde{\boldsymbol{u}} + \boldsymbol{u}_e) \cdot \nabla (\tilde{\boldsymbol{u}} + \boldsymbol{u}_e)\right] = \nabla \cdot \tilde{\boldsymbol{P}} + St\, \hat{\boldsymbol{g}}, \tag{A.25a,b}$$

where $\tilde{\boldsymbol{P}} = -\tilde{p}\boldsymbol{I} + \left[\nabla \tilde{\boldsymbol{u}} + (\nabla \tilde{\boldsymbol{u}})^T\right]$ is the stress tensor of the supplementary solution.

(ii) Take into account, as we did in §A.5.1, the contribution of the eigensolution to the

boundary conditions (A.19) for $\tilde{\boldsymbol{u}}$ on the solid surface:

$$\boldsymbol{n}\cdot\tilde{\boldsymbol{P}}\cdot(\boldsymbol{I}-\boldsymbol{nn}) = \bar{\beta}\,(\tilde{\boldsymbol{u}}+\boldsymbol{u}_e-\boldsymbol{U}_w)\cdot(\boldsymbol{I}-\boldsymbol{nn})\,,$$
$$(\tilde{\boldsymbol{u}}+\boldsymbol{u}_e-\boldsymbol{U}_w)\cdot\boldsymbol{n}=0, \qquad (A.26a,b)$$

where we have used that $\boldsymbol{n}\cdot\boldsymbol{P}_e\cdot(\boldsymbol{I}-\boldsymbol{nn})=0$.

(iii) Take into account the contribution of the eigensolution to the boundary conditions for $\tilde{\boldsymbol{u}}$ and $\tilde{p}$ on the free surface (A.20) that appears due to the fact that now the free surface, being genuinely free, is not necessarily planar, so that

$$Ca\,\boldsymbol{n}\cdot\left(\tilde{\boldsymbol{P}}+\boldsymbol{P}_e\right)=\boldsymbol{n}\nabla\cdot\boldsymbol{n}, \qquad \frac{\partial f}{\partial t}+(\tilde{\boldsymbol{u}}+\boldsymbol{u}_e)\cdot\nabla f=0. \qquad (A.27a,b)$$

(iv) Formulate the matching conditions at the internal boundary that would link $\tilde{\boldsymbol{u}}$ and $\tilde{p}$ with the outer flow. These conditions are necessary to calculate solutions in both the inner region and the outer region; these calculations are carried out simultaneously. At the internal boundary, we enforce continuity on the velocity and the stress:

$$\boldsymbol{u}_e+\tilde{\boldsymbol{u}}=\boldsymbol{u}_{out}, \qquad \boldsymbol{n}_i\cdot\left(\boldsymbol{P}_e+\tilde{\boldsymbol{P}}\right)=\boldsymbol{n}_i\cdot\boldsymbol{P}_{out}, \qquad (A.28a,b)$$

where $\boldsymbol{n}_i$ is a normal to the internal boundary and the subscript *out* marks the velocity and stress in the outer region that also have to be computed.

In the numerical implementation, care must be taken in the evaluation of the term $\boldsymbol{n}\cdot\boldsymbol{P}_e$ in (A.27a) as, although it is integrable, it is singular in the limit $r\to 0$. The term is best evaluated by calculating the stress tensor analytically, rather than using the finite element approximation, or whatever other discretization has been chosen, for the derivatives of the eigensolution's velocity components in (A.24).

An internal boundary separating the inner region from the outer flow should lie sufficiently far away from the contact line for the eigensolution to be well within the inner

region and at the same time not too far for the regularization method to be localized, as opposed to applied to an unnecessarily large region of the overall flow. Another consideration is how the position of the internal boundary correlates with the computational mesh. In our numerical method this is most easily achieved by using one of the arcs formed by the edges of the finite elements; the method is equally applicable for an algorithm with an unstructured mesh, though the ease of defining the internal boundary will be lost.

Conditions of continuity on the actual solution (A.28) can be applied in any numerical scheme, but are especially simple to implement in the finite element method where the continuity of stress across a boundary is naturally accounted for.

In order to illustrate how the method works, we consider a pair of two-dimensional test problems (the moving meniscus and the spreading drop) using a Cartesian frame $\boldsymbol{x} = (x, y)$ with a solid surface at $y = 0$. In our simulations, we fix the parameters to $Ca = 0.1$, $Re = 1$, $\bar{\beta} = 10$ whilst $St = 0$ for the propagating meniscus and $St = 1$ for the drop spreading. As our interest here lies in the numerical approximation of these flows, as opposed to a detailed comparison with experiment, we may consider, for simplicity, the dynamic contact angle to have a fixed value of $\alpha = 3\pi/4$.

The first test problem is the steady motion of a meniscus that a liquid-gas interface forms between plane-parallel walls. In a frame moving with the contact line, the problem is time-independent and hence the time derivatives in both the inner and outer region are zero. The velocity of the solid substrate in the moving reference frame is $\boldsymbol{U}_w = (1, 0)$.

Figure A.14 shows the velocity fields as they have been computed and the resulting (combined) velocity field. In the top picture, we can see the outer flow and a much weaker supplementary flow in the inner region. When the eigensolution is superimposed back on top of the supplementary velocity field in the inner region, the streamlines are seen to not feel the presence of the internal boundary — the matching conditions work perfectly leaving no 'scar' on the flow. As one can observe, peculiarities of the underlying (supplementary) flow in the inner region, such as flow reversal, are of little consequence

as their effect is negligible compared to that of the eigensolution. In the plots of pressure in this figure, we show both the pressure using our transition region, demonstrating no 'scar' on the pressure field, and additionally, to demonstrate the effect of our method, show the pressure computed for this problem without using our special approach.

Finally, we show that our method is equally applicable to time-dependent flows. As an illustration, we consider the spreading of a two-dimensional liquid drop over the solid surface, with the axis of symmetry at $x = 0$. The drop is driven from its initially cylindrical shape by gravity. In Figure A.15, we show a snapshot of the streamlines near the contact line in a frame moving with the contact line. The free surface is in a state of evolution and hence no longer represents a streamline. Again, a comparison of the two plots in the figure show that the position of the transition line does not effect the overall flow.

A.6 Conclusion

We have shown that straightforward application of a standard numerical method to a seemingly ordinary fluid-mechanical problem can lead to very persistent numerical artifacts, despite the fact that the conventional preliminary asymptotic analysis of a possible source of difficulties (the corner formed by smooth parts of the domain's boundary) does not flag up any concerns.

A surprising result from the present study is that errors in approximating the velocity field manifest themselves as spurious behaviour in the pressure field. This artifact could remain hidden if the spatial resolution of the code in the potentially problematic region is too low, but it will inevitably manifest itself in the mesh-dependence of the numerical results once the spatial resolution is increased. As we have shown, it is the presence of an underlying eigensolution that creates these numerical artifacts in the pressure distribution, despite the fact that the eigensolution itself has a globally constant pressure.

If the eigensolution is not removed prior to computations, one invariably ends up

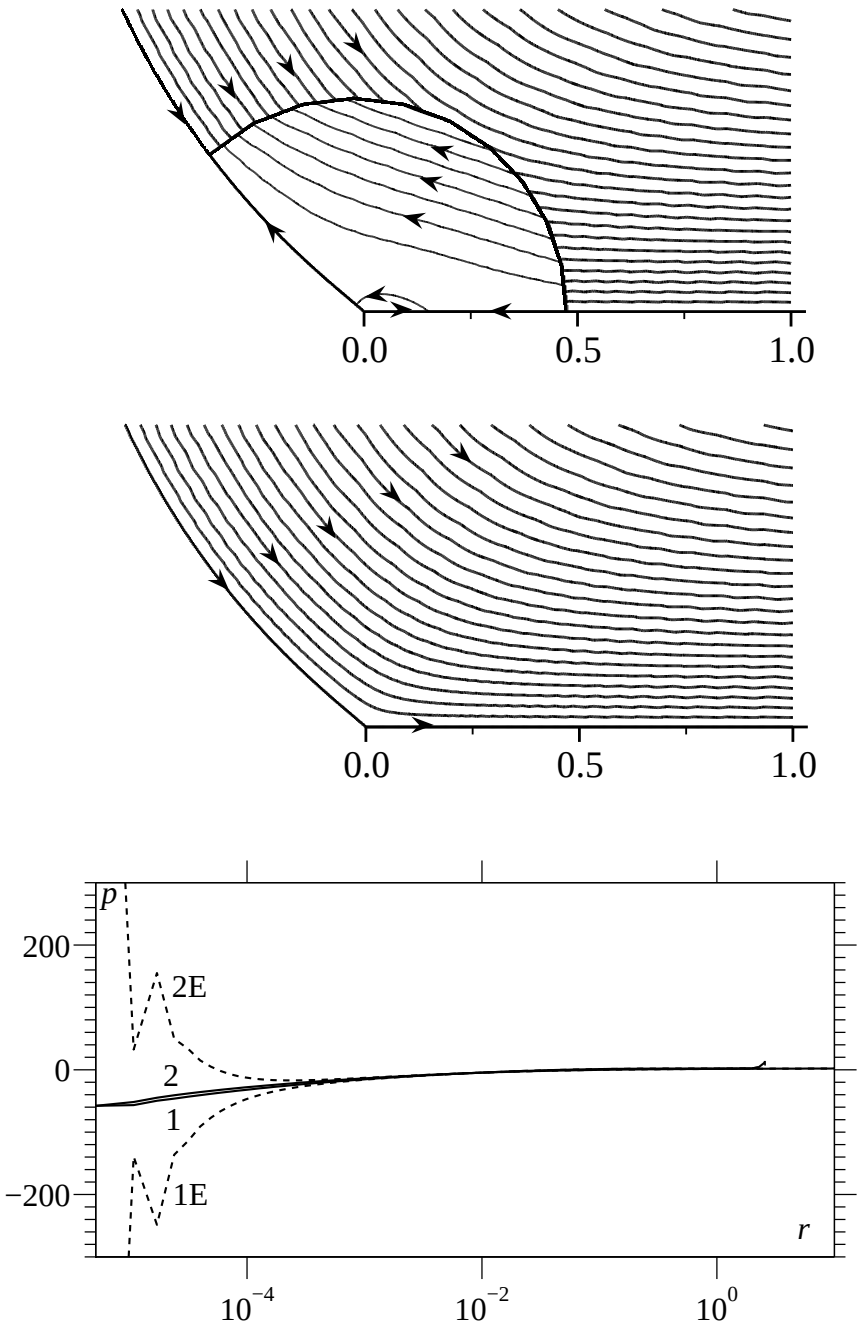

Figure A.14: Streamlines near the contact line of a propagating meniscus. The free surface and solid surface both correspond to $\psi = 0$. A is computed to be 1.4551. Top: streamlines of the calculated velocity field with increments of $\psi = -0.02$ in the inner region and $\psi = 0.02$ in the outer region. Middle: plot showing the actual streamlines obtained after superimposing the eigensolution with the calculated solution in the inner region. Bottom: plot of pressure along the liquid-solid (1) and liquid-gas (2) interfaces compared to those obtained with a standard approach (1E and 2E).

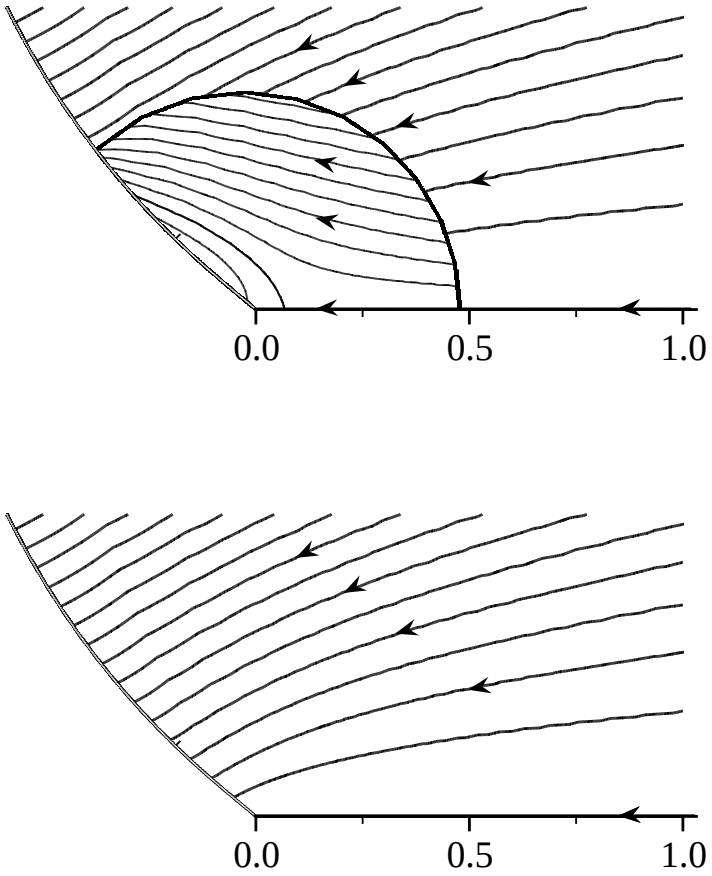

Figure A.15: Snapshot at $t = 1.5$ of the streamlines near the contact line in a spreading liquid drop. The solid surface corresponds to $\psi = 0$. A is computed to be 1.6025. Streamlines in all plots are in increments of $\psi = -0.05$. Top: plot showing the computed velocity field in both the inner and outer regions. Bottom: plot showing the actual streamlines obtained after superimposing the eigensolution with the calculated solution in the inner region.

with huge pressure spikes whose position and magnitude are both mesh-dependent. The numerical analysis indicates that the cause of this numerical instability is the errors in approximating the velocity gradient, as in the eigensolution this gradient is singular at the corner.

The 'mechanism' of this error generation could be the subject of a pure mathematical investigation, which could determine general conditions when cross-effects between the velocity and pressure lead to artifacts in the behaviour of one of these parameters in the numerical computations. This exciting new direction of research lies outside the scope of the present work.

The developed method of removing numerical artifacts in the pressure distribution is not only successful with respect to the model case of a steady two-dimensional Stokes flow in a corner region, but, as is shown, it admits a straightforward generalization which makes it applicable to a general case of unsteady free-boundary Navier-Stokes flow. In practical applications to problems of dynamic wetting one often has a situation where in the process of computations the contact angle varies in a wide range, from the angles where a standard numerical code produces no artifacts to those where the pressure spikes and multivaluedness invariably appear. General-purpose numerical algorithms should be developed so that the present method is turned off for acute angles, where the pressure is naturally single-valued, and switched on for obtuse angles to suppress spurious numerical behaviour.

The failure of standard numerical algorithms to approximate flow in a corner is not limited to the formulation considered in the present paper. For example, an alternative mathematical approach to the moving contact-line problem (Dussan V, 1976; Zhou & Sheng, 1990; Somalinga & Bose, 2000) is to prescribe the velocity as an explicit function of distance from the corner, so that, in a frame moving with the contact line, the velocity at the contact line is zero and it tends to the speed of the solid in the far field. When the Dirichlet conditions of this type are applied instead of the Navier-slip (i.e. Robin-type)

condition that we have examined, one again observes spurious numerical features, though in a different range of the corner angles to those presented here. This case is examined in Sprittles & Shikhmurzaev (2009*b*).

Bibliography

Afkhami, S., Zaleski, S. & Bussmann, M. 2009 A mesh-dependent model for applying dynamic contact angles to VOF simulations. *Journal of Computational Physics* **228**, 5370–5389.

Ashgriz, N. & Mashayek, F. 1995 Temporal analysis of capillary jet breakup. *Journal of Fluid Mechanics* **291**, 163–190.

Attané, P., Girard, F. & Morin, V. 2007 An energy balance approach of the dynamics of drop impact on a solid surface. *Physics of Fluids* **19**, 012101.

Attinger, D., Zhao, Z. & Poulikakos, D. 2000 An experimental study of molten microdroplet surface deposition and solidification: transient behavior and wetting angle dynamics. *Journal of Heat Transfer* **122**, 544–546.

Babuska, I. & Aziz, A.K. 1972 *Mathematical Foundations of the Finite Element Method with Applications to Partial Differential Equations*. Academic Press, New York.

Baer, T.A., Cairncross, R.A., Schunk, P.R., Rao, R.R. & Sackinger, P.A. 2000 A finite element method for free surface flows of incompressible fluids in three dimensions. Part 2. Dynamic wetting lines. *International Journal for Numerical Methods in Fluids* **33**, 405–427.

Basaran, O.A. 1992 Nonlinear oscillations of viscous liquid drops. *Journal of Fluid Mechanics* **241**, 169–198.

Bayer, I.S. & Megaridis, C.M. 2006 Contact angle dynamics in droplets impacting on flat surfaces with different wetting characteristics. *Journal of Fluid Mechanics* **558**, 415–449.

Beard, K.V., III, H.T. Ochs & Kubesh, R.J. 1989 Natural oscillations of small raindrops. *Nature* **342**, 408–410.

Bergeron, V., Bonn, D., Martin, J.Y. & Vovelle, L. 2000 Controlling droplet deposition with polymer additives. *Nature* **405**, 772–775.

Bergeron, V. & Quéré, D. 2001 Water droplets make an impact. *Physics World* .

Betelú, S., Diez, J., Thomas, L., Gratton, R. & Marino, B. 1997 A boundary element method for viscous gravity currents. *International Journal for Numerical Methods in Fluids* **25**, 1–19.

Blake, T.D., Bracke, M. & Shikhmurzaev, Y.D. 1999 Experimental evidence of nonlocal hydrodynamic influence on the dynamic contact angle. *AIChE Journal* **40**, 229–242.

Blake, T.D., Clarke, A. & Ruschak, K.J. 1994 Hydrodynamic assist of wetting. *AIChE Journal* **40**, 229–242.

Blake, T.D. & Shikhmurzaev, Y.D. 2002 Dynamic wetting by liquids of different viscosity. *Journal of Colloid and Interface Science* **253**, 196–202.

Bonn, D., Eggers, J., Indekeu, J., Meunier, J. & Rolley, E. 2009 Wetting and spreading. *Reviews of Modern Physics* **81**, 739–805.

Braun, H.G. & Meyer, E. 1999 Thin microstructured polymer films by surface-directed film formation. *Thin Solid Films* **345**, 222–228.

Burns, S.E., Cain, P., Mills, J., Wang, J. & Sirringhaus, H. 2003 Inkjet printing of polymer thin-film transistor circuits. *MRS Bulletin* **28**, 829–834.

Bussmann, M., Chandra, S. & Mostaghimi, J. 2000 Modeling the splash of a droplet impacting a solid surface. *Physics of Fluids* **12**, 3121–3132.

Cairncross, R.A., Schunk, P.R., Baer, T.A., Rao, R.R. & Sackinger, P.A. 2000 A finite element method for free surface flows of incompressible fluids in three dimensions. Part 1. Boundary fitted mesh motion. *International Journal for Numerical Methods in Fluids* **33**, 375–403.

Calvert, P. 2001 Inkjet printing for materials and devices. *Chemistry of Materials* **13**, 3299–3305.

Chandra, S. & Avedisian, C.T. 1991 On the collision of a droplet with a solid surface. *Proceedings: Mathematical and Physical Sciences* **432**, 13–41.

Chaudhury, M.K. & Whitesides, G.M. 1992 How to make water run uphill. *Science* **256**, 1539–1541.

Chen, Q., Ramé, E. & Garoff, S. 1997 The velocity field near moving contact lines. *Journal of Fluid Mechanics* **337**, 49–66.

Christodoulou, K.N., Kistler, S.F. & Schunk, P.R. 1997 Advances in computational methods for free surface flows. In *Liquid Film Coating*. Chapman & Hall.

Christodoulou, K.N. & Scriven, L.E. 1989 The fluid mechanics of slide coating. *Journal of Fluid Mechanics* **208**, 321–354.

Clarke, A. 1995 The application of particle tracking velocimetry and flow visualisation to curtain coating. *Chemical Engineering Science* **50**, 2397–2407.

Clarke, A., Blake, T.D., Carruthers, K. & Woodward, A. 2002 Spreading and imbibition of liquid droplets on porous surfaces. *Langmuir* **18**, 2980–2984.

Clarke, A. & Stattersfield, E. 2006 Direct evidence supporting nonlocal hydrodynamic influence on the dynamic contact angle. *Physics of Fluids* **18**, 048106.

Cox, R.G. 1986 The dynamics of the spreading of liquids on a solid surface. Part 1. Viscous flow. *Journal of Colloid and Interface Science* **168**, 169–194.

Daniel, S., Chaudhury, M.K. & Chen, J.C. 2001 Fast drop movements resulting from the phase change on a gradient surface. *Science* **291**, 633–636.

Darhuber, A.A. & Troian, S.M. 2005 Principles of microfluidic actuation by modulation of surface stresses. *Annual Review of Fluid Mechanics* **37**, 425–455.

Davidson, M.R. 2000 Boundary integral prediction of the spreading of an inviscid drop impacting on a solid surface. *Chemical Engineering Science* **55**, 1159–1170.

Davis, S.H. 2000 Interfacial fluid dynamics. In *Perspectives in Fluid Dynamics: A Collective Introduction to Current Research*. Cambridge University Press.

Davis, S.H. & Hocking, L.M. 1999 Spreading and imbibition of viscous liquid on a porous base. *Physics of Fluids* **11**, 48–57.

Davis, S.H. & Hocking, L.M. 2000 Spreading and imbibition of viscous liquid on a porous base. II. *Physics of Fluids* **12**, 1646–1655.

Ding, H. & Spelt, P.D.M. 2007 Journal of fluid mechanics **576**, 287–296.

Dong, H. 2006 Drop-on-demand inkjet drop formation and deposition. PhD thesis, Georgia Institute of Technology.

Dong, H., Carr, W.W., Bucknall, D.G. & Morris, J.F. 2007 Temporally-resolved inkjet drop impaction on surfaces. *AIChE Journal* **53**, 2606–2617.

Dupuis, A., Léopoldès, J., Bucknall, D.G. & Yeomans, J.M. 2005 Control of drop positioning using chemical patterning. *Applied Physics Letters* **87**, 024103.

Dupuis, A. & Yeomans, J.M. 2004 Lattice Boltzmann modelling of droplets on chemically heterogenous surfaces. *Future Generation Computer Systems* **20**, 993–1001.

Dussan, E.B. 1979 On the spreading of liquids on solid surfaces: Static and dynamic contact lines. *Annual Review of Fluid Mechanics* **11**, 371–400.

Dussan V, E.B. 1976 The moving contact line: The slip boundary condition. *Journal of Fluid Mechanics* **77**, 665–684.

Dussan V, E.B. & Davis, S.H. 1974 On the motion of a fluid-fluid interface along a solid surface. *Journal of Fluid Mechanics* **65**, 71–95.

Eggers, J. 2004 Toward a description of contact line motion at higher capillary numbers. *Physics of Fluids* **16**, 3491–3494.

Fortin, M. 1981 Old and new finite elements for incompressible flows. *International Journal for Numerical Methods in Fluids* **1**, 347–364.

Fukai, J., Miyatake, O., Poulikakos, D., Megaridis, C.M. & Zhao, Z. 1993 Modeling of the deformation of a liquid droplet impinging upon a flat surface. *Physics of Fluids A* **5**, 2588–2599.

Fukai, J., Shiiba, Y., Yamamoto, T., Miyatake, O., Poulikakos, D., Megaridis, C.M. & Zhao, Z. 1995 Wetting effects on the spreading of a liquid droplet colliding with a flat surface: Experiment and modeling. *Physics of Fluids* **7**, 236–247.

Fukai, J., Tanaka, M. & Miyatake, O. 1998 Maximum spreading of liquid droplets colliding with flat surfaces. *Journal of Chemical Engineering of Japan* **31**, 456–461.

Ganesan, S. 2006 Finite element methods on moving meshes for free surface and interface flows. PhD thesis, Otto-von-Guericke University.

Gao, F. & Sonin, A.A. 1994 Precise deposition of molten microdrops: The physics of digital microfabrication. *Proceedings: Mathematical and Physical Sciences* **444**, 533–554.

Gau, H., Herminghaus, S., Lenz, P. & Lipowsky, R. 1999 Liquid morphologies on structured surfaces: From microchannels to microchips. *Science* **283**, 46–49.

Gentner, F., Rioboo, R., Baland, J.P. & De Coninck, J. 2004 Low inertia impact dynamics for nanodrops. *Lamgmuir* **20**, 4748–4755.

Gresho, P.M. & Sani, R.L. 1999*a* *Incompressible Flow and the Finite Element Method. Volume 1. Advection-Diffusion*. John Wiley & Sons, LTD.

Gresho, P.M. & Sani, R.L. 1999*b* *Incompressible Flow and the Finite Element Method. Volume 2. Isothermal Laminar Flow*. John Wiley & Sons, LTD.

Grissom, W.M. & Wierum, F.A. 1981 Liquid spray cooling of a heated surface. *International Journal of Heat and Mass Transfer* **24**, 261–271.

Gupta, K.K. & Meek, J.L. 1996 A brief history of the beginning of the finite element method. *International Journal for Numerical Method in Engineering* **79**, 209–229.

Harlow, F.H. & Shannon, J.P. 1967 The splash of a liquid drop. *Journal of Applied Physics* **38**, 3855–3866.

Heil, M. 2004 An efficient solver for the fully-coupled solution of large displacement fluid-structure interaction problems. *Computer Methods in Applied Mechanics and Engineering* **193**, 1–23.

Hocking, L.M. 1977 A moving fluid interface. Part 2. The removal of the force singularity by a slip flow. *Journal of Fluid Mechanics* **79**, 209–229.

Hocking, L.M. & Rivers, A.D. 1982 The spreading of a drop by capillary action. *Journal of Fluid Mechanics* **121**, 425–442.

Hoffman, R.L. 1975 Study of the advancing interface. *Journal of Colloid and Interface Science* **50**, 228–241.

Holman, R.K., Cima, M.J., Uhland, S.A. & Sachs, E. 2002 Spreading and infiltration of ink-jet printed polymer solution droplets on a porous substrate. *Journal of Colloid Science* **249**, 432–440.

Hong, C.M. & Wagner, S. 1999 Inkjet printed copper source/drain metallization for amorphous silicon thin-film transistors. *IEEE Electron Device Letters* **21**, 384–386.

Huh, C. & Scriven, L.E. 1971 Hydrodynamic model of steady movement of a solid/liquid/fluid contact line. *Journal of Colloid and Interface Science* **35**, 85–101.

Jansons, K.M. 1985 Moving contact line on a two-dimensional rough surface. *Journal of Fluid Mechanics* **154**, 1–28.

Jansons, K.M. 1987 Determination of the macroscopic (partial) slip boundary condition for a viscous flow over a randomly rough surface with a perfect slip microscopic boundary condition. *Physics of Fluids* **31**, 15–17.

Jiang, T.S., Oh, S.G. & Slattey, J.C. 1979 Correlation for dynamic contact angle. *Journal of Colloid and Interface Science* **69**, 74–77.

Jimack, P.K. & Wathen, A.J. 1991 Temporal derivatives in the finite-element method on continuously deforming grids. *SIAM Journal on Numerical Analysis* **28**, 990–1003.

Joseph, D.D., Nelson, J., Renardy, M. & Renardy, Y. 1991 Two-dimensional cusped interfaces. *Journal of Fluid Mechanics* **223**, 383–409.

Khatavkar, V.V., Anderson, P.D., Duineveld, P.C. & Meijer, H.E.H. 2007 Diffuse-interface modelling of droplet impact. *Journal of Fluid Mechanics* **581**, 97–127.

Kikuchi, N. & Oden, J.T. 1988 *Contact Problems in Elasticity*. SIAM, Studies in Applied Mathematics.

Kim, H.-Y. & Chun, J.-H. 2001 The recoil of liquid droplets upon collision with solid surfaces. *Physics of Fluids* **13**, 643–659.

Kim, H.-Y., Feng, Z.C. & Chun, J.H. 2000 Instability of a liquid jet emerging from a droplet upon collision with a solid surface. *Physics of Fluids* **12**, 531–541.

Kistler, S.F. 1993 Hydrodynamics of wetting. In *Wettability*. Marcel Dekker.

Kistler, S.F. & Scriven, L.E. 1983 Coating flows. In *Computational Analysis of Polymer Processing*. Elsevier Science Publishing Company, New York.

Kochurova, N.N. & Rusanov, A.I. 1981 Dynamic surface properties of water: surface tension and surface potential. *Journal of Colloid and Interface Science* **81**, 297–303.

Lam, C.N.C., Ko, R.H.Y., Yu, L.M.Y., Ng, A., Li, D., Hair, M.L. & Neumann, A.W. 2001 Dynamic cycling contact angle measurements: Study of advancing and receding contact angles. *Journal of Colloid and Interface Science* **243**, 208–218.

Lamb, H. 1932 *Hydrodynamics*. Dover, New York.

Langtangen, H.P., Mardal, K. & Winther, R. 2002 Numerical methods for incompressible viscous flow. *Advances in Water Resources* **25**, 1125–1146.

Lauga, E. & Stone, H.A. 2003 Effective slip in pressure-driven Stokes flow. *Journal of Fluid Mechanics* **489**, 55–77.

Lesser, M.B. & Field, J.E. 1983 The impact of compressible liquids. *Annual Review of Fluid Mechanics* **15**, 97–122.

Lewis, P.E. & Ward, J.P. 1991 *Finite Element Method. Principles and Applications*. Addison Wesley.

Lim, T., Han, S., Chung, J., Chung, J.T. & Ko, S. 2009 Experimental study on spreading and evaporation of inkjet printed pico-liter droplet on a heated substrate. *International Journal of Heat and Mass Transfer* **52**, 431441.

Lötstedt, P. & Petzold, L. 1986 Numerical solution of nonlinear differential equations with algebraic constraints 1: Convergence results for backward differentiation formulas. *Mathematics of Computation* **46**, 491–516.

Lukyanov, A.V. & Shikhmurzaev, Y.D. 2007 A combined BIE-FE method for the Stokes equations. *IMA Journal of Applied Mathematics* .

Maier, C., Wiesche, S. & Hofer, E.P. 2000 Impact of microdrops on solid surfaces for DNA-synthesis. In *Proceedings of the 2000 International Conference on Modeling and Simulation of Microsystems*.

Mao, T., Kuhn, D.C.S. & Tran, H. 1997 Spread and rebound of liquid droplets upon impact on flat surfaces. *AIChE Journal* **43**, 2169–2179.

Mavriplis, D.J. 1997 Unstructured grid techniques. *Annual Review of Fluid Mechanics* **29**, 473–514.

Mehdi-Nejad, V., Mostaghimi, J. & Chandra, S. 2003 Air bubble entrainment under an impacting droplet. *Physics of Fluids* **15**, 173–183.

Meradji, S., Lyubimova, T.P., Lyubimov, D.V. & Roux, B. 2001 Numerical simulation of a liquid drop freely oscillating. *Crystal Research and Technology* **36**, 729–744.

Michel, T., Mock, U., Roisman, I.V., Rühe, J. & Tropea, C. 2005 The hydrodynamics of drop impact onto chemically structured surfaces. *Journal of Physics: Condensed Matter* **17**, 607–622.

Mock, U., Michel, T., Tropea, C., Roisman, I.V. & Rühe, J. 2005 Drop impact on chemically structured arrays. *Journal of Physics: Condensed Matter* **17**, 595–605.

Moffatt, H.K. 1964 Viscous and resistive eddies near a sharp corner. *Journal of Fluid Mechanics* **18**, 1–18.

Navier, C.L.M.H. 1823 Mémoire sur les lois du mouvement des fluides. *Mém. de l'Acad. de Sciences l'Inst. de France* **6**, 389–440.

Ngan, C.G. & Dussan V, E.B. 1982 On the nature of the dynamic contact angle: an experimental study. *Journal of Fluid Mechanics* **118**, 27–40.

Park, H., Carr, W.W., Zhu, J. & Morris, J.F. 2003 Single drop impaction on a solid surface. *AIChE Journal* **49**, 2461–2471.

Pasandideh-Fard, M., Qiao, Y.M., Chandra, S. & Mostaghimi, J. 1996 Capillary effects during droplet impact on a solid surface. *Physics of Fluids* **8**, 650–659.

Perelaer, J., Smith, P.J., van den Bosch, E., van Grootel, S.S.C., Ketelaars, P.H.M.J. & Schubert, U.S. 2009 The spreading of inkjet-printed droplets with varying polymer molar mass on a dry solid substrate. *Macromolecular chemistry and physics* **210**, 495–502.

Petrov, J.G., Ralston, J., Schneemilch, M. & Hayes, R.A. 2003 Dynamics of partial wetting and dewetting in well-defined systems. *Journal of Physical Chemistry B* **107**, 1634–1645.

Priezjev, N.V., Darhuber, A.A. & Troian, S.M. 2005 Slip behaviour in liquid films on surfaces of patterned wettability: Comparison between continuum and molecular dynamics simulations. *Physical Review E* **71**, 041608.

Qian, T., Wang, X. & Sheng, P. 2003 Molecular scale contact line hydrodynamics of immiscible flows. *Physical Review E* **68**, 016306.

Qian, T., Wang, X. & Sheng, P. 2005 Hydrodynamic slip boundary condition at chemically patterned surfaces: A continuum deduction from molecular dynamics. *Physical Review E* **72**, 022501.

Ramos, S.M.M., Charlaix, E., Benyagoub, A. & Toulemonde, M. 2003 Wetting on nanorough surfaces. *Physical Review E* **67**, 031604.

Rayleigh, J.W.S. 1879 On the capillary phenomena of jets. *Proceedings of the Royal Society of London* **29**, 71–97.

Rein, M. 1993 Phenomena of liquid drop impact on solid and liquid surfaces. *Fluid Dynamics Research* **12**, 61–93.

Renardy, Y., Popinet, S., Duchemin, L., Renardy, M., Zaleski, S., Josserand, C., Drumright-Clarke, M.A., Richard, D., Clanet, C. & Quéré, D. 2003 Pyramidal and toroidal water drops after impact on a solid surface. *Journal of Fluid Mechanics* **484**, 69–83.

Rioboo, R., Marengo, M. & Tropea, C. 2002 Time evolution of liquid drop impacts onto solid, dry surfaces. *Experiments in Fluids* **33**, 112–124.

Rowlinson, J.S. & Widom, B. 1982 *Molecular Theory of Capillarity*. Clarendon Press, Oxford.

Ruckenstein, E. & Jain, R.K. 1974 Spontaneous rupture of thin liquid films. *Journal of the Chemical Society, Faraday Transactions* **70**, 132–147.

Ruschak, K.J. 1980 A method for incorporating free boundaries with surface tension in finite element fluid-flow simulators. *International Journal for Numerical Methods in Engineering* **15**, 639–648.

Saha, A.A. & Mitra, S.K. 2009 Numerical study of capillary flow in microchannels with alternate hydrophilic-hydrophobic bottom wall. *Journal of Fluids Engineering* **131**, 639–648.

Scardovelli, R. & Zaleksi, S. 1999 Direct numerical simulation of free-surface and interfacial flow. *Annual Review of Fluid Mechanics* **31**, 061202.

Schiaffino, S. & Sonin, A.A. 1997 Molten droplet deposition and solidification at low Weber numbers. *Physics of Fluids* **9**, 3172–3187.

Schönfeld, F. & Hardt, S. 2009 Dynamic contact angles in CFD simulations. *Computers and Fluids* **38**, 757–764.

Sedov, L.I. 1965 *Two-dimensional Problems of Hydrodynamics and Aerodynamics*. Interscience.

Shaw, A. 2005 Coalescence of two liquid volumes. PhD thesis, The University of Birmingham.

Shi, J.-M., Breuer, M. & Durst, F. 2004 A combined analytical-numerical method for treating corner singularities in viscous flow predictions. *International Journal for Numerical Methods in Fluids* **45**, 659–688.

Shikhmurzaev, Y.D. 1993 The moving contact line on a smooth solid surface. *International Journal of Multiphase Flow* **19**, 589–610.

Shikhmurzaev, Y.D. 1997*a* Moving contact lines in liquid/liquid/solid systems. *Journal of Fluid Mechanics* **334**, 211–249.

Shikhmurzaev, Y.D. 1997*b* Spreading of drops on solid surfaces in a quasi-static regime. *Physics of Fluids* **9**, 266–275.

Shikhmurzaev, Y.D. 2005 Singularity of free-surface curvature in convergent flow: Cusp or corner? *Physics Letters A* **345–385**, 378.

Shikhmurzaev, Y.D. 2006 Singularities at the moving contact line. Mathematical, physical and computational aspects. *Physica D* **217**, 121–133.

Shikhmurzaev, Y.D. 2007 *Capillary Flows with Forming Interfaces*. Chapman & Hall/CRC, Roca Raton.

Somalinga, S. & Bose, A. 2000 Numerical investigation of boundary conditions for moving contact line problems. *Physics of Fluids* **12**, 499–510.

Sprittles, J.E. 2007 Dynamic wetting/dewetting processes in complex liquid-solid systems: MPhil(qual) .

Sprittles, J.E. & Shikhmurzaev, Y.D. 2007 Viscous flow over a chemically patterned surface. *Physical Review E* **76**, 021602.

Sprittles, J.E. & Shikhmurzaev, Y.D. 2009*a* A continuum model for the flow of thin liquid films over intermittently chemically patterned surfaces. *The European Physical Journal Special Topics* **166**, 159–163.

Sprittles, J.E. & Shikhmurzaev, Y.D. 2009*b* Viscous flow in corner regions: Singularities and hidden eigensolutions. *International Journal for Numerical Methods in Fluids (To Appear)* .

Squires, T.M. & Quake, S.R. 2005 Microfluidics: Fluid physics at the nanoliter scale. *Reviews of Modern Physics* **77**, 977–1026.

Suckling, P.M. 2003 The impact and spreading of a drop on a surface. PhD thesis, The University of Birmingham.

Summers, J.L., Wilson, M.C.T., Lee, Y.C., Gaskell, P.H., Kapur, N. & Thompson, H.M. 2005 An assessment of the lattice Boltzmann methods for coating flow simulation. In *6th European Coating Symposium*.

Tanner, L.H. 1979 The spreading of silicone drops on horizontal surfaces. *Journal of Physics D: Applied Physics* **12**, 1473–1484.

Templeton, C.C. & Rushing, S.S 1956 Oil-water displacements in microscopic capillaries. *Journal of Petroleum Technology* **8**, 211–214.

Thompson, P.A. & Troian, S.M. 1997 A general boundary condition for liquid flow at solid surface. *Nature* **389**, 360–362.

Tilton, J.N. 1988 The steady motion of an interface between two viscous liquids in a capillary tube. *Chemical Engineering Science* **43**, 1371–1384.

Šikalo, Š., Marengo, M., Tropea, C. & Ganic, E.N. 2002 Analysis of impact of droplets on horizontal surfaces. *Experimental Thermal and Fluid Science* **25**, 503–510.

Šikalo, Š., Wilhelm, H.-D., Roisman, I.V., Jakirlić, S. & Tropea, C. 2005 Dynamic contact angle of spreading droplets: Experiments and simulations. *Physics of Fluids* **17**, 062103.

Van Dam, D.B. & Le Clerc, C. 2004 Experimental study of the impact of an ink-jet printed droplet on a solid substrate. *Physics of Fluids* **16**, 3403–3414.

Washburn, E.W. 1921 The dynamics of capillary flow. *Physical Review* **17**, 273–283.

Weinstein, O. & Pismen, L.M. 2008 Scale dependence of contact line computations. *Mathematical Modelling of Natural Phenomena* **3**, 98–107.

Wilson, M.C.T., Summers, J.L., Gaskell, P.H. & Shikhmurzaev, Y.D. 2001 Moving contact-line models and the effect of hydrodynamic assist of dynamic wetting. In *IUTAM Symposium on Free Surface Flows* (ed. A.C. King & Y.D. Shikhmurzaev). Kluwer Academic Publishers.

Wilson, M.C.T., Summers, J.L., Shikhmurzaev, Y.D., Clarke, A. & Blake, T.D. 2006 Nonlocal hydrodynamic influence on the dynamic contact angle: Slip models versus experiment. *Physical Review E* **83**, 041606.

Worthington, A.M. 1876-1877 On the forms assumed by drops of liquids falling vertically on a horizontal plate. *Proceedings of the Royal Society of London* **25**, 261–272.

Xia, Y., Qin, D. & Yin, Y. 2001 Surface patterning and its application in wetting/dewetting studies. *Current Opinion in Colloid & Interface Science* **6**, 54–64.

Xu, L., Zhang, W. & Nagel, S.R. 2005 Drop splashing on a dry smooth surface. *Physical Review Letters* **94**, 184505.

Yarin, A.L. 2006 Drop impact dynamics: Splashing, spreading, receding, bouncing... *Annual Review of Fluid Mechanics* **38**, 159–192.

Yokoi, K., Vadillo, D., Hinch, J. & Hutchings, I. 2009 Numerical studies of the influence of the dynamic contact angle on a droplet impacting on a dry surface. *Physics of Fluids* **21**, 072102.

Young, T. 1805 An essay on the cohesion of fluids. *Philosophical Transactions of the Royal Society (London)* **95**, 65–87.

Zhao, B., Moore, J.S. & Beebe, D.J. 2001 Surface-directed liquid flow inside microchannels. *Science* **291**, 1023–1026.

Zhou, M. & Sheng, P. 1990 Dynamics of immiscible-fluid displacement in a capillary tube. *Physical Review Letters* **64**, 882–885.

Zienkiewicz, O.C. & Taylor, R.L. 1989 *The finite element method*. McGraw-Hill.